TECHNISCHE UNIVERSITÄT MÜNCHEN

Walter Schottky Institut
Zentralinstitut für physikalische Grundlagen der Halbleiterelektronik
Fakultät für Physik

Hybrid organic-inorganic heterojunctions for photovoltaic applications

Roland Dietmüller

Vollständiger Abdruck der von der Fakultät für Physik
der Technischen Universität München
zur Erlangung des akademischen Grades eines

Doktors der Naturwissenschaften
(Dr. rer. nat.)

genehmigten Dissertation.

Vorsitzender:	Univ.-Prof. Dr. Harald Friedrich
Prüfer der Dissertation:	1. Univ.-Prof. Dr. Martin Stutzmann
	2. Univ.-Prof. Dr. Peter Müller-Buschbaum

Die Dissertation wurde am 31.05.2012 bei der Technischen Universität München eingereicht
und durch die Fakultät für Physik am 05.07.2012 angenommen.

Contents

Zusammenfassung

Das Ziel der organischen Photovoltaik sind effiziente und flexible Solarzellen, die sich günstig aus Lösungen herstellen lassen. In den letzten Jahren wurden beachtliche Fortschritte erzielt, trotzdem sind organische Solarzellen derzeit weder im Hinblick auf die Effizienz noch auf die Lebensdauer mit anorganischen Solarzellen konkurrenzfähig. Doch geringe Herstellungskosten und neue Anwendungsgebiete könnten die Nachteile organischer Solarzellen wettmachen. Eine interessante Möglichkeit organische Solarzellen weiterzuentwickeln ist die Verbindung von organischen und anorganischen Halbleitern. Denn anorganische Halbleiter in Form von Nanopartikeln können ebenfalls aus Lösungen prozessiert werden. So können die anorganischen Halbleiter ihre Vorteile, wie zum Beispiel ein breites Absorptionsspektrum, in eine hybride organisch-anorganische Solarzelle einbringen.

Hybride Solarzellen lassen sich, analog zu der Herstellung von organischen Solarzellen, als sogenannte „bulk heterojunction“ Solarzellen realisieren. Solche Solarzellen besitzen einen im gesamten Volumen der aktiven Schicht verteilten Heteroübergang und lassen sich herstellen, indem man anorganische Halbleiternanopartikel mit organischen Halbleitern mischt. Der Vorteil von Volumenheteroübergängen ist, dass Exzitonen aus den organischen Halbleitern aufgrund der großen Grenzfläche effizient getrennt werden können. Hybride Solarzellen wurden bereits mit einer Vielzahl anorganischer und organischer Halbleiter realisiert.

In dieser Arbeit wurden Siliziumnanokristalle, welche in einem Mikrowellenreaktor hergestellt wurden, in Volumenheteroübergängen mit organischen Halbleitern untersucht. Dabei wurden sphärische Siliziumnanokristalle, welche eine scharfe Größenverteilung besitzen, mit Durchmessern zwischen 4 nm und 33 nm verwendet. Siliziumnanokristalle sind ungiftig und besitzen ein breites Absorptionsspektrum. Dies zeichnet Siliziumnanokristalle gegenüber Halbleiternanokristallen aus Materialien wie CdSe oder ZnO, welche bisher für hybride Solarzellen verwendet wurden, aus. Als organische Halbleiter für hybride Solarzellen bieten sich das Polymer Poly(3-Hexylthiophen) (P3HT) und das Fulleren-Derivat [6,6]-Phenyl-C_{61}-Buttersäure-Methylester (PCBM) an, welche sich in rein organischen Solarzellen als Standardhalbleiter etabliert haben. Aufgrund der Lage der jeweiligen Energieniveaus ist P3HT in rein organischen Solarzellen der Elektronendonor und PCBM der Elektronenakzeptor.

Mit Hilfe der lichtinduzierten Elektronenspinresonanz-Spektroskopie (LESR) wurde an Gemischen aus Siliziumnanokristallen und P3HT oder PCBM die Generation und Trennung von

Ladungsträgern unter Beleuchtung nachgewiesen. In den Gemischen konnten jeweils lichtinduzierte positive P3HT-Polaronen oder negative PCBM-Radikale detektiert werden. Dabei war die Erzeugung von bis zu 2.8×10^{17} g^{-1} positiven P3HT-Polaronen in P3HT/Siliziumnanokristall-Gemischen ähnlich effizient wie in dem rein organischen Referenzsystem P3HT/PCBM. Da P3HT außerdem ein breiteres Absorptionsspektrum als PCBM hat, wurden die weiteren Messungen an P3HT/Siliziumnanokristall-Gemischen durchgeführt. So wurde mit LESR-Messungen bei unterschiedlichen Wellenlängen gezeigt, dass beide Materialien zur Generation von Ladungsträgern beitragen. Über zeitabhängige LESR-Messungen konnte außerdem beobachtet werden, dass in den P3HT/Siliziumnanokristall-Gemischen ein schneller (<1 s) Ladungstransfer stattfindet, der sich klar von dem Verhalten in reinem P3HT unterscheidet.

In Absorptionsmessungen wurde des Weiteren gezeigt, dass in einer P3HT/Siliziumnanokristall-Schicht sowohl P3HT als auch Siliziumnanokristalle zur Absorption im sichtbaren Spektralbereich beitragen. Allerdings ist die Konjugationslänge von P3HT in den Mischschichten leicht reduziert, wie durch Absorptionsmessungen im infraroten Spektralbereich gezeigt werden konnte. Die gute Vermischung beider Komponenten, die durch Rasterkraft- und Elektronenmikroskopmessungen bestätigt wurde, konnte durch die Verwendung von Chloroform als gemeinsames Lösungsmittel erreicht werden.

Mit P3HT und Siliziumnanokristallen als aktive Schicht, eingebettet zwischen zwei Kontakten, wurden funktionierende Solarzellen hergestellt. Damit konnten Leerlaufspannungen von bis zu 0,76 V erzielt werden. Mit Hilfe von spektral aufgelösten Photostrommessungen wurde außerdem der Beitrag von beiden Halbleitern zum Photostrom nachgewiesen, was im Einklang mit den LESR-Messungen bei unterschiedlichen Wellenlängen ist. Des Weiteren konnte auch mit elektrisch detektierter magnetischer Resonanz gezeigt werden, dass beide Halbleiter zum Stromtransport beitragen. In den P3HT/Siliziumnanokristall-Solarzellen werden unter Beleuchtung Elektronen aus dem P3HT in die Siliziumnanokristalle transferiert, während die Löcher aus den Siliziumnanokristallen in das P3HT abgegeben werden. Die Effizienz von 0,01 % muss allerdings noch verbessert werden. Dieser niedrige Wert ist wahrscheinlich auf die hohe Dichte von Grenzflächendefekten auf der Oberfläche der Siliziumnanokristalle zurückzuführen, welche als Rekombinationszentren wirken.

Ein geordneter Volumenheteroübergang, der gleichzeitig eine große Grenzfläche und Transportpfade für Ladungsträger gewährleistet, ist eine vielversprechende Möglichkeit hybride Solarzellen zu verbessern. Um einen solchen Heteroübergang herzustellen, wurde in dieser Arbeit die Methode der Softlithographie auf Schichten aus Siliziumnanokristallen angewandt. Dabei wurden Strukturgrößen von ungefähr 200 nm erreicht. Da das Aspektverhältnis aber noch zu klein war, konnte mit strukturierten Siliziumnanokristallschichten keine Verbesserung der Effizienz von P3HT/Siliziumnanokristall-Solarzellen erreicht werden.

In hybriden Solarzellen ist es wichtig, die relative Lage der Energieniveaus der beiden Halbleiter zu kennen. Denn zum einen muss die Bandanordnung eine Trennung der Exzitonen zulassen, aber gleichzeitig soll auch eine möglichst hohe Leerlaufspannung erzeugt werden. Aufgrund des großen Einflusses der Morphologie auf das Verhalten der Solarzelle ist es allerdings schwierig, die exakte Bandanordnung in Volumenheteroübergängen zu bestimmen. Darum wurden in dieser Arbeit auch hybride Heteroübergänge mit Volumenhalbleitern anstelle von Nanokristallen untersucht.

An Heteroübergängen aus P3HT und Volumen-Silizium wurden Strom-Spannungs-Kennlinien unter Beleuchtung mit unterschiedlichen Wellenlängen gemessen. Damit wurden selektiv Ladungsträger in P3HT, in Silizium oder in beiden Materialien erzeugt. Aus diesen Messungen konnte auf eine ungünstige Bandanordnung zwischen dem Valenzband von Silizium und dem höchsten besetzten Molekülorbital (HOMO) von P3HT geschlossen werden: Der Transfer von lichtinduzierten Löchern aus dem Silizium in das P3HT wird durch eine Barriere stark erschwert. So wurde, im Gegensatz zu Solarzellen mit Siliziumnanokristallen, nur eine Leerlaufspannung von 0,1 V gemessen. Das heißt auch, dass für die Bandanordnung in hybriden Heteroübergängen mit Siliziumnanokristallen andere Effekte, wie zum Beispiel die Oberflächendefekte, verantwortlich sind.

Aufgrund der Barriere für Löcher, welche in P3HT/Silizium-Heteroübergängen identifiziert wurde, ist für hybride Heteroübergänge ein anorganischer Halbleiter mit einem energetisch tiefer liegenden Valenzband besser geeignet. Darum wurde Silizium durch den Volumenhalbleiter 6H-SiC ersetzt, bei dem das Valenzband weit unterhalb des HOMO von P3HT liegt. Um die Dunkelkennlinien des P3HT/6H-SiC-Heteroübergangs zu beschreiben, wurde ein Ersatzschaltkreis verwendet, der eine Diode, einen Parallelwiderstand und einen Serienwiderstand durch Raumladungseffekte berücksichtigt. Die Strom-Spannungs-Kennlinien des P3HT/6H-SiC-Heteroübergangs konnten durch die thermionische Emission von Elektronen aus dem Leitungsband von 6H-SiC über eine Barriere in das niedrigste unbesetzte Molekülorbital (LUMO) von P3HT beschrieben werden. Aus den Fit-Parametern konnte die Barrierenhöhe mit 1,1 V bestimmt werden. Dieser Wert ist in sehr guter Übereinstimmung mit dem Wert von 0,9 V, welcher durch temperaturabhängige Messungen der Leerlaufspannung unter Beleuchtung bestimmt wurde und dem Abstand zwischen dem Leitungsband von 6H-SiC und dem HOMO von P3HT entspricht. Somit wurde die Bandanordnung der P3HT/6H-SiC über zwei verschiedene Ansätze bestimmt. Unter Beleuchtung wurde außerdem eine Leerlaufspannung von 0,55 V bei Raumtemperatur gemessen, was 6H-SiC zu einem möglichen Kandidaten für hybride Solarzellen macht.

1 Introduction

Harvesting energy directly from sunlight is increasingly recognized as an essential component of the future global energy production. The decreased availability of fossil fuel sources and the realization of the negative long-term effects of CO_2 emissions into the atmosphere are driving research for renewable energy resources. On the other hand, more energy from the sun hits the earth in one hour than all of the energy consumed on our planet in an entire year. Thus, capturing even a small fraction of the 120 000 TW [Lew07] that reaches the earth could significantly change the overall energy balance.

Photovoltaics

The solar cell is considered a major candidate for obtaining energy from the sun, since it can convert sunlight directly to electricity with a high conversion efficiency. The photovoltaic effect, i.e. the generation of a voltage when a device is exposed to light, was discovered by Becquerel in 1839 [Bec39]. However, it was not until 1954 that the solar cell received increased attention, initiated by monocrystalline silicon solar cells by Chapin *et al.* with an efficiency of approximately 6% [Cha54]. Nowadays, mono- and multicrystalline silicon solar cells are the dominant cell type, covering about 84 % of the market [Mil07], and record silicon solar cells do achieve conversion efficiencies of 25 % [Zha98].

The key aim of all solar cell technologies is to increase conversion efficiencies and to reduce production costs to compete with other forms of power generation. This target is most likely to be reached via a cost reduction by the use of new technologies and materials, not only by cost reductions through economies of scale. Such new technologies and materials, including thin films, thin silicon, organic photovoltaics, and multijunction concentrator approaches have the potential to significantly reduce the costs per watt. In contrast to other technologies, organic photovoltaics has two distinctive advantages which makes it an especially promising approach and could lead to the most significant cost reduction: Organic compounds are inexpensive to synthesize and can be solution-processed in a roll-to-roll process with high throughput at low temperatures. The concept of the organic bulk heterojunction solar cell, where two organic semiconductors are blended to form an interpenetrating network to facilitate exciton dissociation [Yu95], and the Nobel Prize in Chemistry for Alan J. Heeger, Alan G. MacDiarmid, and

Hideki Shirakawa in the year 2000 for their work on semiconducting and metallic polymers [Hee01] have led to intensive research activities on the field of organic photovoltaics. Today, single-junction solar cells already achieve efficiencies of about 8 % [Kon10] for devices on a laboratory scale by using new low-bandgap polymers.

Organic-inorganic bulk heterojunctions with inorganic nanocrystals

Nevertheless, inorganic semiconductors have several advantages compared to organic semiconductors, such as the broader absorption spectrum or that they can be doped to a specific level. In addition, inorganic semiconductors can also be processed from solution, if *e.g.* nanocrystals in an appropriate solvent are employed. When combining organic semiconductors and inorganic semiconductor nanocrystals for photovoltaic applications, the unique properties of both materials can be used, while at the same time the advantages of a bulk heterojunction can be preserved. Organic-inorganic hybrid bulk heterojunctions have been realized with several inorganic materials, such as ZnO [Bee04] or CdSe [Gre96]. From many materials, for instance CdSe, not only spherical nanocrystals, but also elongated or branched nanocrystals can be synthesized via colloid chemistry. Such nanostructures lead to a better intermixing with the organic part and provide additional transport paths. With branched CdSe nanocrystals, record efficiencies of up to 3.1 % for hybrid bulk heterojunctions have been achieved [Day10].

However, many inorganic semiconductors used for hybrid solar cells, e.g. CdSe or ZnO, are either toxic or their absorption spectra are not matched to the solar spectrum. This is not the case for silicon nanocrystals, which can be produced *e.g.* via gas-phase growth [Kni04]. Furthermore, silicon is naturally abundant and one of the best investigated materials available. Also, it exhibits a broad absorption range, which makes it an ideal counterpart to organic semiconductors with their narrow absorption bands. A promising organic semiconductor for hybrid solar cells with silicon nanocrystals is poly(3-hexylthiophene) (P3HT), which is used in most of the state-of-the-art organic solar cells [Ma05]. P3HT has a high mobility and acts as an electron donor in organic solar cells [Cho04]. Furthermore, P3HT has proven to work with different inorganic nanocrystals in hybrid solar cells [Huy02, Gue07].

Organic-inorganic bilayer heterojunctions

In hybrid bulk heterojunctions for solar cell applications the relative positions of the energy levels is very important. On the one hand, the band offsets must be large enough to enable exciton dissociation at the interface. On the other hand, to obtain a high open-circuit voltage,

the band offsets should be as small as possible. Furthermore, the film morphology has a large influence on the properties of a bulk heterojunction. An active layer, where both materials are blended on the nanometer scale and still preserve current paths to the contacts, is crucial for an efficient exciton dissociation and charge transport. However, it is difficult to separate the effects of the morphology and of the band-alignment on a bulk heterojunction. Thus, to obtain more information on the band offset at the interface of the heterojunction, one has to consider flat bilayer heterojunctions.

For hybrid bilayer heterojunctions made of a molecular organic semiconductor and silicon, fundamental work has been done by Forrest *et al.* [For84a, For84b]. It was found that the current-voltage characteristics can be described as a combination of thermionic emission and space-charge limited current. Such hybrid bilayer heterojunctions have also been realized with amorphous silicon and P3HT for solar cell applications. However, in these heterojunctions only a small efficiency could be achieved and, when compared to other organic semiconductors on amorphous silicon, the importance of the relative position of the highest occupied molecular orbital relative to the valence band of the inorganic counterpart could be demonstrated [Gow06]. Instead of replacing the organic part, one can also replace the silicon by an inorganic semiconductor with a significantly different valence band position. This has been done for example in the work of Olson *et al.*, where, by alloying the zinc oxide acceptor with magnesium, the band offset could be successfully varied and a significant increase of the open-circuit voltage could be achieved [Ols07]. Another interesting material, regarding the positions of the valence and conduction band edges, is the wide bandgap semiconductor 6H-SiC. Furthermore, as a consequence of different stacking sequences, SiC can be found in more than 250 polytypes which differ in various properties such as the bandgap [Fis90]. This makes it a very promising material for the investigation of the influence of different positions of the band edges on the performance of the hybrid heterojunction.

Chapter overview

The aim of this work is to study the properties of hybrid heterojunctions, bulk heterojunctions as well as bilayer heterojunctions, with regard to photovoltaic applications. In **Chapter 2** an overview over the different aspects of semiconductor heterojunctions will be provided. Here, specific aspects of organic semiconductors and semiconducting nanocrystals are highlighted. Moreover, the theory of semiconductor junctions and the practical application of semiconductor junctions as solar cells are discussed.

Chapter 3 introduces the materials which were used during the course of this work. The physical properties of the inorganic semiconductors, bulk silicon, silicon nanocrystals, and silicon carbide, as well as the organic semiconductors, P3HT and PCBM, are presented.

In **Chapter 4** the sample preparation, for bulk heterojunctions as well as for bilayer heterojunctions, is described. Additionally, the experimental methods to characterize the structural, chemical, optical and electrical properties of the samples are explained in this chapter.

The investigation of hybrid bulk heterojunctions with silicon nanocrystals is shown in **Chapter 5**. Here, the optical properties and the morphology are discussed, and via light-induced electron spin resonance measurements the photo-induced charge transfer in the bulk heterojunctions is demonstrated. Moreover, solar cell prototypes made of P3HT and silicon nanocrystals are presented and the contribution of both components to the photocurrent will be revealed. On top of that, soft lithography of silicon nanocrystals is introduced as a method to fabricate ordered heterojunctions.

Hybrid bilayer heterojunctions are studied in **Chapter 6**, where the heterojunctions are built up from P3HT and silicon or 6H-SiC. In both cases the band alignment is derived from the current-voltage characteristics. Furthermore, the photovoltaic properties of the heterojunctions are analyzed.

In **Chapter 7** the results are summarized and an outlook is given.

2 Physics of Semiconductor Heterojunctions

This chapter presents a review of the basic physics and properties of semiconductors and semiconductor devices which are relevant for this work. Besides an overview of the characteristics of organic semiconductors and inorganic nanocrystals, semiconductor junctions will also be discussed. Furthermore, starting from the case of a metal-semiconductor junction, semiconductor-semiconductor junctions, including hybrid organic-inorganic heterojunctions, will be reviewed. Finally, solar cells and the photo-induced charge generation therein will be the focus of the last section.

2.1 Semiconductors

In addition to the well-known inorganic semiconductors, such as silicon, organic semiconductors as a new class of semiconductors have been developed during the last decades. The unique properties of these organic semiconductors will be described in Subsection 2.1.1. However, also silicon nanocrystals exhibit some interesting properties which differ from the bulk silicon properties and will be discussed in Subsection 2.1.2.

2.1.1 Organic semiconductors

Organic semiconductors can be separated into two classes, which are small molecules and polymers. Semiconducting small molecules, such as pentacene, are typically evaporated in an ultra high vacuum system. Semiconducting polymers, for instance poly[p-phenylene vinylene] (PPV), are made soluble with various side groups and are processed from solution, as evaporation of the polymers would decompose them. Mostly polymers were used for this thesis, hence, mainly the properties of semiconducting polymers will be highlighted below. Furthermore, as the semiconducting polymers are used for heterojunctions and solar cells in this thesis, especially the optical and electrical properties of semiconducting polymers will be highlighted.

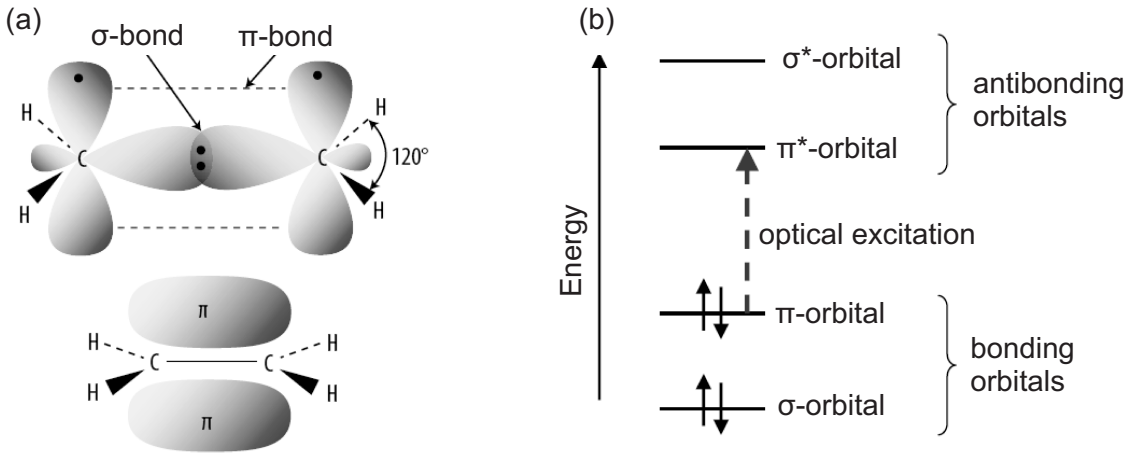

Figure 2.1: *(a) Ethene is the most simple example of a conjugated π-electron system with σ- and π-bonds. (b) The scheme shows the energy levels of a π-conjugated molecule. The lowest electronic excitation is between the bonding π-orbital and the antibonding π*-orbital. From Reference [Brü08b].*

The semiconducting character of organic semiconductors stems from conjugated π-electron systems, which are built up from the p_z-orbitals of sp^2-hybridized carbon atoms as shown in Figure 2.1 (a) for the example of an ethene molecule. The optical absorption in semiconducting molecules, which is shown schematically in Figure 2.1 (b), takes place via the excitation of electrons from the bonding to the antibonding orbital of the conjugated π-electron system. The bonding π-orbital is the highest occupied molecular orbital (HOMO) of a conjugated molecule, while the antibonding π^*-orbital is the lowest unoccupied molecular orbital (LUMO). As the difference of the HOMO to the LUMO energy level is typically in the range of $1.5 - 3$ eV [Brü08b], the electronic excitation with light in the visible and the near ultraviolet spectral region is possible.

The electron-hole pair, which is created after light absorption, is strongly bound, in contrast to inorganic semiconductors, and localized on one single molecule. Thus, the exciton is a Frenkel exciton with a typical binding energy of about several hundreds of meV for polymers [Brü08b, Cam96, Alv98]. When comparing this value to the thermal energy at room temperature of about 25 meV it is obvious that the absorption of light does not create free charge carriers in organic semiconductors. Furthermore, the diffusion length of such excitons in polymers is, with only several nanometers, very small [Bra08]. Also in inorganic semiconductors excitons do exist, but they are much more delocalized and, due to the higher relative permittivity of $\varepsilon_r \approx 12$ for silicon compared to $\varepsilon_r \approx 3$ for organic semiconductors, the Coulomb attraction is reduced. Thus, excitons in crystalline silicon have a binding energy of only about 10 meV and dissociate at room temperature. In contrast, in organic semiconductors, which are also referred to as excitonic semiconductors, excitons do not dissociate at room temperature, which

has important consequences for applications. For example, to create free charge carriers in organic solar cells, a bicontinuous blend of two organic semiconductors is produced. At the interface of the two materials the excitons can be dissociated if the band offset is larger than the exciton binding energy. However, it should be noted that, in spite of the high exciton binding energy, also semiconducting polymers show photoconductivity as excitons can be dissociated by defects or impurities [Rey06].

Analogous to inorganic semiconductors, the mobile charged states in organic semiconductors which are responsible for the current are electrons and the holes. However, organic semiconductors are van der Waals bonded solids, implying a considerably weaker intermolecular bonding as compared to covalently bonded inorganic semiconductors. As a consequence, the electronic wavefunctions are less delocalized among neighboring molecules. This has direct implications for the charge carrier transport, as the electronic interaction between adjacent molecules is quite weak [Brü08a]. Furthermore, one has to bear in mind that transport of electrons or holes in organic semiconductors involves ionic molecular states. $E.g.$ when there is an additional electron in the molecular solid, by injection or by photo-generation, this electron creates a negatively charged radical anion M^- out of a neutral molecule M. Such an additional electron can then move from one molecule to the next and the charged molecule always polarizes the surrounding molecules. This electronic polarization follows the movement of the charge instantaneously [Sch05]. That is why the negative and positive charge carriers are usually termed negative and positive polarons, respectively. In addition, a polaron has a strong electron-phonon coupling and the additional charge is altering the configuration of the molecule. In organic semiconductors the electron-phonon interactions are comparable to the electronic interactions, in contrast to covalently bound inorganic semiconductors [Cor07]. The negative polarons occupy polaron levels inside the forbidden band near the LUMO of the molecules, while the positive polarons occupy polaron levels near the HOMO. Upon increasing of the polaron density, the energetic distance between the polaronic bands of the positive and negative polaron and the HOMO and LUMO, respectively, decreases and the polaronic bands occupy the HOMO and LUMO [Mol04]. Nevertheless, at low polaron densities the energy lowering due to the polarization can reach in some polymers, such as polythiophene, several hundreds of meV. In such a case the charge carrier forms its own trap state on the polymer chain, which is called self-trapping [Brü08a, Mol04]. Furthermore, locally varying polarization energies due to different molecular environments in polymer solids lead to a Gaussian density of states for the distribution of transport sites as shown in Figure 2.2. The width of the Gaussian density of states in amorphous organic solids is typically in the range of about 200 meV [Brü08a]. Thus, the band tails resemble those of amorphous inorganic semiconductors.

Depending on the degree of order, the charge carrier transport mechanism in organic semiconductors can fall between two cases, either band or hopping transport. Band transport is typically observed in molecular crystals, reaching a mobility, μ, of about $1-10\ \mathrm{cm}^2/\mathrm{Vs}$, which

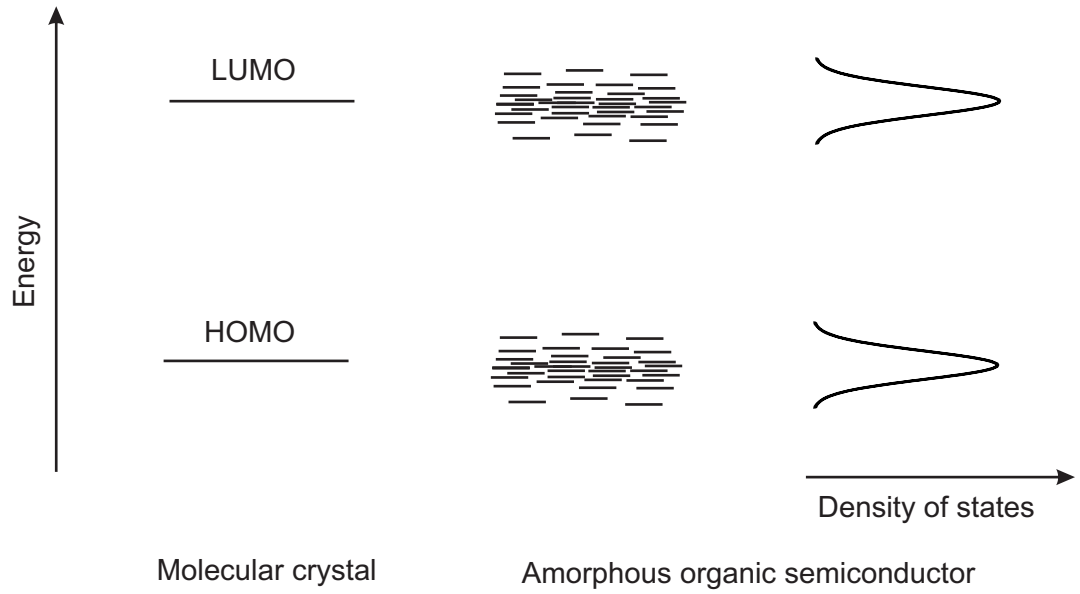

Figure 2.2: *Energy levels of a molecular crystal and an amorphous organic semiconductor. The width of the Gaussian density of states in amorphous organic semiconductors is typically in the range of 200 meV [Brü08a].*

is about two orders of magnitude lower as in inorganic semiconductors, where *e.g.* electrons in crystalline silicon reach mobilities of about 1000 cm^2/Vs. In unordered organic solids, for instance polymers, the mobility is even lower than in molecular crystals, about $10^{-3} - 10^{-5}$ cm^2/Vs [Brü08b]. This is mainly due to the hopping transport from one polymer chain to the next and also due to the intramolecular hopping from one π-conjugated region to the next on the same polymer. The mobility depends on the temperature, where the hopping transport increases with increasing temperature. Furthermore, the mobility increases with increasing electric field, which is also observed for other disordered materials, as the energy barriers are decreased in the direction of the electric field [Blo97]. An additional parameter influencing the mobility is the charge carrier density: At low charge carrier density most of the charge carriers are localized, thus the effective mobility is low. With increasing charge carrier density the localized states will fill up and the mobility increases [Brü08b].

Besides the hopping transport processes between strongly localized molecular states, polarons can be trapped by additional states in the gap between the HOMO/LUMO level distributions. For such trap states several sources exist: Impurities, due to the incorporation of molecules of another species, which have another HOMO/LUMO position lying in the energy gap, will form trap states. Structural imperfections will lead to a fluctuating conjugation length which will broaden the distribution of the HOMO/LUMO levels. The states in the tail of this distribution will form trap states if the distribution is broad enough. Furthermore, structural defects occur with enhanced probability at grain boundaries in polycrystalline layers, resulting in discrete trap

states in the gap [Brü08a]. In addition, forbidden states in the middle of the band gap can also be added to allow for dangling bond groups such as chain ends [Mol04].

Another interesting point is that certain polymers, such as poly(3-hexylthiophene) (P3HT), form a microcrystalline structure due to their self-organizing properties. Such a process is critically affected by the regioregularity, the impurity concentration, the molecular weight, and the choice of the solvent. For a solvent with a high boiling point the polymer has more time to form a microcrystalline structure by better chain alignment. This leads to stronger interchain interactions resulting in reduced polaronic relaxation energies and improved mobilities. Depending on the mentioned parameters, variation of the mobilities by several orders of magnitude are possible [Cha04, Ho07, Cho04].

One disadvantage of organic semiconductors, compared to inorganic semiconductors, is degradation and the bad long term stability. Under ultraviolet illumination chemical bonds in polymers break up and oxidization occurs, so called photo-oxidization. The oxidization creates more deep traps in the polymer which leads to a reduction of the charge carrier mobility [Pac06]. To avoid oxidization, it is necessary to process the organic semiconductors under inert gas atmosphere. Nevertheless, also under argon atmosphere a slow degradation takes place, which increases with higher temperature and illumination intensity [Pad01].

However, providing a good encapsulation, semiconducting polymers have the large advantage, compared to inorganic bulk semiconductors, that they can be deposited from the liquid phase. This facilitates a low-cost and high throughput fabrication of devices. For large scale applications an inkjet printing process would be preferable. However, inkjet printing is not trivial due to the requirement of accurate placement, problems with the wetting of the nozzle plate, and adhesion properties of the substrate [Loo08]. Other ways to produce polymer layers, which are mainly used in research labs and also were used in this work, are spin coating or simple drop casting of the polymer solution.

2.1.2 Semiconductor nanocrystals

Semiconducting inorganic nanocrystals with their typical diameter smaller than 100 nm have interesting properties, placing them between volume semiconductors and molecules. Equal to the volume semiconductors, they have an ordered crystal structure. On the other side, due to the small size, various properties, for instance the electrical transport, are quite different to volume semiconductors.

A large variety of semiconductors have been used for the growth of nanocrystals. Many of the group II-VI semiconductors, as *e.g.* CdSe, have been synthesized very controlled via wet-chemical processes [Pen01, Gap98]. However, often nanocrystals contain heavy metals such as Pb or Cd. Thus, for large scale applications as solar cells, silicon would be the preferred

choice as it is a non-toxic material and naturally abundant. Silicon nanocrystals, which will be discussed in more detail in Subsection 3.1.3, have already been produced via a gas phase process with a narrow size dispersion [Nis02, Kni04]. Furthermore, silicon is one of the best studied materials available, facilitating the investigation of combinations of silicon with less investigated materials such as polymers in hybrid organic-inorganic devices.

One big advantage of semiconductor nanocrystals is that printable nanocrystal dispersions can be easily produced and thus potential low-cost methods, as ink-jet printing, can be used to form thin semiconducting films. However, compared with bulk semiconductors, the inter-particle properties will dominate the quality of films made of nanocrystals. Thus, the interface conditions and defects have to be taken into account when working with nanocrystals. In particular the electronic transport of a nanocrystal layer will be dominated by the exact interface properties. In the literature, the transport between silicon nanocrystals has been described by hopping processes, nevertheless the conduction properties of semiconductor nanocrystal layers are strongly dependent on the actual processing conditions [Raf06, Lec08a]. For nanocrystals which are produced via colloidal chemistry, the aggregation of the nanocrystals is hindered by organic molecules which surround the nanocrystals. These molecules are typically not conjugated and, thus, form an isolating layer which will be a tunneling barrier for charge carriers. A similar problem for the charge transport is the oxidization of the nanocrystals, where the oxide also forms a barrier. In addition, even without any barrier, defects at the interface act as trap states and recombination centers and can significantly reduce the transport properties.

A further point which should be mentioned, and which changes the properties of nanocrystals compared to the bulk, is quantum confinement. When the size of a nanocrystal is so small that the quantum mechanical confinement energy of electrons and holes exceeds the thermal energy $k_B T$, the observed behavior changes from bulk-type towards zero-dimensional. For nanocrystals smaller than typically 5 nm, this effect leads to an effective increase of the bandgap [Del93, Led00, Gap98].

2.2 Semiconductor junctions

2.2.1 Metal-semiconductor contacts

Metal-semiconductor contacts have been studied extensively because of their importance in semiconductor devices, both as rectifying and as ohmic contacts. However, in this subsection mainly the rectifying Schottky contact will be discussed, as it is a model system for ideal and real semiconductor contacts.

Theory of the ideal Schottky contact

The basic theory for the Schottky contact was formulated by Schottky in 1938, who proposed that the potential barrier at the metal-semiconductor contact arises from stable space charges in the semiconductor [Sch38]. When joining metals and semiconductors with different work functions, charges will be transfered until a common Fermi level is established in thermal equilibrium. Thus, for a metal and a semiconductor brought into contact, the work functions of the metal, Φ_M, and of the semiconductor, Φ_{SC}, are important. For the case of a metal and a n-type semiconductor with $\Phi_M > \Phi_{SC}$ and without any surface states, electrons will move from the semiconductor to the metal. As a consequence of the charge transfer, in the semiconductor a space-charge region, in which all donors are ionized, builds up. This is shown in the scheme of Figure 2.3, where a metal and a n-type semiconductor is shown before (a) and after contact (b) . The width W of the space charge region is

$$W = \sqrt{\frac{2\varepsilon_r\varepsilon_0 V_{bi}}{eN_D}}, \tag{2.1}$$

with the build-in potential $V_{bi} = \frac{1}{e}(\Phi_M - \Phi_{SC})$, the elementary charge e, the vacuum permittivity ε_0, the relative permittivity ε_r, and the donor impurity concentration N_D [Sze07]. The size of the space-charge region can reach from few nanometers for $N_D = 10^{19}\text{cm}^{-3}$ up to the μm-range for $N_D < 10^{15}\text{cm}^{-3}$, while the electrons in the metal have a penetration depth of typically a few angstrom, given by the Thomas-Fermi screening. The barrier that electrons have to overcome to be injected into the semiconductor conduction band, the so-called Schottky barrier, is

$$\varphi_{Bn} = \frac{1}{e}(\Phi_M - \xi), \tag{2.2}$$

with the electron affinity ξ of the semiconductor. Such a metal-semiconductor contact with an energy barrier $e\varphi_{Bn} >> k_B T$ acts as a rectifier, a so called Schottky diode. For a positive applied potential at the metal side, the forward direction, electrons are injected from the semiconductor to the metal as the build-in potential V_{bi} is decreased. For a negative bias at the metal, the reverse direction, electrons cannot move from the metal to the semiconductor due to the Schottky barrier φ_{Bn}. For a p-type semiconductor with $\Phi_{SC} > \Phi_M$ the barrier for hole injection into the semiconductor is, analogous to the n-type semiconductor Schottky barrier:

$$\varphi_{Bp} = \frac{1}{e}\left(E_{gap} - \Phi_M + \xi\right). \tag{2.3}$$

For the latter case of $\Phi_{SC} > \Phi_M$, the metal-semiconductor contact is only rectifying for a p-type semiconductor, while for a n-type semiconductor the contact would be ohmic. For the opposite case, $\Phi_M > \Phi_{SC}$, the contact is ohmic for a p-type semiconductor and rectifying for a n-type semiconductor.

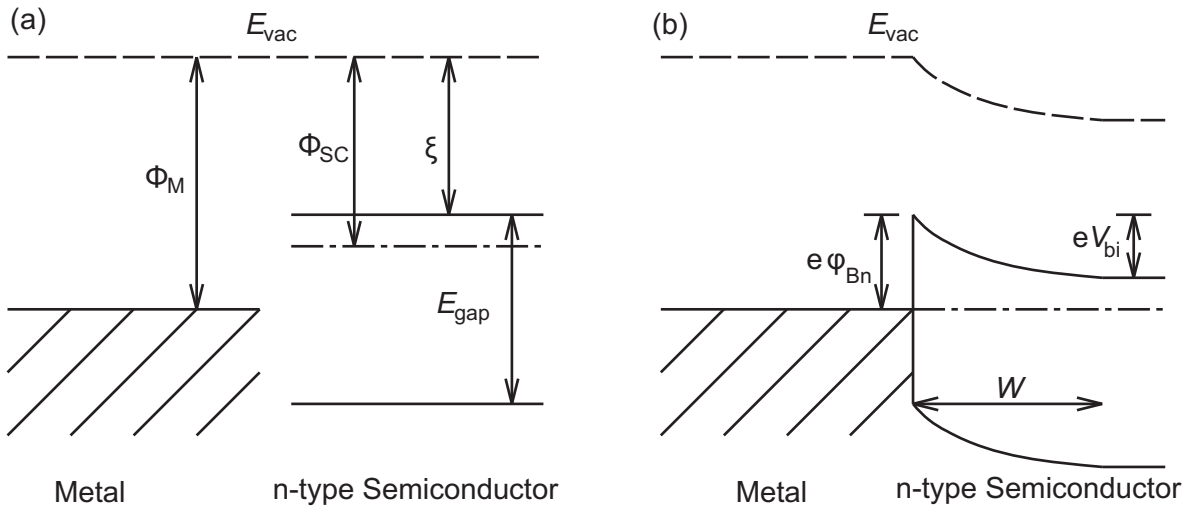

Figure 2.3: *Energy band diagrams of a metal and a n-type semiconductor whith* $\Phi_M > \Phi_{SC}$ *separated (a) and in contact (b). A detailed explanation of the symbols is given in the text.*

Thermionic emission

The current transport in metal-semiconductor Schottky diodes is mainly due to majority carriers, in contrast to *p-n* junctions, where the minority carriers are responsible for the current transport. For Schottky diodes several mechanisms for the current transport exist, *e.g.* emission of electrons over the barrier into the metal, quantum mechanical tunneling of electrons through the barrier, recombination in the space-charge region, diffusion of electrons in the depletion region, and hole injection from the metal. For Schottky diodes with moderately doped semiconductors, *e.g.* doped silicon with $N_D \leq 10^{17}\text{cm}^{-3}$, operated at room temperature, the dominant transport process is emission of electrons from the semiconductor over the potential barrier into the metal [Sze07]. For more heavily doped semiconductors the tunneling current may become more significant. For highly doped semiconductors with $N_D > 10^{19}\text{cm}^{-3}$, the space charge region is thin enough that only tunneling dominates, while in the intermediate region with $10^{17}\text{cm}^{-3} < N_D < 10^{19}\text{cm}^{-3}$, both mechanisms, tunneling and thermionic emission are involved in the transport [Pan66, Sch84]. Thus, for common moderately doped semiconductors, the transport can be adequately described by the thermionic emission theory. In this theory the effects resulting of drift- and diffusion processes are neglected and the current flow depends solely on the barrier height. The total current is given by the diode equation [Sze07]

$$I = I_S \left[\exp\left(\frac{eV}{nk_B T} \right) - 1 \right], \tag{2.4}$$

with the current I, the reverse saturation current I_S, the applied voltage V, and the Boltzmann constant k_B, and the ideality factor n. The reverse saturation current I_S is defined by

$$I_S = AA^*T^2 \exp\left(-\frac{e\varphi_{Bn}}{k_B T}\right), \tag{2.5}$$

where A is the area of the diode and A^* is the effective Richardson constant for thermionic emission, neglecting the effect of optical-phonon scattering, given by

$$A^* = \frac{4\pi e m^* k_B^2}{h^3}. \tag{2.6}$$

Here, m^* is the effective mass of the charge carrier and h is the Planck constant. For free electrons ($m^* = m$) the Richardson constant is 120 A/cm^{2}K^2 [Sze07].

The barrier height of a metal-semiconductor contact can be measured, besides activation energy, capacitance-voltage, and photoelectric methods, by current-voltage characteristics. For the latter method, when the saturation current is obtained by fitting of the measured current-voltage characteristics, the barrier height can be obtained from the equation:

$$\varphi_{Bn} = \frac{k_B T}{e} \ln\left(\frac{AA^*T^2}{I_S}\right), \tag{2.7}$$

which follows from Equation 2.5.

Real Schottky contacts with inorganic semiconductors

The barrier height of the Schottky contact should be proportional to the work function of the metal, as can be seen from Equations 2.2 and 2.3. However, the dependence of the work function found in experiments is much weaker due to non-ideal interfaces [Cow65, Sch84]. Thus, in reality, a couple of variations to the described ideal Schottky contact exist.

One possibility for a deviation of the ideal behavior is a surface dipole at the interface. A surface dipole can build up *e.g.* due to adsorbed molecules. Furthermore, for compound semiconductors, such as silicon carbide, the elements have different values of the electronegativity which leads to a surface dipole. Such a surface dipole introduces a potential step at the interface and, hence, changes the Schottky barrier.

A further change of the height of the Schottky barrier can be introduced by surface states at the semiconductor surface. Dangling bonds, which are unsaturated bonds, are an example for such surface states. For group-IV elements, such as silicon, these dangling bonds lie in the middle of the bandgap [Sze07]. Dangling bonds can capture charge carriers which results in a pinning of the Fermi level in the middle of the energy gap and in a surface band bending. In such a

case, the barrier height of the Schottky barrier is independent of the work function of the metal. Surface states in the bandgap can also be generated by the contact to the metal, where the tail of the electron wave function of metals forms surface states, so-called metal induced gap states [Hei65]. Such metal induced gap states, which not necessarily have to lie in the middle of the bandgap [Ter85], pin the Fermi level similar to other surface states such as dangling bonds.

A further effect, the image-force lowering, also known as the Schottky effect, can reduce the Schottky barrier height. Here, electrons in the semiconductor near the metal surface induce a positive mirror charge in the metal. This creates a potential in the semiconductor which is superimposed with the Schottky barrier and lowers the height of the barrier [Sze07]. Finally, for certain metal-semiconductor combinations, a thin isolating layer, *e.g.* an oxide, can form. Charge carriers have to tunnel through this so-called Mott barrier, which reduces the current significantly.

Metal-semiconductor contacts with organic semiconductors

For metal-semiconductor contacts with doped organic semiconductors, the theory as discussed above can be applied, including the band bending in the semiconductor. However, for typical organic semiconductors, one can assume that band bending will not occur, as organic semiconductors are not intentionally doped and have a significant bandgap and thus have only few charge carriers which could contribute to a band bending [Sek01].

At the organic-metal interface especially dipoles can have a large effect on the band alignment. In Figure 2.4 the influence of interface dipole formation on the energy band diagram is illustrated. For the formation of dipoles at the organic-metal interface chemical reactions are one possible reason [Ish99]. Thereby it makes a large difference if the metal is deposited on the polymer or the other way round [Bra08]. When metals are deposited on conjugated materials, the formation of covalent bonds between metal and carbon atoms changes the hybridization of those carbon atoms, *e.g.* from sp^2 to sp^3, and thus, the π-conjugation is broken at these sites. The metal-carbon bond leads to a redistribution of the charge density and often the metal atoms become positively charged as electrons are transferred to the organic part. Consequently, interface dipoles are formed at the metal-on-organic interface [Kon95, Ett97]. However, depending on the amount of impurities in the organic layer, which react with the evaporated metal, surface states with large dipole densities can lead to a change in the potential ranging from +0.5 eV to -0.5 eV [Ett97]. On the other hand, several studies have demonstrated that an interface dipole can also appear when depositing the organic material on a metal surface [Yan02, Ren05]. Apart from that, for the case of Mg and the molecule tris(8-hydroxyquinoline)aluminum (Alq3), even when the morphologies of metal-on-organic and organic-on-metal interfaces are quite different, as the metal evaporated on the organic layer penetrates the organic matrix, both contacts produce identical electrical characteristics [Kah03].

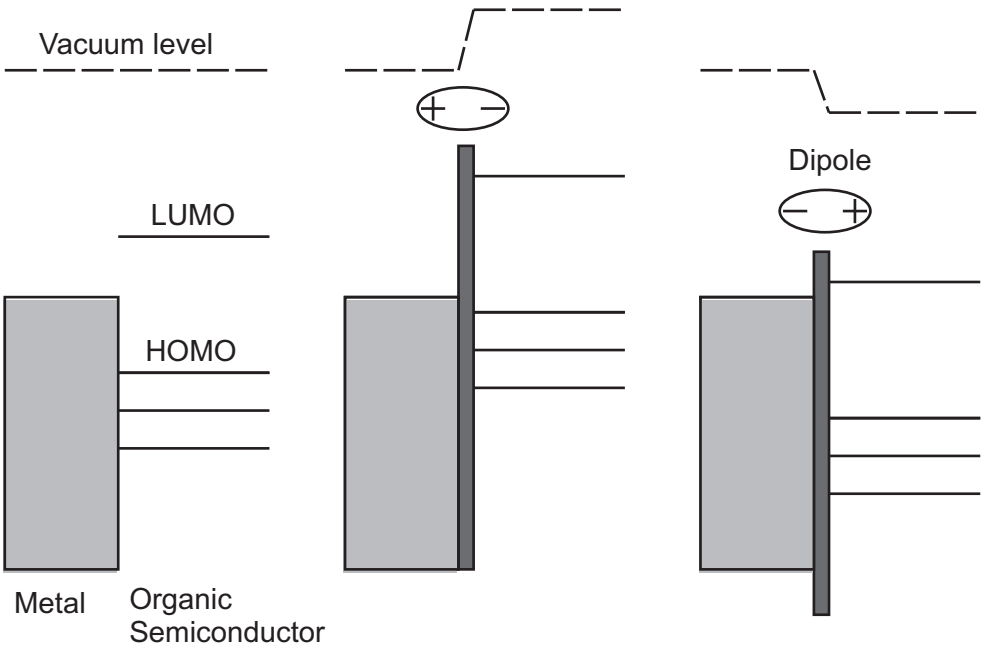

Figure 2.4: *Sketch of the impact of the formation of an interface dipole on the electronic levels at the metal-organic semiconductor interface.*

In addition to interface dipoles, chemical reactions of the organic layer with the metal can also introduce interface states in the organic layer that pin the Fermi level. In contrast to metals, for indium tin oxide (ITO) such a behavior is more pronounced, and an upward shift of the HOMO and LUMO relative to the Fermi level has been observed [Pei00, Pei03]. Fermi level pinning was also found by Tengstedt *et al.* [Ten06] for conjugated polymers, *e.g.* P3HT, where the Fermi level of the metal substrate and the positive polaronic level of the polymer align, whenever the metal Fermi level is below the energy level of the positive polaron. Only for metal Fermi levels above the positive polaron energy level vacuum level alignment takes place. The observation is rationalized by the assumption of an electron transfer from the polymer into the substrate. This creates a positive polaron in the polymer for metals with Fermi levels below the positive polaron energy level, which results in dipole-induced potential steps as large as 2.1 eV. Such an alignment of organic semiconductors under the creation of a positive or negative polaron due to charge transfer and subsequent pinning of the polaron level to the Fermi level is also described by Braun *et al.* [Bra09]. There, only for substrate work functions lying between the polaron states of the organic semiconductor vacuum level alignment has been observed.

Furthermore, during metal evaporation, a significant diffusion into the organic layer has also been observed, depending on the deposition rate of the metal and the substrate temperature [Due02, Sek01]. Finally, mirror charges can also have an influence on the energetics of the organic-metal interface, in which the effect is larger than in inorganic semiconductors as the relative permittivity is smaller [Brü08a].

Ohmic contacts

Ohmic contacts are required for every semiconductor device in order to pass current in and out of the device. To produce such an ohmic contact with a very low resistance and a linear current-voltage characteristics, various strategies do exist. One common way is to highly dope the semiconductor near the interface to the metal. From Equation 2.1 it is obvious that for very large donor concentrations N_D the space charge region W becomes very small. Hence, charge carriers can tunnel through the barrier. This approach is successfully used for inorganic semiconductors [Sze07].

Another strategy for ohmic contacts is to achieve a low contact barrier height. Thus, by choosing an appropriate metal with a work function minimizing the energy barrier at a metal-semiconductor interface one can achieve ohmic contacts. This is a well-known design rule in organic semiconductor devices, in which low work function metals are used for electron injection and high work function metals are used for hole injection [She04]. In particular, if undoped organic semiconductors are used this is the only way to make ohmic contacts.

2.2.2 Semiconductor-semiconductor junctions

The *p-n* junction, a bipolar contact from the same semiconductor with different doping types, is of great importance in modern devices, *e.g.* in solar cells. Thus it will be described shortly. Heterojunctions, which are junctions formed between two dissimilar semiconductors, will also be highlighted here for inorganic heterojunctions, while organic-inorganic heterojunctions will be the topic of the following subsection.

p-n junctions

When a n-type and a p-type semiconductor are in contact, electrons from the n-type semiconductor flow into the p-type region and recombine with holes flowing into the n-type region. Due to this diffusion current ionized donors and acceptors are left near the interface which form a space charge region. Thus, a drift current builds up which is opposite to the diffusion current. In thermal equilibrium both currents reach the same size and the Fermi levels of both semiconductors have the same energetic position. Such a process only can take place between two materials with free charge carriers. The current-voltage characteristics of an abrupt *p-n* junction is given by the Shockley equation, which is the ideal diode law [Sze07]:

$$I = I_S \left[\exp\left(\frac{eV}{nk_B T} \right) - 1 \right], \tag{2.8}$$

where the ideality factor n, which is $1 \leq n \leq 2$, is $n = 1$ in the case without recombination and $n = 2$ for complete recombination in the space-charge region. However, in reality the behavior of solar cells still differ considerable from this model, as ideality factors of 3 to 4 are often measured for industrial solar cells [Bre09]. The reverse saturation current I_S is defined, in contrast to thermionic emission diodes, by:

$$I_S = \frac{eD_p n_i^2}{L_p N_D} + \frac{eD_n n_i^2}{L_n N_A}. \tag{2.9}$$

D_p and D_n are the diffusion coefficients of the minority charge carriers, n_i is the intrinsic charge carrier concentration, and L_p and L_n are the diffusion lengths of the minority charge carriers.

Heterojunctions

An ideal heterojunction is characterized by the offset ΔE_{CB} of the conduction band edges and ΔE_{VB} of the valence band edges. The offsets for the ideal heterojunction, neglecting *e.g.* interface dipoles, are given by the electron affinity rule, thus for $\Delta E_{CB} = \Delta\xi$. In addition, for bipolar heterojunctions, which are also called anisotype heterojunctions, space-charge regions in the doped semiconductors build up. The total built-in potential V_{bi} is equal to the sum of the two built-in voltages V_{bi1} and V_{bi2}. As at equilibrium the Fermi levels are equal, the total build-in voltage is given by $V_{bi} = \frac{1}{e}|\Phi_{SC1} - \Phi_{SC2}|$ [Sze07]. In Figure 2.5 the energy band diagrams for (a) two isolated semiconductors of opposite types and with different bandgaps and (b) their idealized anisotype heterojunction at thermal equilibrium are shown.

The depletion widths W_1 and W_2 of the two semiconductors are [Sze07]

$$W_1 = \sqrt{\frac{2N_{A2}\varepsilon_1\varepsilon_2 V_{bi}}{eN_{D1}(\varepsilon_1 N_{D1} + \varepsilon_2 N_{A2})}},\ W_2 = \sqrt{\frac{2N_{D1}\varepsilon_1\varepsilon_2 V_{bi}}{eN_{A2}(\varepsilon_1 N_{D1} + \varepsilon_2 N_{A2})}}, \tag{2.10}$$

where N_{D1} and N_{A2} are the donor and the acceptor densities, respectively, and ε_1 and ε_2 are the relative permittivities of the semiconductors.

The description of the current-voltage characteristics of such a heterojunction can be greatly simplified by assuming a graded junction where ΔE_{CB} and ΔE_{VB} become smooth transitions inside the depletion region. With this assumption, the current-voltage characteristics exhibit an exponential behavior as regular *p-n* junctions with the appropriate parameters in the reverse saturation current I_S:

$$I_S = \frac{eD_{n2} n_{i2}^2}{L_{n2} N_{A2}} + \frac{eD_{p1} n_{i1}^2}{L_{p1} N_{D1}}. \tag{2.11}$$

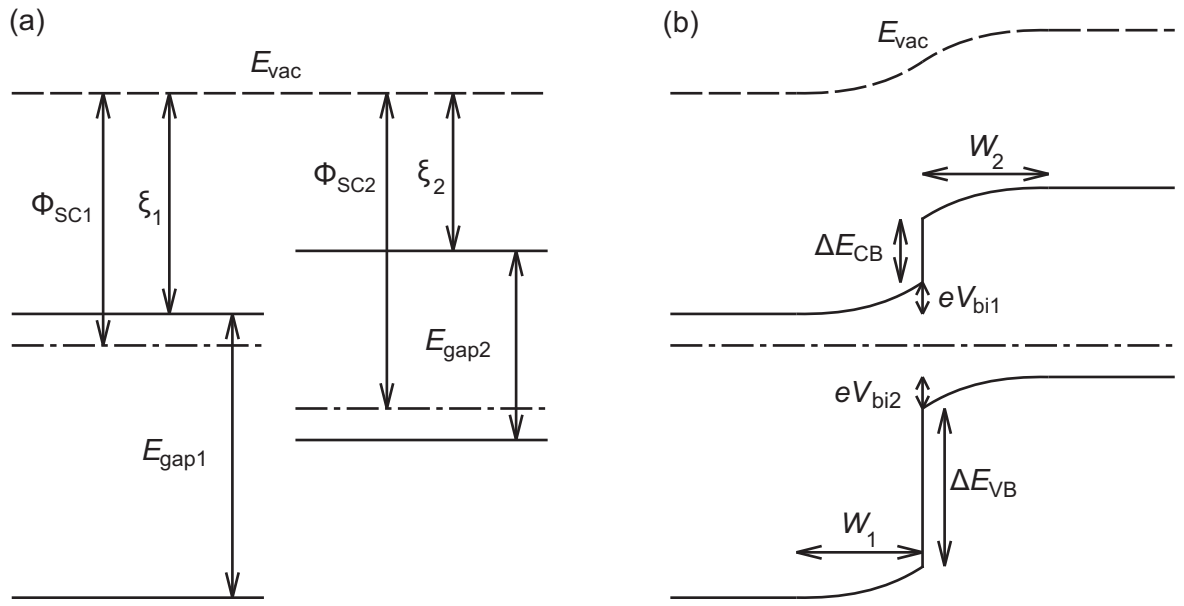

Figure 2.5: *Schematic view of the energy band diagrams for (a) two isolated semiconductors of opposite doping types and with different bandgaps and (b) their idealized anisotype heterojunction at thermal equilibrium.*

Here, D_{p1} and D_{n2} are the diffusion coefficients of the minority charge carriers, n_{i1} and n_{i2} are the intrinsic charge carrier concentrations, and L_{p1} and L_{n2} are the diffusion lengths of the minority charge carriers.

However, for real heterojunctions similar problems as in metal-semiconductor contacts exist. In particular, interface traps and dipoles have a large influence on the band alignment of two semiconductors.

2.2.3 Hybrid organic-inorganic heterojunctions

The energy level alignment at the heterojunction interface is determined, as described in the last Subsection 2.2.2, by the electron affinities, which determine the band offsets. For doped semiconductors also space-charge regions build up due to a matching of the Fermi levels. Additionally, effects such as interface defects or dipoles, which are described in Subsection 2.2.1 play an important role. Due to such effects the assumption of a vacuum level alignment at the heterojunction can only be a first orientation. This also holds for organic-inorganic heterojunctions, which have been less extensively studied compared to metal-organic interfaces. Nevertheless, a short review of the literature will be given in this Subsection.

The importance of the interface dipoles has been demonstrated by surface modifications of the inorganic semiconductor for a TiO_2/P3HT heterojunction solar cell. By chemical binding of various molecules on the inorganic semiconductor the dipole at the hybrid interface could be

tuned and, hence, also the open-circuit voltage could be varied by 0.25 V [Goh07]. For the evaporation of a semiconducting oligomer on a silicon substrate, an interface dipole-induced potential step of 0.3 eV was only observed for p-type silicon but not for n-type silicon. For this oligomer on ITO and Au substrates also dipole-induced potential steps of 0.2 eV and 1.1 eV, respectively, were observed, while the work function of the organic film stayed constant [Pap06]. Additionally, a bend-bending of about $0.2 - 0.3$ eV was observed in the silicon and also in the organic layer, where the space-charge region was only several nanometer [Pap05]. Thus, band bending can only be expected in organic semiconductors from molecules residing in close vicinity of the interface, as only such molecules can take part in charge exchange. Yet, band bending-like behavior has been demonstrated for lightly doped organic films, where the doping can come from impurities left from the synthesis or is induced by the oxygen in the atmosphere. Notably, properly purified organic materials that are protected from exposure to the atmosphere do not show band bending-type behavior even for micrometer-thick films. Hence, a flat-band situation in the interfacial region is expected [Bra09, Ish99].

Furthermore, fundamental work on organic-inorganic heterojunction devices has been done by Forrest *et al.* with the molecular semiconductor 3,4,9,10-perylenetetracarboxylic dianhydrid (PTCDA) which was evaporated on n-type and p-type silicon [For84a, For84b]. The doping type of the silicon as well as the contact metal has been found to significantly influence the current-voltage characteristics of the heterojunctions. The current-voltage characteristics was described in terms of a combination of thermionic emission and space-charge-limited current. At small voltages the thermionic emission over the potential barrier between the organic and the inorganic semiconductor dominates, while for larger voltages the current is space-charge-limited in the organic layer. The thermionic emission theory and the space-charge-limited current model are discussed in detail in Subsections 2.2.1 and 2.3.4.

2.3 Solar cells

In addition to state-of-the-art *p-n* homojunction solar cells made of silicon, also heterojunction can be used for solar cell applications. For inorganic semiconductors both solar cell types will be shortly discussed in Subsection 2.3.1. Organic solar cells are typically heterojunctions where both semiconductors are mixed to form a so-called bulk heterojunction. This concept will be highlighted in Subsection 2.3.2. Solar cells which deal with both, organic and inorganic semiconductors, will finally be presented in Subsection 2.3.3.

2.3.1 Inorganic solar cells

p-n junction solar cells and general solar cell parameters

The standard solar cells today are monocrystalline or multicrystalline silicon *p-n* junctions with a market share of about 85% [Mil07]. When a *p-n* junction is illuminated, photons are absorbed, and the generated excitons dissociate at room temperature in silicon. The photo-induced minority charge carriers, both holes and electrons, diffuse inside the n-type and p-type region, respectively, of the *p-n* junction. When reaching the build-in field, the minority charge carriers cross the *p-n* interface and, under short-circuit conditions, a photocurrent in the reverse direction of the diode flows. Thus, the photocurrent I_{Ph} has to be subtracted in the current-voltage characteristics of the *p-n* diode from Equation 2.8:

$$I = I_{\mathrm{S}} \left[\exp\left(\frac{eV}{nk_{\mathrm{B}}T} \right) - 1 \right] - I_{\mathrm{Ph}}. \tag{2.12}$$

The current-voltage characteristics of an ideal *p-n* junction solar cell is shown in Figure 2.6 (a) in a linear and (b) a semilogarithmic diagram in the dark (black line) and under illumination (red line). Under illumination the curve passes through the fourth quadrant and, therefore, power can be extracted from the device to a load. In Figure 2.6 the short-circuit current, I_{SC}, which is equal to the photocurrent at $V = 0$, and the open-circuit voltage, V_{OC}, which is equal to the photovoltage at $I = 0$, are shown. Additionally, also the quantities I_{m} and V_{m}, which correspond to the current and voltage at the maximum power output, are drawn in the figure. The fill factor FF is defined by

$$FF = \frac{V_{\mathrm{m}} I_{\mathrm{m}}}{V_{\mathrm{OC}} I_{\mathrm{SC}}}, \tag{2.13}$$

which is the ratio of the maximum power output relative to the product of $V_{\mathrm{OC}} \times I_{\mathrm{SC}}$ and can reach around $0.8 - 0.9$ for good solar cells. The ideal conversion efficiency η of a solar cell is defined as the ratio of the maximum power output to the incident power of the light P_{Light}:

$$\eta = \frac{V_{\mathrm{m}} I_{\mathrm{m}}}{P_{\mathrm{Light}}} = FF \frac{V_{\mathrm{OC}} I_{\mathrm{OC}}}{P_{\mathrm{Light}}}. \tag{2.14}$$

From Equation 2.12 the open-circuit voltage can be derived by setting $I = 0$:

$$V_{\mathrm{OC}} = \frac{nk_{\mathrm{B}}T}{e} \ln\left(\frac{I_{\mathrm{Ph}}}{I_{\mathrm{S}}} + 1 \right). \tag{2.15}$$

As the photocurrent is in a first approximation proportional to the illumination intensity, the open-circuit voltage exhibits a logarithmic dependence on the illumination intensity. Furthermore, for a given photocurrent, the open-circuit voltage increases logarithmically with decreasing saturation current. The short-circuit current, as can be seen from Equation 2.12, is equal to

the absolute value of the photocurrent $I_{SC} = -I_{Ph}$ at $V = 0$. The highest reported small area cell efficiency for crystalline silicon is 25.0% as reported by Zhao *et al.* [Zha98, Gre10], which is not too far from the calculated maximum efficiency of about 30% for a material with a bandgap of 1.1 eV [Sho61].

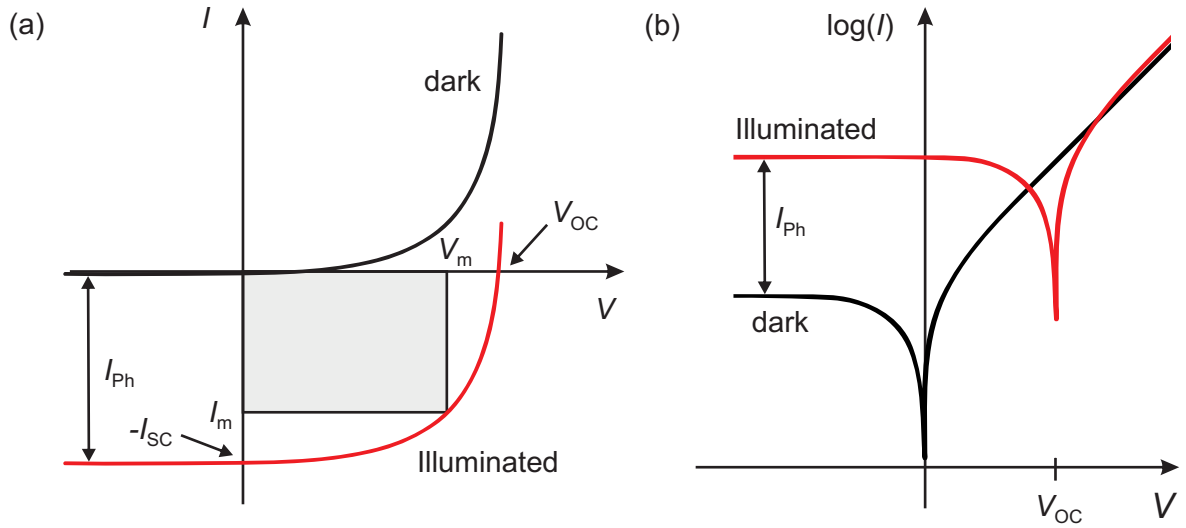

Figure 2.6: *Current-voltage characteristics of an ideal p-n junction solar cell (a) in a linear and (b) in a semilogarithmic plot in the dark (black line) and under illumination (red line). The determination of the maximum power output is also indicated.*

Solar radiation

The sun emits primarily electromagnetic radiation in the ultraviolet to infrared spectral range with a maximum at about 500 nm. This can be approximated by a black body with a temperature of 5800 K, resulting from a nuclear fusion reaction. The intensity of solar radiation in free space at the average distance of the earth from the sun has a value of 1353 W/m^2. The atmosphere attenuates the sunlight before it reaches the earth´s surface, mainly due to reflection and absorption in water vapor in the infrared and ozone in the ultraviolet, and scattering by airborne dust and aerosols. The degree to which the atmosphere affects the sunlight received at the earth´s surface is quantified by the air mass (AM). The solar spectrum for AM1, representing the sunlight at the earth´s surface when the sun is at zenith, is shown in Figure 2.7. However, for terrestrial applications in moderate latitudes the AM1.5 spectrum, with the sun 45° above the horizon, is a satisfactory average and has a total incident power of about 1000 W/m^2.

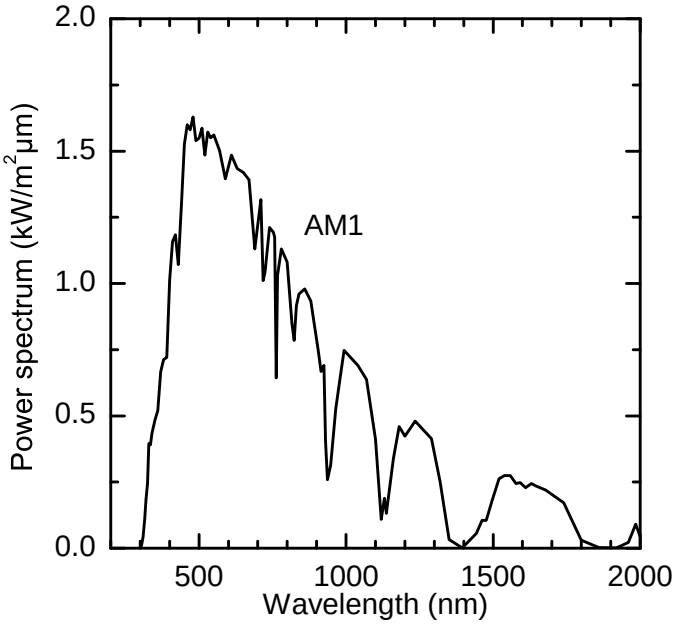

Figure 2.7: *Solar spectrum for AM1. From Reference [Wue00].*

Inorganic heterojunction solar cells

For silicon, p-doping and n-doping is easily achieved. In contrast, for other materials, which may have a higher absorption coefficient, this is not always possible. Thus, heterojunctions are applied where the absorber layer is combined with an opposite doped semiconductor to form a solar cell. An example for such a solar cell is the so-called CIGS solar cell with the n-type CdS buffer layer and the p-type Cu(In,Ga)Se_2 absorber layer, where gallium replaces the indium partially to increase the bandgap. Another example is a p-type CdTe absorber based solar cell which also has a n-type CdS window layer [Mil07]. CdS has a large bandgap of 2.4 eV and thus transmits most of the solar radiation. Hence, it acts as a transparent contact and is necessary for the build-up of the space-charge region at the heterojunction which is responsible for the charge extraction from the p-type material. As it is an electron conducting layer and must not absorb photons, it is (with 10^{17} cm^{-3}) up to two orders of magnitude higher doped than the absorber materials. Furthermore, due to the direct bandgaps of the absorber layers, resulting in high absorption coefficients, only a few micrometers of the p-type absorber layer are needed and most of the photons are absorbed in the space-charge region of the absorber at the heterojunction interface. Dependent on the doping level of the absorber layer, the space-charge region is typically in the range of half a micrometer, resulting in an efficient charge collection [Poo07]. For inorganic heterojunction solar cells based on compound semiconductors, efficiencies of up to 16.5% for CdTe/CdS solar cells [Wu02] and up to 19.5% for CIGS solar cells [Con05] were reported.

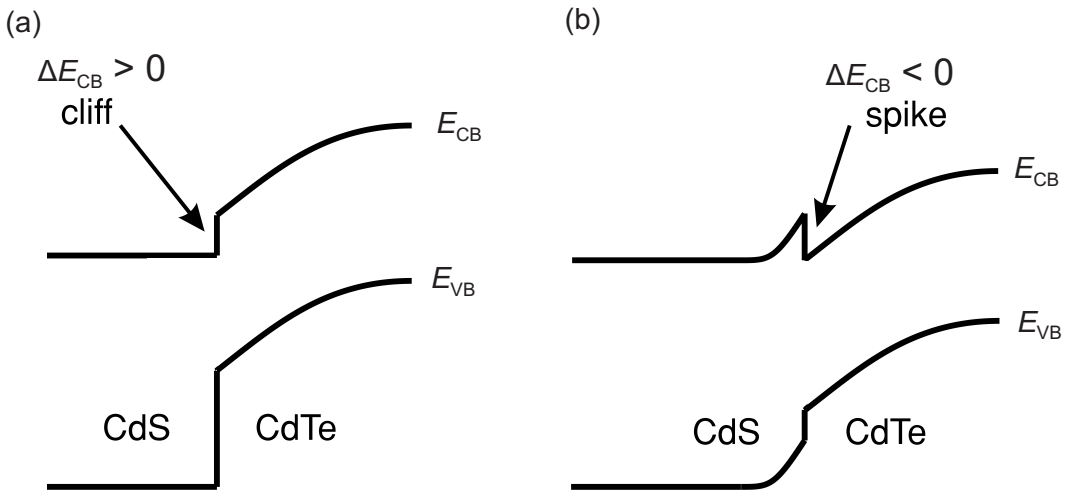

Figure 2.8: *Definition of (a) a cliff ($\Delta E_{\mathrm{CB}} > 0$) and (b) a spike ($\Delta E_{\mathrm{CB}} < 0$) in the alignment of the conduction bands at the CdS/CdTe interface. From Reference [Poo07].*

The relative alignment of the energy bands at the heterojunction is crucial for the performance of the heterojunction solar cells. The important parameter is the conduction band offset ΔE_{CB}. This will be discussed for the case of CdTe/CdS solar cells: If ΔE_{CB} is too large, there is a "cliff" in the band diagram with the conduction band of CdTe above the conduction band of CdS at the junction, resulting in a decrease of the open-circuit voltage. On the other hand, if ΔE_{CB} is negative, there is a "spike" in the band diagram with the conduction band of CdS above the conduction band of CdTe at the junction. Such a barrier decreases the short-circuit current. These two cases are shown in Figure 2.8 (a) and (b). The differences are due to different electron affinities and space-charge regions in the CdS. The mismatch is not too critical as a value of $|\Delta E_{\mathrm{CB}}| < 0.3$ eV can be tolerated. However, there is much scatter in the offset values reported in the literature [Poo07].

For CdTe/CdS an ohmic back contact is a problem as CdTe can not be highly doped, leading to a Schottky barrier at the CdTe/metal interface that points in the opposite direction as the solar cell heterojunction. Thus, the current-voltage characteristics can be described by a two-diode model. Therein, for the solar cell junction an ideal Shockley law is assumed and the back contact is described by thermionic emission. The two diodes are in series, hence the current through the contact and the junction is the same, while the voltages are summed [Poo07].

2.3.2 Organic solar cells

In recent years, the development of thin film plastic solar cells has made significant progress. As organic polymer solar cells can be processed at room temperature and without high vacuum conditions, this makes them an interesting alternative to inorganic solar cells. The most efficient

solar cells are made from polymer-fullerene bulk heterojunctions. Nevertheless, also organic bilayer heterojunction solar cells will be highlighted.

Mechanisms of charge generation in organic solar cells

As already described in Subsection 2.1.1, one big difference of organic semiconductors, as compared to inorganic semiconductors, is that the exciton binding energy is much larger. Hence, excitons can not be dissociated by thermal energy at room temperature nor by the electrical field of a drift solar cell. For the dissociation of the Frenkel excitons heterojunctions are used, where the band offsets are larger than the exciton binding energy. Such a heterojunction and the relevant processes of an organic solar cell are shown in Figure 2.9: The absorption takes place in this example in the electron donor, as the semiconductor is called from which electrons are extracted, while the electron receiving semiconductor is called an acceptor. For standard fullerene-polymer solar cells the polymer acts as a donor and is also the main absorber of the solar radiation. Directly after the absorption an exciton is created, which either recombines or diffuses to the heterojunction interface. Additionally, a small fraction of excitons is dissociated at impurities and defects in the organic semiconductor. When the exciton reaches the interface, it can be dissociated in a free electron and hole via a so called charge-transfer state where the electron and hole still are weakly bound. The prerequisite for the dissociation is that the energetic difference between the LUMO of the donor and the LUMO of the acceptor is larger than the excitonic binding energy. Furthermore, the HOMO of the acceptor has to lie energetically below the HOMO of the donor, as otherwise the complete exciton would be transferred in an energy transfer process. Following the dissociation, the electron is transferred to the cathode and the hole to the anode via hopping processes [Bra08, Mol06].

Organic bilayer heterojunctions

The most basic way to realize an organic solar cell is a layer system built up from two organic layers deposited on each other with a flat interface. This concept is called a bilayer heterojunction [Hop04b]. The ideal structure consists of each an electron donor and an acceptor, which have a band offset large enough to dissociate excitons. With such a structure, already 1986 an efficiency of 1 % was achieved [Tan86]. The semiconductors can both be evaporated or, after depositing the first layer from solution, only the upper layer can be evaporated [Ros00, Sar93]. The processing of both layers from solution is difficult, as the solvent of the upper layer typically dissolves the underlying layer. The evaporation process allows only molecules to be deposited, as polymers would be destroyed during evaporation. The best reported efficiency up to now is 4.2 % in a system made of copper phthalocyanine (CuPc), C_{60}, and one additional exciton blocking layer [Xue04]. The current-voltage characteristics of that organic bilayer heterojunction could be described by a modified ideal diode equation which includes a series resistance

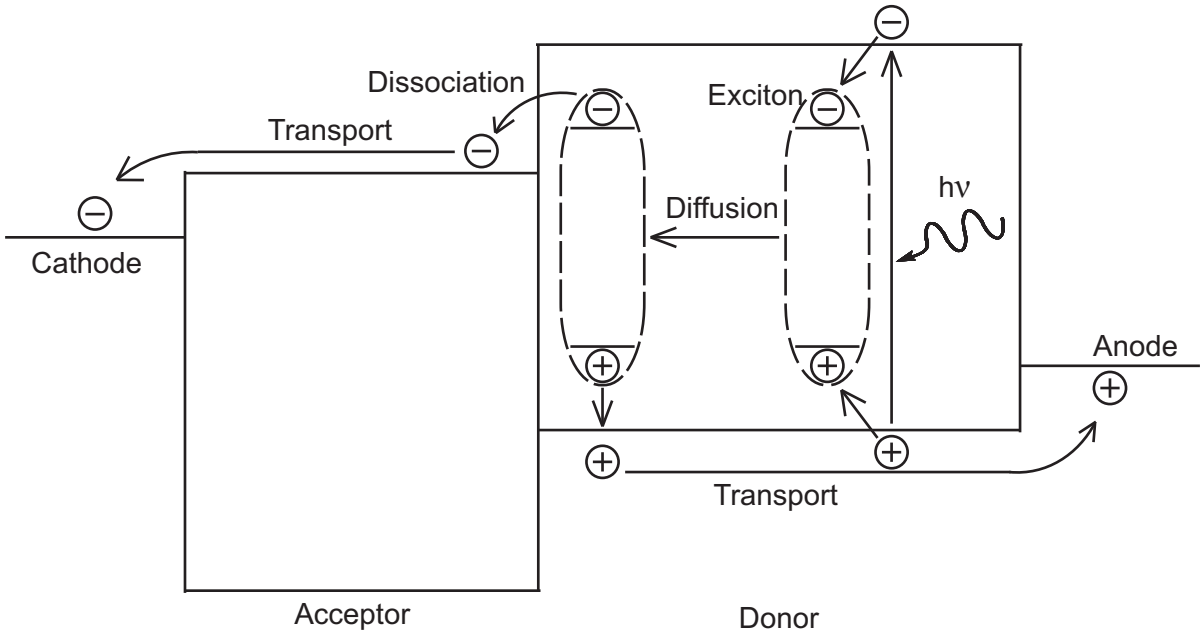

Figure 2.9: *Schematic view of an organic heterojunction solar cell where the absorption of photons takes place in the donor. The processes in such a heterojunction, from the photon absorption, exciton creation, exciton diffusion and dissociation, up to the charge transport to the contacts, are indicated.*

[Xue04]. However, a general problem for bilayer heterojunctions is the small interface between the donor and the acceptor. Due to the small exciton diffusion length for organic molecules of only several nanometers, this limits the efficiency, as only few excitons reach the interface and can be dissociated [Peu03].

Organic bulk heterojunctions

To overcome the limitation of a bilayer heterojunction, the small interface, the two organic materials can be mixed. Such a heterojunction is called a bulk heterojunction and provides an enhanced interface area where excitons can dissociate [Bra01b]. The intermixing of the donor and the acceptor layer can be reached by two methods: The most common way is to dissolve both organic semiconductors in the same solution and to use this mix to deposit the active layer [Sar92, Yu95]. After deposition, *e.g.* via spin-coating or drop-casting, the solvent evaporates, leaving a close mix of the electron donor and acceptor. This procedure provides a large interface but the morphology is not perfect, as often percolating pathways to the respective charge extracting electrodes are missing [Hop06]. For such solvent processed systems, there is a strong dependence of the final morphology on the specific solvent used, the solvent evaporation time, surface interactions, and post-production annealing [Hop04a, Hop04b]. The other way to fabricate bulk heterojunctions is to structure one semiconductor on the nanometer scale before

applying the other semiconductor to fill the structure. For such a structure the charge transport to the electrodes should be facilitated while the large interface, the advantage of a bulk heterojunction, is maintained. However, the ideal structure size of about $10-20$ nm is not easy to realize in organic materials and up to now only structure sizes of about 200 nm have been realized via nanoimprint lithography [Kim07]. Here, inorganic semiconductors are promising, as with inorganic mesoporous materials [Coa03b] or with inorganic nanocrystals [Gue08] smaller structure sizes can be realized, as discussed later on. In Figure 2.10 (a) a disordered and (a) an ideal ordered bulk heterojunction are shown schematically.

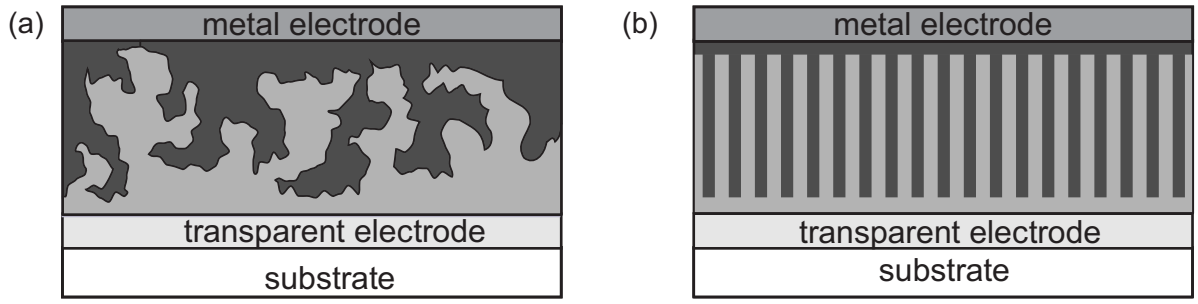

Figure 2.10: *Schematic view of (a) a disordered and (b) an ideal ordered bulk heterojunction.*

Applying the concept of the bulk heterojunction, internal monochromatic quantum efficiencies of up to 96% and external monochromatic quantum efficiencies of 70% can be achieved [Sch02]. Thus, in spite of the small diffusion length in conjugated polymers of only a few nanometers [Mar05, Zho06], due to the bulk heterojunction concept excitons can be separated quite efficiently. The photo-induced charge separation takes place very fast with measured transfer times of around 45 fs [Bra01c]. The maximum open-circuit voltage, $V_{\mathrm{OC}}^{\mathrm{max}}$, which can be achieved in an organic solar cell can be approximated by the difference of the energy levels of both organic semiconductors to $V_{\mathrm{OC}}^{\mathrm{max}} = E_{\mathrm{HOMO}}^{\mathrm{donor}} - E_{\mathrm{LUMO}}^{\mathrm{acceptor}}$ [Bra01a]. For solar cells based on P3HT and [6,6]-phenyl-C_{61}-butyric acid methyl ester (PCBM), efficiencies of up to 5% were achieved [Ma05, RR05, Shr06]. The best organic bulk heterojunction solar cell to date achieves a certified efficiency of 8.3% and has been developed by Konarka Technologies [Kon10]. Such high performance solar cells typically use low-bandgap polymers and PCBM [Che09]. The routes to a further enhancement of the efficiency of organic solar cells are a tuning of the donor-acceptor interface by tuning the energy levels, the development of small bandgap polymers and the creation of an ordered nanostructure with an appropriate domain size below 10 nm [May07].

2.3.3 Hybrid organic-inorganic solar cells

Despite the achievements in the field of organic solar cells, inorganic semiconductors still have several advantages: They possess a much broader absorption spectrum than organic semicon-

ductors, they can be doped to a specific n-type or p-type doping level, and they have a higher mobility. In addition, to make solution processing also possible with inorganic semiconductors, one interesting approach are semiconductor nanocrystals which can be dispersed in an appropriate solvent. This provides an easy processability and also allows for the use of size-dependent band gap tuning of the nanocrystals [Gue08]. Furthermore, it has been demonstrated that impact ionization occurs with high efficiency in semiconductor nanocrystals, leading to carrier multiplication via the formation of several excitons for one absorbed high-energy photon [Sch04].

While preserving the advantage of solution precessing, hybrid organic-inorganic solar cells containing inorganic semiconductor nanocrystals and organic semiconductors are promising for several reasons: Due to the high surface to volume ratio of nanocrystals, a large interfacial area to the organic counterpart can be realized. Thus, the size of the inorganic nanocrystals defines the morphology of the bulk heterojunction. For this purpose, also the use of structured inorganic semiconductors, on which the organic semiconductor is applied, is an interesting option to form ordered bulk heterojunctions. Another advantage is the ability to engineer interfacial band offsets and hence to modify the photovoltage due to functionalization of the inorganic semiconductor [Hsu10, Goh07], by different doping levels of the inorganic semiconductor [For84a], or by tuning the bandgap of the inorganic semiconductor, *e.g.* by substitution of Mg into ZnO [Ols07]. Concerning the absorption of the sun light, the spectral range of the absorption can be enhanced in hybrid organic-inorganic solar cells due to the broader absorption spectra of inorganic semiconductors compared to organic semiconductors. In organic solar cells fullerenes contribute only to a small part of the total absorption, thus, the inorganic semiconductor should replace the fullerenes in hybrid solar cells. In addition, the morphological stability in organic solar cells is an issue, as under operating conditions a morphological degradation *e.g.* due to growing fullerene domains takes place [Hop04b]. Thus, replacing the fullerenes in hybrid solar cells will also enhance the morphological stability.

A schematic view of the working principle of a hybrid solar cell is shown in Figure 2.11. The processes taking place in the organic donor are described analogous to organic solar cells in Figure 2.9. For the inorganic part, the main difference is the small exciton binding energy, allowing the formation of free charge carriers at room temperature, in contrast to organic semiconductors. For the dissociation of excitons at the organic-inorganic interface, the offset between the LUMO of the electron donor, $E_{\mathrm{LUMO}}^{\mathrm{donor}}$, and the conduction band edge of the inorganic semiconductor, E_{CB}, must be larger than the exciton binding energy. Additionally, to inhibit energy transfer from the organic to the inorganic semiconductor and to allow for holes to be transferred to the organic counterpart, the valence band edge of the inorganic semiconductor, E_{VB}, must be energetically below the HOMO of the donor, $E_{\mathrm{HOMO}}^{\mathrm{donor}}$.

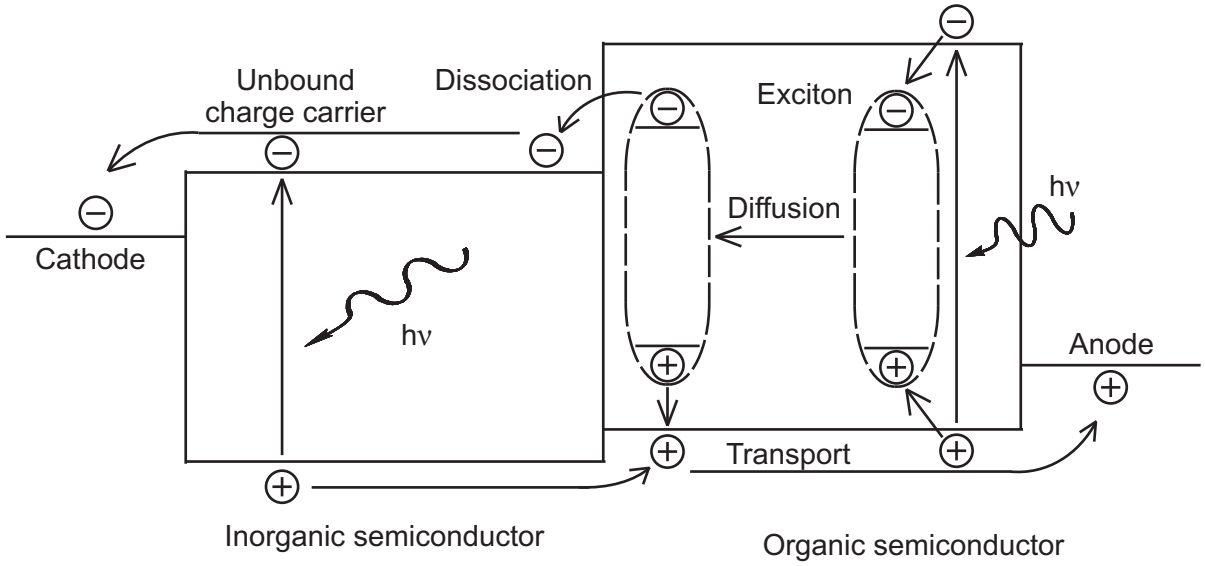

Figure 2.11: *Schematic view of a hybrid heterojunction solar cell. Absorption takes place both in the organic semiconductor, which acts as an electron donor, and in the inorganic semiconductor, which transfers holes to the organic semiconductor. The processes taking place in a hybrid heterojunction, from the photon absorption, photo-induced charge and exciton generation, exciton diffusion and dissociation, up to the charge transport to the contacts, are indicated.*

Hybrid bulk heterojunction solar cells

As for organic solar cells, also for hybrid solar cells the bulk heterojunction concept offers the possibility to efficiently dissociate the excitons created in the organic part. For hybrid heterojunctions which are completely fabricated from solution, the range of the applied inorganic nanostructures spans from nanocrystals over elongated nanocrystals, so-called nanowires, up to branched nanocrystals [Mil05]. By using elongated nanocrystals a network is formed that provides pathways for the charges, thus, a hopping transport from nanocrystal to nanocrystal is avoided and band conduction is prevalent which improves the efficiency substantially [Huy02]. However, phase separation is, as in organic solar cells, still a problem. Thus, the approach of an ordered bulk heterojunction is a promising route to increase the efficiency of hybrid solar cells. To obtain structured inorganic semiconductors, one can either use porous semiconductors via etching [Lev04], grow nanowires on a substrate [Tsa07], or use mesoporous materials, *e.g.* TiO_2 produced by a sol-gel process [Coa05a]. For the incorporation of polymers into such nanostructures, several options doe exist, *e.g.* coating of the inorganic nanostructures with appropriate molecules that facilitate the wetting of the nanopores or the heat treatment of the polymer layer resulting in a filling of nanopores of $5 - 10$ nm [Coa05b].

A schematic view of both types of hybrid bulk heterojunctions is shown in Figure 2.12, where in (a) a heterojunction with nanoparticles is shown and in (b) an ordered bulk heterojunction with a porous inorganic semiconductor.

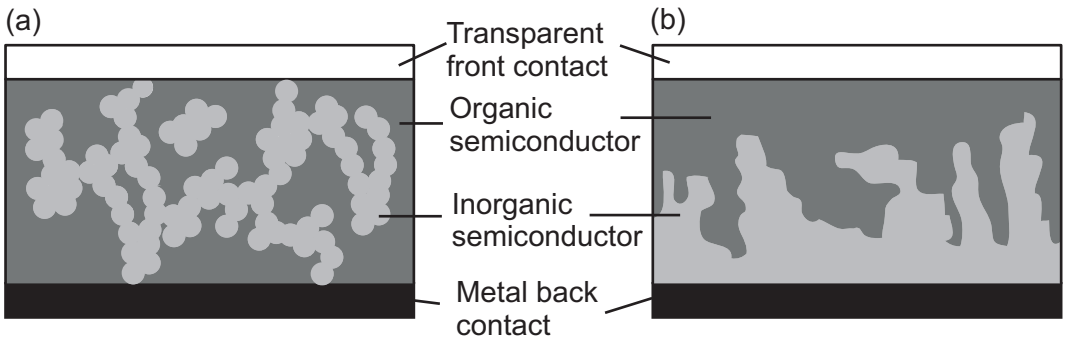

Figure 2.12: *Schematic illustration of hybrid bulk heterojunctions with (a) incorporated nanoparticles and (b) with an structured inorganic semiconductor.*

A large variety of hybrid material systems for solar cell applications has already been investigated [Gue08]: Typically a polymer, *e.g.* P3HT or poly(2-methoxy-5-(2'-ethylhexyloxy)-paraphenylenevinylene) (MEH-PPV), has been combined with inorganic nanoparticles. Thus, hybrid bulk heterojunction solar cells have been realized with nanoparticles of CdS [Gre96], PbS [Gue07], ZnO [Bee04], TiO_2 [Bou07], and Si [Nie09, Liu09]. The highest reported efficiency of 3.1 % was achieved with branched CdSe nanocrystals and a low bandgap polymer [Day10]. For P3HT/CdSe nanowire bulk heterojunctions 1.7 % have been achieved [Huy02] which could be increased to 2.6 % [Sun06] by using a high boiling point solvent leading to the formation of P3HT nanofibers.

For ordered hybrid solar cells with a porous TiO_2 filled with P3HT, efficiencies of 0.5 % have been achieved [Coa03b]. An interesting approach to form nanoporous layers in TiO_2 is nanoimprinting of an inorganic TiO_2 sol-gel precursor that has not yet dried [Goh05a, McG09]. In bulk heterojunctions made of amorphous silicon, which was nanostructured by an etching step and subsequently infiltrated with P3HT, efficiencies of about 0.3 % have been reported [Gow08]. For solar cells made of semiconducting polymers and silicon nanowires, produced by etching of a silicon wafer or by growing via chemical vapor deposition, efficiencies of $0.01 - 0.07$ % have been reported [Ale08, Che07].

The dye-sensitized solar cells, also known as Grätzel cells [O´R91], which are prominent hybrid organic-inorganic heterojunction solar cells, will not be discussed here, as the working principle relies on dyes and an electrolyte, both of which is not used in this work.

Hybrid bilayer heterojunction solar cells

For hybrid solar cells the bulk heterojunction concept is advantageous due to the large interface. However, for the investigation of basic properties relevant for solar cells, such as the band alignment, flat bilayer heterojunctions are more adequate, as the interface morphology is less complex and the number of parameters is reduced. In addition, inorganic volume semiconductors can be used with well known properties.

An optimized band alignment in hybrid solar cells, either by molecular dipoles [Goh07] or by optimization of the band offset by varying the band positions of the inorganic semiconductor [Ols07] is important. Also the chemistry of the substrate surface plays an important role, influencing the order of the polymer layer and thus changing the solar cell efficiency [Hsu10].

Some work has been done on bilayer heterojunction solar cells made of a semiconducting polymer and amorphous silicon: Already a high efficiency of 1.6 % has been reported, though this results mainly from the underlying Schottky solar cell with doped amorphous silicon instead of the hybrid heterojunction [Ale07]. More reliable is the value of 0.16 % for the efficiency achieved by Gowrishankar *et al.* with an amorphous silicon/P3HT heterojunction [Gow06]. Besides the electron transfer from the P3HT to the amorphous silicon they propose a second contribution to the current via an energy transfer. Thereby excitons are transferred from the P3HT to the amorphous silicon, followed by a back transfer of the holes to the polymer. The energy transfer is described in the framework of the Förster energy transfer [För59]. Such a transfer is only possible if the bandgap of the polymer is larger than that of the semiconductor and a spectral overlap between the photoluminescence of the polymer and the absorption of the semiconductor exists, which is the case for amorphous silicon and P3HT. Thus, not only the relative positions of the LUMO and the conduction band, but also of the HOMO and the valence band are important for such a heterojunction. This was supported by comparison with the polymer MEH-PPV which exhibited a significantly smaller solar cell efficiency due to lower hole back transfer due to the lower HOMO of MEH-PPV as compared to P3HT. A Förster energy transfer has also been used for hybrid bulk heterojunction solar cells to improve the efficiency by introducing a further organic layer between a P3HT and a TiO_2 layer [Liu05].

2.3.4 Equivalent circuit

For the description of the current-voltage characteristics of a solar cell, an equivalent circuit can be introduced. The ideal solar cell has a diode current-voltage characteristics, where a constant-current source of photocurrent, I_{Ph}, is in parallel with the diode. For a practical solar cell, this ideal equivalent circuit will be modified to include the series resistance, R_{S}, for ohmic losses in the connecting leads, the contacts and in the semiconductors. In addition, the shunt resistance, R_{Sh}, will be included to account for leakage currents, *e.g.* at grain boundaries or at

the surface. The equivalent circuit should include R_S added in series with the diode, and R_{Sh} added in parallel with the diode. The equivalent circuits for (a) ideal solar cells and (b) real solar cells are shown in Figure 2.13. For steady-state measurements, as performed in this work, the

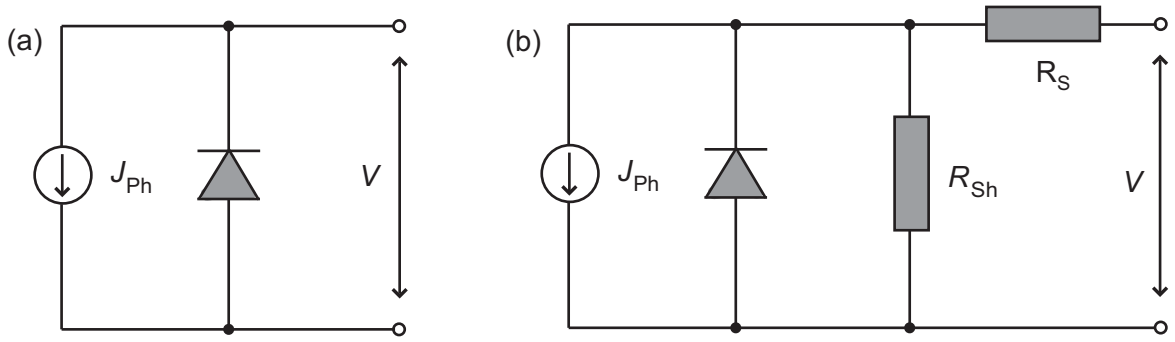

Figure 2.13: *Equivalent circuit diagrams of (a) an ideal solar cell and (b) of a real solar cell, where the series resistance R_S and the shunt resistance R_{Sh} are considered.*

capacitance can be neglected. Thus, considering the two resistances, the diode current-voltage characteristics is modified to [Wue00]:

$$I = I_S \left(\exp \frac{e\,(V - R_S I)}{n k_B T} - 1 \right) + \frac{V - R_S I}{R_{Sh}} - I_{Ph}. \tag{2.16}$$

This model for the current-voltage characteristics does not take into account any additional conduction mechanisms. In particular, the space-charge-limited current (SCLC) mechanism, which has a nonlinear current-voltage dependence and has been reported in a large variety of organic and inorganic semiconductors and solar cells, is not taken into account [Pal06b]. The SCLC is described in more detail below.

An ideal solar cell would have $R_S = 0$ and $R_{Sh} \to \infty$, while real solar cells differ from this which changes the current-voltage characteristics and reduces the area of the current-voltage characteristics in the fourth quadrant, which reduces mainly the fill factor and thus the efficiency. Both, R_S and R_{Sh}, can be estimated from the current-voltage characteristics of a real solar cell via the differential resistances at $I = 0$ and $U = 0$, respectively:

$$R_S \approx \left(\frac{\partial U}{\partial I} \right)_{I=0}, \quad R_{Sh} \approx \left(\frac{\partial U}{\partial I} \right)_{U=0}. \tag{2.17}$$

space-charge-limited current

The space-charge-limited current model describes charge transport in a low conductivity material, where the concentration of injected charge may exceed the intrinsic charge concentration and, thus, space charge builds up in the sample [Ros55, Lam56]. Investigations have shown that bulk conduction in disordered semiconductors, *e.g.* in undoped conjugated polymers or in

nanoparticle ensembles, is described well by the hopping transport of electrons and holes, taking into account space charge effects and traps of different depths [Chi04, Raf05]. The disorder in such materials is well approximated by an exponential shape of the distribution of states:

$$n(E) = \frac{N_\mathrm{t}}{E_\mathrm{t}} \exp\left(-\frac{E}{E_\mathrm{t}}\right). \tag{2.18}$$

Here $n(E), E, N_\mathrm{t}$, and E_t are the trap density of states, the energy, the total trap density and the characteristic trap energy, respectively. E_t is often expressed as a characteristic temperature T_t from $E_\mathrm{t} = k_\mathrm{B} T_\mathrm{t}$, where a larger T_t accounts for a trap lying deeper in the bandgap.

When applying a voltage to a semiconductor with an exponential trap distribution, three regions can be distinguished, corresponding to ohmic, trap filling and space-charge-limited current: At small voltages, where the conduction is due to the intrinsic thermally generated charge carriers, an ohmic conduction with $I \approx V$ is observed. For intermediate voltages traps will be filled up due to charge injection. A rapid increase in current with small increase in voltage is observed, where a steep slope indicates a narrow distribution of gaps, while a low slope implies a extended distribution. This region has a power law dependence of current density on the bias voltage given by [Chi04, Pal06b]:

$$I = k_\mathrm{SCLC} V^m. \tag{2.19}$$

Here, k_SCLC is related to the film thickness, trap distribution, and conductivity of the transport path, where $m = l + 1$, with $m > 2$ and $l = T_\mathrm{t}/\mathrm{T}$. When all traps are occupied by injected charge carriers, the trap free space-charge-limited current region is reached, where a space charge accumulates near the injecting electrode and limits the current. This behavior is described by the Mott-Gurney law [Mot40]:

$$I = \frac{9}{8} \varepsilon_\mathrm{r} \varepsilon_0 \mu \frac{V^2}{d^3}, \tag{2.20}$$

where μ and d are the mobility and the thickness of the semiconductor, respectively. In Figure 2.14 these three regimes of the current of a semiconductor with an exponential trap distribution are shown in a double-logarithmic current-voltage plot.

Both in inorganic solar cells, such as CIGS [Tan03], and in organic solar cells [Chi03a], SCLC has been found to play an important role. Also in hybrid bulk heterojunction solar cells with CdSe nanowires and P3HT SCLC has been observed, limiting the forward current of the diode, where the onset of the SCLC is dependent on the metal contacts used for the solar cell [Huy03]. And in organic-inorganic bilayer heterojunctions at higher voltages also the SCLC limits the current [For84a]. Furthermore, in organic semiconductors, such as P3HT [Nik03, Chi04], and in inorganic nanoparticles, such as CdSe/ZnS nanocrystals [Hik03] or silicon nanocrystals [Raf05, Bur97], SCLC behavior has been reported.

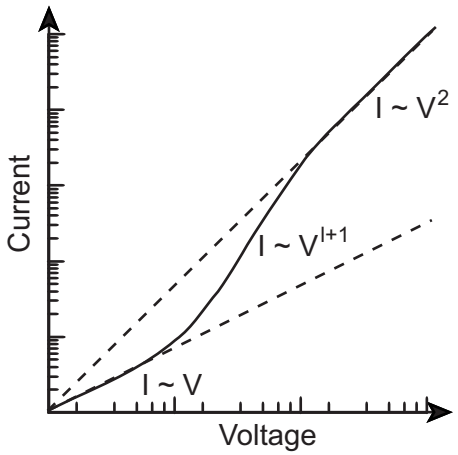

Figure 2.14: *Double-logarithmic plot of the current of a semiconductor with exponential trap distribution where the ohmic, the trap filling, and the space-charge-limited current regimes are indicated.*

Modified equivalent circuit including space-charge-limited current effects

Generally, in organic solar cells, the electrical characteristics are essentially interface-dependent under the low voltage regime, while they are bulk-dependent in the high voltage regime [Mol06]. In the high voltage regime, the current density varies with V^m. This behavior is illustrated in Figure 2.15, where the different regimes of the current-voltage characteristics of an organic solar cell are shown.

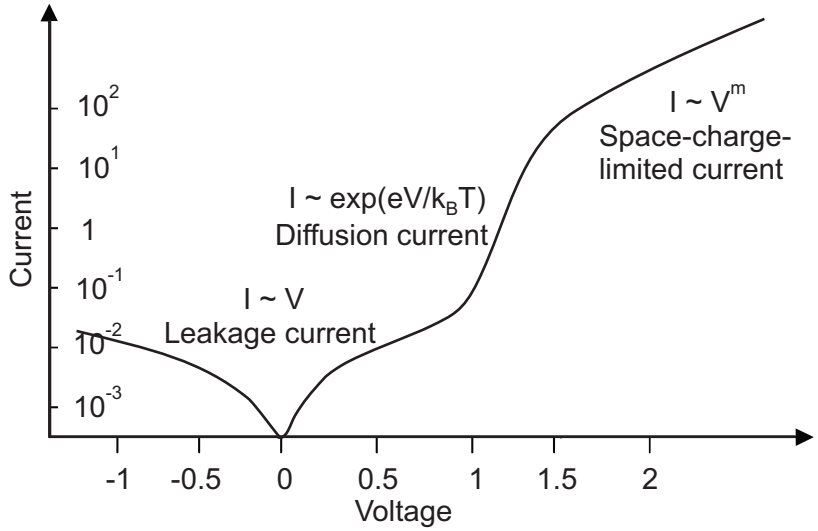

Figure 2.15: *Typical dark current-voltage characteristics of an organic solar cell, where the different voltage regimes are indicated. After Reference [Mol06].*

To model the current-voltage characteristics of hybrid heterojunctions, the SCLC effect has to be included. For this purpose, different approaches can be found in the literature: To describe

the behavior of hybrid bulk heterojunction solar cells with CdSe nanowires and P3HT, Huynh *et al.* include the SCLC effect by incorporating a quadratic voltage dependence $I \approx V^2$ in the Shockley equation [Huy03]. However, with a quadratic term, only the trap-filled regime of the SCLC is considered. Pallares *et al.* can successfully model the behavior of a solar cell made of p-type amorphous silicon carbide on n-type crystalline silicon by inclusion of a SCLC term in the general form of Equation 2.19 [Pal06b]. They separated the junction effects from the bulk region effects by an equivalent circuit consisting of an ideal diode, accounting for the junction, in series with a parallel combination of an ohmic resistance and a nonlinear SCLC resistance term, accounting for the bulk effects. However, the parallel combination of the resistances is not very plausible, as the current in the solar cell will be limited by the higher resistance and the resistance due to SCLC enhances the total series resistance [Mol06]. Forrest *et al.* investigated a hybrid heterojunction with doped silicon and a semiconducting molecule, which is described by a thermionic emission diode at low voltages and by SCLC at higher voltages [For84a]. There, the space-charge current is modeled by an effective voltage-dependent resistance which is in series with the voltage-independent series resistance.

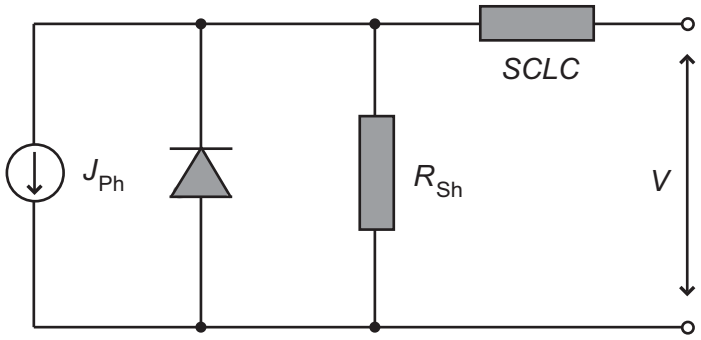

Figure 2.16: *The modified equivalent circuit diagram for a solar cell, where it is assumed that space-charge-limited current (SCLC) effects mask the series resistance.*

Similar to the discussed models, in this work we assume that the SCLC is the dominant series resistance which comes into play at higher electric fields and outnumbers the ohmic resistance. Hence, the ohmic term, R_S, can be neglected. Instead, a nonlinear SCLC resistance element is included, which accounts for the SCLC transport. The resulting equivalent circuit diagram is shown in Figure 2.16. With this modification, for a given applied voltage, V, a voltage drop at the heterojunction, V_J, and a voltage drop in the bulk, V_B, takes place, with $V = V_J + V_B$. For $R_{Sh} = \infty$ and without illumination, the applied voltage is given by:

$$V = \frac{nk_BT}{e} \ln\left(\frac{I}{I_S} + 1\right) + \left(\frac{I}{k}\right)^{\frac{1}{m}}. \tag{2.21}$$

3 Materials

In this chapter the different semiconductors which are treated in this work will be described. Particular attention will be given to the optical and electronic characteristics of the semiconductors. In the first Section 3.1, the properties of the inorganic semiconductors will be highlighted. Besides the bulk inorganic semiconductors, crystalline silicon and silicon carbide, also silicon nanocrystals will be discussed. In the second Section 3.2, the properties of the organic semiconductors, poly(3-hexylthiophene) (P3HT) and [6,6]-phenyl-C_{61}-butyric acid methyl ester (PCBM), will be highlighted.

3.1 Inorganic semiconductors

3.1.1 Silicon

Approximately 26 % of the earth´s crust consists of silicon, where it can be found bonded to oxygen as silica and silicates [Bin99]. It is the principal component of most semiconductor devices, such as microchips or solar cells. *E.g.* the market share for crystalline and multicrystalline silicon solar cells was about 90 % in 2007 [Mil07]. The silicon bandgap of 1.12 eV at room temperature [Sze07] is near the optimum bandgap, as calculated from Shockley and Queisser in 1961 [Sho61]. This fact, together with the availability of silicon, the sophisticated production technology, and the high level of knowledge, prevails the disadvantages of silicon for solar cells, in particular the high costs of bulk crystalline silicon and the low absorption coefficient. The low absorption coefficient of silicon is due to the fact that crystalline silicon is an indirect semiconductor. The absorption coefficient of crystalline silicon is shown in Figure 3.1 as the dashed line.

For heterojunctions with silicon, the energetic positions of the valence band and conduction band edges relative to the vacuum level are important to determine the band offsets, as described in Subsection 2.2.2. For the electron affinity, ξ, of silicon the value of 4.05 eV can be found in the literature [Sze07, Iof10, Lev96]. By adding 1.12 eV [Sze07] for the bandgap to the electron affinity, the distance of the valence band maximum to the vacuum level can be calculated to 5.17 eV.

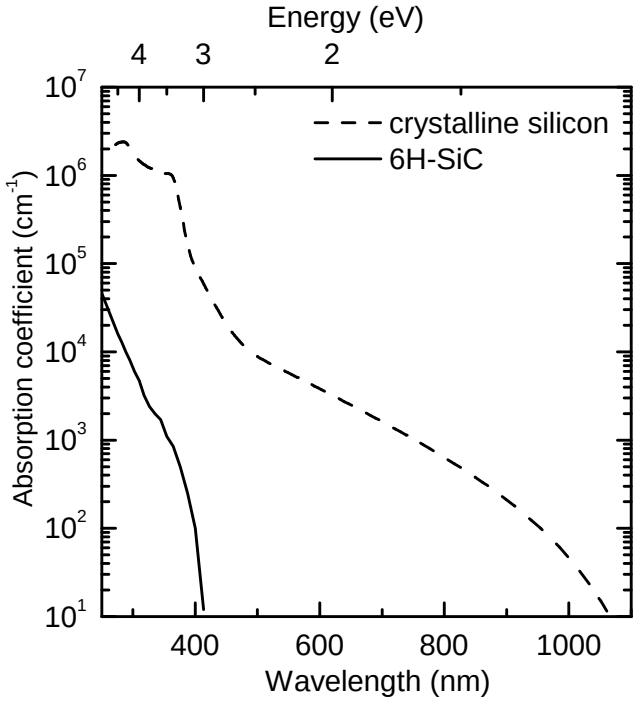

Figure 3.1: *Absorption coefficients of crystalline silicon and 6H-SiC. From References [Das55, Hul99] and [Phi60], respectively.*

For the fabrication of hybrid heterojunctions, silicon wafers with eight different doping levels and types were used in this work. In Table 3.1 the doping properties of the different wafers are summarized. Additionally, the distances of the Fermi levels, E_{F}, of the doped silicon wafers relative to the intrinsic Fermi level, E_{i}, of undoped silicon in the middle of the bandgap at room temperature are given [Sze07]. The silicon wafers had a thickness in the range of $360-525\ \mu$m, and all but the n^{--}-Si wafer (111) had an orientation of (100). All silicon wafers were produced by the Czochralski process and were polished on the side on which the P3HT was deposited. The energetic positions of the band edges and the Fermi levels are summarized at the end of this chapter in Figure 3.8.

3.1.2 Silicon carbide

Silicon carbide is a group-IV compound semiconductor which is used in various semiconductor devices, *e.g.* in diodes [Mat91] or transistors [Pal93]. It has a good temperature stability and, hence, is used particularly in high power devices. Additionally, as silicon carbide is, after diamond, the second hardest material, it is also used as abrasive. Due to the different values of the electronegativity, χ, of silicon with $\chi = 2.55$ and carbon with $\chi = 1.9$ on the Pauling scale, the Si-C bond has an ionic fraction, resulting in a polar silicon carbide crystal. The binding energy of Si-C with 3.1 eV is higher than for Si-Si with 2.35 eV, leading to very stable

Type	Doping element	Specific resistance (Ω cm)	Dopant concentration (cm^{-3})	$E_F - E_i$ (± 0.05 eV)
n^+	Sb	$0.01 - 0.02$	$4 - 9 \times 10^{18}$	0.55
n	P	$0.3 - 1.5$	$3 \times 10^{15} - 2 \times 10^{16}$	0.35
n^-	P	$14 - 23$	$2 - 3 \times 10^{14}$	0.25
n^{--}	P	$3000 - 6000$	$7 \times 10^{11} - 1.5 \times 10^{12}$	0.10
p^{--}	B	$75 - 95$	$1.5 - 2.5 \times 10^{14}$	-0.25
p^-	B	$4.5 - 6$	$2 - 3 \times 10^{15}$	-0.35
p	B	$0.1 - 1$	$1.5 \times 10^{16} - 1 \times 10^{17}$	-0.40
p^+	B	$0.01 - 0.02$	$4 - 9 \times 10^{18}$	-0.50

Table 3.1: *Summary of the different silicon wafer types used in this work. The physical properties are valid for room temperature.*

Si-C bilayers [Sie02]. For silicon carbide, due to different stacking sequences of the Si-C bilayers, various polytypes can build up. Already more than 250 polytypes have been reported in the literature [Fis90]. Additionally, for hexagonal polytypes the surface can be distinguished, depending on the polarity, in the C-face or the Si-face. Only bulk silicon carbide is used in this work, nevertheless, also silicon carbide nanoparticles and nanowires, which are important for bulk heterojunctions, have been produced using various methods [She03, Hon03, Liu07]. Furthermore, SiC can be covalently functionalized with organic molecules [Sch08, Ros09] and polymers [Ste10] in order to tune the interfacial chemical and electrical properties.

In this work the hexagonal 6H-SiC (α-SiC) is used, which is a wide bandgap semiconductor with an indirect bandgap of 3.0 eV at 300 K [Lev01]. The n-type 6H-SiC substrate (SiCrystal AG) was doped to 1×10^{18} cm^{-3} with nitrogen donors and had a resistivity of $\approx 1 \times 10^{-2}$ Ω cm. The (0001) surface of the 300 μm thick wafer was polished (NovaSiC) to a root mean square (RMS) roughness of ≤ 0.3 nm and was used for formation of the heterojunctions. Both faces of the 6H-SiC, the Si-face and the C-face were applied at the hybrid interface. The absorption coefficient of 6H-SiC is shown in Figure 3.1 as the solid line.

The Fermi level of the n-type 6H-SiC used in this work is about 120 meV below the conduction band minimum [Pel84]. The value for the absolute position of the valence band maximum of 6H-SiC was determined theoretically by van de Walle *et al.* [Wal03] and experimentally by Dillon *et al.* [Dil59] to be 5.9 eV and 6.0 eV, respectively, below the vacuum level. On the other hand, our own contact potential difference measurements of the work function indicate a value of about 3.9 eV for the conduction band minimum, leading to a valence band energy of about 7 eV, which is in agreement with the value of 6.7 eV reported by Pelletier *et al.* [Pel84]. Furthermore, in contact potential difference measurements the difference between the two polarities was determined to be about 100 meV. The energetic positions of the band edges and of the Fermi level are shown again in Figure 3.8.

3.1.3 Silicon nanocrystals

Gas phase production of silicon nanocrystals

Silicon nanocrystals can be produced by a variety of production methods, *e.g.* etching of silicon wafers, colloidal chemistry, laser ablation, or gas phase growth [Lec08a]. However, especially the colloidal chemistry and the gas phase production of silicon nanocrystals are methods which are scalable to an industrial production level. The silicon nanocrystals used in this work stem from a gas phase reactor and were produced by our cooperation partners Hartmut Wiggers at the Universität Duisburg-Essen and by Evonik Degussa GmbH Creavis in Marl. For the production of silicon nanocrystals, gaseous silane precursors, mainly monosilane (SiH_4) are applied, which can be diluted with noble gases. In addition, hydrogen can be used to passivate the surfaces and to reduce the reaction kinetics. For a doping of the silicon nanocrystals, dopant gases such as diborane (B_2H_6) and phosphine (PH_3) can be added. To react inside the reactor, the precursor gases have to be transferred to radicals which can be done by hot surfaces, laser irradiation, or plasma heating [Lec08a]. The latter method was applied for the nanocrystals used in this work. The energy to dissociate the gas molecules is coupled into the reactor via a microwave plasma [Kni04]. In Figure 3.2 a schematic view of such a microwave plasma reactor is given. As can be seen from the figure, the precursor gases enter the reactor inside a tuned microwave cavity. There the high electromagnetic field amplitude heats the precursor gases and leads to a plasma containing radical silane compounds. Then, the radicals nucleate and the nanocrystals grow. At the end of the silica tube, a pump system brings the nanocrystals to the extraction chamber, where a filter is situated.

Properties of silicon nanocrystals

The grown nanocrystals exhibit a regular spherical shape, and the size distribution is relatively small. The size distribution follows a log-normal distribution function, which is typical for such continuous growth processes [Gra76]. The log-normal distribution is given by:

$$f(x,\sigma) = \frac{1}{(2\pi)^{\frac{1}{2}} \ln\sigma} \exp\left(-\frac{(\ln x - \overline{\ln x})^2}{2\ln^2\sigma}\right). \tag{3.1}$$

Here, $\overline{\ln x}$ is the mean value of the distribution and σ is the standard deviation. Typical values of $\sigma = 1.15 - 1.3$ are observed for silicon in the range of $4 - 20$ nm, while for larger nanocrystals in the range of $30 - 50$ nm values of $\sigma = 1.5$ are observed [Kni04]. The mean size of the grown nanocrystals depends mainly on the concentration of the silane, the microwave power, and the total gas pressure. Most of the silicon nanocrystals studied in this work had an average size of about $20 - 30$ nm, but many different nanocrystals with sizes between 4.3 nm up to 33 nm were

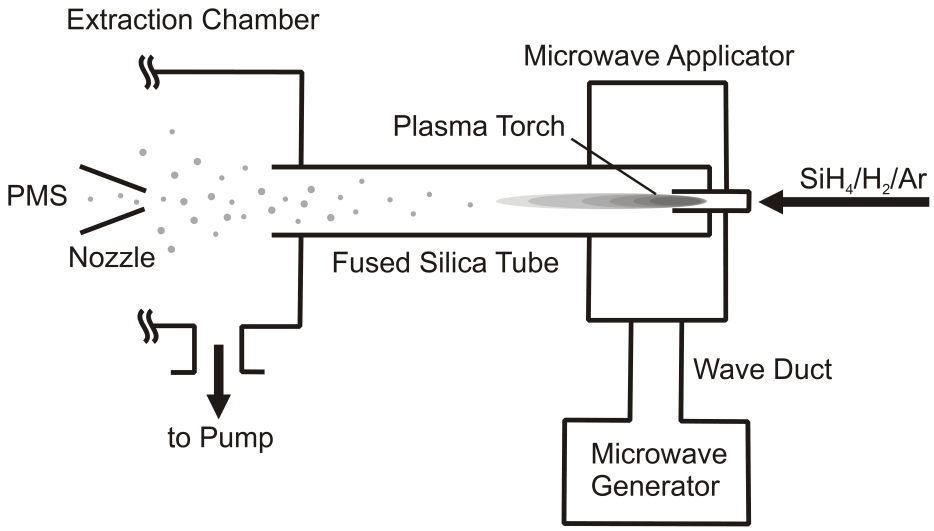

Figure 3.2: *Schematic view of the gas phase production of silicon nanocrystals in a microwave plasma reactor. The reaction zone is limited to a small microwave-heated reactor volume close to the precursor entrance. For monitoring the nanocrystal size distribution in-situ, a particle mass spectrometer (PMS) is applied. From Reference [Lec08a]*

also used in the experiments. Quantum confinement of the nanocrystals can be neglected in the frame of this work, as it starts to play a role if the particle size falls below the free-exciton Bohr radius, which amounts to about 4 nm in crystalline silicon [Del93]. Furthermore, the smallest nanocrystals were only used in experiments regarding the morphology of the sample. In addition to the intrinsic silicon nanocrystals, also phosphorus-doped nanocrystals were produced and could be used for this work. For the nanocrystals used in this work the microwave power was $1200 - 1800$ W, the total gas pressure $10 - 100$ mbar, and the silane flux $5 - 180$ sccm. An overview over the exact process parameters of the nanocrystals used in this work is given in Table 3.2.

In Figure 3.3 a high resolution transmission electron image of silicon nanocrystals is shown. It demonstrates the spherical shape of the nanocrystals and that only one crystalline domain is present. Furthermore, a thin, irregular oxide shell, which is typically about 1 nm thick, is present at the nanocrystal surface.

The absorption coefficient of spin-coated silicon nanocrystal layers has been determined by reflection and transmission measurements and by photothermal deflection spectroscopy by Lechner [Lec08a] and is shown in Figure 3.4 as a solid line. The fabrication of silicon nanocrystal dispersions and the deposition via spin-coating is described in Subsection 4.1.1. As the spin-coated silicon nanocrystal layers exhibit a porosity of about 60 % [Lec08a], the spectrum is corrected, which leads to a good overlap with the absorption coefficient of crystalline silicon, which is also shown as a dashed line, in the ultraviolet spectral region. However, above 400 nm

Sample	P (W)	p (mbar)	SiH_4 (sccm)	Ar (sccm)	H_2 (sccm)	PH_3 (sccm)	[P] (cm^{-3})	[SiH_4] (10^{-3})	d (nm)
201106	1200	10	5	7045	3350	-	-	0.97	4.3
220807	1800	20	30	7270	2350	0.3	5×10^{20}	3.1	6.1
160807	1800	80	60	8040	2350	0.2	2×10^{20}	5.7	12
130406	1800	100	60	16540	4000	-	-	2.9	16
270307	1800	50	100	8900	1800	0.15	6.5×10^{19}	10	18
100406	1800	100	180	9620	4000	-	-	9.0	21
040407	1800	80	100	8900	2000	0.15	6.5×10^{19}	10	23
250906	1800	100	155	8350	2350	0.05	1.6×10^{19}	14	29
100506	1800	100	180	9620	1800	-	-	16	33

Table 3.2: *Process parameters for the intrinsic and phosphorus-doped silicon nanocrystals which were used in this work. Here, the microwave power, P, the reactor pressure, p, and the SiH_4, Ar, H_2, and PH_3 gas fluxes are given. [SiH4] denotes the silane gas concentration in the precursor, while [P] is the nominal phosphorus concentration in the particles with the average diameter d.*

the silicon nanocrystal absorption is stronger than in crystalline silicon and is similar to the absorption in microcrystalline silicon, which is shown as a dotted line. The enhanced absorption in this spectral region can be due to internal scattering and absorption via defect states of the silicon nanocrystals [Lec08a]. Thus, the absorption takes place also below the energy gap as in microcrystalline silicon.

The chemical purity of silicon nanocrystals was analyzed by glow discharge mass spectroscopy and by inductively coupled plasma spectroscopy and a significant contamination level in the range of up to few ppm was found [Lec08a]. Especially metal impurities, which may stem from the microwave reactor, contribute to the impurity level of about 10^{17} cm^{-3}. In addition, silicon nanocrystal samples which were ball-milled with yttrium stabilized zirconia beads, exhibit zirconium contamination levels of about $10 - 1000$ ppm. Zirconia is an insulator, hence, only the metal impurities may be important for the electrical properties. However, as the number of defects in the silicon nanocrystals is much larger, as will be discussed below, the influence of the impurities can be neglected.

The number of paramagnetic defects of the silicon nanocrystals can be measured via electron spin resonance experiments. There, for silicon nanocrystals a g-factor of about 2.006 is observed which stems from silicon dangling bond defects [Ste08]. Silicon dangling bonds can act as traps for holes and electrons, as their energetic levels lie near the middle of the bandgap. The amount of dangling bonds in the silicon nanocrystal powder is typically 3×10^{18} cm^{-3} [Per07]. For spin-coated layers, this amount increases by one order of magnitude, indicating that the ball-milling introduces additional defects in the nanocrystals most probable from mechanical damage or a low quality oxide on surfaces of broken-up agglomerates [Lec08b]. By etching

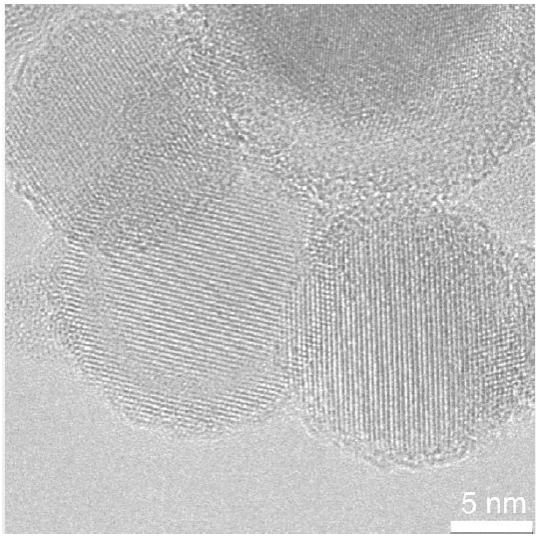

Figure 3.3: *High resolution transmission electron image of silicon nanocrystals. A thin, irregular oxide layer surrounds the crystals. From Reference [Kni04].*

the surface oxide with hydrofluoric acid, only 10 % of the defects can be removed, thus, only a small part of the defects lie at the oxidized surface [Lec08b]. In addition, with a low temperature annealing step, a further reduction of the defect density by up to a factor of 10, in combination with an etching step, can be obtained, which is explained by structural changes in the nanocrystals [Nie10]. In Subsection 5.2.1 electron spin resonance measurements on silicon nanocrystals will be shown and discussed in more detail.

The amount of doping impurities in the silicon nanocrystal is given by the nominal doping concentration, which is calculated from the ratio of precursor silane and doping gases. However, this does not have to be the analytical determined value, which was determined by glow discharge mass spectroscopy and secondary ion mass spectroscopy [Lec08a]. For phosphorus doping, which was additionally examined by electron spin resonance experiments, the incorporation efficiency is close to 100 % independently of the nanocrystal size. However, about 95 % of the donors segregate to the surface region of the nanocrystals during growth [Ste09]. Hence, an etching step, which removes the surface oxide layer, also removes most of the phosphorus donors [Lec08b]. Nevertheless, the etching step in hydrofluoric acid increases the conductivity by about two orders of magnitude. In addition, as the defect density is high, only doping concentrations of $> 1 \times 10^{19}$ cm^{-3} lead to a increase of the conductivity in silicon nanocrystal layers. The conductivity of etched silicon nanocrystal layers increases from 10^{-10} Ω^{-1} cm^{-1} for undoped nanocrystals to 10^{-7} Ω^{-1} cm^{-1} for nanocrystals which were doped $> 1 \times 10^{19}$ cm^{-3} [Lec08b]. This is explained by compensation of the charge carriers by the dangling bonds in the sample.

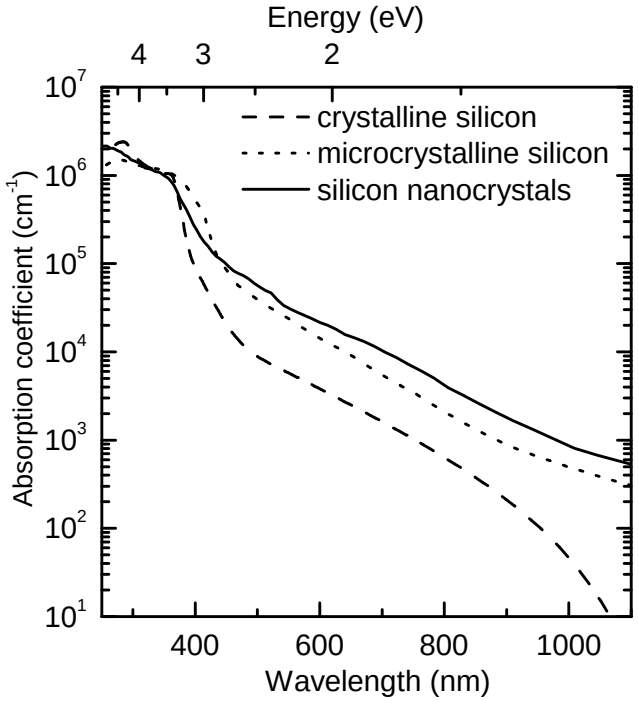

Figure 3.4: *Absorption coefficients of silicon nanocrystals (solid line), crystalline silicon (dashed line) and microcrystalline silicon (dotted line). From References [Lec08a], [Das55, Hul99], and [Stu94], respectively.*

3.2 Organic semiconductors

3.2.1 Poly(3-hexylthiophene) (P3HT)

Structural properties of P3HT

The organic semiconducting polymer poly(3-hexylthiophene) (P3HT) has a π-conjugated electron system, which is built up from the p_z-orbitals of sp^2-hybridized carbon atoms in thiophene. The sulfur of the thiophene ring adds additional electrons to the delocalized π-electron system. The thiophene rings, together with the hexyl chains, which make P3HT soluble in a variety of organic solvents, can be seen in the molecular structure of P3HT in Figure 3.5. The hexyl chains in this figure are ordered in a head-to-tail structure, which leads to better electrical conductivity values than other arrangements, *e.g.* head-to-head structures [Che92]. In the head-to-tail structure the hexyl chains are all pointing in the same direction, the head of one hexyl chain of one monomer unit pointing to the tail of the hexyl chain of the next monomer unit. If many repeat units of the polymer are derived from the same monomer, it has a high regioregularity, leading to reduced defect densities in the polymer [Che92]. Furthermore, highly regioregular P3HT, due to the higher order, has a more extended π-electron conjugation length, compared

to regiorandom P3HT, and hence has also a higher mobility [Pan00]. Thus, for state-of-the-art P3HT/PCBM solar cells, a regioregular P3HT is used, which has a high regularity in the head-to-tail coupling of the monomers [Kim06]. The P3HT used in this work was purchased from Rieke Metals and had an average molecular mass of 40000 amu and a high head-to-tail regioregularity of $90-93$ %.

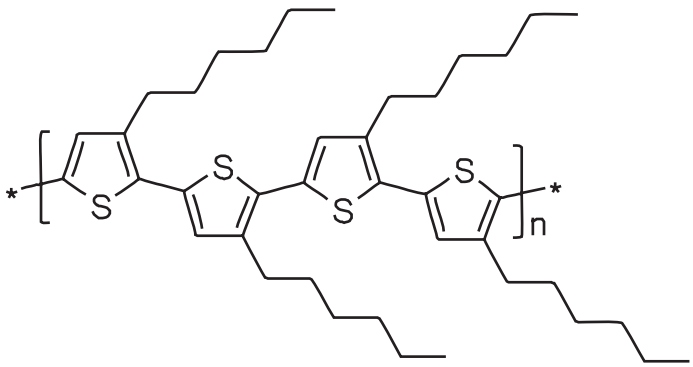

Figure 3.5: *Molecular structure of P3HT in head-to-tail configuration. From Reference [Dye10a].*

Optical and electrical properties of P3HT

In Figure 3.6 the absorption spectrum of P3HT (solid line) is shown. The spectrum was calculated from transmission and reflection measurements of a spin-coated P3HT layer. From the absorption spectrum an optical band of 1.9 eV can be determined. Due to the high absorption coefficient, a 100 nm thick P3HT layers absorbs already about 63 % of the light at a wavelength of 550 nm. This follows from the Lambert-Beer law where the transmitted light intensity, I_{light}, decreases exponentially with the thickness of the sample, d, and the absorption coefficient, α, with $I_{\text{light}} = I^0_{\text{light}} \exp(-\alpha d)$, where I^0_{light} is the incident light intensity. Due to the higher absorption coefficient of P3HT in the visible spectral region as compared to silicon, organic solar cells can be much thinner than crystalline silicon solar cells.

The exact position of the HOMO and the LUMO level relative to the vacuum level is unclear and many different literature values do exist [Liu05, Cas06, Yi06, Tak05] . For the HOMO all values lie in the range from 4.7 eV [Chi03a] to 5.2 eV [Tha07], while for the LUMO values between 2.6 eV [Chi03a] and 3.2 eV [Oku08] have been reported. The differences in the position of the HOMO and LUMO level of P3HT may be explained by variations in the exact process parameters and by the purity and molecular weight of the P3HT. The bandwidths of the stated values (grey band) and the mean values (black line) are shown in Figure 3.8. The Fermi level of P3HT was determined by contact potential measurements to be about 4.4 eV below the vacuum level, which is in good agreement with the literature value of about 4.6 eV [Cas06]. The Fermi level is also shown as a red dash-dotted line in Figure 3.8.

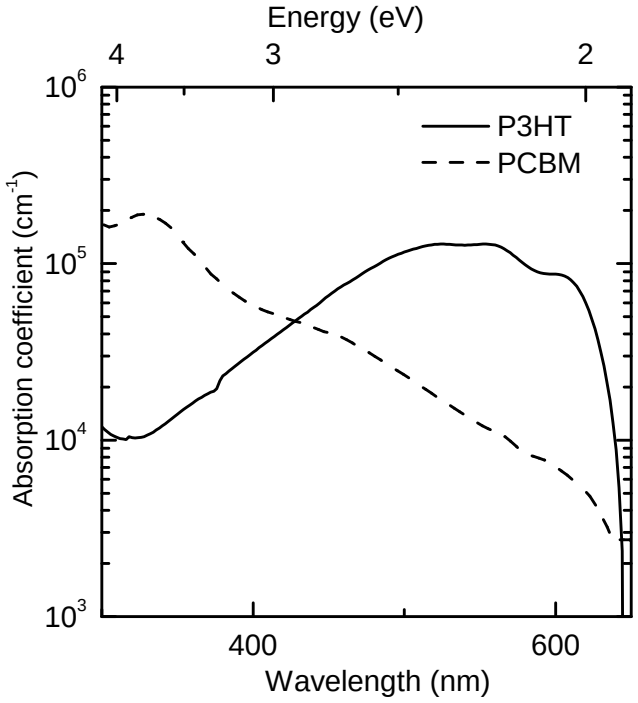

Figure 3.6: *Absorption coefficients of P3HT and PCBM. Data for PCBM from Reference [Hop04a].*

In ITO/P3HT/Al layer systems, the ambipolar mobility in P3HT has been measured with a hole mobility of $\mu_h = 3 \times 10^{-4}$ cm^2/Vs and an electron mobility to $\mu_e = 1.5 \times 10^{-4}$ cm^2/Vs [Cho04]. However, also a hole mobility as low as $\mu_h = 3 \times 10^{-5}$ cm^2/Vs has been measured in such layer systems [Chi04], while in field effect transistors, already high hole moblity values of up to 0.1 cm^2/Vs have been reached [Sir98]. Furthermore, the mobility depends on many factors, *e.g.* the molecular mass [Goh05b] or the head-to-tail regioregularity [Sir98]. Additionally, when P3HT is illuminated in air, the polymer will degrade due to photo-oxidation, forming functional groups which reduce the conjugation length and lead to a lower mobility and a poorer performance of P3HT based optoelectronic devices [Cha08, Abd97]. Another important parameter, the exciton diffusion length in P3HT, has been determined to be only several nanometers, with values ranging from $3-9$ nm [Sha08, Goh07, Kro03, Lüe04].

3.2.2 [6,6]-phenyl-C_{61}-butyric acid methyl ester (PCBM)

[6,6]-phenyl-C_{61}-butyric acid methyl ester (PCBM) is the most commonly used fullerene derivative, as it is soluble in common organic solvents, in contrast to pure C_{60} fullerenes. The molecular structure of PCBM, which is mainly a C_{60} fullerene which is functionalized to make it soluble, is shown in Figure 3.7. The PCBM which was investigated in this work was purchased from Solenne BV.

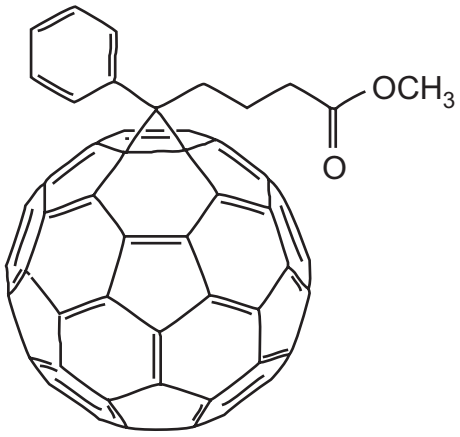

Figure 3.7: *Molecular structure of PCBM. From Reference [Wik10].*

Thin films which are spin-cast from chloroform are amorphous, while when a high boiling point solvent, such as dichlorobenzene, is used, the PCBM molecules form crystals [Bra08]. In blends of PCBM with P3HT, PCBM has a very low crystallinity after spin-coating, whereas after an annealing step at 130 °C the morphology changes and larger van der Waals crystals of PCBM with sizes larger than 10 μm are formed [Sav05, Bra08]. For a pure PCBM layer, a high electron mobility of $\mu = 1 \times 10^{-2}$ cm^2 V^{-1} s^{-1} has been reported [Mih03]. This electron mobility is reduced by several orders of magnitude in composite P3HT/PCBM films [Shi07]. Furthermore, as for conjugated polymers, also the conductivity in fullerenes decreases when oxygen, which creates deep traps, comes into play [Lee94].

The bandgap of PCBM is about 2$\pm$0.2 eV, which is the bandgap of C_{60} molecules [Dre96]. The LUMO position of PCBM is about $3.7 - 3.8$ eV and the HOMO lies at about $5.5 - 5.9$ eV [AI05, Chi03b] which is shown in Figure 3.8. From these values, which are well below the HOMO/LUMO values of conjugated polymers such as P3HT, it is clear that PCBM is a good electron accepting material. This property, together with its high electron mobility makes it the standard electron acceptor in organic photovoltaics. However, one disadvantage of PCBM is the lower optical absorption, compared to P3HT, as can bee seen in Figure 3.6.

Summary of the energy level positions of all semiconductors

In Figure 3.8 the values for the positions of the energy levels of the organic and inorganic semiconductors used in this work are shown. The values stem from the literature and also were experimentally determined (red lines) as described in this chapter. The mean values of the energy band edges are shown as black lines, while the range of the values is represented as a grey band and the Fermi levels are shown as dash-dotted lines.

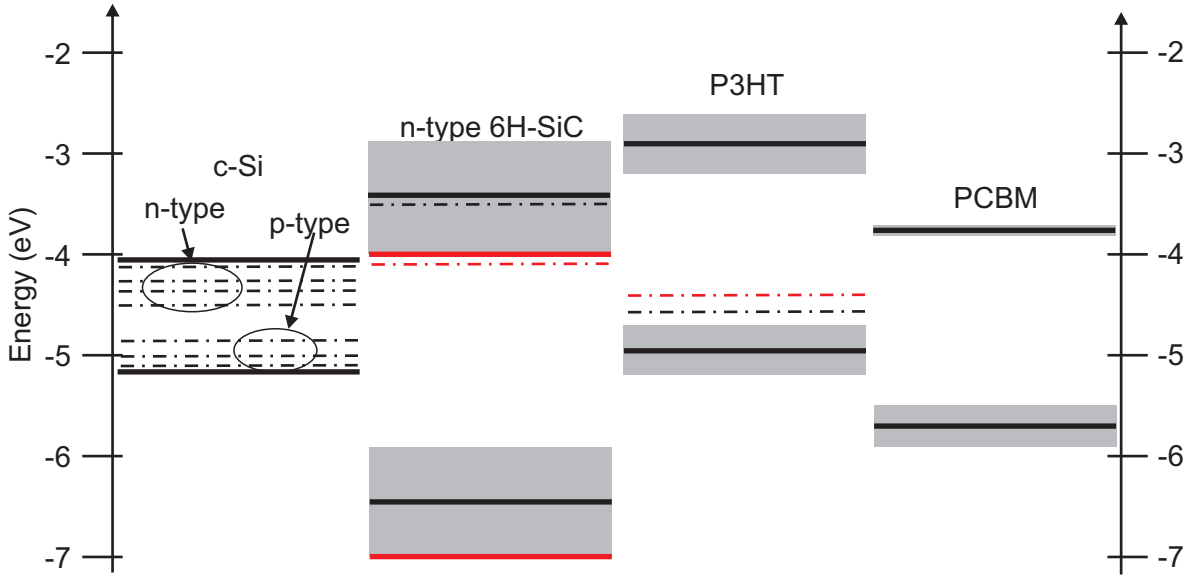

Figure 3.8: *The positions of the energy levels of the organic and inorganic semiconductors used in this work. The grey bands are the range of the literature values (see text for details) for the energy levels, the black lines the average values, the dash-dotted lines the literature values of the Fermi levels, and the red lines are the measured values.*

4 Sample Preparation and Experimental Methods

In the first part of this chapter, the preparation of the samples, both heterojunctions with silicon nanocrystals as well as bilayer heterojunctions, is described in detail. In the second part, the experimental methods which were applied to characterize the heterojunctions will be reviewed.

4.1 Sample preparation

In this section, the preparation of the heterojunctions with silicon nanocrystals, especially the preparation of the silicon nanocrystal dispersions and of the mixed P3HT/silicon nanocrystal (P3HT/Si-nc) solutions will be highlighted. Furthermore, for heterojunctions with bulk semiconductors, the fabrication of ohmic contacts is an important point, which, among other things, will be described in the second part of this section.

4.1.1 Heterojunctions with silicon nanocrystals

Silicon nanocrystal dispersions

Silicon nanocrystals can be preferentially dispersed in polar solvents, which is most probable due to the polar Si-O bonds at the surface of the oxidized particles. In ethanol, stable dispersions with up to 6 wt% are achieved. However, also in acetone, cyclohexanone, tetrahydrofuran, or chloroform dispersions are possible, whereby the quality of the dispersion decreases with decreasing polarity of the solvents. For this work, silicon nanocrystal dispersions were prepared either in ethanol at 5 wt% or in chloroform at 0.5 %, if the silicon nanocrystal dispersion was mixed with an organic solution. The silicon nanocrystals were typically dispersed via ultrasound or via ball milling with yttrium stabilized zirconia beads (ZrO_2:Yt). For the ball milling process, a mixture of the silicon nanocrystals and the ZrO_2:Yt beads, which were added in a comparable amount, was placed on a shaker (Eppendorf Thermomixer Compact) and than stirred for typically four hours. The typical agglomerate size after the ball milling has been determined to

about 65 nm [Lec08a]. Such dispersions are stable on the time scale of several weeks. However, the ball milling increases the defect density of the silicon nanocrystals significantly by one order of magnitude to typically $2-3\times10^{19}$ cm^{-3}, most probably due to mechanical damage [Lec08b, Per07]. Also ultrasound was applied to disperse the silicon nanocrystals and to avoid such a strong increase of the defect density. This method was used for the dispersion of the silicon nanocrystals for the hybrid solar cells with silicon nanocrystals. Here, the silicon nanocrystals were dispersed for typically 30 min which resulted only in a slight increase of the defect density, as measured via electron spin resonance. However, the silicon nanocrystals were not so well dispersed as after ball milling, leading to a lower long term stability of the dispersion. Furthermore, if the ultrasound was applied for a longer timescale of several hours, a further increase of the defect density up to a similar value as obtained via ball milling was observed.

For some purposes the silicon nanocrystals were etched in diluted hydrofluoric acid (5 % in H_2O) for one minute and dispersed in a solvent afterwards. The etching of the silicon nanocrystals was carried out by drop-casting the nanocrystal solution on a polyvinylidene fluoride filter (Millipore, Filtercode: VVPP) with a pore size of 0.1 μm. Via a vacuum pump the solvent has been extracted before the hydrofluoric acid was drop-casted on the silicon nanocrystal film on the filter for one minute. Afterwards, the nanocrystals were rinsed with ethanol several times. After the final extraction of the ethanol, the filter which was covered with a dry silicon nanocrystal layer was transferred into the desired solvent. Finally, the nanocrystals were removed from the filter via ultrasound. By etching with hydrofluoric acid, the oxide shell of the as-received silicon nanocrystals is etched away [Ste08]. Furthermore, the defect concentration is reduced by about 10 %, indicating that only a small fraction of the defects lies at the oxidized surface [Lec08b]. Also the number of phosphorus donors is reduces by a factor of 20, as most of the phosphorus atoms are segregated in the oxide shell [Ste09].

Solutions with P3HT and PCBM

For the work with organic semiconductors it is important to avoid oxidation. Thus, most of the preparation and also a large part of the characterization was done in inert gas atmosphere. For this purpose, a glove box (Labmaster 130, MBraun) filled with argon and typical residual impurities of $H_2O < 1$ ppm and $O_2 < 1$ ppm was available. P3HT was dissolved either in 1,2-dichlorobenzene with 2 wt% or in chloroform with 0.5 wt% for the mixture with silicon nanocrystals, by stirring at 40 °C with a magnetic stirrer for several hours. The P3HT solution with chloroform was chosen, as chloroform is also an appropriate solvent for the silicon nanocrystals. However, using 1,2-dichlorobenzene, which has a higher boiling point, leads to a better layer morphology due to the slower evaporation of the solvent making it the standard solvent for P3HT. PCBM was dissolved, such as P3HT, with 0.5 wt% in chloroform by stirring

at 40 °C with a magnetic stirrer for several hours. For a reference sample made of PCBM and P3HT, both solutions were mixed in a weight ratio of 1:1 by mixing the solutions and stirring them at 40 °C with a magnetic stirrer for typically 24 h.

Samples for electron spin resonance

The ball-milled silicon nanocrystal dispersions and the P3HT or PCBM solutions, all in a concentration of 0.5 wt% in chloroform, were mixed in a weight ratio of 1:1 by ultrasound and by mechanical shaking for 10 min each. Then typically 100 μl of the mixed solution and of the single components were transferred to transparent quartz tubes which were heated up to about 45 °C to evaporate the solvent. The sample tubes were sealed afterwards with wax to avoid oxidation. For samples for electrically detected magnetic resonance measurements, the solutions were directly drop-casted onto a gold interdigit contact structure to enhance the current through the active layer. The gold contacts consisted of 112 digits of typically 10 μm width and with a distance of 10 μm and were patterned via photolithography on a polyimide polymer foil (Kapton, Dupont).

Hybrid solar cells with silicon nanocrystals

The hybrid solar cells with silicon nanocrystals were fabricated by deposition of the active layer, containing P3HT and silicon nanocrystals, onto an ITO-coated glass substrate as a front contact and the following evaporation of a metal back contact. The single steps of the sample preparation are described below.

ITO as a front contact was chosen, as ITO, which is a standard front contact for organic solar cells [Li05], is transparent in the visible spectral range, has a small resistance, and its work function of about $4.5-4.8$ eV [Bra08] lies in the range of the HOMO level of P3HT ($4.7-5.2$ eV, see Subsection 3.2.1) and, thus, an ohmic contact to the P3HT is formed [Chi03b]. The ITO-coated substrates (purchased from Delta Technologies, $R_S = 5-15\ \Omega$) were cut to 15×15 mm^2 and the ITO was etched with 37 % hydrochloric acid for 10 min in ultrasound, leaving only an ITO contact of 5×15 mm^2 in the middle of the substrate, where the ITO was covered carefully with adhesive tape. Afterwards the substrates were cleaned in acetone, isopropanol, and water for 10 min each in ultrasound. In addition, the cleaned ITO substrates were put for 10 min in an oxygen plasma at 200 W (100E-Plasma Systems from Technics Plasma) to flatten the ITO surface and to enhance the work function to about 4.8 eV [Kim98, Kim99] for a better alignment with the HOMO of P3HT. The ITO covered substrate had a thickness of 1.1 mm, whereby the ITO was about 150 nm thick. The transmission of the ITO is $75-90$ % in the relevant spectral region from $400-1100$ nm. In typical organic solar cells, in addition a poly(3,4-ethylenedioxythiophene)/poly(styrenesulfonate) (PEDOT/PSS) layer is

spin-coated onto the ITO to further flatten the ITO surface and to enhance the work function for a better hole extraction [Bra08]. However, when an additional layer of PEDOT/PSS (Baytron P from H. C. Starck) was spin-coated onto the ITO layer no influence on the current-voltage characteristics of the hybrid solar cells was observed. This may either be explained by pinholes in the PEDOT/PSS layer or by a work function of the PEDOT/PSS, which ranges in the literature from $4.7-5.2$ eV [Els08], similar to the work function of the ITO which, hence, does not have an influence on the device performance. However, as no effect was observed, no PEDOT/PSS layer was applied in our devices.

On the ITO substrate the active layer was deposited by spin-coating (KL-VT-50 from LOT-Oriel) of 90 μl of a P3HT/Si-nc solution with typically 750 rpm. Either one layer or several layers spin-coated on top of each other were typically deposited. The P3HT/Si-nc solution for the active layer was fabricated by mixing both components in ultrasound for 30 min. To obtain homogeneous P3HT/Si-nc solutions, both materials are dissolved in chloroform with 0.5 wt% before mixing as described above. For additional measurements, the active layer was also spin-coated on glass, polyimide foil or on thin gold layers with a similar wetting behavior. For a typical 0.5 wt% P3HT/Si-nc solution in chloroform, an active layer thickness of about 75 ± 20 nm was obtained. However, due to the high surface roughness of the active layer (see Subsection 5.1.2), this is an average value.

As a rear electrode aluminum is commonly used in organic solar cells [Bra08] due to its low work function of 4.1 eV which makes it an appropriate electron-collecting contact. Furthermore, this work function lies close to 4.05 eV of the conduction band edge of silicon, reducing an energy loss when electrons are extracted from the silicon via the aluminum back contact. Here, for the back contacts 50 nm aluminum were deposited in high vacuum with a rate of $1-2$ nm/s by thermal evaporation (K950X from Emitech) with a shadow mask. The eight contacts per sample had an area of 1.3 mm^2 each and were connected with larger contact pads. As the ITO was etched away under the contact pads, short-circuits due to the contacting of the sample were prevented. Finally, the contacts pads were covered with conductive silver paste to enhance the contact properties to the contact pins. The sample was mounted in a homemade sample holder, where all contacts and the ITO were connected simultaneously with gold-coated contact pins (GKS 967, Ingun). Thus, current-voltage characteristics of the contacts in the dark and under illumination with white light or with high-power LEDs could be recorded consecutively by switching the contacts electronically. The schematic sample geometry is shown in Figure 4.1, where in (a) the contact geometry in top view and in (b) a cross section of the sample are shown.

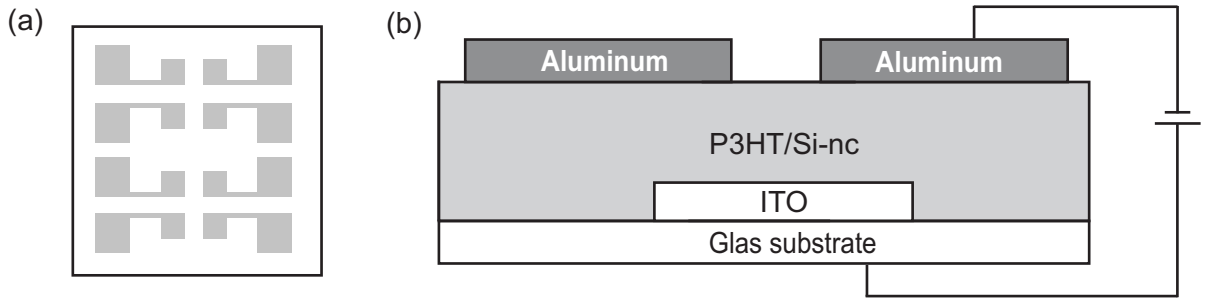

Figure 4.1: *Schematic view of (a) the contact geometry in top view and of (b) the cross section of the sample.*

Hybrid solar cells with silicon nanocrystal layers structured via soft lithography

Another method which was investigated in this work to produce bulk heterojunction solar cells with silicon nanocrystals is the nanostructuring of the silicon layer to achieve an ordered bulk heterojunction. Promising methods to fabricate ordered bulk heterojunction structures for solar cells are the nanoimprint lithography and the soft lithography. Both techniques have been developed since the mid nineties as low-cost alternative to common lithographic techniques for the fabrication of micro- and nanostructures and aim to generate nanostructures using rigid and elastomeric molds, respectively [Xia98, Guo07]. Furthermore, with these techniques very small structure sizes can be realized, as optical diffraction is not a limiting factor. Soft lithography has been applied for microstructuring of conducting and semiconducting polymers [Beh99, Gat05, Kim07]. In addition, soft lithography with gold or titanium dioxide (TiO_2) nanoparticles has also been reported [Wil04, Ima07]. For hybrid solar cells, a structured TiO_2 layer, in which P3HT was infiltrated, has been fabricated via soft lithography of a sol-gel TiO_2 [Goh05a, Coa05b]. Additionally, organic solar cells with ordered heterojunctions based on PCBM and a polythiophene derivative, which have been fabricated via nanoimprinting show an enhancement when compared to unstructured organic solar cells [Kim07]. P3HT has also been nanostructured by nanoimprinting, showing a slight enhancement of the efficiency of organic solar cells when compared to planar structures [Sca10].

However, the advantage of the soft lithography is that the mold is flexible, and thus can be applied on *e.g.* prestructured ITO on glass or on flexible plastic substrates. The typical mold material used for soft lithography, poly(dimethylsiloxane) (PDMS), a silicon-based polymer, is durable, transparent above a wavelength of about 280 nm, chemically inert and resistant to many solvents [Gat05]. PDMS is applied to the master prior to the polymerization in liquid form and therefore adapts to the surface of the master and can be removed from the master after polymerization. However, the elastomeric character of PDMS can cause problems if the aspect ratio, defined by the height relative to the width of the structure, is too large. Then the structure collapses and sticks together due to van der Waals interactions [Xia98]. In the literature several

soft lithographic techniques are reported [Xia98, Gat05]. In this section, mainly soft molding is applied. To this end, the PDMS stamp is pressed onto a solution, *e.g.* a polymer or nanoparticle layer, with a low pressure of < 1 N cm^{-2} immediately after it was deposited. With an appropriate chosen solvent, the solvent can evaporate by diffusion through the mold and after a certain time the stamp can be removed and a patterned structure remains. The principle of the soft lithography process is shown in Figure 4.2.

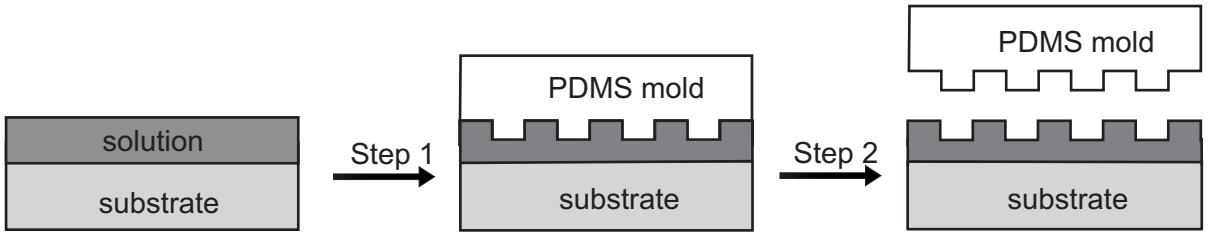

Figure 4.2: *Schematic illustration of the soft lithography process.*

In this work, a silicon wafer with a 350 nm pitch grating was used as a master for the PDMS. The silicon master was fabricated by using a combination of interference lithography and reactive-ion etching [Har07] and was provided by Stefan Harrer and Giuseppe Scarpa from the Institute for Nanoelectronics at the Technische Universität München. The grooves of the master were about 50 nm deep, which was determined by AFM measurements of the master as shown in Figure 4.3 (a). For the fabrication of the PDMS stamp the Sylgard 184 silicone elastomer kit from Dow Corning was used. The two components, the silicon base and the corresponding liquid curing agent, were mixed in a ratio of 10:1 by volume before the liquid PDMS was distributed uniformly onto the master and cured at 70 °C for 2 h. Afterwards, the PDMS mold could be peeled off carefully from the master. The pattern of the master was transferred to the PDMS mold quite well, as apparent from Figure 4.3 (b), where the AFM image of the mold is shown. However, the edges of the PDMS mold are rounded and the depth of the grooves of the mold is slightly reduced as compared to the master. This is due to the influence of the surface tension after releasing the stamp from the master [Odo02]. Furthermore, the compression modulus of Sylgard 184 PDMS with about 2 N mm^{-2} is relatively low, which means that the resolution which is achievable with the stamps is limited to about 100 nm [Odo02, Sch00], which corresponds roughly to the structure size of the master. Each mold could be used several times when the mold was cleaned for 30 min in isopropanol in an ultrasound bath. However, the number of embossing processes is limited, as the quality of the mold decreases due to residua of the embossed material, which adhere to the mold.

To produce ordered bulk heterojunctions with an organic polymer and silicon nanocrystals via soft lithography, either the polymer or the nanocrystals can be embossed and afterwards the structured layer can be covered with the counterpart. However, for an intimate contact between the nanocrystals and the P3HT it is favorable to emboss first the nanocrystal layer and then

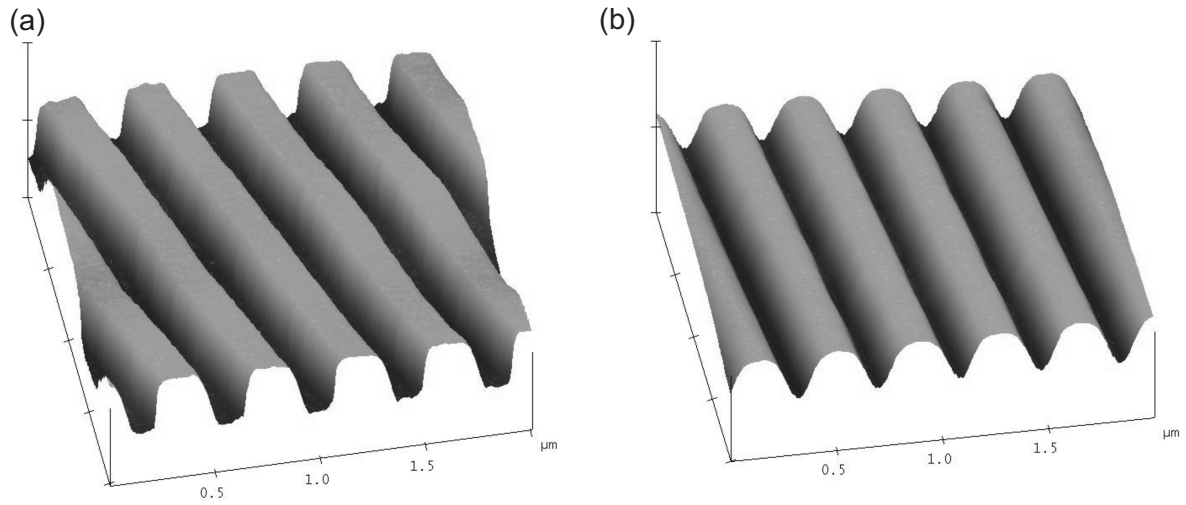

Figure 4.3: *AFM surface plots of (a) the silicon master and (b) the corresponding PDMS mold. The scan area is* $2 \times 2\ \mu m^2$*, the total height is 150 nm.*

apply the polymer solution. In this way the polymer can wet the nanocrystals and the structure. The other way round, the spherical nanocrystals would only have a close contact with the polymer on a small area and would have problems to fully wet the grooves of the structure. The nanocrystal layers were structured as follows: An amount of about 20 μl of an ethanol-based dispersion of the silicon nanocrystals, with a $5-6$ wt% concentration, which was found to give the best results, was drop-casted onto the substrate. Immediately afterwards, the PDMS mold was placed on the dispersion and was slightly pressed against the substrate. Then, the sample was annealed at 80 °C for about 5 minutes to evaporate the ethanol, which also diffuses into the PDMS, before the PDMS mold could be peeled off the substrate. As a substrate etched ITO coated glass, as for bulk heterojunction solar cells, was used. As a reference structure without a structured silicon nanocrystal layer, also an amount of 75 μl of silicon nanocrystals were spin-coated with 1200 rpm on an ITO substrate. Afterwards, also the reference sample was annealed at 80 °C for 5 min to evaporate the ethanol. In the next step, P3HT, which was solved in the nonpolar solvent 1,2-dichlorobenzene with 2 wt%, was spin-coated on the silicon nanocrystal layer. Then, aluminum contacts were deposited by thermal evaporation through a shadow mask as described above.

4.1.2 Heterojunctions with bulk semiconductors

Ohmic back contacts

For the preparation of heterojunctions with bulk inorganic semiconductors, ohmic back-contacts to the inorganic semiconductors are essential. Here, ohmic contacts were achieved by forming a

highly doped region in the semiconductor near the metal-semiconductor interface. This enables charge carriers to tunnel through the Schottky barrier, as described in Subsection 2.2.1.

For the $360 - 525\ \mu$m thick silicon wafers, the processing of ohmic contacts was dependent on the doping type. To achieve a highly doped interface region on n-type silicon, antimony, as an element of the 5th main group, was used as a donor. The following steps were necessary to form an ohmic contact on n-type silicon with antimony doping: Via thermal evaporation, performed in a high vacuum evaporation system (Leybold L560), a 70 nm thick gold-antimony alloy (Au/Sb 99:1) was deposited on the n-type silicon. Before, the silicon had been etched in vapor of 50% hydrofluoric acid to remove the natural oxide, which has been validated by contact angle measurements. Then the n-type silicon with the gold-antimony alloy layer was annealed in high vacuum for 3 min at 500 °C. At the eutectic temperature of 363 °C an eutectic between gold and silicon is formed, in which also the antimony atoms are solved. When cooling under the eutectic temperature, the gold is expelled from the silicon, while the antimony remains in the silicon and, hence, forms the highly doped layer [Wer94]. As the gold contact on the antimony doped n-type silicon is not very homogeneous, a second evaporation step is performed. Thereby, after another hydrofluoric acid etching step, 10 nm of chromium, for an enhanced adhesion, and 100 nm gold are evaporated successively to establish a stable ohmic contact.

For ohmic contacts via a highly doped tunneling contact on p-type silicon, aluminum has been used as an acceptor. Following the removal of the natural oxide of the silicon, as described above, 60 nm of aluminum were evaporate on the p-type silicon. Then an annealing step for 10 min at 500 °C in high vacuum follows. As 500 °C is below the eutectic temperature of aluminum and silicon, which is 577 °C, aluminum diffuses into the p-type silicon near the interface and generates a highly p-doped layer and an ohmic contact.

Ohmic contacts on the 300 μm thick n-type 6H-SiC can be achieved as described by Schoell [Sch06] via the thermal evaporation of 50 nm of chromium and of 50 nm of gold on the sample, followed by an annealing step at 900 °C for 5 min in high vacuum. Prior to the evaporation step, the natural oxide has been removed by etching in hydrofluoric acid, as already described for silicon. To illuminate the sample through the back contact, the ohmic contact was applied only on a part of the sample surface.

Photolithography

Photolithography was applied to define the size of the hybrid heterojunction on the inorganic semiconductor and to avoid short-circuits by reducing the overall heterojunction area. The inorganic substrates were cleaned for 10 min each in acetone and isopropanol in an ultrasound bath and then were covered with photoresist via spin-coating at 6000 rpm for 40 s. As a chemically stable photoresist SU-8 2002 from Microchem was used. Afterwards, the samples were baked (soft bake) for 2 min at 95 °C, covered with a photo mask, and exposed to UV light for 13 s in a

mask aligner (MJB 3, Karl Suss). The photo mask was patterned with circles of 0.5 mm^2. After the post exposure bake for 2 min at 95 °C the sample was developed for 1 min. All photolithographic steps were repeated for a second time to close possible pinholes in the photoresist layer. Finally, a hard bake for 1 h at 180 °C was performed to achieve the final high chemical stability. An additional advantage of the photoresist layer is that the short-circuiting of the heterojunction during the contacting of the top contact is circumvented.

Surface treatment

To remove the isolating and defect rich natural oxide of the inorganic semiconductors the following surface treatment was carried out: The samples were oxidized for 5 min at 200 W in an oxygen plasma (100E-Plasma Systems from Technics Plasma) and then were held into the vapor of 50 % hydrofluoric acid for 1 min. Both steps were repeated a second time. On silicon a H-termination of the surface was achieved [Bau06a]. This was confirmed by contact angle measurements, where the contact angle increased from $52° \pm 3°$ up to $81° \pm 3°$ after the surface treatment due to the achieved H-termination. The H-termination was only stable for several minutes in air, hence etching and the subsequent processing was performed in the glovebox. On 6H-SiC an OH-termination is achieved with this procedure [Sch06, Sey04].

Deposition of P3HT

The P3HT (Rieke Metals, Inc.) was dissolved at 2 wt% in 1,2-dichlorobenzene. The solvent was chosen due to its high boiling point of 179 °C, which resulted in a slower evaporation and therefore in a better morphology and a higher mobility [Cha04]. The polymer was deposited in inert gas atmosphere on the inorganic semiconductors either by spin-coating or by drop-casting. For the latter method, which was applied for the P3HT/Si heterojunctions, 1 μl of the P3HT solution was deposited in the holes of the photoresist by drop-casting which led to a layer thickness of $1 \pm 0.3 \mu$m. Due to the thickness of this layer, pinholes in the layer, which would short-circuit the P3HT layer, were effectively avoided. However, the thick layer also increased the resistance and absorbed most of the photons in the absorption range of P3HT. Nevertheless, as silicon has a broader absorption range, the silicon could still be excited with light of longer wavelengths. This was not possible for heterojunctions with 6H-SiC, where a thick P3HT layer would not allow photon absorption in the 6H-SiC at the heterojunction interface. Thus, for P3HT/6H-SiC heterojunctions, a thinner P3HT layer was deposited via spin-coating of P3HT at 1200 rpm for 2 min. This resulted in a P3HT layer thickness of 150 ± 10 nm.

Transparent front contacts

As the last step of the sample preparation for bilayer heterojunctions, transparent front contacts on top of the P3HT layer were established. The front contacts were produced by the deposition of either ITO in the case of the P3HT/silicon heterojunction or of gold for the P3HT/6H-SiC heterojunction.

As already mentioned previously, due to the appropriate work function, ITO forms an ohmic contact to P3HT. Several ways to deposit ITO exist, such as sputter-coating, chemical vapor deposition, sol-gel processes, spray-pyrolysis, or evaporation [Tah98]. Due to the equipment that was available the ITO layers for bilayer heterojunctions were evaporated using evaporation sources from MaTecK with 90/10 wt% of In_2O_3/SnO_2. In the literature both, thermal evaporation [Sal98] and e-beam evaporation [Geo00] are reported. For this work, also both methods were tried, however, the latter one exhibited better properties regarding the transmittance and the conductivity. To investigate this discrepancy, energy-dispersive X-ray spectroscopy (EDX) was used to compare the elemental composition of the ITO layers. While the elemental compositions of the evaporation source and the e-beam deposited layer coincided, the EDX spectrum of the thermally evaporated ITO layer exhibited a much higher amount of tin, as compared with the evaporation source composition. This can be understood by the lower SnO_2 melting temperature of 1127 °C compared to the In_2O_3 melting temperature of 1565 °C, which seems to lead to a higher evaporation rate of the SnO_2 during the thermal evaporation process. Thus, e-beam evaporation was applied for the ITO front contacts of the hybrid bilayer heterojunctions in this work. To further enhance the conductivity and the transmittance of the deposited ITO layers, a high substrate temperature and a small evaporation rate is favorable [Agn85, Fal06, Miz80]. Hence, the smallest possible evaporation rate of 0.1 nm/s was chosen during evaporation. In addition, via a heater an elevated substrate temperature could be chosen during the evaporation. As the glass transition temperature of highly regioregular P3HT, where the micro-crystalline structure melts, is about 225 °C [Hug04, Kim05], this limits the maximum substrate temperature. Thus, the substrate temperature was set to about 170 °C. The transmission of the evaporated 70nm thick ITO layer was about 50 % to 75% in the relevant spectral range from 400 nm up to 1100 nm.

For the excitation of charge carriers in 6H-SiC also from the P3HT side through the top contact, ultraviolet light is necessary. However, ITO, which has a bandgap of about 3.6 eV [Goy85], absorbs light with wavelengths smaller than 344 nm and, hence, can not be used as front contact for the P3HT/6H-SiC heterojunction. As an alternative semitransparent front contact to the P3HT, a 7 nm thick semitransparent gold contact was thermally evaporated as an ohmic front contact on the P3HT. The transmission of the gold layer was about 50% - 70% in the relevant spectral region from 200 nm up to 600 nm. In measurements of pure P3HT layers with gold contacts, it was confirmed that the P3HT/gold contacts are ohmic, which has also been reported

in the literature [Chi03b]. This can be explained, as in the case of ITO, by similar values of the HOMO of P3HT and the work function of 5.1 eV of gold. In Figure 4.4 a schematic diagram of the sample structures of (a) P3HT/silicon and of (b) P3HT/6H-SiC heterojunctions is shown.

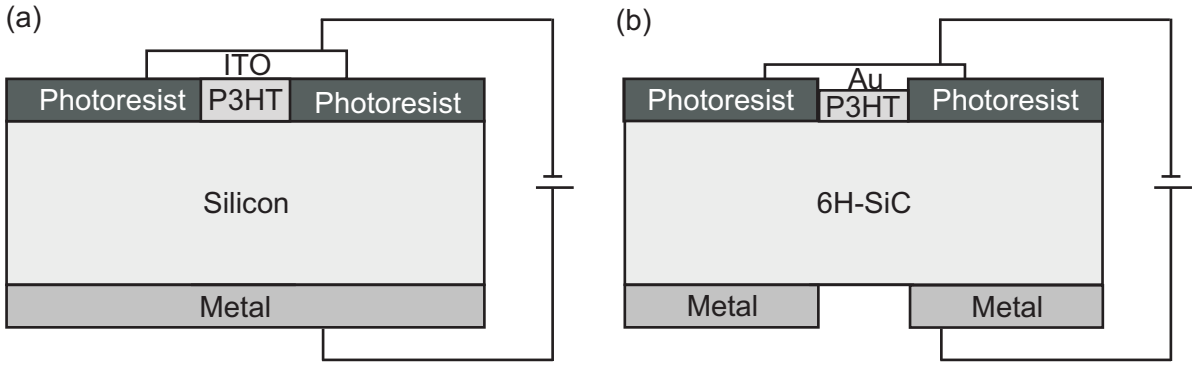

Figure 4.4: *Schematic view of the sample structure of (a) P3HT/silicon and of (b) P3HT/6H-SiC heterojunctions with the photoresist layer which defines the heterojunction interface area.*

4.2 Experimental methods

This section includes a summary of the experimental techniques used in this work. It starts with a description of the methods for the structural and chemical analysis. Then, the optical spectroscopy is introduced briefly. Finally, the two most important characterization methods of this work, the electrical characterization and the electron spin resonance, are reviewed.

4.2.1 Structural and chemical analysis

Energy-dispersive X-ray spectroscopy

For the comparison of the elemental composition of the ITO contacts, which were made via thermal and e-beam evaporation, energy-dispersive X-ray spectroscopy (EDX) was applied. Here, the ITO samples were exposed to a high-energy electron beam in a scanning electron microscope (S-3200N, Hitachi). Thereby, electrons from the inner shells of the atoms of the ITO are excited. Then electrons from the outer shells fill the vacancies in the inner shells and the difference of the energy between the shells is released in the form of X-rays. The intensity and the energy of the emitted X-rays are measured by an energy-dispersive detector (Link Pentafet, OXFORD). As the energy of the X-rays is characteristic for the element from which they were emitted, this allows to measure the elemental composition of the sample.

Adsorption spectroscopy

For the determination of the surface area of porous or colloidal structures a frequently used method is the measurement of the adsorption of gases on the surface as a function of temperature. By the extension of Langmuir´s monolayer adsorption theory, Brunauer, Emmett, and Teller (BET) deduced the adsorption isotherm for the adsorption of gas molecule multilayers on a surface [Bru38]. With this theory, the experimentally determined quantity of adsorbed gas can be fitted as a function of the gas equilibrium pressure and the amount of gas adsorbed in the first monolayer and all further layers. For the silicon nanocrystals examined in this work, BET measurements have been performed at the Universität Duisburg-Essen using N_2 gas at a temperature of 77 K. From the specific BET-surface, σ_{BET}, which was obtained by normalizing to the sample mass, the silicon nanocrystal diameter, d_{BET}, can be readily calculated if a spherical nanocrystal shape is assumed. Thus, in the case of silicon nanocrystals with the density $\rho = 2.33\ \mathrm{g\ cm^{-1}}$ the nanocrystal diameter is given by:

$$d_{\mathrm{BET}} = \frac{2575}{\sigma_{\mathrm{BET}}/\mathrm{m^2\,g^{-1}}}\mathrm{nm}. \tag{4.1}$$

As the silicon nanocrystals grown in the microwave reactor resemble spherical particles, the BET results for the diameter are in good agreement with complementary transmission electron microscopy and in-flight mass spectroscopy measurements [Kni04].

Atomic force microscopy

With atomic force microscopy (AFM) the surface morphology can be scanned. AFM measurements were performed in tapping mode operation (Veeco Multimode AFM with a Nanoscope IIIa controller). In this operation mode, a silicon cantilever is mechanically excited at its resonant frequency of typically 300 kHz, while the sample is scanned in x-y direction with a piezoelectric actuator. The silicon cantilever tip interacts with the sample surface, which leads to a damping of the oscillation. The oscillations of the cantilever are detected by a laser which is reflected from the cantilever to a photodiode array which is used to regulate the cantilever distance to the sample. The lateral resolution of AFM measurements is limited by the radius of the cantilever tip to about 20 nm, while the vertical resolution can reach the sub-nanometer range. Special care has to be taken that the tip is not degraded which leads to a loss of horizontal resolution.

Optical microscopy

Optical images of the samples were obtained by using a Zeiss optical microscope. A digital camera is connected to the microscope and could be used to directly record images of the

sample with a magnification of 50x up to 1000x. Transmission and reflection images could be recorded for illumination in bright and dark field mode, where especially the latter provides structural information regarding the smoothness of the sample.

Scanning electron microscopy

For scanning electron microscopy (SEM) an electron beam originating from a heated tungsten wire is accelerated in an electric field and focused by a system of condenser lenses on the surface of the sample. The sample is then scanned line by line in vacuum. The electron beam which hits the sample generates secondary electrons which are detected and transformed into an image of the surface morphology. SEM exhibits three-dimensional images of the sample with a large depth of field with magnifications of up to 15000x for SEM images recorded in this work with different electron microscopes. For images of samples produced via soft lithography a Hitachi S-3200N SEM was used routinely, while a Hitachi S-4000 SEM was also used due to its higher resolution. Furthermore, cross section views of samples were provided by our cooperation partner at Evonik Degussa (Aqura Analytical Solutions, Marl), where the samples were cleaved at cryogenic temperatures. The acceleration voltages were typically in the range of $5 - 30$ kV. To avoid charging effects for low-conductivity samples, a thin gold film of about 10 nm was sputtered onto the samples prior to the SEM measurements.

Profilometer measurements

For the determination of the thickness of the polymer layers, a profilometer (Dektak Profiler, Veeco, Sloan Technology Division) was used. During the measurement the sample is moved under a diamond microtip which touches the sample and, thus, scans the surface profile. The movement of the microtip is detected via induction and is shown as a height profile. The radius of the microtip is 2.5 μm and the force of the tip on the substrate is typically in the mN range. The scan length was typically about 1 μm. For the measurement a part of the active layer was removed by scratching down to the substrate and the resulting step was analyzed. With this method, a height profile resolution of $\pm$20 nm can be achieved.

Contact potential difference measurements

One technique to determine the work function of a material is the contact potential difference (CPD) measurement. Thereby, the work function difference between two materials, which form the two sides of a parallel plate capacitor, is measured. When a connection of the two materials is established, electrons will flow from the material with the lower work function to the material with the higher work function. As the two materials are forming a capacitor, the electrical

charge which is flowing will charge the capacitor which forms an electric field in the gap and a drop in the local vacuum level across the capacitor gap. The potential energy drop is equal to the difference in the work functions [Kro99]:

$$eV_{\mathrm{CPD}} = \Phi_1 - \Phi_2. \tag{4.2}$$

During the measurement, the capacitor is vibrated periodically, so that a steady state alternating current develops in the capacitor which is easily monitored with an amplifier. Thus, a bias voltage can be adjusted until the alternating current is nullified. This is the case when the applied bias voltage is equal and opposite to the CPD. This measurement principle is shown schematically in Figure 4.5, where the Fermi levels of two materials are drawn which are (a) isolated, (b) short-circuited, and (c) connected with a bias voltage equal and opposite to the CPD.

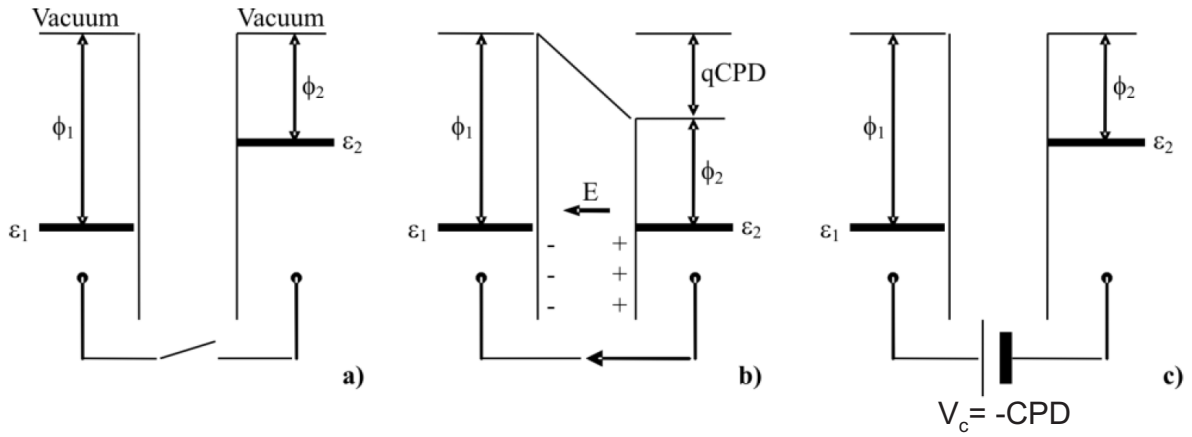

Figure 4.5: *Schematic energy diagrams of a contact potential difference measurement with a parallel plate capacitor formed by two different materials with different work functions: (a) isolated, (b) short-circuited, and (c) connected through a bias voltage equal and opposite to the contact potential difference. From Reference [Pal06a].*

The CPD setup can also be applied to the measurement of illumination induced changes in work functions of semiconductors. For this purpose, one has to make an ohmic contact to the semiconductor sample and connect it to the metallic reference electrode. Since the work function of the metallic electrode does not change under illumination, the relation

$$e\Delta V_{\mathrm{CPD}} = \Delta\Phi_{\mathrm{SC}} = -eV_{\mathrm{SPV}}, \tag{4.3}$$

is assumed, where V_{SPV} is the surface photovoltage, which indicates the magnitude of band bending at the surface of the semiconductor. Such a band bending stems from a surface space charge region, which is typically due to surface states which capture the majority carriers. Under above-bandgap illumination, the photo-induced charge carriers can redistribute a significant

amount of charge and, thus, reduce the space charge region and the band bending. When the intensity is high enough, this results in complete flattening of the surface band bending [Kro99]. This photo-saturation technique is the most used surface photovoltage based tool to determine the surface potential.

Contact potential difference measurements were performed for inorganic semiconductors in air directly after the etching step and for P3HT in vacuum with a semitransparent gold reference electrode and a control unit (Kelvin Probe S and a Kelvin Control 07, respectively, from Besocke Delta Phi GmbH). For surface photovoltage measurements the inorganic semiconductor was illuminated with UV light, while P3HT was illuminated with white light to avoid photochemical reactions. The intensity of the illumination was stepwise increased until a saturation was observed.

Contact angle

The contact angle between a drop of H_2O and the sample surface could be determined with a video camera. The value of the contact angle allows to conclude if the surface has a hydrophobic or hydrophilic nature. This was mainly done to verify if the termination of the inorganic semiconductors had been successful.

4.2.2 Optical spectroscopy

Optical spectrometer

For the determination of the transmission and the reflection of the semiconductors and the transparent contacts, a optical spectrometer (Lambda 900, Perkin Elmer) was employed. The spectrometer is equipped with both, a halogen and a deuterium lamp, and thus is able to cover a spectral region of $186-3280$ nm, which corresponds to the near infrared, visible, and ultraviolet parts of the electromagnetic spectrum. The detection of the infrared light is provided by a PbS photo-detector. For the visible and ultraviolet light a photomultiplier records the intensity. The spectrometer has a double monochromator which lowers the stray light effectively. At the beginning of each measurement, a lamp spectrum is recorded, to which the resulting sample spectrum is normalized. From the measured reflection and transmission spectra the absorption coefficient, α, can be calculated via the following equation which takes into account multiple internal reflections [Pan75]:

$$\alpha(\lambda) = -\ln\left(\frac{T(\lambda)}{(1-R(\lambda))^2}\right)\frac{1}{d}, \tag{4.4}$$

where $T(\lambda)$ and $R(\lambda)$ are the spectral transmittance and reflectance of the sample and d is the sample thickness, respectively.

Fourier transform infrared spectroscopy

Infrared spectroscopy is based on the absorption of infrared radiation which causes excitations of vibrational states in the sample. Thus, an infrared spectrum provides a set of absorption bands, depending on the exact molecular structure of organic and inorganic compounds. Fourier transform infrared (FTIR) setups employ interferometric techniques with moving mirrors for the collection of spectral information. The full intensity is recorded as a function of the mirror position and than the spectrum is calculated as an inverse Fourier transform of the interferogram [Gün03].

In this work, infrared spectroscopy was used to gain structural information of P3HT in pure P3HT and in mixed P3HT/Si-nc samples. For this purpose, solutions with different compositions were drop-casted on a substrate which was coated with a 100 nm thick gold layer. After the evaporation of the solvent, reflection spectra were acquired at room temperature at vacuum in a Bruker Vertex 70v spectrometer. The spectra were obtained in the spectral range of $370 - 5000$ cm^{-1} with a resolution of 1 cm^{-1} by averaging at least 1000 scans. Additionally, a background correction was performed with an empty gold-coated sample holder.

4.2.3 Electrical characterization

Current-voltage characteristics

To investigate the carrier transport mechanisms of semiconductor contacts or junctions, current-voltage measurements were performed. To prevent the oxidation of the organic part, the current-voltage measurements were performed in an inert gas atmosphere of an argon filled glovebox ($H_2O < 1$ ppm and $O_2 < 1$ ppm).

The current-voltage characteristics were recorded with a Keithley 2400 SourceMeter which was connected to the samples with coaxial cables and accessed by a LabVIEW program. The voltage range was typically -1 V $-$ +1 V to avoid damages due to too high current densities. The voltage steps were typically 0.05 V. To exclude hysteresis effects due to trapped charges, a delay time of up to 1 s was used between the voltage steps. For the same reason most current-voltage characteristics were measured cyclically, *i.e.* two measurements, one from -1 V to +1 V and one from +1 V to -1 V, were performed and subsequently averaged. For all current-voltage characteristics shown in this work, the potential was applied to the front contact, that is, for bilayer heterojunctions on the Au or ITO contact or, in the case of bulk heterojunctions, on the ITO side of the sample.

Photocurrent measurements

The photocurrent of the samples was measured either by spectrally resolved photoconductivity measurements, providing information over a large spectral range, or by illumination with different high power light-emitting diodes (LED) or a halogen lamp, providing a higher light intensity. The 150 W halogen lamp was also used to simulate the light intensity of a solar spectrum at AM 1.5 which is about 100 mW/cm^2, even if the spectrum does not match exactly the solar spectrum.

For spectrally resolved photocurrent measurements the samples were illuminated with monochromatic light that was focused on the samples. Depending on the spectral region ($200 - 3200$ nm), a halogen lamp or a xenon lamp could be chosen for the illumination, where the xenon lamp has a higher intensity at smaller wavelength. The white light is split up by the diffraction grating of the monochromator. Behind the exit slit optical filters absorb light from higher diffraction orders. For a higher sensitivity, the light was chopped at a frequency of typically 5 Hz and the photosignal was recorded with a lock-in amplifier (EG&G 7260). The sample was mounted in a cryostat under high vacuum and could be cooled down to about 90 K by liquid nitrogen for a better signal-to-noise ratio. Furthermore, when a bias illumination with a green LED was used, the photoconductivity signal of P3HT could be enhanced, as traps were filled by charge carriers. The typical bias voltage for an efficient extraction of the photogenerated charge carriers was -1 V. A Keithley 617 electrometer was used as voltage source and the photocurrent was detected either by a current amplifier SR570 from Stanford Research or by a variable load resistance. The recorded spectra were normalized by dividing by the lamp spectrum recorded with a pyrometer at the sample position.

For the photocurrent measurements with high light intensity at a certain wavelength, different high power LEDs were used. A green LED with a center wavelength of $\lambda = 525$ nm was used to selectively excite the P3HT, which exhibits a maximum in the absorption of 1.3×10^5 cm^{-1} at that wavelength. However, for thick P3HT layers, nearly no photons are transmitted through the layer, which for certain measurements is not desired. Thus, for heterojunctions, where both semiconductors should be excited and which are illuminated through a P3HT layer, a wavelength would be favorable where P3HT is excited but still photons are transmitted to the heterojunction. For this purpose a red LED with a center wavelength of $\lambda = 655$ nm was used, as this wavelength lies near the onset of the absorption of P3HT. As LEDs have typical spectral widths of about ± 20 nm around the center wavelength, at $\lambda = 655$ nm a part of the photons, with smaller wavelengths than 655 nm, will be absorbed mainly in the P3HT, while the rest will reach the underlying inorganic semiconductor. Furthermore, an infrared LED with a center wavelength of $\lambda = 810$ nm is also used, where for P3HT/Si heterojunctions the light is not absorbed in the P3HT but only in the silicon. For the illumination in the ultraviolet spectral range, which was used for the excitation of 6H-SiC, a LED with a center wavelength

of $\lambda = 300$ nm was used. The light intensity of the latter LED is about 8 mW/cm^2, whereas for all other LEDs it is about 20 mW/cm^2. In Figure 4.6 the center wavelengths of the LEDs are shown together with the absorption coefficients of the semiconductors which were used in the investigated bilayer heterojunctions.

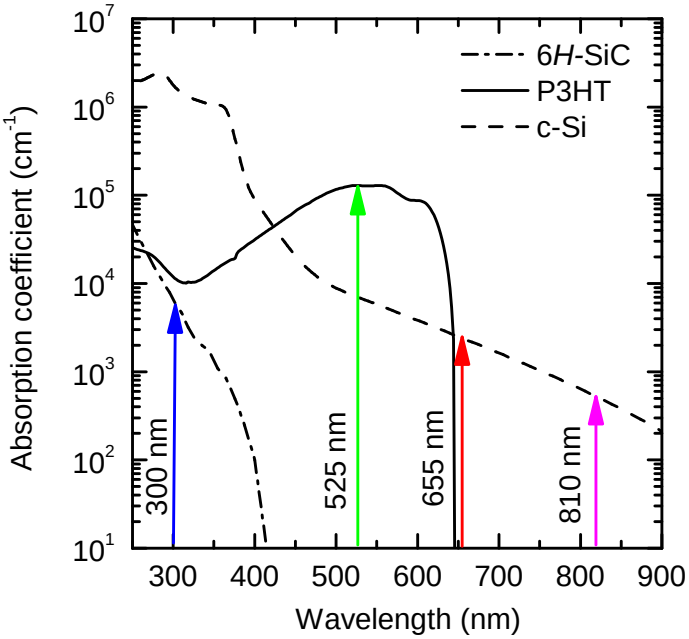

Figure 4.6: *Center wavelengths of the high power LEDs shown together with the absorption coefficients of the semiconductors used for hybrid bilayer heterojunctions.*

Current-temperature measurements

Temperature-dependent measurements of the current-voltage characteristics were performed under high vacuum in the cryostat of the photocurrent setup which could be cooled down to about 90 K by liquid nitrogen. To measure the small currents at low temperatures, a Keithley 617 electrometer was used. In principle, it is also possible to heat the sample and to measure at elevated temperatures above room temperature with the employed setup. However, to avoid changes in the P3HT morphology, measurements were only performed far below temperatures of about 100 °C, where structural changes of P3HT start to appear [Coa03a, Ma05].

4.2.4 Electron spin resonance experiments

Electron spin resonance

Electron spin resonance (ESR) is a powerful tool to gain information about the density and the nature of paramagnetic defects. The measurement method relies on the Zeeman effect, which is

the splitting of the degenerate energy level of an unpaired electron when an external magnetic field, B_0, is applied. When photons of the energy $h\nu$ are absorbed by paramagnetic states in the lower energy level, they are excited to the higher energy level by a spin flip. From the intensity of the absorbed photons the density of paramagnetic states can be determined, while the photon energy and the external magnetic field are characteristic for the spin state which is involved in the transition:

$$h\nu = \Delta E = g\mu_B B_0. \tag{4.5}$$

Here, g is the characteristic g-factor of the paramagnetic state and μ_B is the Bohr magneton. For magnetic fields of 1 T, which are typical for ESR experiments, the energy required for a spin-flip of a free electron with $g \approx 2.0023$ lies in the spectral range of microwaves ($\nu \approx 9$ GHz). For electrons in atoms which are assembled in a solid, non-zero orbital angular momentum contribute to the g-factor as well as the influence of the crystal fields, which leads to a g-factor that deviates from the g-factor of the free electron. Thus, the g-factor is a fingerprint of paramagnetic states in solids, *e.g.* defects in a crystal. A schematic view of the microwave absorption and a subsequent spin-flip at the resonant magnetic field, B_{res}, is shown in Figure 4.7 (a) in a so-called Breit-Rabi diagram.

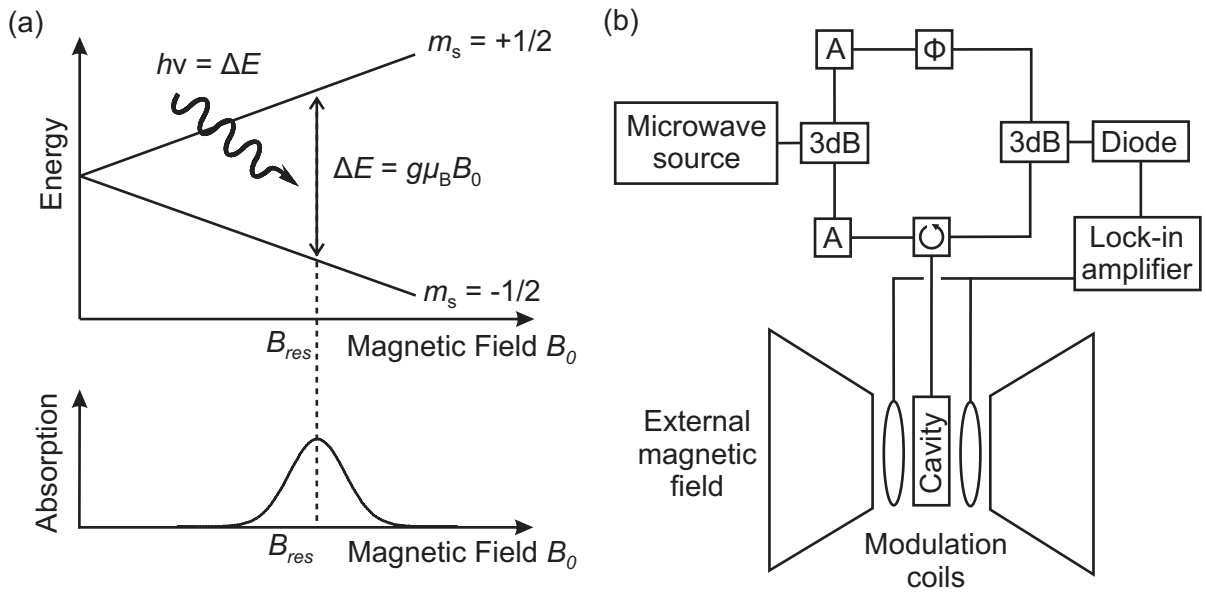

Figure 4.7: *(a) Schematic view of the microwave absorption and a Breit-Rabi diagram showing the resonance condition for microwave absorption during ESR experiments. (b) Experimental setup for ESR experiments.*

In Figure 4.7 (b), a schematic view of the ESR setup is shown. From the microwave source, the microwave is coupled via a tubular waveconductor to a 3 dB splitter, which splits half of the signal to the upper reference arm, and the other half to the lower sample arm, where the microwave is coupled into the cavity resonator, where the sample is mounted, by a circulator. The cavity is tuned critically, so that no microwave is reflected from the cavity. Only under resonance condi-

tions microwave power is reflected from the cavity. The microwave fraction which is reflected, is led to another 3 dB splitter, where the signal is combined with the microwave of the reference arm. The combined microwave power is then detected by a diode. In the reference arm, the microwave passes a phase shifter and an attenuator, which can also be found in the sample arm. To increase the signal-to-noise ratio, a lock-in amplifier is used. For this reason, the magnetic field is modulated by two Helmholtz coils on each side of the resonator.

The ESR measurements were performed in a Bruker continuous wave X-band spectrometer of about 9.4 GHz using a magnetic field modulation at 100 kHz for the lock-in detection. The sample is mounted in a helium flow cryostat where temperatures from room temperature down to 5 K could be achieved. Typical magnetic fields of $327.5 - 332.5$ mT were applied. The g-factor was calibrated using a di-phenyl-picryl-hydrazyl reference, which has a g-factor of $g = 2.0036$. The spin density was calibrated with a phosphorus-doped crystalline silicon reference sample.

Light-induced electron spin resonance

When the paramagnetic centers, which can be detected by ESR, are induced by excitation with light, this is called light-induced electron spin resonance (LESR). This technique is especially interesting for composites, where a photo-induced charge transfer takes place upon illumination, *e.g.* in organic solar cells. In addition to the creation of paramagnetic centers by the white light illumination, via illumination with different wavelengths different paramagnetic species can be be selectively investigated. Furthermore, the decay of the light-induced signal can be monitored and, thus, also information about the recombination kinetics of the paramagnetic states can be obtained.

The illumination of the LESR samples was performed with a Schott KL 1500 LCD cold light source from Zeiss with a 150 W halogen lamp through a band pass filter which only transmits light between 340 and 680 nm. In addition, the samples were illuminated by LEDs with different wavelengths to gain spectral information. The light was coupled into the cavity by a bundle of flexible glass fibers.

Electrically detected magnetic resonance

In contrast to the conventional detection of ESR, in electrically detected magnetic resonance (EDMR), the transitions between Zeeman levels are observed as a change in the electrical conductivity of the sample. Responsible for the change of the conductivity are spin-dependent recombination and hopping processes. Such processes become spin-dependent whenever they include steps whose probabilities are determined by spin selection rules, such as the Pauli principle. Furthermore, the conductivity can also change due to spin-dependent scattering, where

the scattering cross-section is dependent on the mutual spin orientation of the two scattering partners. The advantages of EDMR are its very high sensitivity, which can be orders of magnitude higher than ESR, and its selectivity, as EDMR is only sensitive to paramagnetic centers in the current path.

The EDMR spectra in this work were recorded under white light illumination and a bias voltage of 30 V which was applied with a Hewlett Packard E3612A voltage source. The current through the sample was pre-amplified and converted into a voltage with a Stanford Research SR570 current amplifier. The output of the current amplifier was then forwarded to the Stanford Research SR830 lock-in amplifier, which was also used for the standard ESR measurements.

5 Hybrid Bulk Heterojunctions with Silicon Nanocrystals

In this chapter hybrid bulk heterojunctions with silicon nanocrystals will be investigated and their application as solar cell devices will be demonstrated. In Section 5.1, the morphology and the optical properties of composites of P3HT and silicon nanocrystals will be characterized. In Section 5.2, the photo-induced charge transfer between silicon nanocrystals and organic semiconductors will be investigated with light-induced electron spin resonance experiments. The solar cell properties of hybrid bulk heterojunctions will be summarized in Section 5.3. In Section 5.4, imprint lithography of silicon nanocrystals will be discussed and applied to produce ordered bulk heterojunction solar cells with structured silicon nanocrystal layers.

5.1 Optical properties and morphology

5.1.1 Optical properties

The use of inorganic nanoparticles in hybrid compounds for photovoltaic applications has several reasons which have been described in Subsection 2.3.3. One point is the enhancement of the absorption spectrum due to the inorganic part. This argument also holds for bulk heterojunctions with silicon nanocrystals, which absorb in a much broader spectral region when compared to organic semiconductors, as can be seen from the absorption spectra shown in Chapter 3. In typical P3HT/PCBM solar cells, the absorption takes place to a large part in the P3HT, as the PCBM does only significantly contribute to the photocurrent in the UV spectral range (see Figure 3.6). However, this is only a small fraction of the photocurrent as the solar radiation decreases drastically at wavelengths below 450 nm (see Figure 2.7). In contrast, a bulk heterojunction made of P3HT and silicon nanocrystals (P3HT/Si-nc) also absorbs in the energy range below the HOMO-LUMO transition of P3HT, due to the contribution of the silicon nanocrystals.

For a direct comparison, in Figure 5.1 the absorption coefficients of a pure P3HT layer (dashed line), a pure silicon nanocrystal layer (dotted line), and of a P3HT/Si-nc composite layer (solid

line), which was mixed in a 1:1 ratio, are shown. The silicon nanocrystals have an average diameter of 18 nm and are doped with phosphorus to 6.5×10^{19} cm^{-3} (nanocrystal sample 270307). The absorption coefficients for the mixed layer and for the P3HT layer were calculated from reflection and transmission measurements and the absorption spectrum of the silicon nanocrystal layer was taken from Reference [Lec08a]. The absorption of the P3HT/Si-nc layer was normalized to the pure silicon nanocrystal layer as the determination of the film thickness for mixed P3HT/Si-nc layers is difficult due to the high surface roughness (see Subsection 5.1.2). All three layers were deposited on a glass substrate via spin-coating. From the figure one can see that the absorption of the P3HT layer strongly decreases for wavelength larger than about 650 nm, while the P3HT/Si-nc layer additionally absorbs significantly in the wavelength range above 650 nm, following the absorption coefficient of the silicon nanocrystals. Thus, the silicon nanocrystals enhance the absorption range of P3HT/Si-nc bulk heterojunctions into the near-infrared spectral region, when compared to pure P3HT.

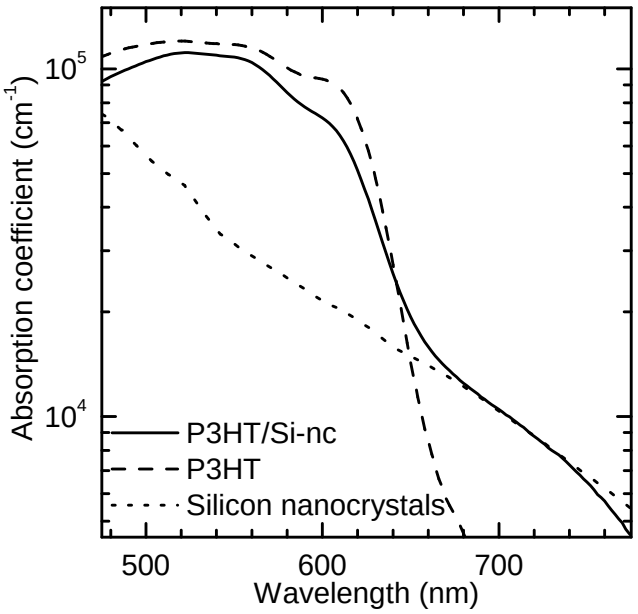

Figure 5.1: *Absorption coefficients of a P3HT, a silicon nanocrystal and a P3HT/Si-nc layer. The P3HT/Si-nc spectrum is normalized to the silicon nanocrystal spectrum which is taken from Reference [Lec08a].*

As an additional feature, in the pure P3HT layer (Figure 5.1, dashed line) a fine structure in the $\pi - \pi^*$ transition around the absorption peak, including a shoulder at a wavelength of about 600 nm, is visible. This fine structure results from vibronic transitions, which only do appear in presence of crystallinity, reflecting a high fraction of ordered phase and therefore a high conjugation length in the polymer [Sun89]. But also in the mixed layer (Figure 5.1, solid line), this shoulder can be seen. This shoulder is not as pronounced as in the P3HT layer, showing that the incorporation of the silicon nanocrystals shortens the conjugation length of the P3HT while

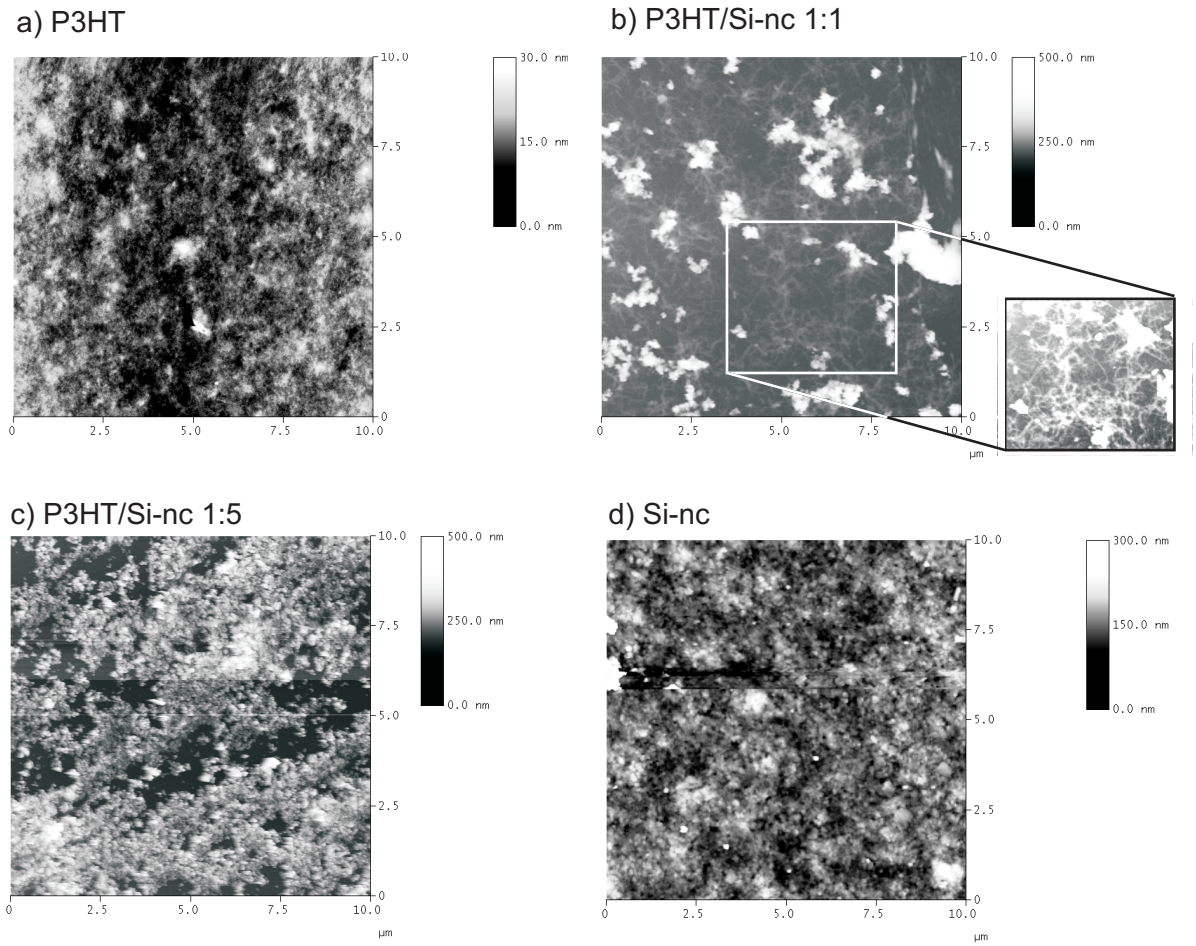

Figure 5.2: *AFM images of (a) a P3HT layer, P3HT/Si-nc composite layers with different mixing ratios of (b) 1:1 and (c) 1:5, and (d) a silicon nanocrystal layer.*

maintaining a certain degree of order in the P3HT phase. That the mixing of the P3HT with the silicon nanocrystals reduces the order in the P3HT is also indicated by the moderate increase of the dark ESR polaron defect density by a factor of 2 in P3HT/Si-nc samples when compared to pure P3HT or to a P3HT/PCBM sample, as will be shown later on in Section 5.2.

5.1.2 Morphology

AFM measurements

To get an insight in the morphology of bulk heterojunctions with P3HT and silicon nanocrystals, AFM images were taken. In Figure 5.2 AFM micrographs of a pure P3HT layer (a), and of P3HT/Si-nc composite layers with mixing ratios of 1:1 (b) and 1:5 (c), and a silicon nanocrystal layer (d) with a size of $10 \times 10\ \mu m^2$ are shown. The P3HT is covering the complete

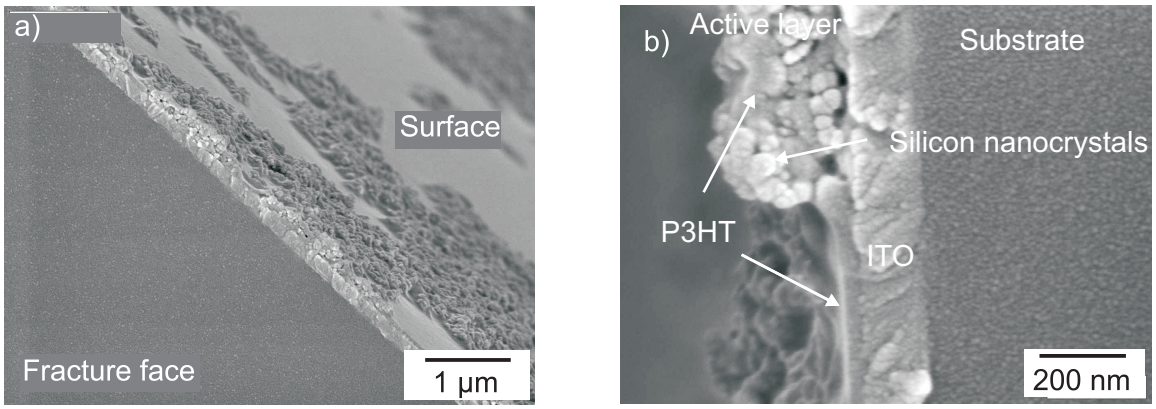

Figure 5.3: *SEM images of a P3HT/Si-nc bulk heterojunction. In (a) the surface of the sample can be seen, while (b) shows a magnification of the cross section view.*

substrate and makes a relatively smooth layer with maximum height values of 30 nm, which is in accordance with AFM images of P3HT in the literature [Sca08]. The AFM images of the layers with silicon nanocrystals (b)-(d), in contrast, show a height scale of $300 - 500$ nm, with a large surface roughness. This fact can be explained by the deposition of agglomerates of silicon nanocrystals, which is in accordance with the previous observed aggregation of silicon nanocrystals [Lec08a]. For samples with a weight ratio of 1:1, the aggregation of the silicon nanocrystals is obvious from the AFM image, leading to large sample areas which are covered only with P3HT. The P3HT is visible as a randomly oriented filament structure in the magnification of Figure 5.2 (b), where a higher contrast has been chosen. The visible filament structure is due to $\pi - \pi$ interaction and a perpendicular alignment of the molecules to the substrate [Sca08]. With a higher silicon nanocrystal content, as shown in Figure 5.2 (c), also a higher silicon nanocrystal coverage of the substrate is achieved, similar to the pure silicon nanocrystal layers of Figure 5.2 (d).

SEM measurements

A further possibility to investigate the morphology of a P3HT/Si-nc bulk heterojunction is scanning electron microscopy (SEM). For SEM images, a P3HT/Si-nc bulk heterojunction was mixed with a ratio of 1:1 and spin-coated onto a glass substrate which was partly coated with ITO. The samples were cleaved at cryogenic temperatures, achieving relative sharp fracture faces. In Figure 5.3, the surface (a) and a magnification of the cross section view (b) is shown. The surface of the sample exhibits a similar structure as the AFM pictures in Figure 5.2. In particular, the aggregation of silicon nanocrystals on only a part of the sample area is obvious from the SEM image. In the upper part of the magnification of the cross section in Figure 5.3 (b), the mixed layer, which was deposited onto an about 150 nm thick ITO layer on a glass substrate, is clearly visible. The silicon nanocrystal agglomerates, which appear as round struc-

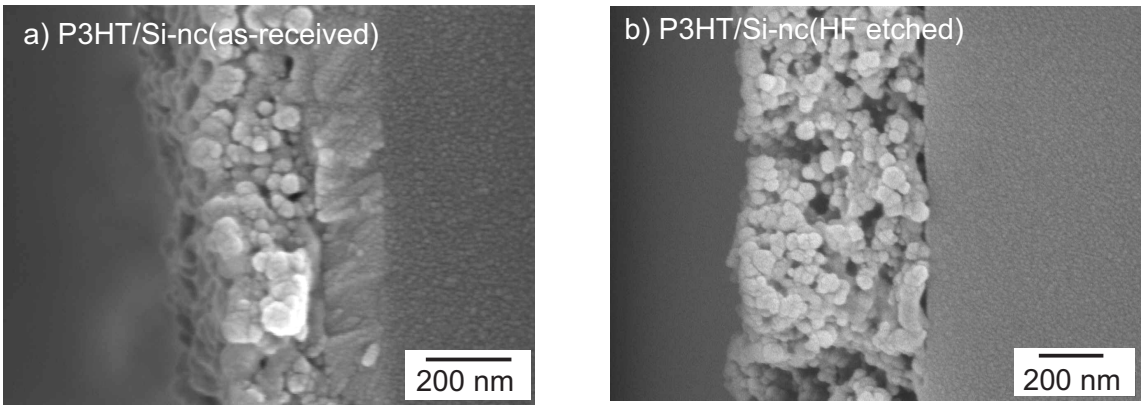

Figure 5.4: *SEM cross section images of P3HT/Si-nc bulk heterojunctions with as-received (a) and HF-etched silicon nanocrystals (b).*

tures, have larger diameters compared to the mean diameter of 23 nm of the single nanocrystals (nanocrystal sample 040407). This is in agreement with the findings of silicon nanocrystal agglomerates exceeding the particle diameter [Lec08a]. The P3HT, which is not structured, is located between the silicon nanocrystals and also covers the ITO layer. Thus, no phase separation on a large scale takes place and both components are mixed. However, due to the size of the silicon nanocrystal agglomerates, a blending on the scale of only a few nanometers, which would be desirable for exciton splitting in a hybrid solar cell, is not achieved. The fine structure of the small light dots which are visible even on the glass surface are artefacts of the gold layer, which was sputtered onto the sample to avoid charging effects. The lower part of Figure 5.3 (b) exhibits an about $40-50$ nm thick P3HT layer on top of the ITO. Here the silicon nanocrystals are not incorporated in the layer. Nevertheless, the substrate is covered with a P3HT layer, as could already be observed in the AFM image of Figure 5.2 (b). Thus, already with a 1:1 mixing ratio it seems that at least a short-circuit from the ITO to a top contact could be avoided by the P3HT layer.

As described in Subsection 4.1.1, the etching of the silicon nanocrystals with hydrofluoric acid (HF) leads to a removal of the natural oxide. This may have an influence on the charge transfer between the nanocrystals the P3HT and will be investigated in Sections 5.2 and 5.3. In addition, the etching step also leads to a termination of the nanocrystal surface with hydrogen [Ste08]. Thus, the question arises how a change in the surface termination changes the morphological properties of bulk heterojunctions. In Figure 5.4, SEM cross section images of blends of P3HT with (a) as-received and (b) etched silicon nanocrystals on an ITO-coated glass substrate and a bare glass substrate are shown, respectively. The mean diameter of the silicon nanocrystals is 23 nm (nanocrystal sample 040407). At first glance the bulk heterojunction with the etched nanocrystals seems to be more porous. In addition, both layers seem to exhibit a comparable amount of silicon nanocrystals, which in both cases dominate the cross section structure. However, the cleavage of the substrates leads to severe damage of the active layer surfaces and, in

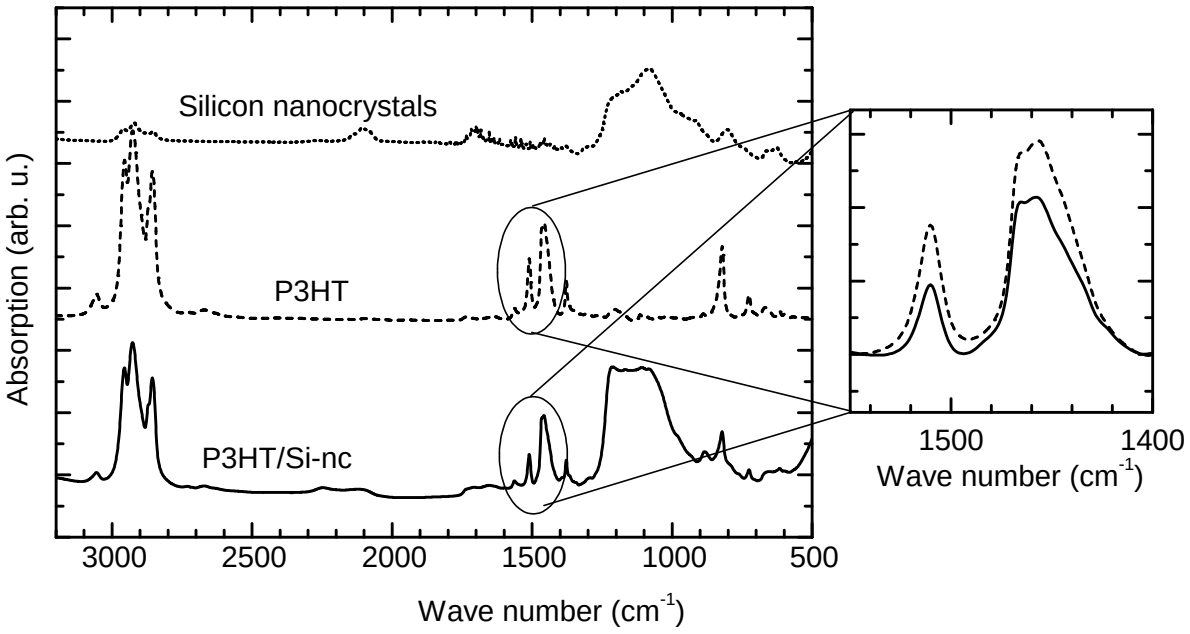

Figure 5.5: *FTIR absorption spectra of silicon nanocrystal, P3HT and P3HT/Si-nc layers. The magnification on the right side shows the C=C ring stretching vibrations of the thiophene rings in pure P3HT and in a P3HT/Si-nc bulk heterojunction sample.*

contrast to the substrate, no smooth cross section surface is achieved. Taking this into account, it is difficult to conclude from Figures 5.4 (a) and (b) if the etching has an influence on the intermixing behavior and on the porosity. The different height of the active layer is also not a sign for a different blending behavior, as the AFM and SEM images above show a large variation in the height of the active layer.

FTIR measurements

To further quantify the decrease of the order of P3HT upon mixing with silicon nanocrystals, as already discussed in Subsection 5.1.1, FTIR measurements were performed in reflection. In Figure 5.5, the FTIR absorption spectra for silicon nanocrystals (sample 100406), P3HT and mixed P3HT/Si-nc layers are shown for wave numbers between 3200 and 500 cm^{-1}. The broad band at 1100 cm^{-1} originates from the O stretching of Si-O-Si bonds at the surface of the silicon nanocrystals [Ste08] and, therefore, appears only in the silicon nanocrystal containing layers (dotted and solid line). The pure P3HT layer (dashed line) shows various bands such as the aromatic C-H out-of-plain vibrations at about 820 cm^{-1} and the aliphatic C-H stretching modes at 2850, 2920, and 2950 cm^{-1} [Che95]. Furthermore, several peaks due to C=C stretching vibrations are visible at around 1500 cm^{-1}. These peaks, in particular the intensity ratio of the symmetric C=C ring stretching vibration at about 1460 cm^{-1} to the asymmetric C=C ring stretching vibration at about 1510 cm^{-1}, are indicative for the conjugation length in the polymer

backbone [Fur87]. In our case, as shown in the magnification on the right side of Figure 5.5, the ratio of the peak areas of the symmetric to the asymmetric C=C ring stretching vibration in pure P3HT is 3.7, while for the P3HT/Si-nc mixture it is 6.2. This indicates a smaller conjugation length of the polymer backbone in the case of the P3HT/Si-nc mixture. This can be explained by the mixing of the P3HT with the silicon nanocrystals. Both values agree with the values of 3.2 for regioregular P3HT and 5.3 for regiorandom P3HT which were found by Pandey *et al.* [Pan00]. In addition, these authors observe a decrease in the hole mobility of about one order of magnitude when comparing regioregular and regiorandom P3HT, which is explained by a less efficient polymer chain packing in the regiorandom P3HT. In our case, the decrease of the conjugation length is not due to a decrease in the regioregularity but due to the incorporation of the silicon nanocrystals, which most probable disturb the polymer chain alignment and thus do limit the π-conjugation.

From the measurements in this section, we can suggest a typical morphology of the P3HT/Si-nc blends, as shown in Figure 5.6. The silicon nanocrystals are aggregated in larger agglomerates and the P3HT is dispersed between the agglomerates. The formation of large P3HT domains is hindered by the mixing with the silicon nanocrystals, which leads to a reduced conjugation length. Furthermore, the height of the active layer does vary significantly and larger areas of the substrate surface are not coated with silicon nanocrystals at all. However, they are covered with P3HT.

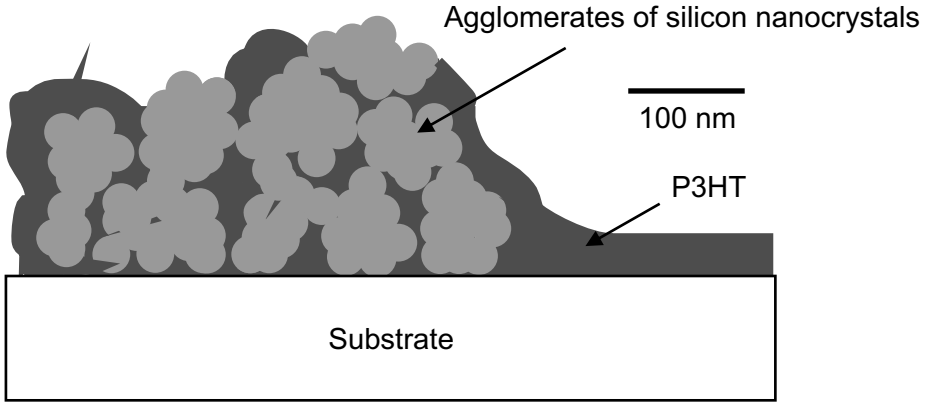

Figure 5.6: *Schematic view of the morphology of P3HT/Si-nc blends.*

These conclusions are valid for spin-coated layers, while the bulk heterojunctions which were made for ESR experiments via the slow evaporation of the solvent of the mixed solutions in a quartz tube on the timescale of hours (see Subsection 4.1.1) may have a different morphology. As it was not possible to extract samples from the ESR quartz tubes without their destruction, no information on the morphology of the ESR samples, which will be discussed in the next section, was available. However, due to the slower evaporation a stronger phase separation between the silicon nanocrystals and the P3HT may occur.

5.2 Photo-induced charge transfer detected via light-induced electron spin resonance

The most crucial point in hybrid solar cells is the efficient charge transfer between the electron donor and the electron acceptor, which can in principle be investigated by various experimental techniques such as photocurrent yield spectroscopy, photo-induced absorption, or light-induced electron spin resonance (LESR) [Pie04]. LESR is especially useful for the spectroscopy of electronic states, which are directly or indirectly populated under the influence of external illumination. LESR experiments already have provided direct evidence for charge transfer as opposed to energy transfer in organic solar cells [Sar92, DC01, AI05] and in hybrid composites with CdSe nanocrystals [Pie04] due to the different g-factors of the photogenerated states. Thus, in this section, we will study the photo-induced charge transfer between silicon nanocrystals and P3HT or PCBM via LESR measurements.

5.2.1 Hybrid composites with silicon nanocrystals and P3HT or PCBM

P3HT and PCBM

Before the ESR and LESR measurements on hybrid composites with silicon nanocrystals are highlighted, ESR and LESR experiments on pure organic and inorganic samples are discussed. In Figure 5.7, the ESR (solid line) and LESR (dash-dotted line) spectra are shown for (a) pure P3HT and PCBM and (b) a P3HT/PCBM bulk heterojunction measured at 5 K. The spectra in (a) were scaled up by a factor of 10 for a better comparison with the P3HT/PCBM spectra in (b). The measurements were performed at 5 K, as the ESR signal amplitude increases and the peaks narrow towards lower temperatures especially for the fullerenes, which could not be detected via LESR at room temperature. This has also been observed in organic polymer-fullerene composites [Sar92, DC01, Kri07] and in C_{60}^{-} ions [Ree00]. The LESR measurements were performed with a white light source as described in Subsection 4.2.4. The preparation of the samples for the LESR experiments by drying of the solutions in quartz tubes is described in detail in Subsection 4.1.1.

In Figure 5.7 (a) a clear dark signal can already be observed for pure P3HT, which increases upon illumination. The g-factor of the P3HT sample can be determined to $g = 2.0020$, which can be attributed to positive polarons in P3HT (P^+). For the dark ESR signal of PCBM in Figure 5.7 (a) only a weak broad signature can be observed, while under white light illumination two clearly distinguishable peaks appear. The larger peak with a g-factor of $g = 2.0001$ can be attributed to negative PCBM anions ($PCBM^-$) [Ree00]. Both g-values for the P^+ and for the

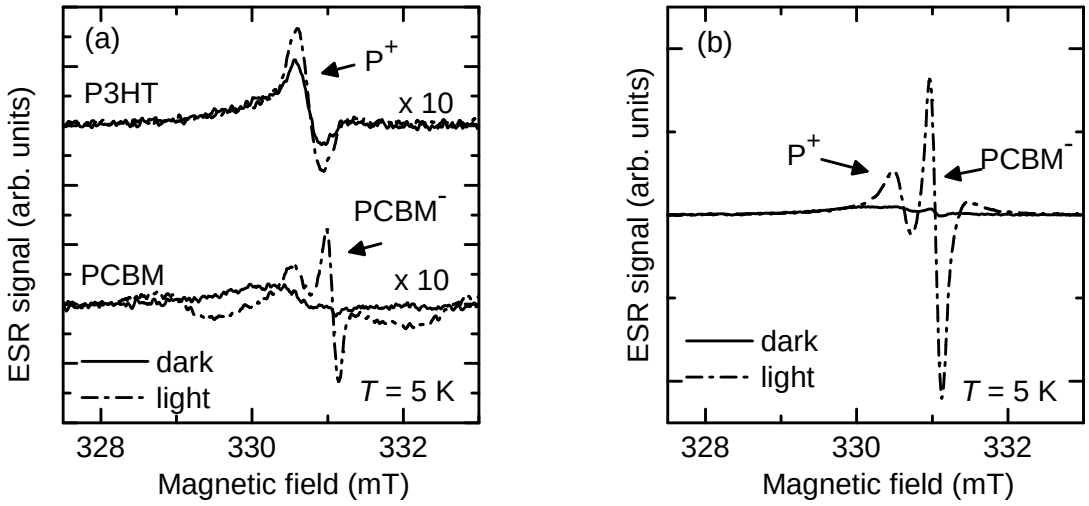

Figure 5.7: *ESR (solid line) and LESR spectra (dash-dotted line) of pure P3HT and PCBM (a) and of a P3HT/PCBM (1:1) composite (b) measured at 5 K. The spectra in (a) were scaled up by a factor of 10 for a better comparison with the spectra in (b).*

$PCBM^-$ as well as the corresponding peak-to-peak linewidths, ΔB_{pp}, which are specified in Table 5.1, agree with the literature values of $g = 2.002$ for P^+ and $g = 2.000$ for $PCBM^-$ [DC01, AI05, Mar06]. The dark ESR signals observed in pure P3HT and PCBM samples can be attributed to defects, for instance chain ends, sp^3-defects, or impurities [Mur98, DC01]. Under illumination in P3HT also an interchain charge transfer takes place [DC01]. The origin of the LESR features in pure PCBM is unknown. One suggestion is a possible intramolecular charge transfer from the side groups onto the fullerene [Dya99].

In the P3HT/PCBM composite sample, shown in Figure 5.7 (b), the total number of paramagnetic states increases by more than one order of magnitude under illumination. The densities of paramagnetic states in the dark are 2.5×10^{16} g^{-1} for P^+ and 8.9×10^{15} g^{-1} for $PCBM^-$. Both increase under illumination to the same value of $5-6 \times 10^{17}$ g^{-1}. This increase is a strong evidence of light-induced charge transfer between P3HT and PCBM [Sar92, AI05]. To quantify the total number of spins, we have confirmed by variation of the microwave power and the temperature, that the ESR measurements were done in an unsaturated regime and that the magnetic susceptibility follows a Curie law. The typical microwave power used for ESR measurements was between 0.002 mW and 0.02 mW, while a modulation amplitude of about $1-2$ G was used.

The process of the photo-induced charge transfer is depicted schematically in Figure 5.8 (a). In Figure 5.8 (b), the energy levels of P3HT and PCBM are shown, where the curved arrow indicates the electron transfer and the small vertical arrows illustrate the detected paramagnetic states. The absorption of the photons mainly takes place in the P3HT due to its higher absorption coefficient. The created excitons can than diffuse to the interface between P3HT and PCBM and

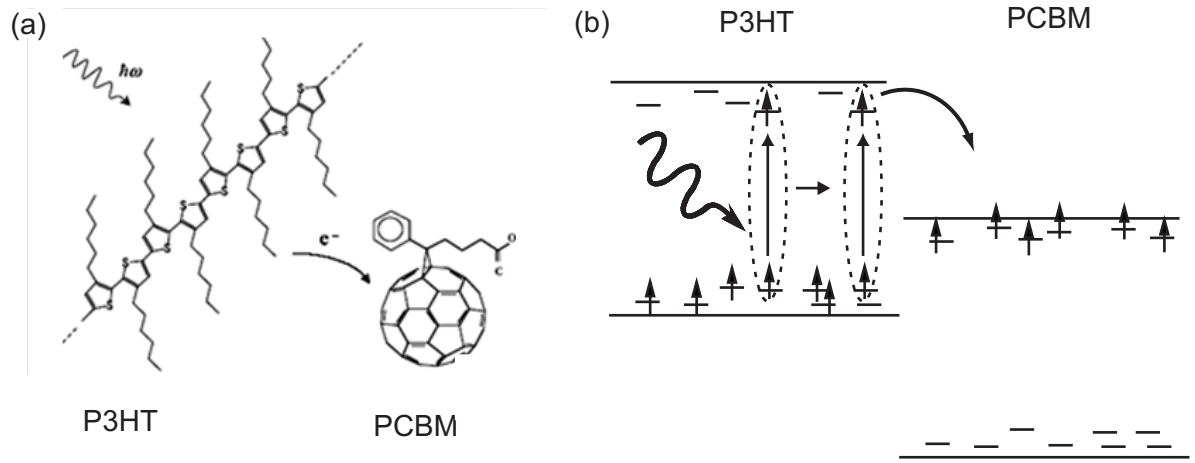

Figure 5.8: *(a) Schematic view of the photo-induced electron transfer from P3HT to PCBM, taken from Reference [Dye10b]. (b) Schematic view of the energy levels of P3HT and PCBM. The curved arrow indicates the transfer direction of electrons while the small vertical arrows illustrate the generated paramagnetic states, which are detected via ESR.*

can be dissociated by an electron transfer to the PCBM which acts as electron acceptor. Thus, a P^+ in the P3HT and a $PCBM^-$ in PCBM are created, which both are paramagnetic states and can be detected via ESR.

Silicon nanocrystals

The ESR (solid line) and LESR (dash-dotted line) spectrum of a silicon nanocrystal sample, which is made from undoped silicon nanocrystals (nanocrystal sample 100506) with a mean diameter of about 33 nm, are shown in Figure 5.9 (a). The measurements were done at a temperature of 5 K. The silicon nanocrystal sample, which is made by a dispersion fabricated by ball-milling, exhibits an asymmetric signal with a g-value of $g = 2.0065$. This is in agreement with previous results, where the spectrum of silicon nanocrystals displays typically a broad resonance centered at about $g \approx 2.006$, which originates from different configurations of silicon dangling bonds [Ste08]: The spectrum of as-received silicon nanocrystals is a superposition of an isotropic resonance centered at $g = 2.0055$ originating from silicon dangling bonds in a disordered environment and an axially symmetric powder pattern with $g_\perp = 2.0088$ and $g_\parallel = 2.0021$ due to silicon dangling bonds, so called P_b centers, at the interface between the crystalline core of the silicon nanocrystals and their native oxide shell [Bau06b, Per07, Ste07]. The density of the silicon dangling bonds is strongly increased by about one order of magnitude due to surface damage produced by the ball milling process used to disperse the silicon nanocrystals, as described in Subsection 4.1.1 [Per07, Lec08b].

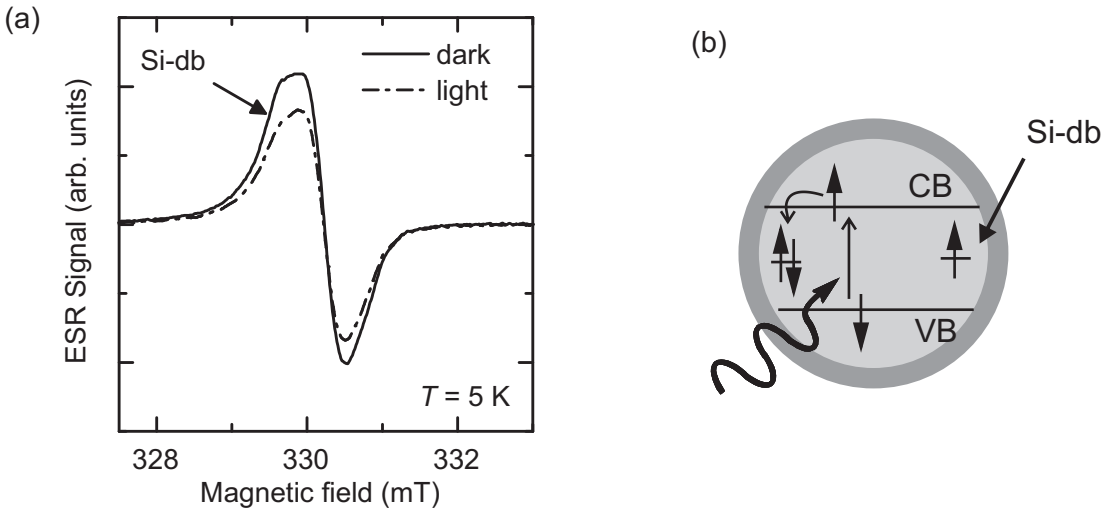

Figure 5.9: *(a) ESR (solid line) and LESR (dash-dotted line) spectrum of a silicon nanocrystal sample. (b) Scheme of a silicon nanocrystal and its energy levels. The silicon dangling bonds (Si-db), which are partially compensated by photo-induced charge carriers, are indicated.*

The paramagnetic silicon dangling bond density observed by ESR decreases reversibly from 9.0×10^{17} g^{-1} to 6.5×10^{17} g^{-1} during illumination due to the compensation of neutral silicon dangling bonds by photoexcited charge carriers. This is shown schematically in Figure 5.9 (b). The compensation of silicon dangling bonds is only observed at low temperatures, as at room temperature the much faster recombination of light-induced charge carriers from charged dangling bonds with photoexcited holes prevents a steady state compensation.

Hybrid composites of silicon nanocrystals and P3HT or PCBM

In Figure 5.10, the spectra of ESR (solid line) and LESR (dash-dotted line) measurements, which were performed on composites of silicon nanocrystals with P3HT or PCBM, are shown. The measurements were done at a temperature of 5 K with undoped silicon nanocrystals with a mean diameter of 33 nm (nanocrystal sample 100506). In the upper part of the figure, two signals of the silicon dangling bonds with $g = 2.0063$ and $\Delta B_{\mathrm{pp}} = 8.0$ G and of the P^+ with $g = 2.0024$ and $\Delta B_{\mathrm{pp}} = 3.0$ G can be observed. Upon illumination, the P^+ signal, which is already visible in the dark spectrum, increases strongly from 6.2×10^{16} g^{-1} to 2.8×10^{17} g^{-1}. A light-induced charge generation, followed by charge separation between the P3HT and the silicon nanocrystals resulting in P^+ on the P3HT can explain the observed LESR spectrum. In the equilibrium of charge generation and recombination, the LESR density of P^+ of 2.8×10^{17} g^{-1} is only a factor two lower than the density of 6.0×10^{17} g^{-1} obtained for photo-induced P^+ in the P3HT/PCBM reference sample. This implies that the degree of the charge separation in the hybrid P3HT/Si-nc composite is roughly comparable to that of the P3HT/PCBM system.

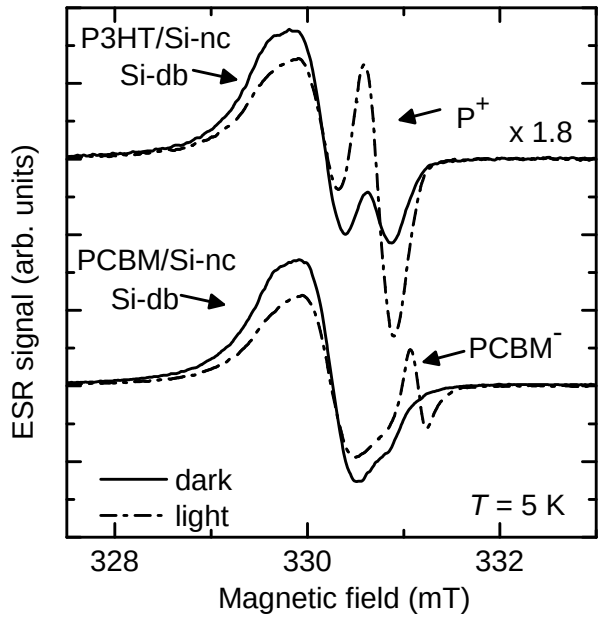

Figure 5.10: *ESR (solid line) and LESR (dash-dotted line) spectra of P3HT/Si-nc and PCBM/Si-nc composite samples measured at 5 K. The spectra of the P3HT/Si-nc sample were scaled up by a factor of 1.8.*

The silicon dangling bond signal decreases from 1.5×10^{18} g^{-1} to 1.0×10^{18} g^{-1}. Such a decrease of the silicon dangling bond signal of about 30 % has already been observed in the pure silicon nanocrystal sample shown in Figure 5.9 and thus takes place without the P3HT. After switching off the illumination of the P3HT/Si-nc sample, the P^+ signal decreases slowly on a timescale of minutes, following a stretched exponential decay, without reaching the dark signal even after 1 h. Only after heating up the sample above room temperature the persistent P^+ signal vanishes. This indicates that the holes are trapped in the P3HT and can only recombine via thermal excitation. However, the silicon dangling bond signal decreases instantaneously after switching off the light and stays constant afterwards. The dynamics of the charge generation and recombination in P3HT/Si-nc samples at room temperature will be discussed in detail in the next Subsection 5.2.2.

Furthermore, when comparing the dark ESR P^+ densities in a pure P3HT sample and in the mixed P3HT/Si-nc sample, which are listed in Table 5.1, an increase of the defect density in the P3HT by a factor of 2.5 is observed. In Subsection 5.1.2 a decrease of the conjugation length of P3HT upon mixing with the silicon nanocrystals has already been observed by absorption measurements in the visible and infrared spectral region. Thus, we can conclude that the reduced conjugation length due to the lower order of the P3HT in the composite sample and not a chemical reaction between the P3HT and the silicon nanocrystals is the origin of the additional defects of the P3HT in the P3HT/Si-nc samples, which have been detected by ESR.

Both spectra of the P3HT/Si-nc sample, which was prepared with the same amount of silicon nanocrystals as the PCBM/Si-nc sample, were scaled up in Figure 5.10 by a factor of 1.8, which is the difference in the measured silicon dangling bond density of the two samples. The lower silicon dangling bond signal in the P3HT/Si-nc sample can be explained by a different distribution of the silicon nanocrystals in the sample tube after the evaporation of the solvent. We have observed that due to this effect the silicon nanocrystals are at a different position in the microwave resonator and the signal may vary by a factor of up to 2.

In the lower part of Figure 5.10, the ESR (solid line) and the LESR (dash-dotted line) spectra of the corresponding PCBM/Si-nc composite sample are shown. In the ESR spectrum only the silicon dangling bond signal with $g = 2.0064$ and $\Delta B_{\mathrm{pp}} = 8.1$ G is observed, while in the LESR spectrum a second signal with $g = 2.0001$ and $\Delta B_{\mathrm{pp}} = 1.6$ G appears, which is attributed to photo-induced PCBM^-. Again, the silicon dangling bond density is reduced to about 60 % of the dark silicon dangling bond density upon illumination, in this case from 2.8×10^{18} g^{-1} to 1.6×10^{18} g^{-1}. The appearance of the PCBM^- signal in the LESR spectrum can again be understood by light-induced charge generation and separation, this time between the silicon nanocrystals and the PCBM, resulting in the formation of PCBM^-. It was found that the PCBM^- density in the illuminated PCBM/Si-nc sample is 7.4×10^{16} g^{-1}, while no PCBM^- signal was detectable in the dark. This density is smaller than the light-induced PCBM^- density in the P3HT/PCBM sample of 5.0×10^{17} g^{-1}, but still significantly higher than the PCBM^- density of 6.8×10^{15} g^{-1} under illumination in the pure PCBM sample. We can estimate the generation rate of the PCBM/Si-nc sample to about 3×10^{22} $\mathrm{cm}^{-3}\mathrm{s}^{-1}$, while for the P3HT/Si-nc sample it is about 1×10^{23} $\mathrm{cm}^{-3}\mathrm{s}^{-1}$ due to the higher absorption (see Figure 3.6) of P3HT in the P3HT/Si-nc sample. For the P3HT/Si-nc and PCBM/Si-nc composite samples and the P3HT, PCBM, P3HT/PCBM, and silicon nanocrystal reference samples the corresponding g-factors, the peak-to-peak linewidths ΔB_{pp}, and the ESR as well as the LESR spin densities are summarized in Table 5.1.

In principle, in the silicon nanocrystals photo-induced conduction band electrons should also be observed for LESR measurements in P3HT/Si-nc samples. Such conduction band electrons have a g-value of $g = 1.9995$ as measured by Young *et al.* in crystalline and porous silicon [You97b, You97a]. However, for silicon nanocrystals these conduction band electrons could only be observed via EDMR and not by ESR measurements, as with EDMR measurements a higher sensitivity is achieved [Kle08]. For holes, which do remain on the silicon nanocrystals after photo-induced charge transfer in the case of PCBM/Si-nc samples, also no LESR signal is observed. This can be explained by a line broadening, which is due to a splitting of the degenerate ground state by inhomogeneous strain, which makes it very difficult to observe holes and shallow acceptor centers even in bulk crystalline silicon [Neu78]. The additional photo-induced charge carriers in the silicon nanocrystals could also compensate silicon dangling bonds and, thus, reduce the silicon dangling bond density. However, for our measurements

Sample	Signal	g-factor	ΔB_{pp}(G)	ESR density (g^{-1})	LESR density (g^{-1})
P3HT	P^+	2.0020	3.4	2.4×10^{16}	3.1×10^{16}
PCBM	$PCBM^-$	2.0001	1.6	1.8×10^{15}	6.8×10^{15}
Si-nc	Si-db	2.0065	8.1	9.0×10^{17}	6.5×10^{17}
P3HT/PCBM	P^+	2.0025	3.0	2.5×10^{16}	6.0×10^{17}
P3HT/PCBM	$PCBM^-$	2.0002	1.6	8.9×10^{15}	5.0×10^{17}
P3HT/Si-nc	Si-db	2.0063	8.0	1.5×10^{18}	1.0×10^{18}
P3HT/Si-nc	P^+	2.0024	3.0	6.2×10^{16}	2.8×10^{17}
PCBM/Si-nc	Si-db	2.0064	8.1	2.8×10^{18}	1.6×10^{18}
PCBM/Si-nc	$PCBM^-$	2.0001	1.6	—	7.4×10^{16}

Table 5.1: *Overview of the g-factor, the peak-to-peak linewidth ΔB_{pp}, the ESR and the LESR spin densities for all samples at 5 K. The origins of the respective paramagnetic states are listed in the second column.*

we do not observe such a reduction. Thus, the additional charges in the silicon nanocrystals either compensate the silicon dangling bonds to an amount which cannot be observed within the accuracy of our measurements, or are in the conduction or valence band, or are trapped in shallow traps such as band tail states.

In Figure 5.11, the light-induced charge transfer and the detected paramagnetic states are illustrated for (a) P3HT/Si-nc and (b) PCBM/Si-nc samples. Furthermore, the positive P^+ state on a P3HT chain and the negative $PCBM^-$ state are also sketched in the figure. The difference in the size of the silicon nanocrystals and the organic counterparts is also illustrated. Considering the smaller structural size of the organic components and the high flexibility of the polymer chains, a good coverage of the silicon nanocrystal surface should be provided, as also illustrated in Figure 5.6.

Position of the energy levels at the organic/silicon nanocrystal interface

In Figure 5.12 (a) the conduction and valence band of silicon as well as the LUMO and the HOMO of P3HT are displayed, based on the average of the literature values given in Section 3.2. The curved arrows indicate the possible transfer directions of electrons and holes, while the vertical arrows illustrate the detected paramagnetic states. Yet, a complete oxide shell on the surface of the silicon nanocrystals, which would work as an insulator between the organic and the inorganic part, would not allow a charge transfer. However, the charge transfer, as observed with the LESR measurements, is very efficient. There are two explanations for the observed behavior despite the oxide shell: First, the oxide shell of the silicon nanocrystals is not perfect and a part of the silicon nanocrystal surface is still H-terminated and hence partly permeable for charge carriers. This is in agreement with previous results [Kni04, Lec08a]. Secondly, a tunneling through the oxide barrier may occur especially in thinner regions of the oxide shell. Thus,

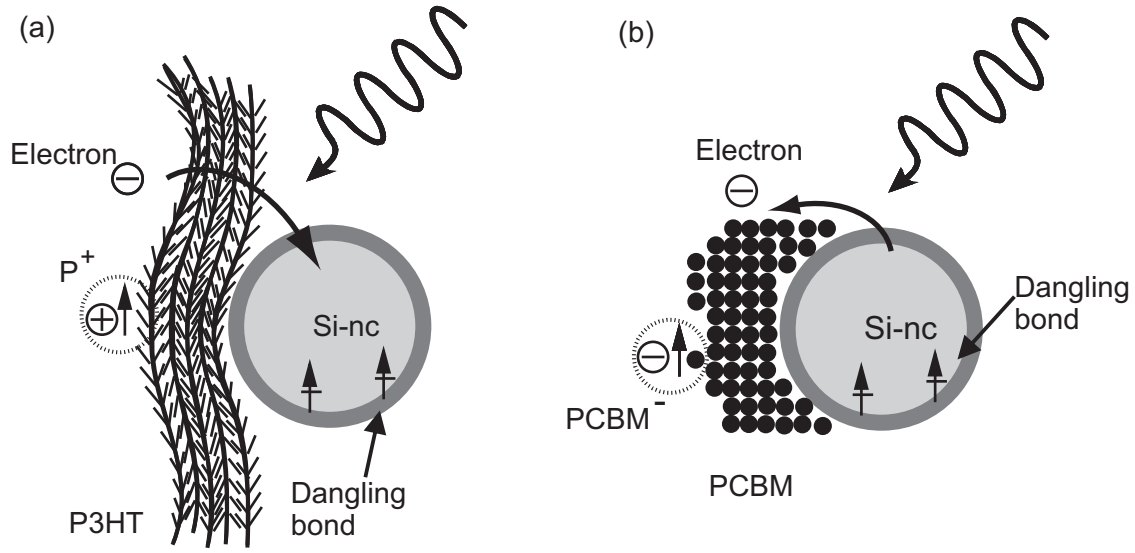

Figure 5.11: *Schematic view of (a) the electron transfer from P3HT to silicon nanocrystals, resulting in P^+ on the P3HT and of (b) the electron transfer from the silicon nanocrystals to the PCBM, resulting in $PCBM^-$.*

an oxide barrier is not taken into account explicitly in the following discussion. Nevertheless, in the next Subsection 5.2.2, the etching of the silicon nanocrystals will be discussed.

The energy levels in the Figure 5.12 are sketched with respect to the vacuum level. One could also go one step further and assume a Fermi level alignment, as described in Section 2.2. For undoped silicon, the Fermi level lies at 4.6 eV in the middle of the bandgap. Also a pinning at silicon dangling bonds, which have energetic positions around the middle of the bandgap [Stu05], could be expected due to the high silicon dangling bond density. In any case, for the P3HT/Si-nc heterojunction, only a slight downward shift of P3HT is expected when taking into account the P3HT Fermi level value of 4.4 eV, as determined by CPD measurements (see Subsection 3.2.1). For PCBM no Fermi level value is given in the literature and it is difficult to measure it with CPD measurements, as for PCBM no closed layers, which would be necessary for CPD, could be achieved. However, the C_{60} molecule, which determines the properties of PCBM, has a Fermi level of about 4.5 eV [Ge07, Ish05]. Thus, also for PCBM/Si-nc interfaces only a negligible shift of the PCBM energy levels is expected either with Fermi level alignment or by pinning of the Fermi level at the dangling bonds of silicon. For these reasons, the energy levels are plotted relative to the vacuum level without any further corrections.

As can be seen from Figure 5.12, the LUMO of P3HT lies clearly above the conduction band of silicon, enabling dissociation of excitons followed by an electron transfer to the silicon conduction band. However, regarding the relative positions the HOMO of P3HT and the valence band of silicon, it is *a priori* not clear if a hole transfer from the silicon valence band to the HOMO of P3HT can take place. This is mainly due to the different literature values found for

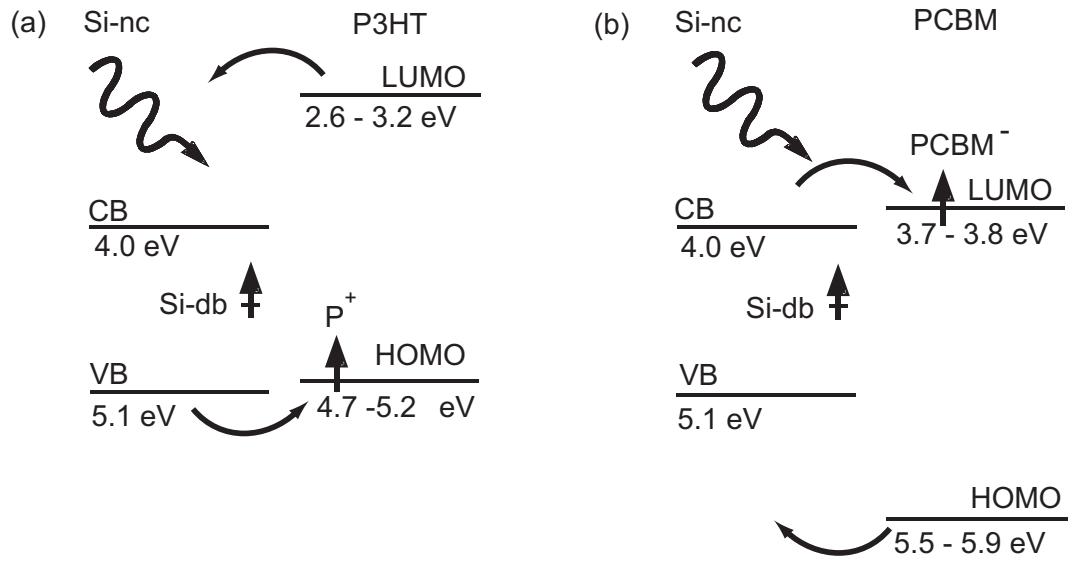

Figure 5.12: *Schematic view of the energy levels of (a) silicon nanocrystal and P3HT and of (b) silicon nanocrystal and PCBM heterojunctions. The curved arrows indicate the possible transfer directions of electrons and holes. The vertical arrows illustrate the detected paramagnetic states.*

the HOMO of P3HT, ranging from 4.7 eV to 5.2 eV, and further possible influences on the band alignment, *e.g.* interface dipoles (see Subsection 2.2.3) and the already discussed Fermi level alignment and pinning at the silicon dangling bonds.

For the explanation of the photo-generation of the P^+ in the P3HT/Si-nc system, one can consider different scenarios which are schematically drawn in Figure 5.13: (1) After the light-induced generation of excitons in P3HT, the excitons dissociate by electron transfer to the silicon nanocrystals, while the holes remain in the P3HT. (2) Alternatively, an energy transfer might occur, whereby excitons are transferred from P3HT to the silicon nanocrystals, followed by a back transfer of the holes, as described for heterojunctions made of P3HT and amorphous silicon [Gow06]. (3) A third possibility is that, after light absorption in the silicon, the holes are transferred from the silicon nanocrystals to the P3HT. (4) A fourth process, the direct excitation of electrons from the HOMO of P3HT into the conduction band of the silicon nanocrystals, could also occur, as a similar process has already been observed for pure organic bulk heterojunctions [Kon05]. In any case, for all the processes described here it is required that the HOMO of P3HT lies energetically above the silicon valence band. As we indeed do detect light-induced P^+ in the P3HT, we can conclude that this requirement is fulfilled, which is a prerequisite for solar cells based on P3HT and silicon nanocrystals. The alignment of the energy levels in hybrid heterojunctions with silicon and P3HT will be further investigated in Section 6.1, where heterojunctions made of crystalline silicon and P3HT are analyzed.

The analogous argument holds for the alignment of the LUMO ($3.7 - 3.8$ eV) of PCBM and the conduction band of silicon in Figure 5.12 (b), where we detect $PCBM^-$ anions in the

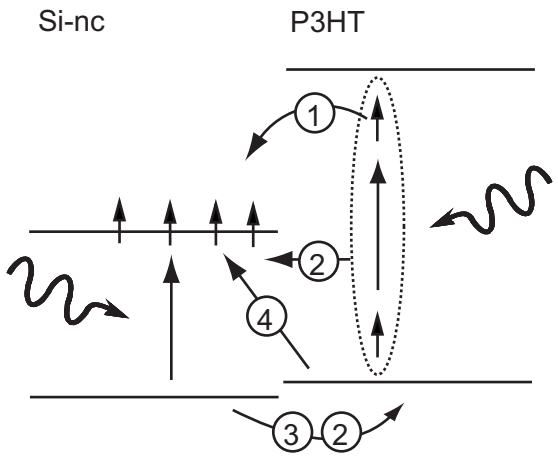

Figure 5.13: *Schematic view of the possible processes from which the detected photo-induced charge transfer could follow. The different processes (1-4) are explained in the text.*

PCBM/Si-nc composite during illumination. Thus, the LUMO of PCBM must be energetically lower than the silicon conduction band, allowing a transfer of electrons from the silicon conduction band to the LUMO of PCBM. This means that the PCBM energy levels are shifted downwards relative to the silicon bands. Despite the fact that PCBM, in contrast to P3HT, is not such a good absorber for the solar spectrum, the PCBM/Si-nc material combination could in principle be used for solar cell applications as well. However, when comparing the density of photo-induced states in Table 5.1, the charge transfer efficiency is higher in the P3HT/Si-nc sample as compared with the PCBM/Si-nc sample, making P3HT/Si-nc composites a promising system for hybrid solar cells, which will be investigated in the next Section 5.3.

5.2.2 Further measurements on composites with silicon nanocrystals and P3HT

As already demonstrated in the last Subsection 5.2.1 a photo-induced charge transfer in bulk heterojunctions made of silicon nanocrystals and PCBM or P3HT can be observed via LESR measurements under white light illumination. As the P3HT/Si-nc system is the more efficient system, which also has the higher absorption coefficient in the region of the solar spectrum, further investigations will concentrate an this system. Consequently, in this subsection the photo-induced charge transfer in the P3HT/Si-nc will be further investigated via room temperature LESR measurements, the comparison with SiO_2 nanoparticles, and wavelength- and time-dependent LESR measurements.

Room temperature light-induced electron spin resonance measurements

As already mentioned, the $PCBM^-$ signal could only be measured at low temperatures, while the P^+ signal was also observed at room temperature. This is due to the higher relaxation rate of fullerene anions, as compared to P^+, which is an intrinsic property of fullerenes [Dya99, Kon05]. For P3HT the room temperature measurements are shown in Figure 5.14, where the ESR (solid line) and LESR (dash-dotted line) of (a) a P3HT/Si-nc composite sample and (b) of a pure P3HT sample are shown. The samples are prepared from the same silicon nanocrystals

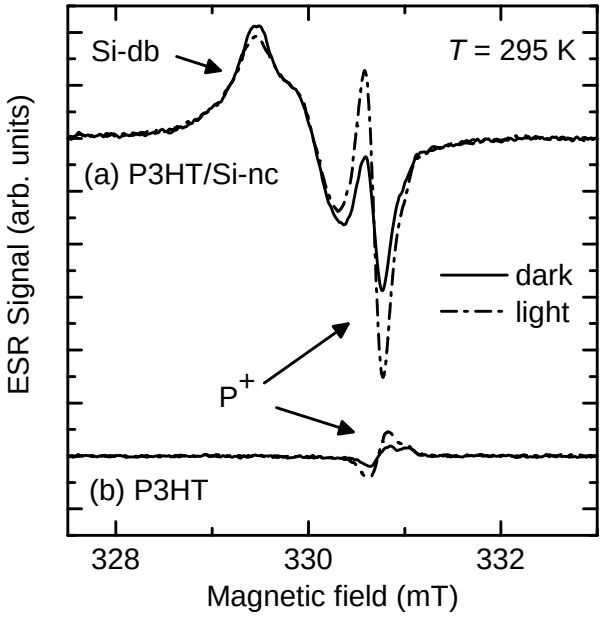

Figure 5.14: *ESR (solid line) and LESR (dash-dotted line) spectra of a P3HT/Si-nc composite (a) and a pure P3HT sample (b) at room temperature.*

as used for the measurements in Figure 5.10 (nanocrystal sample 100506) and show the resonance of silicon dangling bonds at $g = 2.0060$ and of P^+ at $g = 2.0021$. The P^+ signal of the composite sample increases upon illumination from 4.7×10^{16} g^{-1} to 1.3×10^{17} g^{-1}, exhibiting a similar increase as for the measurement at 5 K. Also the value of the pure P3HT sample, which increases from 1.1×10^{16} g^{-1} to 2.1×10^{16} g^{-1} upon illumination, exhibits a similar value as at 5 K. The spectra of the silicon dangling bonds show a slightly different structure, which may be due to different contributions of the different dangling bonds. As mentioned above, only a slight compensation effect of the silicon dangling bonds at room temperature is observed due to a faster recombination, as also observed in pure silicon nanocrystal samples at room temperature.

Sample	ESR density (g^{-1})	LESR density (g^{-1})	LESR-ESR density (g^{-1})
P3HT	1.1×10^{16}	2.1×10^{16}	1.0×10^{16}
P3HT/SiO_2-np	8.42×10^{17}	8.57×10^{17}	1.5×10^{16}
P3HT/Si-nc	4.7×10^{16}	1.27×10^{17}	8.0×10^{16}

Table 5.2: *Overview of the P^+ ESR, LESR, and LESR-ESR spin densities for a pure P3HT, a P3HT/SiO_2-np, and a P3HT/Si-nc sample at 295 K. For the LESR measurements the samples were illuminated with white light.*

Composites of P3HT with SiO_2 nanoparticles

The smaller order of the P3HT in composite samples with silicon nanocrystals has already been discussed above. The increase of the dark ESR signal of P^+ defect states by a factor of 2.5 supports this finding. However, the question arises if the LESR measurements on P3HT/Si-nc samples only exhibit such high P^+ densities due to defects which are generated by the silicon nanocrystals and which are only occupied and visible upon illumination. This would mean that the large LESR P^+ densities are only due to the reduced order and the additional defects of the P3HT, instead of a charge transfer between the P3HT and the silicon nanocrystals. To address this issue, P3HT was also mixed with isolating SiO_2 nanoparticles (SiO_2-np) in order to enhance the defect density without the possibility of a charge transfer. Thus, the P^+ densities of a pure P3HT and of a P3HT/Si-nc sample were compared with the P^+ density of a sample which was made of P3HT and SiO_2 nanoparticles. Thereby, the mixing procedure was exactly the same for the undoped silicon nanocrystals with a diameter of 33 nm and for the SiO_2 nanoparticles (purchased from Sigma-Aldrich) with a diameter of about $10-20$ nm. The results are shown in Table 5.2, where the P^+ ESR, LESR, and LESR-ESR spin densities for a pure P3HT, a P3HT/SiO_2-np, and a P3HT/Si-nc sample at 295 K are summarized. The LESR-ESR spin density is the difference between the LESR and the ESR spin density and is a valuable parameter to quantify the additional spins created under illumination. For the LESR measurements the samples were illuminated with white light. The data for the pure P3HT and the P3HT/Si-nc sample are taken from the previous measurements in Figure 5.14 at 295 K. As already stated, in dark ESR measurements the P^+ density in the P3HT/Si-nc sample is already higher than in the pure P3HT sample. However, upon illumination, a stronger increase is observed in the P3HT/Si-nc sample, as compared to the pure P3HT sample. This can directly be compared in the last row of Table 5.2, where the LESR-ESR spin density is listed. The P3HT/SiO_2-np sample, in contrast, already exhibits a much higher ESR signal which has about the same value as the LESR signal. The reason for the higher P^+ densities in the P3HT/SiO_2-np sample, as compared with the P3HT/Si-nc sample, is unclear. Maybe a chemical reaction takes place between the P3HT and oxygen, which may be located on the surface of the SiO_2 nanoparticles, or also between P3HT and other molecules, which may origin from a chemical contamination during the production

Illumination	Si-db: LESR-ESR density (g^{-1})	P^+: LESR-ESR density (g^{-1})
White light	6.4×10^{17}	3.4×10^{15}
810 nm	1.3×10^{17}	5.9×10^{14}
525 nm	8.5×10^{16}	1.2×10^{15}

Table 5.3: *Overview of the Si-db and P^+ LESR-ESR spin densities for a P3HT/Si-nc sample at 5 K. For LESR measurements the samples were illuminated with white light or with LEDs with wavelengths of 810 nm and 525 nm.*

process. However, the LESR-ESR spin density of the P3HT/SiO_2-np sample is only about 2 % of the corresponding ESR signal and is about half an order of magnitude smaller than the LESR-ESR spin density in the P3HT/Si-nc sample. Hence, we can conclude that the disorder in the P3HT due to the mixing with nanoparticles is not the reason for the observed enhancement of the P^+ LESR density in the P3HT/Si-nc sample, but that the silicon nanocrystals are essential for the P^+ enhancement which is due to a photo-induced charge transfer.

Wavelength-dependent electron spin resonance measurements of composites with silicon nanocrystals and P3HT

In Table 5.3 the LESR-ESR densities between the LESR and the ESR signals of both, the P^+ and the Si-db of a P3HT/Si-nc sample, are listed for different wavelengths. The same silicon nanocrystals (nanocrystal sample 100506) as in the previous sections were used. The LESR-ESR densities under white light illumination were obtained using a 150 W halogen lamp with a cold light filter, which only transmits light between 340 and 680 nm. Furthermore, the LESR-ESR densities were measured during illumination of the sample with LEDs with wavelengths of 810 nm and 525 nm. All measurements were performed at 5 K for a better signal-to-noise ratio. The wavelengths of the LEDs were chosen in such a way that they allow a predominant excitation in only one of the two materials. At a wavelength of 810 nm only the silicon nanocrystals absorb, while when illuminating the sample with a wavelength of 525 nm both materials absorb photons, with P3HT being the dominant component (see Figure 5.1). As with an excitation wavelength of 810 nm P^+ are generated, this is a clear indication that the silicon nanocrystals act as hole donors after photo-induced charge carrier generation in the silicon nanocrystals. This means that for holes in the silicon nanocrystals the HOMO of the P3HT must be energetically favorable and a hole transfer from the silicon nanocrystals to the P3HT takes place as indicated in Figure 5.11. From this finding, one can also conclude that an exciton in the P3HT can split up via an electron transfer to the silicon nanocrystals, as the hole will stay on the P3HT due to the band alignment.

When probing the P^+ LESR-ESR density under the illumination by the 525 nm LED, which has the same power of 35 mW as the 810 nm LED, the P^+ LESR-ESR density increases by a factor

of 2 compared to the illumination by the 810 nm LED. This increase can only result from the additional absorption in P3HT, where the P3HT acts as an electron donor. Hence, both materials, silicon nanocrystals and P3HT, contribute to the photo-generated charge separation. When, in addition, the absorption coefficients of silicon nanocrystals and P3HT at 525 nm in Figure 5.1 are compared, one finds that the P3HT absorption is about a factor of 3 higher than the silicon nanocrystal absorption. Furthermore, at 525 nm the total number of photons is lower than at 810 nm as the two LEDs have the same intensity but different photon energies, but the overall P^+ LESR-ESR density is higher at 525 nm. Thus, one can conclude that P3HT is responsible for the larger part of the LESR signal at 525 nm. This is in accordance with wavelength dependent photocurrent measurements of P3HT/Si-nc bulk heterojunctions (see next Section 5.3), which also show that most of the photo-generated charge carriers at 525 nm result from the P3HT. However, one finds that the overall P^+ LESR-ESR density is much smaller than in the previous experiments. This can be explained by an aging of the sample, which was stored for 4 weeks and does not reach the same P^+ LESR density as directly after its preparation.

Time-dependent electron spin resonance measurements of composites with silicon nanocrystals and P3HT

Furthermore, not only the spectral contribution to the photo-generated charge carriers but also the dynamics of the charge generation and separation of such P3HT/Si-nc heterojunctions is of interest. Via time-dependent LESR measurements one can distinguish between fast charge transfer and slow trapping processes [Hei09]. For this purpose, in Figure 5.15 the time evolution of the ESR and LESR signal of P^+ was measured over a period of 4 minutes for P3HT (dashed line), P3HT/PCBM (dotted line) and P3HT/Si-nc (solid line) samples. The measurements were performed at room temperature, as at low temperatures persistent photo-induced states would make the observation of larger timescales in the order of hours necessary and the change of the silicon dangling bond density would overlap with the P^+ signal which we want to observe. The measurements start in the dark, then white light is switched on (one asterisk), off (two asterisks) and on again. The three spectra are normalized to each other with respect to the P^+ value at about 120s, before the light was switched off, for a better comparison of the time evolution. Furthermore, the dark ESR signal level is indicated by a dash-dotted line for each sample. The silicon nanocrystals for this experiment were undoped and had a mean diameter of 21 nm (nanocrystal sample 100406).

The pure P3HT sample (dashed line) shows a qualitative different time evolution compared to the P3HT/PCBM (dotted line) and the P3HT/Si-nc sample (solid line). While in the mixed samples, a strong increase upon illumination can be seen, in the P3HT only a slow increase upon illumination and, in addition, nearly no decrease after switching off the light can be observed. This can be explained by slow trapping and recombination processes of charge carriers in traps

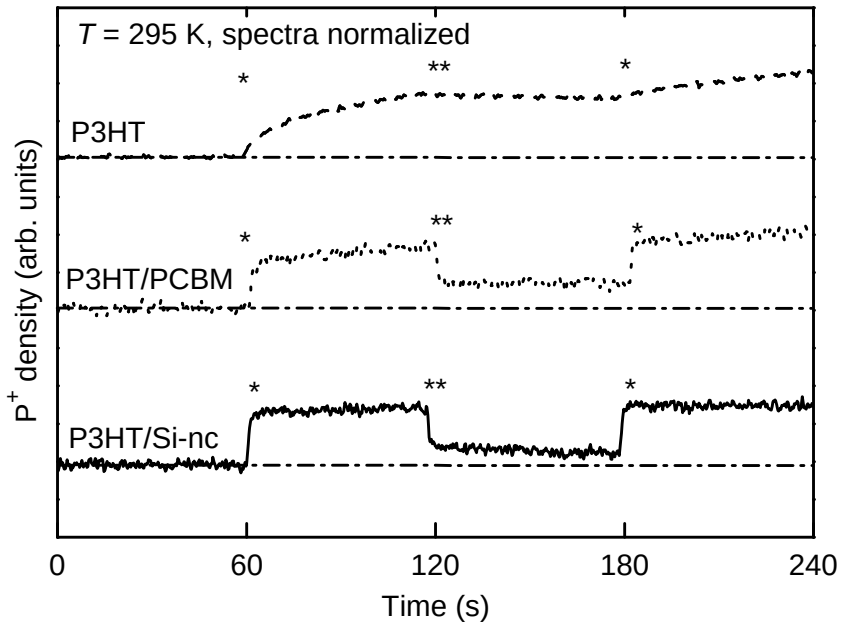

Figure 5.15: *Time-dependent measurements of the P^+ resonance of a P3HT (dashed line), a P3HT/PCBM (dotted line) and a P3HT/Si-nc (solid line) sample. The illumination is switched on at * and switched off at **. The three spectra are normalized to each other with respect to the P^+ value at about 120s, before the light was switched off, and the dark ESR signal levels are indicated by the dash-dotted lines.*

of the P3HT, as in P3HT the only possibility for a dissociation of a photo-generated exciton is a trap [Hei09]. In contrast, the kinetics in the mixed samples exhibit a fast (< 1 s) rise and decay of the P^+ density which, hence, does not come from trap states in the P3HT. Such a behavior accounts for the charge transfer and generation at the interface between two materials and for the generation of mobile charge carriers [Hei09]. The separated charge carriers can recombine via diffusion controlled bimolecular recombination, the so called Langevin recombination [Pop99], and are not limited by the slow recombination from trapped charge carriers [Dya99]. Remarkably, the P3HT/Si-nc sample exhibits similar fast kinetics as the P3HT/PCBM sample, which is a promising result for possible P3HT/Si-nc solar cells.

The results on the time dependence of the LESR signal is in accordance with the findings in Subsection 5.2.1. There, it was described that the light-induced P^+ signal is persistent over hours at 5 K and only vanished on a short timescale by heating up the sample to room temperature, whereas the P^+ signal for mixed samples decreases without illumination as shown in Figure 5.15. The removal of persistent spins due to thermal annealing up to room temperature has already been described in the literature in conjugated polymer/fullerene composites [Dya99]. The slow recombination of the trapped persistent spins at low temperatures can be explained by non-geminate recombination of randomly distributed carriers, similar to amorphous silicon [Sch01]. In addition, the vanishing of the LESR signal at higher temperatures also demonstrates

the reversibility of the photo-induced electron transfer, and one can rule out permanent spins from photochemical reaction products [Sar92].

Light-induced electron spin resonance measurements of composites with HF-etched silicon nanocrystals and P3HT

To investigate the role of the oxide shell of the silicon nanocrystals LESR experiments were performed on P3HT/Si-nc composites with HF-etched silicon nanocrystals. However, the P^+ LESR signal that was observed with the HF-etched silicon nanocrystal is of the order of the P^+ LESR signal in composite samples with as-received nanocrystals. This observation may be explained by a minor influence of the natural oxide of the silicon nanocrystals on the charge transfer. As the oxide is not perfect and the silicon nanocrystals exhibit still some H-termination [Bau06b], a diffusion on the nanometer scale may be enough for the excitons in the P3HT to reach surfaces areas of the silicon nanocrystals with a leaky oxide to dissociate. However, in electrically detected magnetic resonance (EDMR), which will be described in Subsection 5.2.3, and in current-voltage characteristics it is observed that the conductivity of the etched silicon nanocrystal layers increases. Nevertheless, in pure silicon nanocrystal layers, the interface area where two silicon nanocrystals are in contact is much smaller than in hybrid composites where the P3HT covers the whole nanocrystal. Thus, a leaky oxide may lead to large barriers at the contact points of two silicon nanocrystals but not at the P3HT/Si-nc interface. Another possibility would be that the HF-etched silicon nanocrystals do indeed have better charge transfer properties, which are outweighed by a different morphology, where the overall interface between P3HT and the silicon nanocrystals is smaller. However, in Figure 5.4, where the morphology of P3HT/Si-nc composites with as-received (a) and with etched (b) silicon nanocrystals is compared, no large difference could be observed. Nevertheless, the possibility of a different morphology cannot be excluded, as the SEM micrograph only allows conclusions down to a length scale of about 100 nm. Furthermore, the SEM images were taken directly at the breaking edge of the sample, which may not exactly present the bulk properties, as the cross section surface is not flat but most probable build up along an internal P3HT/Si-nc junction.

5.2.3 Electrically detected magnetic resonance measurements

To clarify the contribution of the P3HT and the silicon nanocrystals to the charge transport, EDMR is a promising tool. EDMR was already applied in semiconducting polymer [Swa92] and silicon nanocrystal [Ste08] layers to investigate the charge transport. With the EDMR technique, spin-dependent changes in the current can be detected and paramagnetic states, which are involved in the electronic transport, can be identified. For the detection of a spin-dependent change in the current, a certain current level is necessary. This current level is not achieved with

undoped silicon nanocrystals, thus for this experiment phosphorus doped silicon nanocrystals were used, as in Reference [Ste08]. The silicon nanocrystals had a diameter of 23 nm and were doped up to 6.5×10^{19} cm^{-3} with phosphorus donors (nanocrystal sample 040407). For a further enhancement of the conductivity, all samples were illuminated with white light during the EDMR measurements, which leads to a noticeable photocurrent.

In EDMR experiments on phosphorus-doped silicon nanocrystals, the contribution of the silicon dangling bonds at a *g*-value of about 2.006 and a much weaker contribution of the phosphorus donors can be detected [Ste08]. The main paramagnetic state observed in the EDMR signal, the silicon dangling bonds, is the same as in conventional ESR and can be assigned to the silicon dangling bonds which are involved in the electronic transport. It has been shown that the observed spin resonances lead to a quenching of the photocurrent under illumination, which means that the paramagnetic states are centers for spin-dependent recombination of photogenerated charge carriers [Ste08]. While to our knowledge EDMR experiments on P3HT have not yet been made, on a similar π-conjugated system, the poly(para-phenylenevinylene) (PPV), the EDMR signal could be measured and assigned to the paramagnetic positive polarons [Swa92, Dya97]. In the EDMR measurements we have performed on pure P3HT also paramagnetic states, the P^+, which before have been observed only in ESR measurements, could be detected. Hence, the P^+ states, which are responsible for the charge transport in the P3HT, are also responsible for a spin-dependent current change. The typically observed current change is a decrease of the photocurrent, which is due to a spin-dependent change in the recombination rate and also due to the spin-dependent formation of bipolarons from two polarons, where the bipolarons have a lower mobility than polarons [Swa92, Cas04]. In Figure 5.16, the EDMR spectra of two P3HT/Si-nc samples are shown. Here, the sample of the upper spectra was prepared with as-received silicon nanocrystals and sample of the lower spectra with HF-etched silicon nanocrystals. The upper and the lower spectra are normalized to the same P^+ signal height for a better comparison. The phase shifts α (red line) and β (black line) between the lock-in reference and the EDMR signal were chosen to obtain a maximum signal for the contribution of the P^+ and the silicon dangling bonds, respectively. The etching of the silicon nanocrystals in the lower spectra has been performed to probe the influence of the oxide shell on the charge transport. In EDMR experiments with pure silicon nanocrystal layers, it has already been observed that the signal-to-noise ratio is strongly enhanced upon HF-etching [Ste08].

In the case of P3HT/Si-nc with as-received silicon nanocrystals, a large EDMR signal with a *g*-value of 2.002 can be assigned to the P^+, while only a small contribution of the silicon dangling bonds with a *g*-value of 2.006 can be measured. Thus, most of the detected resonant current change takes place under the participation of P^+, and only a small fraction is due to the silicon dangling bonds. When using HF-etched silicon nanocrystals for the P3HT/Si-nc sample, the EDMR signal of the silicon dangling bonds and the P^+ signal amplitudes have the same values. Thus, the contribution of the silicon dangling bonds to the resonant current change has strongly

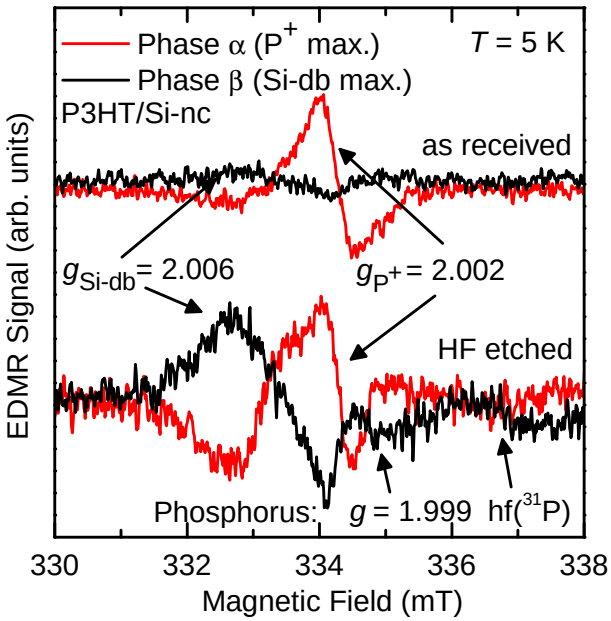

Figure 5.16: *EDMR spectra of P3HT/Si-nc layers with as-received silicon nanocrystals (upper spectra) and HF-etched silicon nanocrystals (lower spectra). The phase shifts α (red line) and β (black line) between the lock-in reference and the signal were chosen to obtain a maximum signal for the P^+ and the silicon dangling-bond resonances, respectively. For a better comparison the spectra of the two samples were normalized to the P^+ signal. The silicon nanocrystals had a mean diameter of 23 nm and were doped up to 6.5×10^{19} cm^{-3} with phosphorus donors.*

increased. Furthermore, additional phosphorus-related EDMR signatures can also be observed due to the better signal-to-noise ratio of the silicon dangling bond signal. The first observed feature is a peak with a g-value of about 1.999, which can be attributed to clusters of two or more closely spaced phosphorus donors or free electrons in silicon [Cul75]. The second feature is a broad peak, denoted hf(^{31}P), which is the observed line of the typical hyperfine signature of substitutional phosphorus in crystalline silicon, where the Zeeman states of the donor electron are split by interaction with the ^{31}P nucleus [Cul75]. The low field partner line of the hf(^{31}P) resonance is not observed due to the overlap with the stronger band of the silicon dangling bonds.

First of all, the EDMR spectra show that the current transport takes place in both, the P3HT and the silicon nanocrystals. This means that both materials are electronically active in the mixed layers, which is an important finding and relevant for applications in solar cells. In the next Section 5.3, the contribution of the two components in P3HT/Si-nc solar cells will be demonstrated via spectrally resolved photocurrent measurements, which supports the results of the EDMR measurements. Additionally, when comparing the spectra of the two P3HT/Si-nc samples, the contribution of the silicon dangling bonds to the spin-dependent current change relative to the P^+-induced current change is higher in the sample with the etched silicon nanocrystals.

Hence, the current paths through the etched silicon nanocrystals have increased compared to the as-received sample. This is in accordance with the finding that the conductivity of silicon nanocrystal layers increases after HF etching, as the oxide is removed [Per07, Lec08a]. The change in the transport paths due to the etched silicon nanocrystals has also a strong influence on the current-voltage characteristics of solar cells with etched silicon nanocrystals, as will be shown in the next Section 5.3, where an increase of the short-circuit current of P3HT/Si-nc solar cells is found with etched silicon nanocrystals.

5.3 Hybrid bulk heterojunction solar cells with P3HT and silicon nanocrystals

The photo-induced charge transfer between organic semiconductors and the silicon nanocrystals has been demonstrated by LESR measurements. Now, the next step is the realization of solar cells with these materials. As already mentioned, the absorption of P3HT has a larger overlap with the solar spectrum as PCBM and also the photo-induced charge transfer in hybrid composites with P3HT, as determined by LESR, is more efficient than in composites with PCBM. Thus, for solar cell applications we will concentrate on bulk heterojunctions with P3HT and silicon nanocrystals.

5.3.1 Band scheme of solar cells made of P3HT and silicon nanocrystals

We first consider the band scheme of P3HT/Si-nc heterojunctions to get an idea of the charge separation and transport in such solar cells. The processes involved and the relative position of the energy levels directly at the interface of P3HT and the silicon nanocrystals have already been shown in Figure 5.12 (a). For a solar cell, contacts on both materials have to be added. As described in Subsection 4.1.1, aluminum and ITO were used as contact materials for the bulk heterojunction due to their appropriate work functions. Here, via the aluminum contact electrons from the silicon nanocrystals can be extracted, while via the ITO contact holes from the P3HT can be extracted. Due to the small energetic difference between the work functions of the metals and the energy levels of the semiconductors, the energy losses at the metal/semiconductor junctions should be small. In addition, analogous to organic solar cells, due to the difference in the work functions of the contacts, this combination provides an electric field over the active layer when the contacts are connected [Bra01b]. The electric field leads to a more efficient extraction of the charge carriers via a drift current instead of a pure diffusion current [Hop04b]. In Figure 5.17 the complete band scheme is shown, where the energy level values of the materials are taken without any further corrections due to possible interface dipoles or

pinning. Furthermore, the expected charge generation and transport mechanisms are plotted under open-circuit conditions.

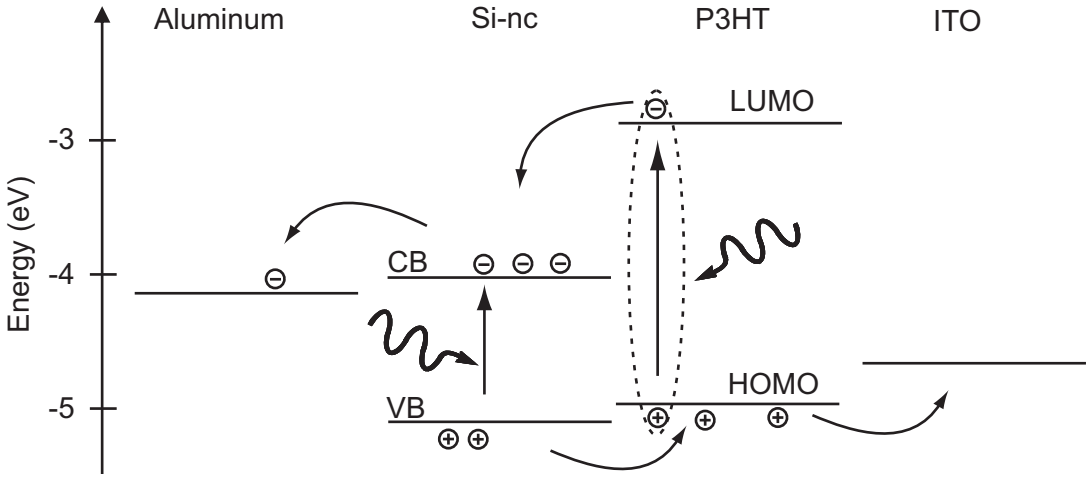

Figure 5.17: *Band scheme and electronic processes of a P3HT/Si-nc bulk heterojunction solar cell under open-circuit conditions.*

5.3.2 Electrical characterization of hybrid solar cells

Bulk heterojunction solar cell with silicon nanocrystals and P3HT

The most efficient hybrid solar cells do use bulk heterojunctions [Gue08]. This has also been observed in our own experiments, which show that bilayer heterojunctions have a smaller photovoltaic effect than bulk heterojunctions (see Subsection 5.4.2). Hence, in this section we will discuss bulk heterojunctions which are fabricated by spin-coating. We investigate both, either only one composite layer or different layers with varying compositions on top of each other to achieve a gradient structure. For the active layers, the composition will be given by a certain weight ratio X:Y, where X is the P3HT and Y the silicon nanocrystal part. For gradient structures, several layers such as X1:Y1, X2:Y2, *etc*. are spin-coated on top of each other, where the layer X1:Y1 is always on the ITO side. There are several advantages of the gradient structure: Firstly, short-circuits could be minimized due to the deposition of several layers. Secondly, in that way a pure P3HT layer is deposited on the ITO contact and a pure silicon nanocrystal layer is deposited on the aluminum side acting as barrier for the "wrong" charge carrier type. This means that, *e.g*. electrons can only be extracted from the active layer via the silicon layer and thus are hindered to diffuse to the ITO side. Furthermore, closed paths for charge extraction could also build up when depositing various layers with different ratios of P3HT and silicon nanocrystals.

The current-voltage characteristics of the P3HT/Si-nc solar cell with the highest measured open-circuit voltage is shown in Figure 5.18 in the dark (solid line) and under illumination with a halogen lamp with an intensity of 100 mW cm^{-2} (dash-dotted line) in a linear (a) and a semilogarithmic plot (b). The solar cell consisted of a ITO-0:1-1:5-5:1-1:0-Al gradient structure. The

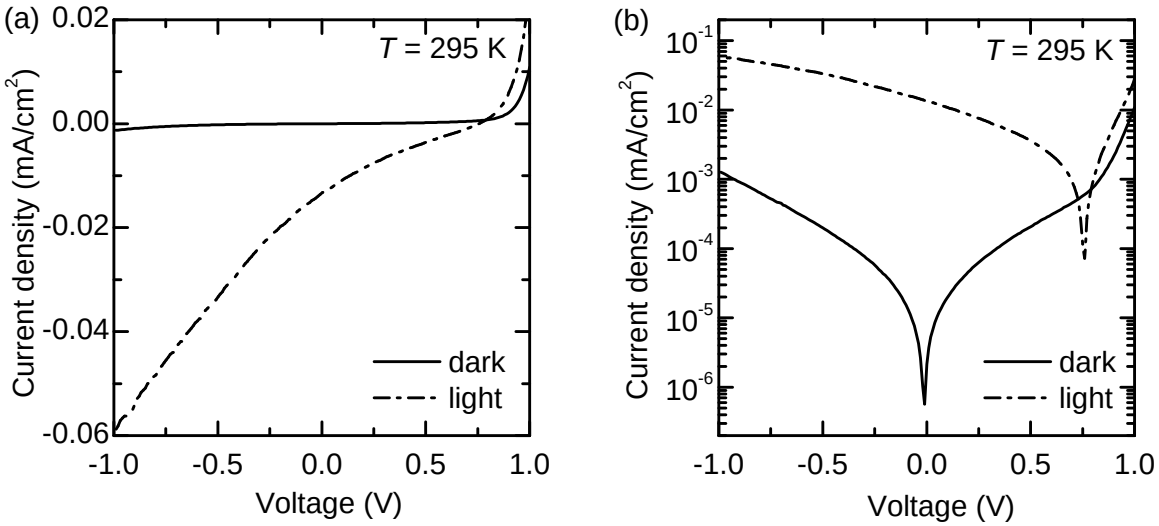

Figure 5.18: *Current-voltage characteristics in the dark (solid line) and under illumination (dash-dotted line) of a P3HT/Si-nc bulk heterojunction solar cell in a linear (a) and a semilogarithmic plot (b). The solar cell is built up from a blend of four spin-coated layers with varying P3HT/Si-nc ratios (0:1-1:5-5:1-1:0).*

silicon nanocrystals have a phosphorus doping concentration of 6.5×10^{19} cm^{-3} and a diameter of about 18 nm (nanocrystal sample 270307). This layer sequence with the silicon nanocrystals deposited directly on the ITO is in contrast to the gradient structure and the band scheme as proposed above. The reason for this will be discussed later. However, the diode direction is as expected from the band scheme in Figure 5.17: In the forward direction, where a positive bias is applied to the ITO, electrons are extracted at the ITO side, while the photogenerated electrons contribute to the reverse current and are extracted via the aluminum contact. Also in further current-voltage measurements, a positive bias always means that a positive bias is applied to the ITO contact.

Under illumination the current-voltage characteristics displays a large open-circuit voltage of 0.76 V and a short-circuit current density of 1.3×10^{-2} mA cm^{-2}. The photocurrent at -1 V is about 1.5 orders of magnitude higher than the dark current. The efficiency of the solar cell is only 0.0020 % which needs to be optimized, as the short-circuit current and also the fill factor of 0.20 are quite low. The low efficiency is probably due to the large amount of defects located at the silicon nanocrystal surface which act as recombination centers. The oxide layer of the silicon nanocrystals may be a further problem which will be discussed later on in this subsection. Furthermore, trapping of charge carriers in the active layer may be a problem. This

trapping is indicated by the voltage dependent photocurrent, where the photo-induced charge carriers are only released when the applied reverse electric field is increased.

Contributions of the P3HT and of the silicon nanocrystals to the solar cell

To investigate the contribution of the P3HT to the P3HT/Si-nc solar cells, a pure P3HT layer, which was sandwiched between an ITO and an aluminum layer, was fabricated. The current-voltage characteristics of such a structure is shown in Figure 5.19 in the dark (solid line) and under illumination (dash-dotted line) in a linear (a) and a semilogarithmic plot (b). Under illumination the structure exhibits an open-circuit voltage of 0.21 V and a short-circuit current density of 9.9×10^{-3} mA/cm^2. With the fill factor of 0.36 and the light intensity of 100 mW/cm^2 of the halogen lamp this results in an efficiency of 0.00074 %. The diode behavior of the

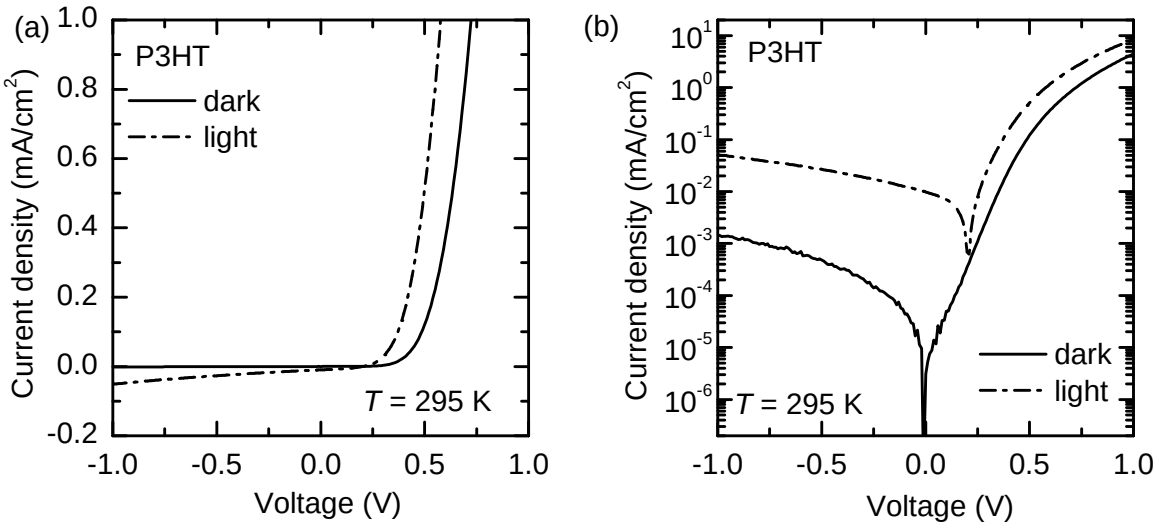

Figure 5.19: *Current-voltage characteristics of a P3HT Schottky solar cell in the dark (solid line) and under illumination (dash-dotted line) in a linear (a) and a semilogarithmic plot (b).*

P3HT can be explained by a Schottky contact: While the ITO/P3HT contact is ohmic, as the HOMO level at about 4.9 eV (see Chapter 3) is close to the ITO work function of 4.75 eV [Kim98], a Schottky contact is established between the aluminum with a work function of about 4.3 eV [Sze07] and the HOMO of P3HT. This is due to the fact that the Fermi level of the P3HT energetically lies below the work function of the aluminum and thus electrons are transferred to the P3HT until the Fermi levels align and a space-charge region in the P3HT has built up (see Subsection 2.2.2). The Schottky contact is a barrier for photo-induced holes from the P3HT, which now are extracted from the P3HT via the ITO contact. Schottky barriers at the P3HT/aluminum interface have also been reported in the literature [Mus98, Llo01]. A similar experiment with only a silicon nanocrystal layer between the metal contacts could not be realized due to short-circuits in the nanocrystal layer.

For the P3HT/Si-nc solar cells, one could thus argue that the photovoltaic effect originates only from a Schottky contact with P3HT and that the silicon nanocrystals do not contribute to the solar cell at all. However, two measurements prove that this is not the case and that the silicon solar cells indeed do contribute to the solar cell. Firstly, the measurements of reference structures with only P3HT as the active layer, as shown in Figure 5.19, exhibit a typical open-circuit voltage of $0.2-0.4$ V, which differs significantly from the observed open-circuit voltage in P3HT/Si-nc composites. Secondly, in wavelength-dependent photocurrent measurements a contribution of the silicon nanocrystals to the photocurrent of the P3HT/Si-nc solar cell can be observed. This is shown in Figure 5.20, which displays the photocurrent spectrum of a P3HT/Si-nc solar cell sample (solid line), which is compared to the absorption coefficients of P3HT (dashed line) and of silicon nanocrystals (dotted line). The nanocrystals used for the solar cell have a mean diameter of 18 nm and are phosphorus doped with 1.6×10^{19} cm^{-3}. The

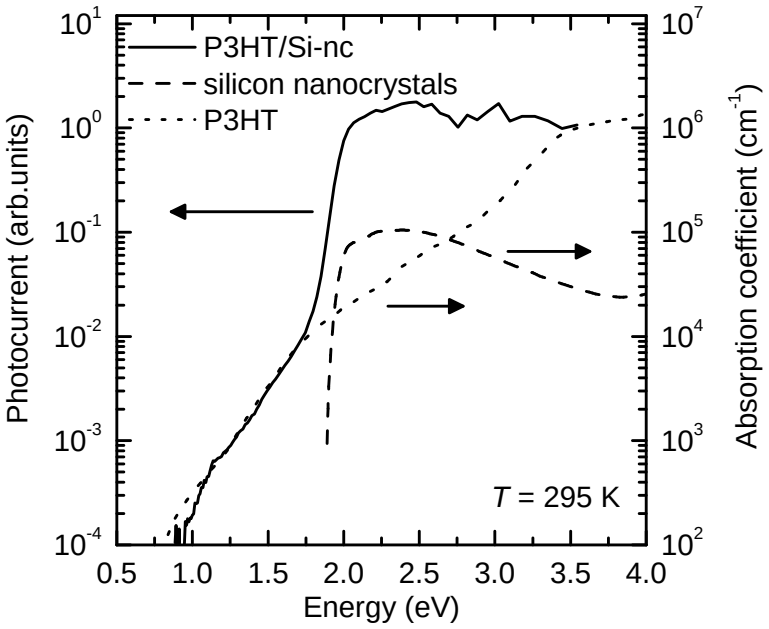

Figure 5.20: *Photocurrent spectrum (solid line) of a P3HT/Si-nc bulk heterojunction solar cell with a blend of four spin-coated layers with changing P3HT/Si-nc ratio (0:1-1:5-5:1-1:0) in comparison to the absorption coefficients of P3HT (dashed line) and of silicon nanocrystals (dotted line) recorded at 295 K and a bias of -0.75 V.*

photocurrent spectrum was recorded in vacuum at a reverse bias of -0.75 V and was normalized to the incident number of photons. The absorption spectra were calculated from optical transmission and reflection measurements and photothermal deflection spectroscopy (see Chapter 3). P3HT does not absorb in the infrared spectral region, where the solar spectrum still has a high intensity. There the silicon nanocrystals absorb, which additionally have a higher absorption coefficient as compared to bulk crystalline silicon due to the defect states, similar to microcrystalline silicon [Lec08a]. The photocurrent spectrum shows a detectable signal down

to 0.9 eV which is consistent with the absorption edge of the silicon nanocrystals and far below the onset of the absorption of P3HT. At the absorption edge of P3HT, the photocurrent strongly increases by about two orders of magnitude and saturates at higher photon energies. Yet, the absorption coefficient of P3HT is roughly one order of magnitude higher than the absorption coefficient of the silicon nanocrystals at the absorption edge of P3HT. This strong increase of the photocurrent in the absorption range of the P3HT is a further indication, in addition to the wavelength-dependent LESR measurements of Subsection 5.2.2, that P3HT is the dominant component in the active layer. Nevertheless, we observe a noticeable photocurrent signal for photon energies between 0.9 eV and 1.8 eV, where P3HT is transparent. Thus, photons in this energy range have to be absorbed in the silicon nanocrystals and the generated electron-hole pairs are separated and contribute to the photocurrent. Consequently, the photocurrent measurement is a clear indication that the silicon nanocrystals contribute to an additional current in the infrared spectral region and, most probably, in the entire spectral range of P3HT/Si-nc solar cells.

Composition of the active layer

To investigate the influence of the active layer composition on the solar cell, several gradient structures with different layer sequences have been produced. First of all, only active layers with a "wrong" layer sequence, where the silicon-rich region is near the ITO contact instead of the aluminum contact as expected from the band scheme in Figure 5.17, show photovoltaic properties as *e.g.* the solar cell in Figure 5.18. Here, a "wrong" layer sequence means that the silicon nanocrystals are spin-coated on the ITO and covered afterwards with the P3HT and an aluminum layer. Such an active layer is in contrast to the ideal band scheme, as proposed in Figure 5.17. However, devices where the P3HT layer is spin-coated as the first layer on the ITO followed by a silicon nanocrystal layer to obtain an ideal band structure only exhibit short-circuits.

Such a behavior can be explained by the observation that the different layers dissolve each other and are mixed with the other layers. In Figure 5.21, SEM images of cross sections of an ITO-0:1-1:5-5:1-1:0-Al sample in different magnifications are shown. Here only one layer can be identified, thus one can conclude that the different layers mix completely during subsequent spin-coating.

From this finding it is obvious that no multilayer structure builds up via sequential spin-coating of the active layer. Nevertheless, we will refer to such structures as gradient structures in the following to distinguish between samples fabricated by several spin-coating steps and samples which are produced with only one spin-coated layer. As the mixing of the different layers also takes place when the last spin-coated layer is a silicon nanocrystal layer, it dissolves the

other layers and a silicon-rich active layer is formed. Such a silicon-rich layer has many short-circuits and hence does not work as a solar cell. From this it follows that a P3HT-rich active layer is needed, which forms a closed layer. P3HT-rich layers can either be obtained by first spin-coating a silicon nanocrystal layer followed by a P3HT layer, or by spin-coating only one P3HT-rich solution on the substrate. Furthermore, for working devices, the photo-induced electrons are always extracted via the aluminum side at short-circuit conditions, es expected from the band scheme. This may be explained by the P3HT Schottky diode which dominates the behavior independent of the exact position of the silicon nanocrystals in the device.

From these findings, solar cells with only one spin-coating process should also lead to a similar result, when they are P3HT-rich to avoid short-circuits. And indeed, the best solar cell was a 5:1 ratio sample with undoped silicon particles of an average diameter of 29 nm (nanocrystal sample 250906). It exhibited an open-circuit voltage of 0.72 V, a short-circuit current of 7.7×10^{-2} mA cm^{-2}, and a fill factor of 0.20, which results in an efficiency of 0.011 %. Also for this sample photocurrent measurements have demonstrated that the silicon nanocrystals contribute to the photo-induced current. Such a proof of the contribution of the silicon nanocrystals in P3HT/Si-nc solar cells to the photocurrent, as shown in Figure 5.20, has been demonstrated for the first time, while for P3HT/Si-nc solar cell published by Liu *et al.* the electrical contribution of silicon nanocrystals was not proven [Liu09]. However, the efficiency of the solar cells fabricated in the frame of this thesis is lower than the efficiency of about 1 % for the solar cells in the work of Liu *et al.*. This large difference may be explained by various facts: The silicon nanocrystals used by Liu *et al.* were handled without any contact to air and their solar cells were fabricated with the unoxidized particles directly after the production. Thus, no oxide layer at the surface of the nanocrystals which limits the charge transport is present. Furthermore, for the fabrication of the silicon nanocrystals a different method, the radio frequency plasma synthesis, was used. As the residence time in the reactor is longer than for silicon nanocrystals from the Wiggers group, their nanocrystals have less defects than our material. Hence, mainly the differences in the silicon nanocrystals, which are used for the solar cells, are the reason for the difference in the efficiency. In addition, the solar cell efficiency in their work was determined with a solar spectrum which has a higher light intensity in the absorption range of the active layer than our halogen lamp. Regarding the P3HT used from Liu *et al.*, it was purchased from the same company as the P3HT used in this work. Thus, differences in the P3HT, *e.g.* the regioregularity, are not expected to contribute to the different efficiencies.

For the preparation of real gradient structures, an alternative to the spin-coating process may be the doctor blade technique, as it only dissolves a part of the underlying layers [Bra02]. However, organic two-layer systems with a sharp interface are typically achieved via vacuum deposition of small molecules [Tsu00, Zho01], as also used in organic light-emitting diodes [Brü08a]. Furthermore, a lamination technique, where the second organic layer is laminated on the first layer has been reported as well as the use of orthogonal solvents which do not dissolve each

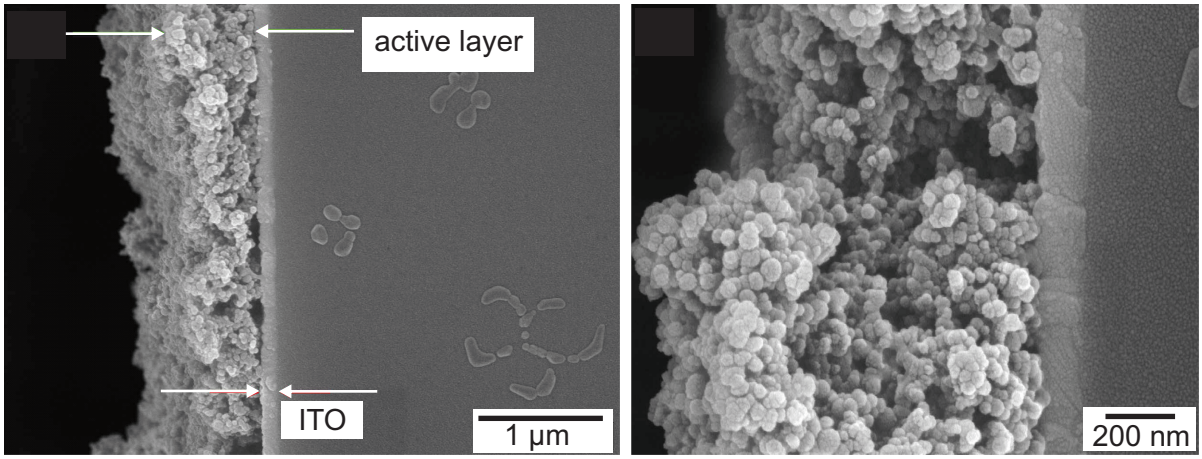

Figure 5.21: *SEM images of an ITO-0:1-1:5-5:1-1:0-Al solar cell sample in different magnifications. No gradient structure is visible in the active layer. The ITO layer on the glass and the active layer are indicated by arrows.*

other [Wie10]. The later technique was also applied in this work, where an additional annealing step was applied between the deposition of the silicon nanocrystals and the P3HT layer, which were deposited from solutions with orthogonal solvents. Via this technique, a bilayer system can be established as will be reported in Subsection 5.4.2. However, such a bilayer system is not an ideal structure due to the small interfacial area and the measured efficiencies are about one order of magnitude lower than those of P3HT/Si-nc bulk heterojunction.

Reproducibility

To get more information about the variations in the current-voltage characteristics between various solar cells, 22 contacts of the same structure on 5 different samples have been characterized. The solar cells were built up from ITO-5:1-Al bulk heterojunctions with silicon nanocrystals of 29 nm diameter and a phosphorus doping concentration of 1.6×10^{19} cm^{-3} (nanocrystal sample 250906). The obtained mean values with the standard deviations for the open-circuit voltage, V_{OC}, the short-circuit current density, J_{SC}, and the efficiency, η, are given in Table 5.4. The fluctuation of the open-circuit voltage is small, while the fluctuation of the short-circuit current density, and accordingly of the efficiency, is much larger. The variations in the short-circuit density may be due to varying layer morphologies. This, in turn, may result from the most critical fabrication step, the spin-coating. There, differences of the active layer morphology mainly due to agglomerates of the silicon nanocrystals may alter the characteristics of the different samples. Furthermore, the aluminum evaporation may also be a step which influences the solar cell behavior. A further investigation of the influence of different parameters on the active layer composition and solar cell behavior will be done in the next subsection.

Value	Mean value	Standard deviation (% of the mean value)
V_{OC}	0.65 V	0.08 V (13 %)
J_{SC}	3.5×10^{-2} mA/cm^2	3.7×10^{-2} mA/cm^2 (107 %)
η	4.4×10^{-3} %	4.5×10^{-3} % (102 %)

Table 5.4: *Mean values and standard deviations for the open-circuit voltage, V_{OC}, the short-circuit current density, J_{SC}, and the efficiency, η, of 22 different contacts on five samples which were produced with exactly the same parameters.*

Doping concentration and size of the silicon nanocrystals

In the solar cells which were discussed until now mostly doped nanocrystals were used. The idea behind this choice was that additional electrons from the phosphorus donors could saturate the silicon dangling bonds which should reduce the recombination in the silicon nanocrystals. Furthermore, if a Fermi level alignment between the silicon nanocrystals and the P3HT is assumed, n-type silicon nanocrystals would lead to favorable energy band alignment as the HOMO of P3HT would lie clearly above the valence band of the silicon nanocrystals. In addition, the conductivity of the nanocrystals can be enhanced, as already observed for pure silicon nanocrystal layers [Lec08a]. To verify if the doping concentration really has an influence on the solar cell performance, a variety of silicon nanocrystals with different doping concentrations was investigated for P3HT/Si-nc solar cells. The nanocrystals also had different sizes, as for different doping levels only nanocrystals with different sizes were available. Functional solar cells which had a high-open-circuit voltage above the open-circuit voltage of P3HT Schottky solar cells have been achieved with four different silicon nanocrystal types: Undoped nanocrystals with a diameter of 16 nm (nanocrystal sample 130506) and three different doped nanocrystals with a doping concentration and size of 1.6×10^{19} cm^{-3} and 29 nm (nanocrystal sample 250906), 5×10^{20} cm^{-3} and 6.1 nm (nanocrystal sample 220807), and 2×10^{20} cm^{-3} and 12 nm (nanocrystal sample 160807) were used. The measured open-circuit voltages were $0.6 - 0.75$ V and the short-circuit current densities were $1 \times 10^{-2} - 8 \times 10^{-2}$ mA cm^{-2} with fill factors of $0.2 - 0.3$. The fluctuations of these values is in the range of the standard deviation as determined for 22 solar cells with the same composition of the active layer as listed in Table 5.4. Thus, a dependence of the efficiency on the doping concentration or the size could not be found within the experimental error.

Influence of the HF etching

As shown in the EDMR experiments in Subsection 5.2.3, the HF etching of the silicon nanocrystals leads to an enhanced spin-dependent current through the nanocrystals in a bulk heterojunction. In addition, it has been observed in pure silicon nanocrystal layers that the conductivity

could be enhanced strongly by HF etching [Lec08a]. To investigate the influence of HF etching on the performance of P3HT/Si-nc solar cells, solar cells with HF etched silicon nanocrystals were made and compared to solar cells with as-received silicon nanocrystals. The nanocrystals were phosphorus-doped with 6.5×10^{19} cm^{-3} and had a diameter of 23 nm (nanocrystal sample 040407). The etching procedure was carried out in diluted HF as described in Subsection 4.1.1. In Figure 5.22, the current-voltage characteristics of two solar cells are shown: The black curves are the current-voltage characteristics of the P3HT/Si-nc sample with the etched nanocrystals in the dark (black solid line) and under illumination (black dash-dotted line), while the red curves correspond to the dark (red solid line) and the illuminated (red dash-dotted line) current-voltage characteristics of the P3HT/Si-nc sample with the untreated nanocrystals. The sample consists of an ITO-0:1-1:5-1:1-5:1-1:0-Al gradient structure.

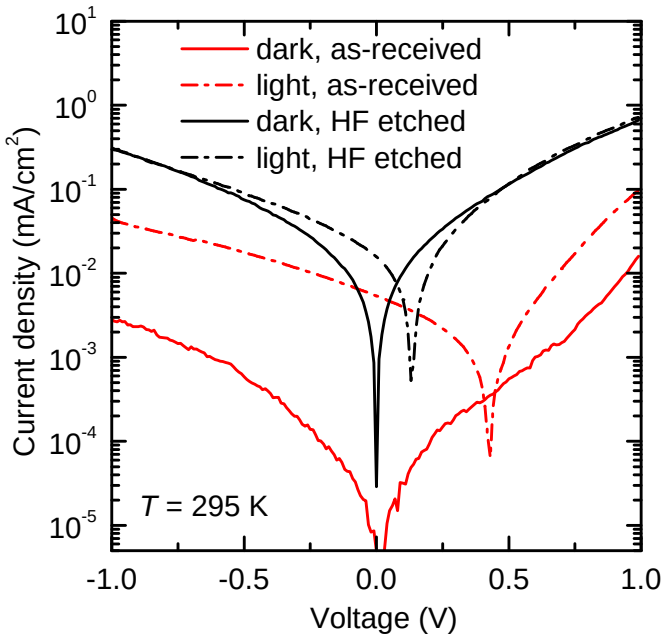

Figure 5.22: *Current-voltage characteristics of a P3HT/Si-nc solar cell with the as-received nanocrystals in the dark (red solid lines) and under illumination (red dash-dotted lines) and of P3HT/Si-nc solar cell with HF-etched nanocrystals in the dark (black solid line) and under illumination (black dash-dotted line) at 295 K.*

In the sample with the HF-etched silicon nanocrystals (black lines) the overall current is much higher than in the reference sample (red lines). This can be explained by the increase of the conductivity of the silicon nanocrystals after HF etching, which in turn is responsible for a higher silicon nanocrystal EDMR signal as it is observed in Figure 5.16 for the sample with the HF-etched silicon nanocrystals. Due to the higher conductivity in the sample with the HF etched silicon nanocrystals, also the difference between the dark current and the photocurrent is much smaller than in the reference sample. Whereas the short-circuit current is higher in the sample with the HF-etched silicon nanocrystals, the open-circuit voltage is smaller than in the reference

sample. This situation leads to about the same efficiency of 4×10^{-4} % in both solar cells. The simultaneous increase of direct current paths in the silicon nanocrystals between the cathode and the anode reduces the open-circuit voltage, as described by Snaith *et al.* for organic solar cells [Sna04]. Furthermore, a change in morphology due to the different surface termination of the silicon nanocrystals may have a large influence on the current-voltage characteristics. And, even if from Figure 5.4 no influence of the etching is obvious on the scale of about 100 nm, the morphology may have changed on a smaller length scale as the oxide shell is removed. In addition, also from the LESR experiments of P3HT/Si-nc bulk heterojunctions with etched silicon nanocrystals in Subsection 5.2.2, where no increase of the P^+ could be found, a different morphology is the most probable reason. As in the LESR experiments with etched silicon nanocrystals, it is difficult to evaluate the influence of the etching without knowing the exact morphology on the nanometer scale. In conclusion, up to now the overall solar cell efficiency could not be improved by the HF etching of the silicon nanocrystals.

5.3.3 Model of the bulk heterojunction solar cell

We have seen from the SEM images in Figure 5.4 that for the gradient structure always a mixed layer forms, instead of a bilayer or multilayer. From the AFM images in Figure 5.2, we could deduce that the morphology changes, depending on the exact volume ratio of the spin-coated solutions. For a qualitative understanding of the behavior of the P3HT/Si-nc solar cell, the different current paths have to be taken into account. Thus, to describe the behavior of such a mixed active layer, an elementary model which includes all contributions to the current-voltage characteristics in parallel can be established. This means the current can flow in parallel through a pure P3HT layer, a pure silicon nanocrystal layer, or through a P3HT/Si-nc heterojunction in both directions. Such a parallel connection is shown in Figure 5.23 similar to the model proposed by Snaith *et al.* [Sna04]. Depending on the exact morphology, the different current paths contribute differently to the current. The two diodes of the P3HT/Si-nc interfaces should lead to a contribution in either direction. However, we observe for all solar cells that the electrons flow to the aluminum contact under open-circuit conditions. As already mentioned, this can be explained by the large influence of the pure P3HT Schottky junction which contributes in any case. In addition, the electric field due to the different work functions of aluminum and ITO will lead to an enhanced extraction of the photo-induced electrons on the aluminum side. The P3HT Schottky diode itself is then influenced by the silicon nanocrystals, which build up further P3HT/Si-nc diodes working in parallel to the P3HT Schottky diode. This additional current paths alter the open-circuit voltage and the short-circuit current depending on the morphology and the P3HT/Si-nc ratio of the active layer.

From the band alignment at the interface between P3HT and silicon, a potential difference of about $0.7 - 1.2$ eV is expected (see Figure 3.8) depending on the exact positions of the HOMO

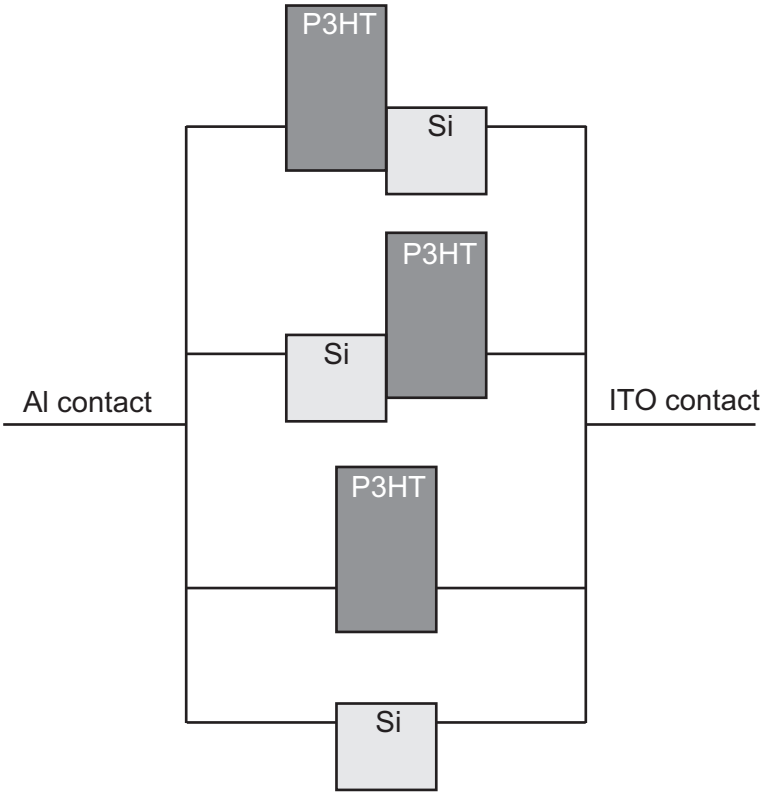

Figure 5.23: *Scheme of the parallel connection of different current paths as an elementary model to describe the observed current-voltage characteristics.*

of P3HT and the conduction band of the silicon and without taking into account any effects such as Fermi level alignment or pinning at interface dipoles. The pure P3HT and pure silicon nanocrystal paths are equivalent to the concept of a shunt resistor added in parallel to the diode in models for photovoltaic devices. This effect leads to a drop in the open-circuit voltage in blend devices as compared to that of bilayer devices. This has also been observed for pure organic bilayer and bulk heterojunctions [Sna04]. Considering this lowering due to a bulk heterojunction instead of a bilayer heterojunction, the observed mean value of 0.65 V (from Table 5.4) is relatively high, confirming that not too much pure P3HT current paths are active in the bulk heterojunction. In addition further effects, such as carrier recombination at the interface or at the electrodes, incomplete splitting of the quasi-Fermi levels, losses at the electrodes, and interface dipoles can reduce the open-circuit voltage [Ols07]. The observed value of the maximum open-circuit voltage is in accordance with findings that the open-circuit voltage of an organic or hybrid solar cell can be described adequately by the energy difference between the HOMO and the LUMO or the valence band and the HOMO, respectively [Bra01a, Ols07]. This is in contrast to the classical description of organic solar cells as a metal-insulator-metal device, where the work functions of the metal dominate the open-circuit voltage. However, the classical description of organic solar cells as a metal-insulator-metal device has already been found not to be an appropriate description of organic solar cells [Ran07, Bra01a, Wal06, Che08].

Several reasons, mainly the P3HT short-circuits, make it difficult to conclude from the solar cell measurements on the exact band alignment at the P3HT/Si-nc heterojunction. However, in the next Chapter 6 this alignment will be determined for heterojunctions made from P3HT and bulk crystalline silicon.

5.4 Soft lithography for heterojunction solar cells

5.4.1 Structuring of silicon nanocrystal layers via soft lithography

The technique of soft lithography has been explained in detail in Subsection 4.1.1. Here, the results of the application of soft lithography to silicon nanocrystals are presented. In Figure 5.24, an AFM image (a) and a SEM image (b) of an embossed silicon nanocrystal layer is shown. The size of the AFM image is about $5 \times 4.5\ \mu m^2$ with a height scale of 100 nm, while

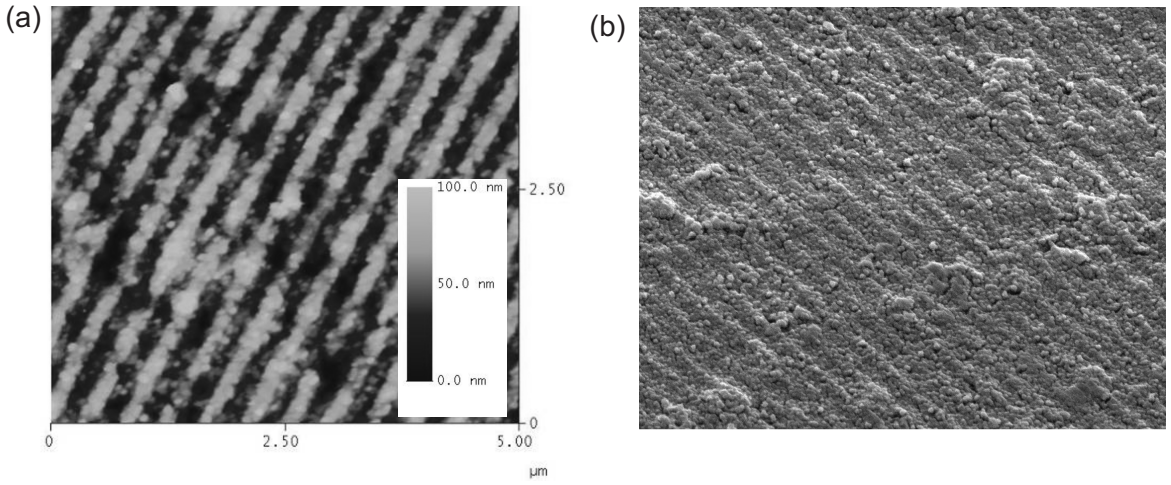

Figure 5.24: *AFM (a) and SEM (b) image of an embossed silicon nanocrystal layer. The size of the AFM image is about $5 \times 4.5\ \mu m^2$ with a height scale of 100 nm, while a magnification of $\times 15000$ was chosen for the SEM image.*

the SEM image was taken with a magnification of $\times 15000$. The silicon nanocrystals had a diameter of about 4 nm (nanocrystal sample 201106) and were dispersed in ethanol with 6 wt%. In both images the groove structure, which was transferred from the PDMS stamp as shown in Figure 4.3, is clearly visible. This demonstrates that structuring of the silicon nanocrystal layer with a structure size of around 200 nm and a height of about 50 nm could be achieved. When comparing the cross-sections of the mold and the structured layer, both, the depth and the periodicity of the mold are reproduced, in spite of the roughness and the imperfections of the layer. However, even if the PDMS mold could be reproduced in principle, defects in the structure caused by large agglomerates of silicon nanocrystals are apparent. In contrast to

typical soft lithography techniques the overall thickness of the nanocrystal layer exceeds the depth of the structure of the PDMS mold. Hence, not the whole silicon nanocrystal dispersion is removed between the mold and the substrate when the mold is pressed against the substrate. Thus, the whole substrate is covered with silicon nanocrystals, which is desired for hybrid bulk heterojunction solar cells, as short-circuits can be avoided. When using dispersions with less than 5 wt% of silicon nanocrystals, the layer quality is not optimal. On the one hand, holes appear in the underlying layer and, in addition, also parts of the substrates are not structured but exhibit the bare substrate. Additional experiments with silicon nanocrystals of different sizes have shown that the size of the nanocrystals does only have a minor effect on the morphology of the layers. However, the number of agglomerates, which reduce the quality of the structures, can be clearly reduced via a longer ball-milling process of the dispersion.

To optimize the structured silicon nanocrystal layers, also a variation of the embossing process, which is described in Subsection 4.1.1, was investigated. For this reason, the mold was only laid on the silicon nanocrystal layer without pressure, which leads to similar good results. Thus, one can conclude that the capillary forces are the main mechanism for the generation of the groove structure. In the literature, soft lithographic methods using capillary forces have already been reported for structuring polymer layers [Suh01]. When using a rigid mold the so-called micromolding in capillaries also was demonstrated for a TiO_2-nanoparticle dispersion, where it was found, as in our experiments, that the condition for an uniform patterning is a high quality of the dispersion of the nanoparticles [Wil04]. The observed large influence of the capillary forces is in accordance with the finding that, when a constant pressure is used for the embossing, small pressures of $0.1 - 0.25$ Ncm^{-2} lead to the best results, since not the pressure but the capillary forces are important for the structuring. Also the additional application of ultrasound during the embossing step could not further enhance the quality of the layers.

5.4.2 Ordered heterojunction solar cells made by soft lithography

To produce ordered heterojunction solar cells with embossed silicon nanocrystal layers the mixed bulk heterojunction structures which were discussed in Section 5.3, are not a suitable concept. Instead, one has to go to heterojunctions, where the P3HT/Si-nc interface is defined by the nanostructured silicon nanocrystal layer. Such ordered heterojunctions will be compared to unstructured reference heterojunctions in the following. Both solar cell types were fabricated with phosphorus-doped silicon nanocrystals with a doping concentration of 6.5×10^{19} cm^{-3} and a diameter of 23 nm (nanocrystal sample 040407). Two different sample types were produced either with a structured or an unstructured silicon nanocrystal layer, which, after an annealing step, was covered with P3HT as described in Subsection 4.1.1. Here, the solvent for the silicon nanocrystals was polar ethanol, while nonpolar 1,2-dichlorobenzene was used for P3HT. In contrast to the bulk heterojunctions, where the P3HT solution and the silicon nanocrystal

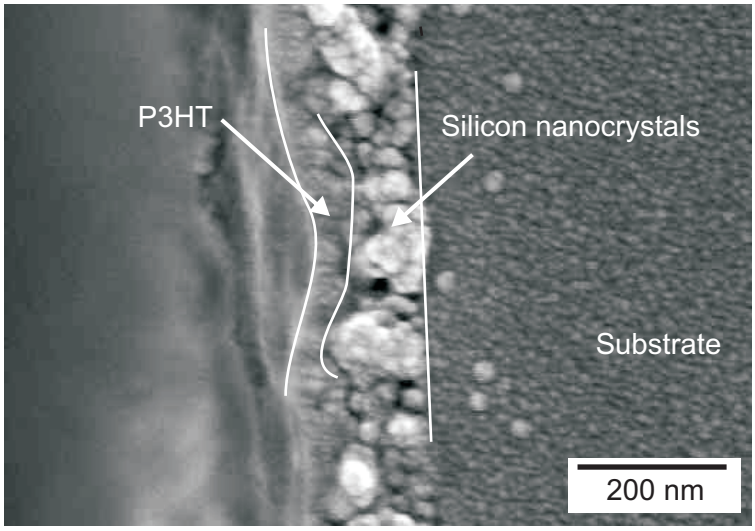

Figure 5.25: *SEM cross section image of a silicon nanocrystal layer which is covered by a P3HT layer.*

dispersion dissolve each other, here the annealing step after the deposition of the nanocrystals and the different solvents allow the formation of a bilayer system. That indeed a bilayer system is obtained can be seen in the SEM image of Figure 5.25, where a cross section view of a silicon nanocrystal layer covered by P3HT is shown.

For the ordered heterojunction solar cell with the structured nanocrystal layer, a part of the samples exhibited a typical open-circuit voltage of P3HT/Si-nc solar cells while another part only showed an open-circuit voltage of about 0.3 V. This can be explained by the observation of completely uncovered areas on some structured nanocrystal layers. In such areas, the P3HT short-circuits between the metal contacts and the behavior of a pure P3HT Schottky solar cell, as shown in Figure 5.19, dominates. However, the structured solar cells without short-circuits showed a high open-circuit voltage, as can be seen from Figure 5.26. There, the current-voltage characteristics in the dark (solid line) and under illumination (dash-dotted line) are shown for a typical ordered heterojunction solar cell with structured silicon nanocrystals.

To compare the behavior of the structured and unstructured heterojunctions, the average values of the solar cell parameters of four different contacts each from structured as well as from unstructured heterojunctions are listed in Table 5.5.

The solar cell parameters of the two solar cell types are very similar and lie in the range of the standard deviations of the values. Especially the efficiencies of the two different heterojunctions are nearly the same. Thus, no influence of the structuring of the silicon nanocrystals can be observed. However, as the increase of the nanocrystal surface area due to soft lithography is only about 20 %, such an increase in the efficiency would lie in the determined error range.

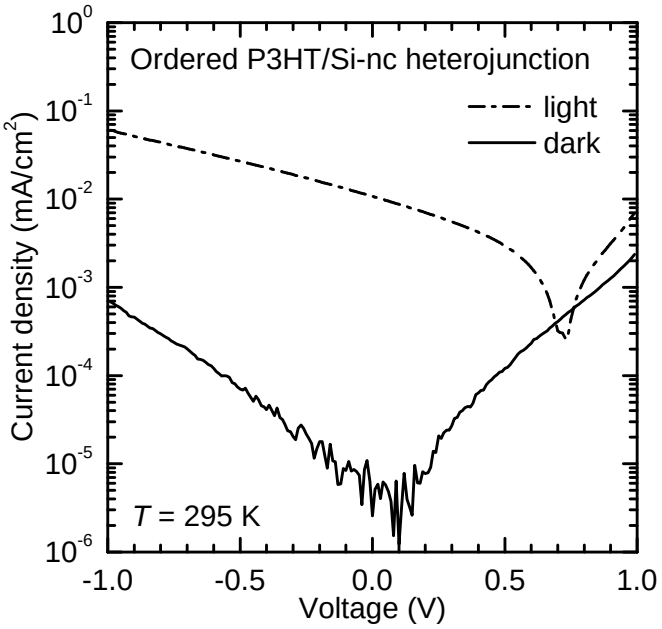

Figure 5.26: *Current-voltage characteristics of a P3HT/Si-nc ordered heterojunction solar cell with a structured silicon nanocrystal layer in the dark (solid line) and under illumination (dash-dotted line) recorded at 295 K.*

However, the devices produced in this section exhibit an efficiency that is about one order of magnitude smaller than the bulk heterojunction devices investigated in Section 5.3. Most probable this is due to the reduced interfacial area between the organic and the inorganic counterparts. Also the thicker silicon nanocrystal layer may hinder an efficient charge transfer in the structured and unstructured heterojunctions as compared to the bulk heterojunctions. Thus, the combination of a thinner silicon nanocrystal layer with a higher aspect ratio may be promising.

Sample	Value	Mean value	Standard deviation (% of the mean value)
Structured heterojunction	V_{OC}	0.70 V	0.12 V (17 %)
	J_{SC}	4.2×10^{-3} mA/cm^2	4.7×10^{-3} mA/cm^2 (110 %)
	FF	0.21	0.0096 (4.6 %)
	η	6.6×10^{-4} %	7.5×10^{-4} % (114 %)
Unstructured heterojunction	V_{OC}	0.63 V	0.01 V (2 %)
	J_{SC}	5.9×10^{-3} mA/cm^2	1.0×10^{-3} mA/cm^2 (17 %)
	FF	0.18	0.019 (11 %)
	η	6.8×10^{-4} %	1.2×10^{-4} % (17 %)

Table 5.5: *Mean values and standard deviations for the open-circuit voltage, V_{OC}, the short-circuit current density, J_{SC}, the fill factor, FF, and the efficiency, η, for four different contacts of a structured and an unstructured heterojunction.*

However, for a higher aspect ratio also a harder PDMS, so-called *h*-PDMS, as used in Reference [Odo02] would be necessary. Nevertheless, the structuring of the silicon nanocrystals and also working solar cells with structured nanocrystal layers have been demonstrated successfully.

6 Hybrid Heterojunctions with P3HT and Silicon or 6H-Silicon Carbide

For heterojunctions made of P3HT and silicon (P3HT/Si), the photo-induced charge separation and photovoltaic effects were demonstrated in the previous chapter. From the observed charge transfer it was possible to determine the positions of the energy levels of the two components with respect to each other. However, the exact positions and the band alignment of the P3HT and silicon energy levels were not investigated. This would be important for a better understanding and an optimization of the P3HT/Si-nc bulk heterojunction with regard to solar cell applications. As heterojunctions with a two-dimensional interface have less degrees of freedom, compared to three-dimensional bulk heterojunctions, P3HT/Si heterojunctions with bulk silicon will be investigated as a model system in the first part of this chapter.

However, as the valence band of silicon and the HOMO of P3HT are placed energetically close to each other, problems regarding an efficient hole transfer can occur. For this reason, 6H-SiC, as an inorganic semiconductor with a different valence band position, is applied for organic-inorganic heterojunctions with P3HT. As in the case of P3HT/Si heterojunctions, the current transport, the photovoltaic properties, and the band alignment of heterojunctions made of P3HT and 6H-SiC (P3HT/6H-SiC) will be examined in the second part of this chapter.

6.1 Heterojunctions made of bulk silicon and P3HT

Heterojunctions made of bulk silicon and P3HT will be investigated for different doping types and levels of silicon. In particular, the dark current-voltage characteristics as well as the behavior of the P3HT/Si heterojunctions under illumination will be analyzed. These current-voltage measurements allow conclusions about the band alignment of the heterojunction. In addition, the P3HT/Si heterojunction will be compared to the bulk heterojunction made of silicon nanocrystals and P3HT.

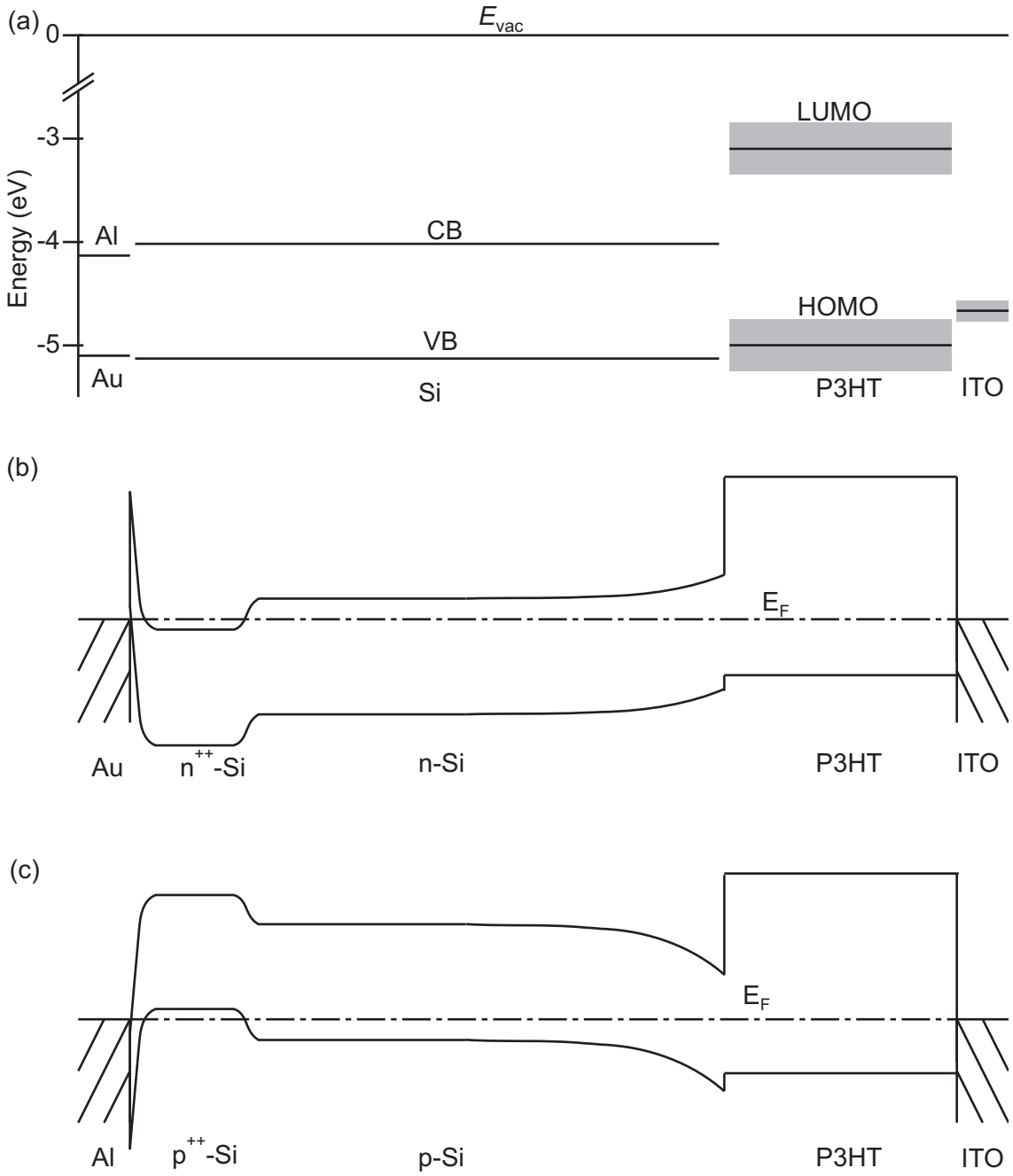

Figure 6.1: *(a) Energetic positions of the energy levels of silicon and P3HT (black lines). For silicon the literature values are taken, while for P3HT the mean value of the literature values (grey bands) for the HOMO and LUMO and the measured contact potential difference value for the Fermi level were taken. (b) Band alignment of n-type silicon and P3HT and of (c) p-type silicon and P3HT as expected theoretically from Fermi level alignment under thermal equilibrium. Additionally the Fermi levels of the contact metals are shown.*

6.1.1 Dark current-voltage measurements of P3HT/Si heterojunctions with p-type and n-type silicon

Theoretical band alignment of silicon and P3HT

The silicon and P3HT energy levels are shown in Figure 6.1 (a). For silicon, the energetic positions of the conduction and valence band edges have been determined in the literature various times, so literature values have been taken (see Subsection 3.1.1). For P3HT the literature values for the energy of the HOMO and the LUMO (see Subsection 3.2.1), which are plotted as grey bands, differ by up to ± 0.3 eV. Thus, in addition the average values of the HOMO and the LUMO are plotted as black lines. The Fermi level of silicon was taken from the literature, while for P3HT the Fermi level was measured via contact potential difference measurements (see Subsection 3.2.1). The alignment of the silicon and P3HT energy levels is predicted via Fermi level alignment, as described in Section 2.2.2. The expected alignments for heterojunctions of P3HT and n-type silicon (P3HT/n-Si) and P3HT and p-type silicon (P3HT/n-Si) are shown in Figure 6.1 (b) and (c), respectively, for moderate doping levels which were mainly used for the heterojunctions in this section. In this theoretic band alignment, no space-charge region builds up in the P3HT, as P3HT is undoped. Thus, without an applied voltage, no band bending occurs in the organic semiconductor. Furthermore it is assumed that no interface dipoles exist, which would lead to an energetic offset.

The P3HT/Si heterojunction samples with the silicon wafer and the 1 μm thick drop-casted P3HT layer have been prepared as described in Subsection 4.1.2. The top contact to the P3HT is formed by e-beam evaporation of ITO onto the heated P3HT layer, as described in Subsection 4.1.2. The energetic position of the Fermi level in ITO is taken from the literature [Bra08] and again the average value (black line) and the range of the values (grey bands) are plotted. However, the ITO/P3HT contact, which is also shown in Figure 6.1, does not exhibit a completely ohmic behavior, as it is typically observed for P3HT which is spin-coated on ITO coated substrates [Chi03b]. This may be due to a hole transfer from the P3HT to the ITO or due to pinning of the P3HT Fermi level at surface defect states in the P3HT, which may be created by the evaporation step. For contacts to n-type and p-type silicon, gold and aluminum, are used, respectively. The metals diffuse into the silicon during an annealing step, which forms highly doped regions in the silicon as depicted in Figure 6.1 (b) and (c), leading to ohmic contacts. Theoretical and experimental details regarding the contacts are described in Subsection 2.2.1 and Subsection 4.1.2, respectively.

Dark current-voltage measurements

The current-voltage characteristics of P3HT/Si heterojunctions with n-type and p-type silicon are depicted in Figure 6.2 (a) and (b), respectively. Here, as for all heterojunctions in this chapter, a positive bias means that a positive potential is applied to the P3HT. The doping levels for the n-type silicon are $7 \times 10^{11} - 1.5 \times 10^{12}$ cm^{-3} (squares) and $4 - 9 \times 10^{18}$ cm^{-3} (circles), while the doping levels for the p-type silicon are $2 - 3 \times 10^{15}$ cm^{-3} (squares) and $4 - 9 \times 10^{18}$ cm^{-3} (circles). The lower doping levels (squares) were used for most of the samples in this section, thus, if no other doping levels are explicitly stated these doping levels were applied. Both figures show a rectifying behavior which changes the direction when the doping type is changed. This proves that the heterojunction properties are responsible for the diode behavior instead of possible Schottky contacts at the metal-semiconductor interfaces, which would lead to a doping-independent rectifying behavior. The change in the diode direction is consistent with the theoretical band alignment in Figure 6.1: For the case of n-type silicon, the electrons are the majority carriers which have to overcome the barrier to the LUMO of P3HT. In contrast, for p-type silicon, the holes are emitted from the valence band over a barrier into the HOMO of P3HT. The barrier for the P3HT/n-Si heterojunction has two contributions, a depletion layer in the silicon and the band offset between the conduction band of silicon and the LUMO of P3HT. In P3HT/p-Si only the depletion layer in silicon at the P3HT/Si interface defines the barrier height. Thus, with the doping type, which is responsible for the direction of the band bending in the silicon, the direction of the diode changes.

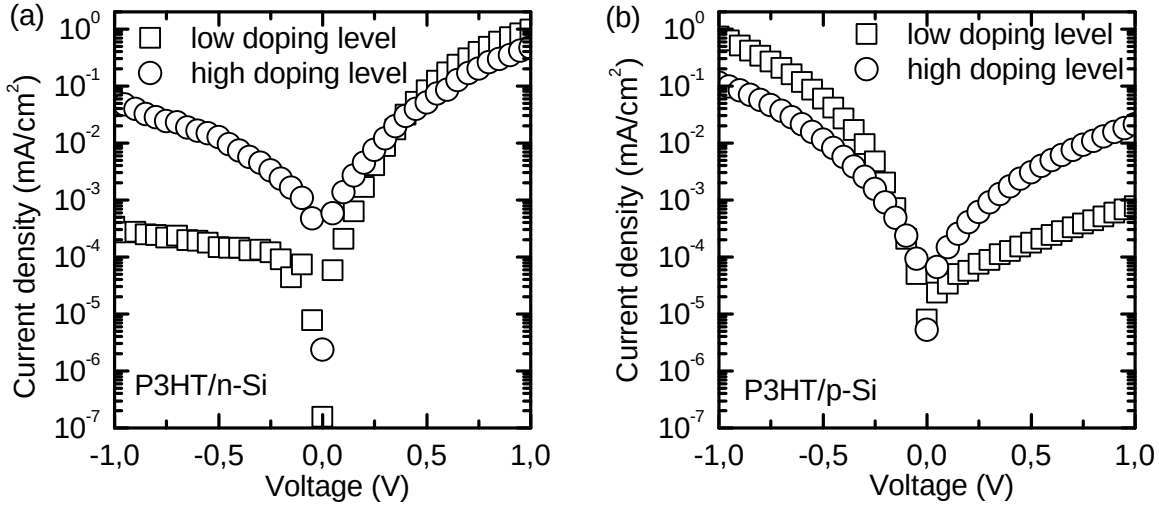

Figure 6.2: *Dark current-voltage characteristics of P3HT/n-Si (a) and P3HT/p-Si heterojunctions (b). The doping levels for the n-type silicon are* $7 \times 10^{11} - 1.5 \times 10^{12}$ *cm*$^{-3}$ *(squares) and* $4 - 9 \times 10^{18}$ *cm*$^{-3}$ *(circles), while the doping levels for the p-type silicon are* $2 - 3 \times 10^{15}$ *cm*$^{-3}$ *(squares) and* $4 - 9 \times 10^{18}$ *cm*$^{-3}$ *(circles).*

Regarding the forward current density of the four heterojunctions, one would expect that the forward current of the P3HT/p-Si heterojunctions is much higher than in the case of the P3HT/n-Si heterojunctions as the barrier is smaller. However, as will be seen in this chapter, the SCLC mechanism limits the forward current and thus lowers all forward currents to a similar level. In the reverse direction, the current for the P3HT/p-Si heterojunction with the low doping level is nearly one order of magnitude higher at $V = +1$ V, compared to the current of the P3HT/n-Si heterojunction with the low doping level at $V = -1$ V. For the latter, in the reverse direction electrons are injected from the ITO into the LUMO of the P3HT, where they have to overcome a large barrier which explains the low reverse current. For P3HT/p-Si heterojunctions, holes from the ITO have not to overcome such a large barrier, thus the reverse current is higher. Nevertheless, the barrier of the P3HT/p-Si heterojunction in the reverse current should be larger than expected from Figure 6.1 to explain the observed current-voltage characteristics. This indicates that the theoretical band alignment, as shown in Figure 6.1, does not apply completely. Maybe there is an additional band offset between the silicon valence band and the HOMO of P3HT, due to an interface dipole, which would provide a larger barrier for the holes in the reverse direction. The current-voltage characteristics could also be explained by an upwards shift of the Fermi level compared to the actual measured value of 4.4 eV, providing a similar barrier for holes and electrons from the ITO. Such a shift of the Fermi level could happen either by unintentional doping by impurities [Mei03, Est08], by pinning [Ten06] or by injection from the metal contact [For84a].

However, it must be mentioned that the reproducibility of the P3HT/Si heterojunctions is not good. The currents at biases of ± 1 V vary typically one order of magnitude when measuring different contacts on one sample. When comparing different samples, the current may even change by up to two orders of magnitude. Nevertheless, the diode behavior can be observed in all samples, even if the rectification ratio may vary. The reasons for the large variations, which have also been observed in heterojunctions with amorphous silicon and P3HT [Ale08], may be found in the properties of the P3HT. First, the P3HT is drop-casted on the silicon, which may lead to differences in morphology and thickness, even though in microscopy images no inhomogeneities are visible. Second, the position of the energy levels may be sensitive to the exact process conditions. Especially the properties of the ITO contact, which is evaporated under simultaneous annealing, may vary due to small changes in process parameters and hence influence the P3HT layer by unintentional doping or the creation of defects.

Different silicon doping levels

P3HT/Si heterojunctions were fabricated with a variety of four different doping levels of each doping type. The properties of the different silicon wafer types which were used for this purpose are listed in Table 3.1. As a common trend, the forward current density of about 0.1 - 1 mA/cm^2

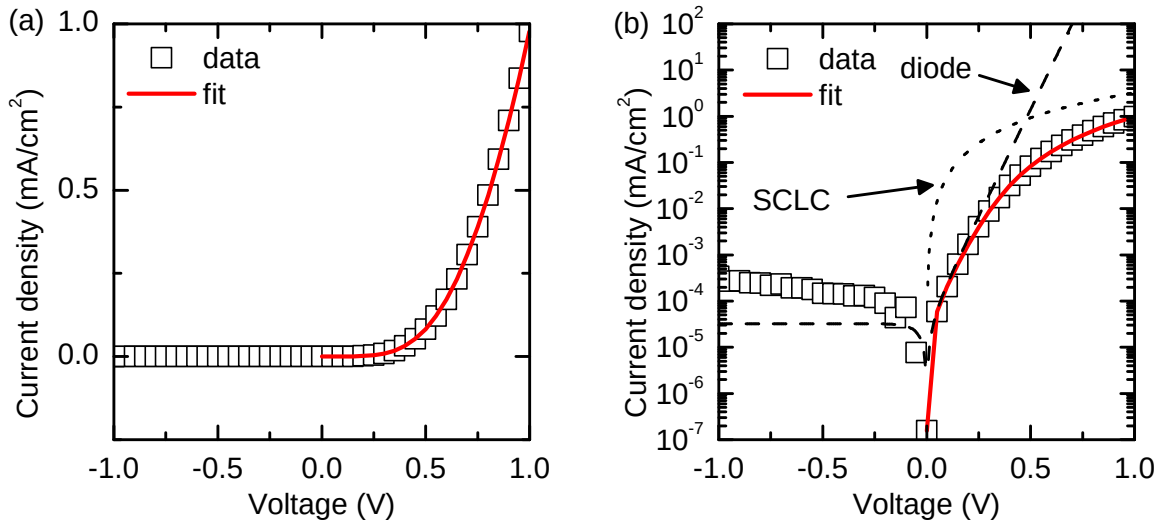

Figure 6.3: *Fit of the dark current-voltage characteristics of a P3HT/n-Si heterojunction in a linear (a) and in a semilogarithmic plot (b). In addition to the measured data (squares), the fit (red line), and the individual contributions to the fit are plotted, including the diode (dashed line) and the SCLC (dotted line).*

was roughly the same for all samples, while the reverse current increased with a higher doping level for both doping types. As shown in Figure 6.2 (a) and (b) at the highest doping levels of $4-9\times10^{18}$ cm^{-3} (circles) for both, the n-type and p-type silicon, the rectification ratio at ±1 V is smaller than one order of magnitude. One possible explanation for the enhancement of the reverse current could be transfer doping of the P3HT from the highly doped silicon. Such additional charge carriers in the P3HT could alter the conductivity of the P3HT and could enhance the reverse charge transport. In contrast, the forward current is dominated by a space-charge limited current mechanism in the P3HT, as will be shown below, and thus remained constant for all doping levels.

Modeling the dark current-voltage characteristics of the P3HT/n-Si heterojunction

In order to gain more information about the transport mechanisms, the current-voltage characteristics of a P3HT/n-Si heterojunction was fitted. For this purpose, the proposed equivalent circuit including a diode and a SCLC resistance, as shown in Figure 2.13, was used, as a simple diode fit does not describe the transport behavior of the heterojunction. To simplify the fit, the shunt resistance, R_{Sh}, of the heterojunction, which has a large value as no short-circuits are visible, is set to infinity and only the interesting forward direction is fitted. In Figure 6.3, the fit (red line) of the dark current-voltage characteristics (squares) of a P3HT/n-Si heterojunction is presented, where the fit shows an excellent agreement with the data. Furthermore, in Figure 6.3 (b), besides the fit also the individual contributions to the fit, the diode (dashed line) and the

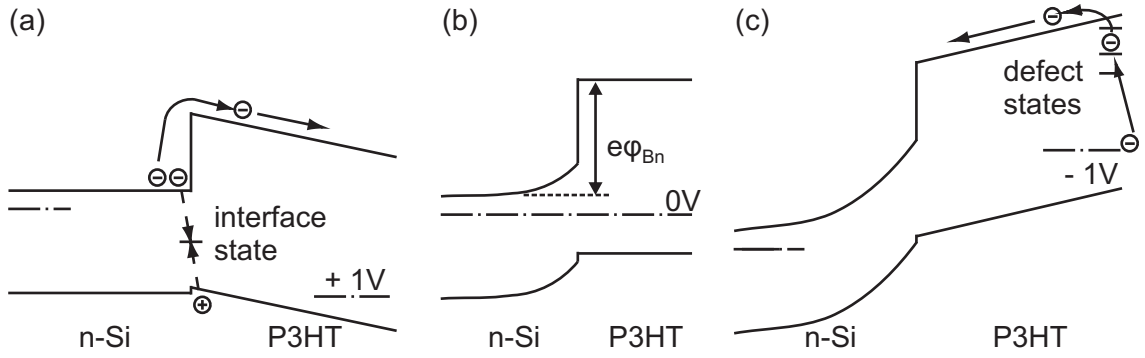

Figure 6.4: *Schematic view of the P3HT/n-Si heterojunction at forward bias (a), without an applied voltage (b), and with reverse bias (c).*

SCLC (dotted line), are shown for the case that the whole voltage would drop at the diode or the SCLC element. The current-voltage characteristics itself is a combination of both elements, which follows the diode up to 0.2 V and is dominated by the SCLC afterwards. As the fit is a series connection of the diode and the SCLC, the voltage is split at both elements. Thus, *e.g.* if a voltage of 0.5 V is applied, 0.35 V drop at the diode and 0.15 V drop at the SCLC element. The fit parameters were $J_S = 2.3 \times 10^{-5}$ mA/cm^2, $n = 1.9$, $k_{SCLC} = 3.2$ mA/(cm^{2}V$^{1.8}$), and $m = 1.8$.

The forward direction is defined by electrons which are emitted to the LUMO of P3HT from the conduction band of silicon. Holes, which are injected from the ITO contact to the P3HT may also contribute to the current via recombination with electrons from the silicon. Such a recombination at the heterojunction interface is suggested by the large ideality factor $n = 1.9$ [Sze07]. Surface defects of silicon and P3HT at the interface may facilitate such a recombination. The reverse current, on the other hand, is composed of electrons which are injected into the P3HT, most possibly via defect states induced by the ITO deposition. Holes which may be injected into the valence band of silicon will recombine in the n-type silicon with the majority charge carriers before reaching the P3HT. These processes are schematically shown in Figure 6.4.

Using the model of the thermionic emission (see Subsection 2.2.1), with the J_S received from the fit and the effective Richardson constant for n-type Silicon of $A^* = 250$ A/cm^{2}K^2 [Sze07], a barrier height $e\varphi_{Bn}$ = 0.9 eV is obtained by using Equation 2.5 when image-force lowering is neglected. The electrons have to overcome this barrier to be emitted from silicon to P3HT. In silicon, nearly all phosphorus atoms are ionized at room temperature [Sze07], thus the barrier is the difference between the conduction band of silicon and the LUMO of P3HT. The value of 0.9 eV corresponds well with the value one would expect from the theoretical band alignment, where a value of 1 eV is obtained. Below, when the behavior of the P3HT/n-Si heterojunction under illumination will be investigated, it will be shown that photo-generated holes can be transfered from the valence band of silicon to the HOMO of P3HT. This is only possible when

the offset between the conduction band of silicon and the LUMO of P3HT is large enough, which supports the large value of the determined barrier.

For voltages higher than 0.2 V the SCLC dominates the current-voltage characteristics and the bigger part of the applied voltage drops over the P3HT layer. Such a nonlinear current-voltage dependence has been reported for a large variety of inorganic and organic materials [Pal06b], where injected carriers control the space charge and the electric-field profile. From the fit parameter $m = 1.8$ one can conclude that the traps are already occupied by electrons when the SCLC is limiting the current [Ant02]. From $k_{\mathrm{SCLC}} = 3.2$ mA/cm^{2}V$^{1.8}$ the effective electron mobility in P3HT can be calculated to $\mu = 9 \times 10^{-3}$ cm^2/Vs following Equation 2.20, with $k_{\mathrm{SCLC}} = \frac{9}{8}\frac{\varepsilon_r \varepsilon_0 \mu}{d^3}$, $\varepsilon = 3.5$, $\varepsilon_0 = 8.85 \times 10^{-12}$ As/V, and $d = 1$ μm. This value is in the range of the literature values in Subsection 3.2.1.

Modeling of the dark current-voltage characteristics of the P3HT/p-Si heterojunction

In Figure 6.5 a typical dark current-voltage characteristics (squares) of a P3HT/p-Si heterojunction, including a fit (red line) of the forward direction, is plotted. The best fit was achieved when using only a power function. This means that the P3HT/p-Si heterojunction diode is dominated by the SCLC effect in the whole forward voltage range. Thus, it is difficult to indicate a possible underlying exponential behavior in the forward direction, which may result from holes, which have to overcome a depletion region when applying a forward bias. The reverse diode behavior of the P3HT/p-Si heterojunction could be explained by a barrier for holes in the reverse direction. Such a barrier may exist for holes when crossing the P3HT to the p-type silicon or when injecting holes from the ITO into the P3HT. From the fit parameter $k_{\mathrm{SCLC}} = 0.7$ mA/cm^{2}V$^{3.6}$ the hole mobility in P3HT is expected to be a factor of 5 lower than for electrons. Although semiconducting polymers usually are better hole conductors, in P3HT hole and electron mobility have been found to have the same order of magnitude [Cho04], which is in agreement with our estimation of the mobility. The value of $m = 3.6$ indicates that the traps for holes are partly unoccupied [Ros55], which is in accordance with the observed lower hole mobility.

6.1.2 Investigation of P3HT/silicon heterojunctions under illumination

Current-voltage characteristics of P3HT/silicon heterojunctions under illumination with LEDs of different wavelengths

Current-voltage measurements under illumination with high power LEDs of different wavelengths were performed on P3HT/n-Si and P3HT/p-Si heterojunctions to obtain information

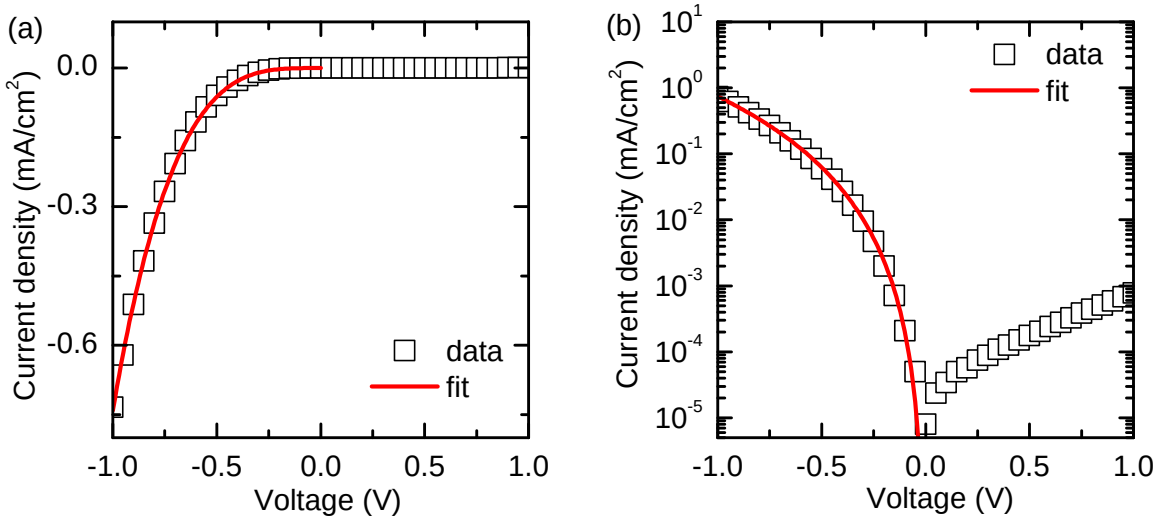

Figure 6.5: *Fit of the dark current-voltage characteristics of a P3HT/p-Si heterojunction in a linear (a) and in a semilogarithmic plot (b). In addition to the measured data (squares), also the fit (red line) is plotted.*

about the photo-induced charge carrier generation and transfer mechanisms. Furthermore, these measurements were performed to gain a more detailed understanding of the relative band alignment at the interface between the two materials. In Figure 6.6 the center wavelengths of the LEDs and the absorption spectra of P3HT and silicon are shown. From Figure 6.6 it can be seen that the 525 nm LED primarily generates charge carriers in the P3HT, as it has a 10 times higher absorption coefficient than silicon in this spectral range. P3HT does not absorb light in the infrared spectral range, thus, the 810 nm LED was chosen to investigate the contribution of silicon to the photo-induced current. As LEDs have typical spectral ranges of about ± 20 nm, at a center wavelength of 655 nm near the onset of the absorption of P3HT both, P3HT and silicon, will absorb light, as the longer wavelengths are transmitted to the silicon while the shorter wavelengths are absorbed in the P3HT. In Figure 6.7 the current-voltage characteristics for P3HT/n-Si (a) and P3HT/p-Si heterojunctions (b) are depicted. The measurements were performed in the dark (black line) and under illumination through the transparent ITO contact on the P3HT side with high power LEDs with wavelengths of 525 nm (green line), 655 nm (red line), and 810 nm (magenta line). For the P3HT/n-Si heterojunction current-voltage characteristics depicted in Figure 6.7 (a), photocurrents of about $1.5 - 2$ orders of magnitude higher than the dark current are detected for all wavelengths. Nevertheless, the open-circuit voltages are smaller than 0.05 V. In contrast to the characteristics obtained for P3HT/p-Si heterojunctions, the direction of the diode is inverted and we observe a pronounced effect for illumination with the infrared LED (magenta line). The inverted direction of the diode indicates that the P3HT/Si diode dominates the current-voltage characteristics for both structures, P3HT/p-Si and P3HT/n-Si, and that the contribution of the P3HT/ITO interface is negligible.

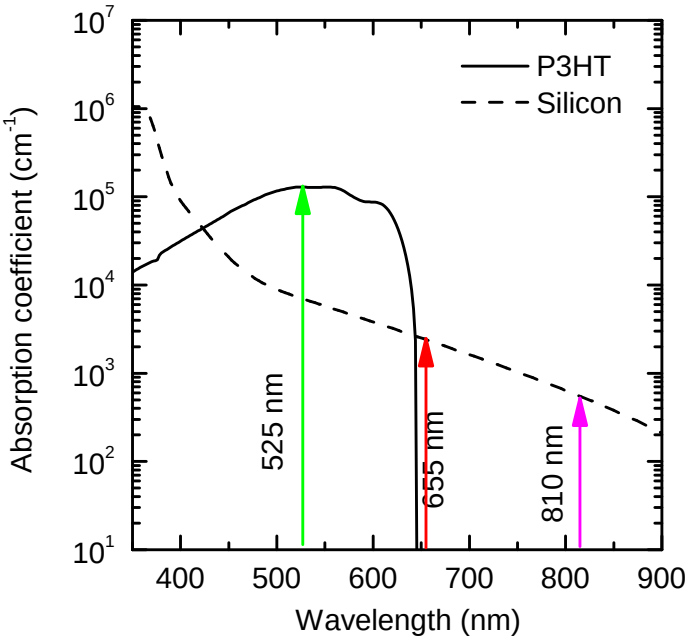

Figure 6.6: *Absorption spectra of silicon (dashed line) and P3HT (solid line). The arrows indicate the center wavelengths of the LEDs. Data for silicon is taken from Reference [Hul99].*

As the direction of the diode is inverted in comparison to the P3HT/p-Si heterojunction, now the photo-induced electrons are extracted via the Au contact and the holes via the ITO contact. Electrons generated in P3HT are transferred to the silicon and are extracted at the Au contact, while the holes move to the ITO contact. Photo-excited free electrons and holes will be generated in silicon under IR or red illumination. In contrast to the situation for p-type silicon, which will be discussed below, the electrons are not trapped by an unfavorable band alignment at the P3HT/Si interface.

The open-circuit voltages of below 0.05 V can be explained to some extent from the small photocurrent. However, despite a photocurrent under reverse voltage, the photo-generated charge carriers are not effectively extracted without any applied voltage. Such a strong voltage dependence is also known in organic solar cells [Kos05] and is explained by a high recombination rate, which leads to small photocurrents and a negligible charge extraction at low voltages, leading to the observed small open-circuit voltages.

The absolute value of the photocurrent is comparable for all wavelengths. However, the photocurrent observed under infrared illumination is the highest, as all absorbed photons generate free charge carriers in silicon. Nevertheless, a larger difference between the photocurrent under infrared illumination and *e.g.* the illumination with the 525 nm LED is expected as for the latter case most photons are absorbed in the bulk P3HT without generating photocurrent. This could be explained by a barrier for holes, limiting the transfer from the valence band of silicon to the HOMO of P3HT. A similar band alignment has also been observed in a heterojunction made of

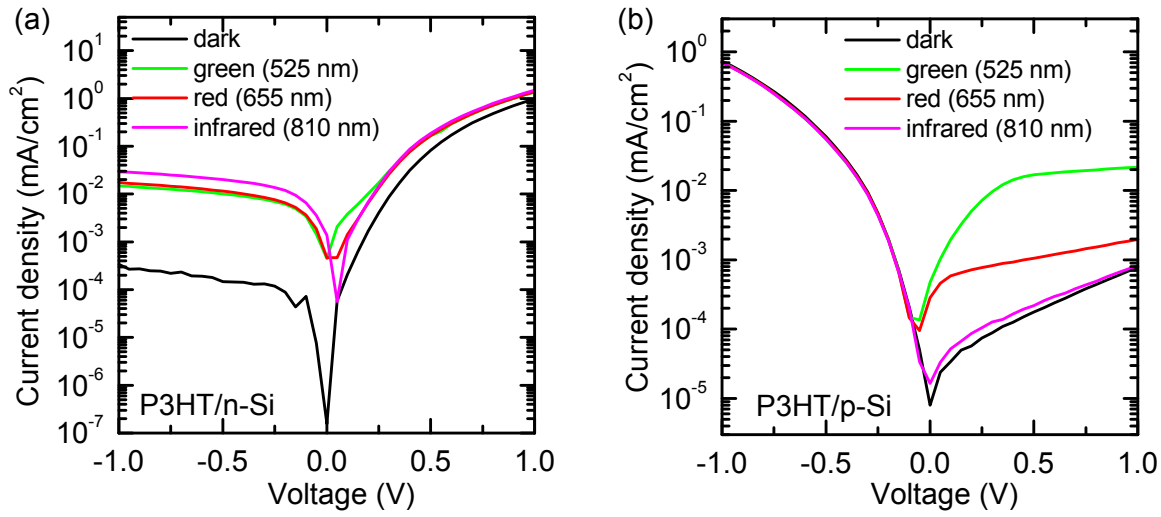

Figure 6.7: *Current-voltage characteristics of P3HT/n-Si (a) and P3HT/p-Si heterojunction solar cells (b) in the dark (black line) and under illumination with three high power LEDs with wavelengths of 525 nm (green line), 655 nm (red line), and 810 nm (magenta line).*

P3HT and amorphous silicon, where a back transfer of holes from the HOMO of P3HT to tail states near the valence band in amorphous silicon has been proposed [Gow06]. Thus, the band alignment is not ideal for an efficient transfer of holes from the valence band of n-type silicon to the HOMO of P3HT.

When investigating p-type silicon based hybrid heterojunctions, as shown in Figure 6.7 (b), upon illumination with the 525 nm LED (green line), one observes a reverse photocurrent which is about 1.5 orders of magnitude higher than the dark current. In contrast, the effect under illumination is much weaker for the illumination with the 655 nm LED (red line). Finally, we observe almost no change of the current-voltage characteristic for the infrared LED (magenta line). However, the open-circuit voltage is very small, with a value below 0.1 V.

The current-voltage characteristics result from the superposition of the characteristics of three interfaces: metal/Si, P3HT/Si, and P3HT/ITO. The metal/Si contact is quite well understood and exhibits a very good ohmic behavior. As already mentioned above, the P3HT/ITO contact does not show a completely ohmic behavior possibly due to the e-beam evaporation deposition. Therefore, the measured curves for the P3HT/p-Si heterojunction most probably result from the superposition of two diodes, P3HT/Si and P3HT/ITO.

For illumination with the 525 and 655 nm LEDs, most of the photons are absorbed in the P3HT layer and excitons are generated there. If these excitons do not recombine before they reach an interface, they can either be separated at the P3HT/p-Si interface or at the not ideally ohmic interface to ITO. The current-voltage characteristics in Figure 6.7 (b) show a photocurrent for a positive voltage applied to the ITO contact which increases the downwards bending at the

interfaces. This means that electrons are extracted via the ITO contact and holes via the Al contact. Therefore, holes of light-induced excitons in P3HT, which reach the P3HT/p-Si interface, are transferred to the p-type silicon while the electrons stay in P3HT and move to the ITO contact. The holes can move as majority charge carriers through the p-type silicon to the Al contact. An equivalent process is possible for a charge separation at the P3HT/ITO interface. Here, the electrons are directly extracted at the ITO contact, whereas the holes move through the P3HT and p-type silicon to the opposite Al contact. Free electrons and holes are generated in the p-type silicon by IR illumination (810 nm). As the direction of the internal field does not change, the hole extraction also takes place via the Al contact and the electrons should move to the ITO contact. But the alignment of the conduction band of p-type silicon and the LUMO level of P3HT does not allow an electron transfer into the P3HT. Instead, the electrons are most probably trapped close to the P3HT/p-Si interface and recombine with holes, as schematically shown in Figure 6.8. As these electrons cannot contribute to the external photocurrent, only a very small effect is detected for IR illumination. In summary, we observe that this structure does not efficiently work as a solar cell, because the only contribution originates from charge carrier excitation in the P3HT and thus the open circuit voltage lies below 0.1 eV.

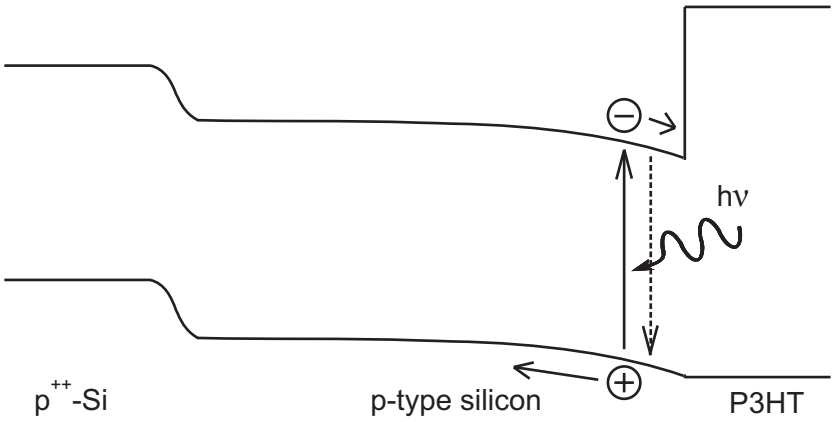

Figure 6.8: *Schematic view of trapping of photo-generated electrons in the silicon with subsequent recombination at the P3HT/p-Si interface.*

Band alignment at P3HT/silicon heterojunctions

Considering the results of the measurements of the current-voltage characteristics in the dark and under illumination, the proposed band alignment as shown in Figure 6.1 has to be adapted: The relative positions of the energy levels of n-type silicon and of P3HT were determined from the fit of the current-voltage characteristics for the P3HT/n-Si heterojunction. There, as already mentioned, a barrier of 0.9 eV between the conduction band of silicon and the LUMO of P3HT was measured. Taking into account the band gap of silicon of 1.1 eV and the transport band gap of P3HT of about 2.0 eV, one can conclude that the valence band and the HOMO of P3HT

have roughly the same energy. And as concluded from the current-voltage measurements of the P3HT/n-Si heterojunction under IR illumination, a barrier for hole transfer in the HOMO of P3HT is present. Such a barrier builds up by an upward band bending of the silicon energy levels at the P3HT/n-Si interface as expected due to Fermi level alignment. Furthermore, as known from the wavelength-dependent measurements on P3HT/Si heterojunctions, also charge carriers from the ITO/P3HT contact contribute to the photocurrent. A downward band bending of the P3HT explains that the excitons at this interface are split up. This band bending also explains that the P3HT/p-Si heterojunction exhibits such a low reverse current as the holes from the ITO have to overcome a barrier into the HOMO of the P3HT. Such a band bending in the P3HT was not assumed at the beginning, as the P3HT is undoped. However, even in undoped P3HT an unintentional doping was reported in the literature [Chi03b, Est08, Mei03], which results in a hole concentration of about $1 \times 10^{15} - 1 \times 10^{17}$ cm^{-3}. Thus, a hole transfer from the P3HT to the ITO, which results in the proposed band bending, is a reasonable assumption.

The additional information gained from the measurements of the P3HT/Si heterojunctions is introduced in the revised band diagrams shown in Figure 6.9. The HOMO of P3HT and the valence band of silicon lie energetically close to each other. This makes the relative positions of these two energy levels sensitive to the exact interface properties which provide different barriers, depending on doping, dipoles, and defects. Thus, the idea to investigate a similar heterojunction with a more clearly defined type II heterojunction made of P3HT and an inorganic semiconductor arises. One promising semiconductor for this purpose is the wide bandgap semiconductor 6H-SiC. Hence, in the following Section 6.2, heterojunctions with P3HT and 6H-SiC will be investigated.

Photovoltaic properties of P3HT/silicon heterojunctions

Additionally to the wavelength-dependent measurements, current-voltage characteristics of the P3HT/Si heterojunctions have been measured under illuminated with a halogen lamp with an intensity of 100 mW/cm^2. The relevant quadrants are shown in Figure 6.10 for heterojunctions with P3HT and n-type silicon (a) and p-type silicon (b), with the dark current (solid line) and the current under illumination (dash-dotted line).

The P3HT/n-Si heterojunction does not show any open-circuit voltage and thus has an efficiency of zero. However, it shows a photocurrent for the relevant wavelengths when a bias is applied. Thus, the problem is the efficient extraction of the photogenerated charge carriers without an applied bias, as already described for the wavelength dependent photocurrent measurements above.

The P3HT/p-Si heterojunction exhibits an open-circuit voltage of 0.15 V, a short-circuit current density of 5.5×10^{-3} mA/cm^2, and a fill factor of 0.22 which leads to the small efficiency of 1.8×10^{-4} %. As the electrons which are excited in the silicon are trapped at the P3HT/p-Si

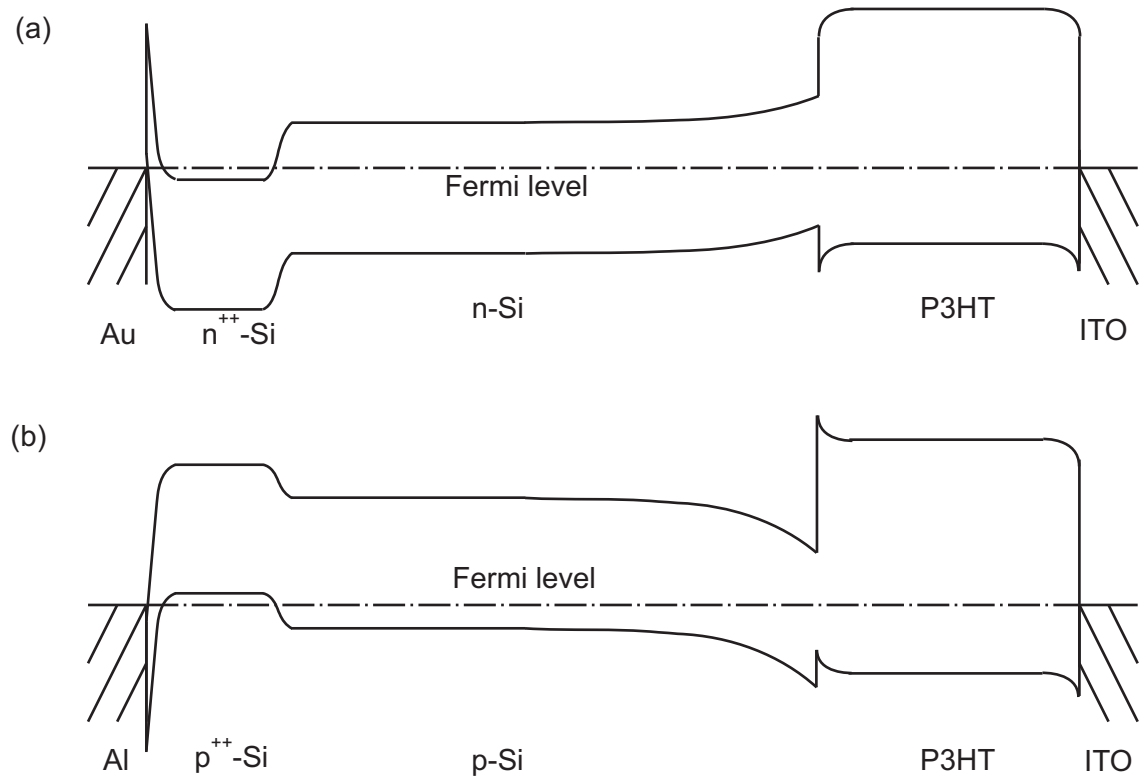

Figure 6.9: *Proposed band alignment of the P3HT/n-Si (a) and the P3HT/p-Si heterojunction (b) as derived from the current-voltage measurements.*

interface, as drawn in Figure 6.8, only the P3HT contributes to the photocurrent. Furthermore, only a small part of the halogen spectrum is absorbed by P3HT. Nevertheless, in contrast to the P3HT/n-Si heterojunction, an open-circuit voltage is observed. Thus, charge carriers which are extracted from the P3HT at the P3HT/p-Si and P3HT/ITO interfaces are responsible for the observed photovoltaic properties. The small fill factor may be due to possible defects at the P3HT interfaces which create a space charge region, which influences the shape of the current-voltage characteristics and reduces the power generation [Gup10, Wag10, Kum09]. Furthermore, the small fill factor is a sign for field-dependent dissociation processes [Man07a], which is in accordance with our observations.

6.1.3 Comparison of heterojunctions made of P3HT and silicon nanocrystals or bulk crystalline silicon

Hybrid heterojunctions made of P3HT and bulk crystalline silicon or with silicon nanocrystals behave quite differently. Compared to the P3HT/Si-nc bulk heterojunctions, the diode characteristics of the P3HT/Si bilayer heterojunction is much more pronounced, as the forward current is higher. However, the open-circuit voltage of the P3HT/Si heterojunctions is signifi-

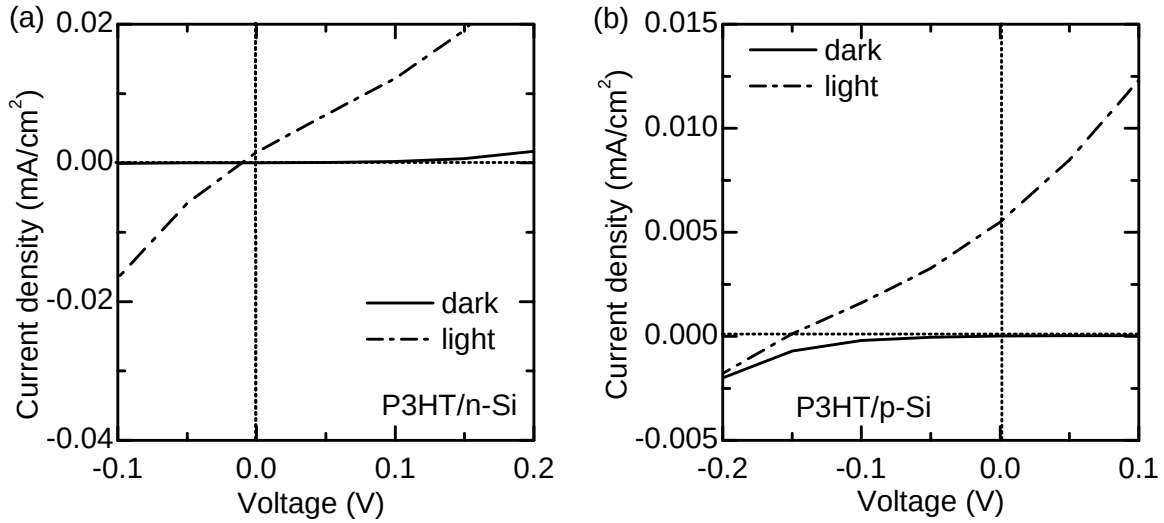

Figure 6.10: *Current-voltage characteristics of P3HT/n-Si (a) and P3HT/p-Si heterojunctions (b) in the dark (solid line) and under illumination (dash-dotted line) with a halogen lamp with an intensity of 100mW/cm^2 from the P3HT side.*

cantly smaller and even for illumination with white light it does not exceed 0.1 V, while in bulk heterojunctions with silicon nanocrystals it can reach up to 0.76 V.

When comparing the two heterojunctions, several differences stand out, which are possible reasons for the discrepancy between the two systems: The heterojunction with the bulk silicon has a much smaller effective interface to dissociate the excitons. Furthermore, the surface termination and, in particular, the defect density of the bulk crystalline silicon and the silicon nanocrystals are different. The different dimension of tens of nanometers for the active layer of the bulk heterojunction and several hundreds of micrometers for the silicon and about 1 μm for the P3HT in the case of the bilayer heterojunction must also been taken into account. Additionally, the different contact materials of the metal/semiconductor interfaces will also influence the open-circuit voltage.

The P3HT/Si-nc bulk heterojunction provides a promising route to a low-cost solar cell, which is corroborated by the high open-circuit voltage which was measured. Despite the differences in the sample structures of the bulk heterojunction and the bilayer heterojunction, the P3HT/Si bilayer heterojunction can provide valuable insights in parameters which could not be investigated with silicon nanocrystals based bulk heterojunctions: The most interesting parameter is the doping level and type, which has no influence on the P3HT/Si-nc heterojunctions, while the doping type is responsible for the diode direction in P3HT/Si bilayer heterojunctions. For the latter case the depletion layer at the semiconductor interface is responsible for the diode characteristics and, thus, the doping is essential. In contrast, for the P3HT/Si-nc bulk heterojunction the P3HT seems to be the dominant semiconductor which determines the diode direction. However, also the high defect density of the silicon nanocrystals and a pinning of the Fermi level may

explain that the doping has no influence in P3HT/Si-nc bulk heterojunctions. Furthermore, in the P3HT/Si bilayer heterojunction the exact alignment of the energy levels could be determined via current-voltage measurements when n-type silicon is used. In contrast, for P3HT/Si-nc bulk heterojunctions only the relative band alignment could be detected via LESR measurements. Hence, as the bilayer heterojunction without silicon nanocrystals is more clearly defined with less degrees of freedom, the investigation of such heterojunctions reveals important properties of organic-inorganic heterojunctions even though a direct comparison between a bulk and a normal heterojunction has turned out to be difficult.

6.2 Heterojunctions made of bulk 6H-silicon carbide and P3HT

As described in the previous Section 6.1, when using a P3HT/n-Si heterojunction for solar cell applications, a barrier between the silicon valence band edge an the HOMO of the P3HT builds up. To overcome this limitation, we choose n-type 6H-SiC, where the valence band edge is well below the HOMO of P3HT, as a counterpart for P3HT to form a hybrid P3HT/6H-SiC heterojunction. The literature values of the energy levels of P3HT and 6H-SiC suggest that the heterojunction should allow an efficient splitting of excitons at the interface, rather than recombination or energy transfer [Gow06], and thus provide a reasonable open-circuit voltage. In addition, the use of 6H-SiC, which has an indirect band gap of 3.0 eV [Lev01], is advantageous as P3HT can be illuminated in the visible spectral range through the 6H-SiC directly at the heterojunction due to the large band gap of 6H-SiC. Hence, a large part of the absorption in the P3HT takes place directly at the interface where the excitons can be dissociated.

The different possibilities for the energetic alignment of two semiconductors have already been described in Section 2.2. Dependent on the exact interface and semiconductor properties, the energy levels can shift relative to each other by up to several hundreds of meV [Ish99]. Thus, in this section, the band alignment of the P3HT/6H-SiC heterojunction will be determined with two different approaches. Furthermore, the photovoltaic properties of the heterojunction will be examined.

6.2.1 Fit of the dark current-voltage characteristics

The positions of the energy levels of P3HT and 6H-SiC are shown in Figure 6.11 (a), in which the range of the literature values (see Chapter 3) for the energy level positions of the two semiconductors is shown in grey and the continuous black lines represent the averages. Also shown in Figure 6.11 (a) are the Fermi levels of n-type 6H-SiC and P3HT as dash-dotted lines and the

values of the work functions of the metals which were used for ohmic contacts. The expected band diagram due to Fermi level alignment of 6H-SiC and P3HT is shown in Figure 6.11 (b), where a space charge region in 6H-SiC with the corresponding band bending is present. In P3HT, which is undoped, no band bending is expected, which was confirmed by surface photovoltage measurements on P3HT under vacuum. The relative alignment of the two semiconductors is derived from the alignment of the Fermi levels of 6H-SiC and P3HT (see Chapter 3). From the estimated band alignment we can conclude that for the P3HT/6H-SiC heterojunction forms a type II heterojunction and hence is able to extract photo-generated charge carriers.

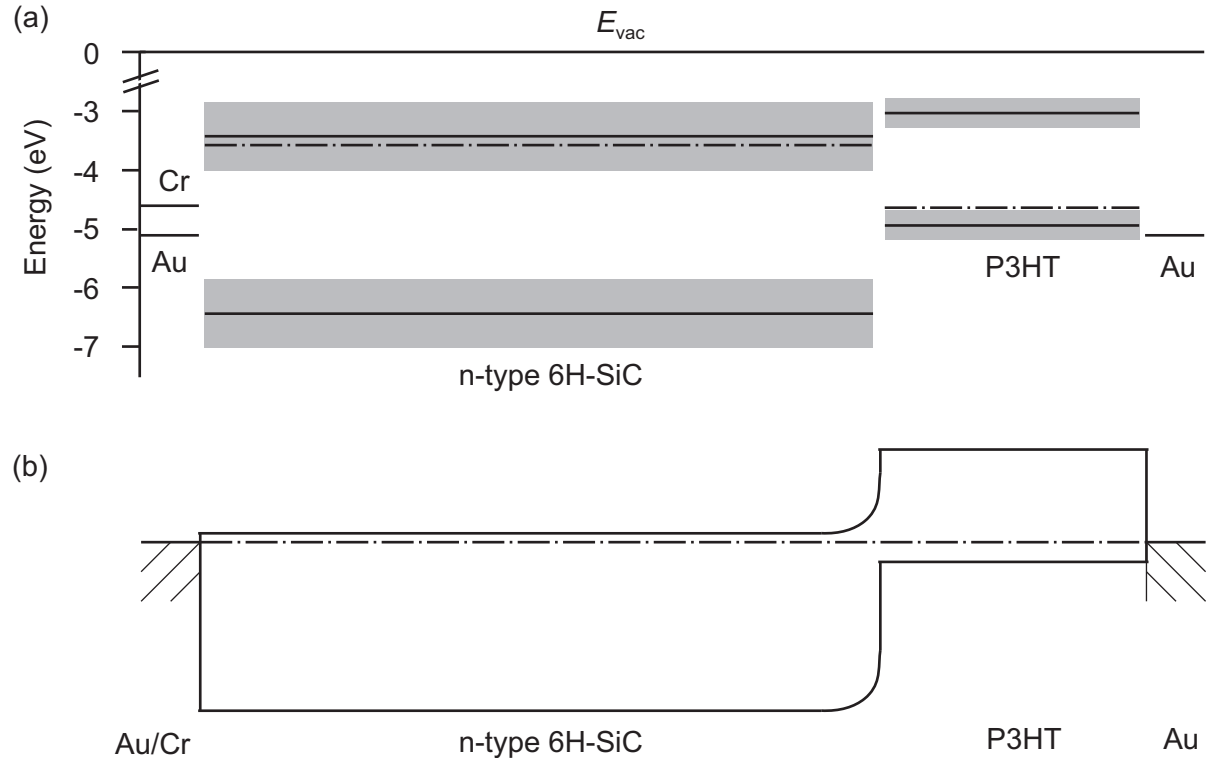

Figure 6.11: *(a) The energy bands of the materials used for the P3HT/6H-SiC heterojunction. The ranges of the literature values for 6H-SiC and P3HT are shown in grey, while the continuous black lines represent the average values. The dash-dotted lines show the Fermi levels in 6H-SiC and P3HT. (b) The band alignment of the P3HT/6H-SiC heterojunction as expected from Fermi level alignment.*

In Figure 6.12 the dark current-voltage characteristic (open squares) of a P3HT/6H-SiC heterojunction is shown in linear and semilogarithmic plots, including the fit (red line) and the individual components of the fit, the shunt resistance R_{Sh} (dashed line), the diode (dotted line) and the space-charge limited current (solid line). The sample preparation of the P3HT/6H-SiC heterojunction, which has, in contrast to the P3HT/Si heterojunction, a 150 nm thick P3HT layer and a transparent gold contact, is described in detail in Subsection 4.1.2. For the current-voltage characteristics the positive voltage corresponds to a positive potential on the P3HT side

of the junction. The symmetric shape of the current-voltage characteristics in the semilogarithmic plot (Figure 6.12 (b)) at small voltages is a strong indication for a shunt resistance R_{Sh} which governs the reverse current of the diode. This can be fitted by R_{Sh} = 5.2 kΩ cm^2, and is also shown in Figure 6.12 (b). Taking this value of R_{Sh}, the current-voltage curve was fitted using the proposed model of a series connection of a diode and a SCLC element, as shown in Figure 2.16. The overall fit, given by the red line in Figure 6.12, is in very good agreement with the data.

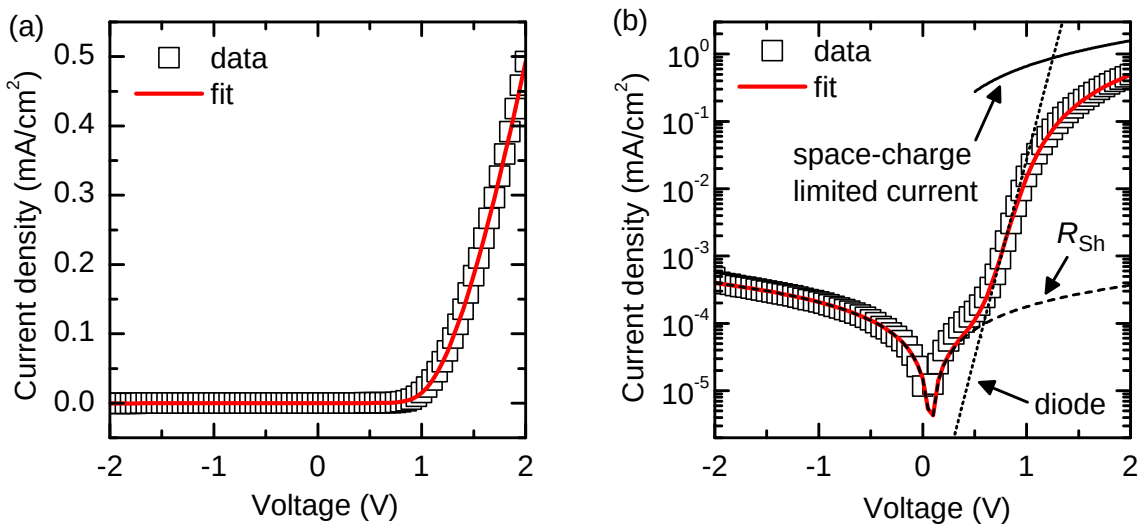

Figure 6.12: *Dark current-voltage characteristics of the P3HT/6H-SiC heterojunction in a linear (a) and a semilogarithmic (b) plot. Besides the measured data (open squares) and the fit (red line), also the different contributions to the fit, the shunt resistance R_{Sh} (dashed line), the diode (dotted line) and the space-charge limited current (solid line) are plotted.*

The extracted diode parameters, which describe the forward direction in the voltage range of 0.6 - 0.9 V, before the SCLC dominates at higher voltages, are the ideality factor n = 2.9 and the saturation current density $J_S = I_S/A = 3.5\times10^{-8}$ mA/cm^2. By using Equation 2.7, a barrier height of $e\varphi_{Bn}$ = 1.1 eV can be extracted from the saturation current. The forward direction is defined by the injection of electrons from the conduction band of 6H-SiC, where most of the donors are ionized at room temperature [Ruf94], into the LUMO of P3HT. Since the P3HT is undoped, injection of holes into the valence band of 6H-SiC should be negligible. The calculated barrier is therefore the barrier for thermionic emission of electrons from 6H-SiC to the LUMO of P3HT. In the reverse direction, electrons are injected from the ohmic Au contact, which is energetically aligned with the highest occupied molecular orbital (HOMO) of P3HT, into the LUMO of P3HT. The electrons must overcome a barrier of about 1.9 eV, though this value could be reduced by the presence of surface defect states. Thus, the forward and the reverse directions of the diode are governed by different barriers at different interfaces, in contrast to standard thermionic emission diodes. Furthermore, a high defect density, leading to a strong

recombination at the heterojunction interface, is indicated by the large ideality factor [Bre09]. The values for the SCLC element, as extracted from the fit of the dark current-voltage characteristics, are $m = 1.3$ and $k = 0.7$ mA/cm^2 V$^{1.3}$. Because of the series connection, the current through the diode and the SCLC resistance is the same, but the voltage is divided over both elements. This means, for example, that at a voltage of 0.5 V about 0.35 V drop at the diode and about 0.15 V drop at the SCLC resistance in the P3HT. However, in Figure 6.12 (b) the different contributions of the space-charge limited current and the diode for the fit are shown under the assumption that the entire voltage drops either at the SCLC resistance or at the diode.

Two different faces of the 6H-SiC sample, the Si face and the C face, were used for P3HT/SiC heterojunctions, but no significant effect on the current-voltage characteristics was observed. This is in accordance with the contact potential difference measurements in which the difference between the two polarities was determined to be only about 100 meV. Thus, compared to the determined barrier height of 1.1 eV, the influence of the crystal polarity can be neglected.

The reproducibility of the current-voltage characteristics of the P3HT/6H-SiC heterojunctions is much better than for P3HT/Si heterojunctions. The differences of the current density at voltages of ± 1 V is smaller than one order of magnitude, which still is high but significantly smaller than the two orders of magnitude which are observed for P3HT/Si heterojunctions. One may conclude that the better reproducibility can be assigned to the processing of the P3HT/6H-SiC samples, where the spin-coating and the evaporation of gold may be more defined than the drop-casting and the ITO evaporation in the case of P3HT/Si samples. However, P3HT/Si samples which were produced by spin-coating and gold evaporation still exhibited a bad reproducibility. The difference in the surface termination of the hydrophilic OH-terminated 6H-SiC and the hydrophobic H-terminated silicon must also be considered. However, a better wetting behavior of the P3HT is observed on hydrophobic surfaces, thus the difference in the surface termination will most probable also not be the reason for the difference in the variations of the current-voltage characteristics. Thus, one can conclude that the reason for the better reproducibility is the difference of the band alignment between the two inorganic semiconductors and the P3HT. For the P3HT/6H-SiC heterojunction, fluctuations of the exact positions of the HOMO of the P3HT relative to the valence band of 6H-SiC only play a minor role, as the energetic distance is large, as can be seen in Figure 6.11. In contrast, such fluctuations may have a large influence on the behavior of the P3HT/Si heterojunction, as the energy difference between the HOMO of P3HT and the valence band of silicon is small, as illustrated in Figure 6.1.

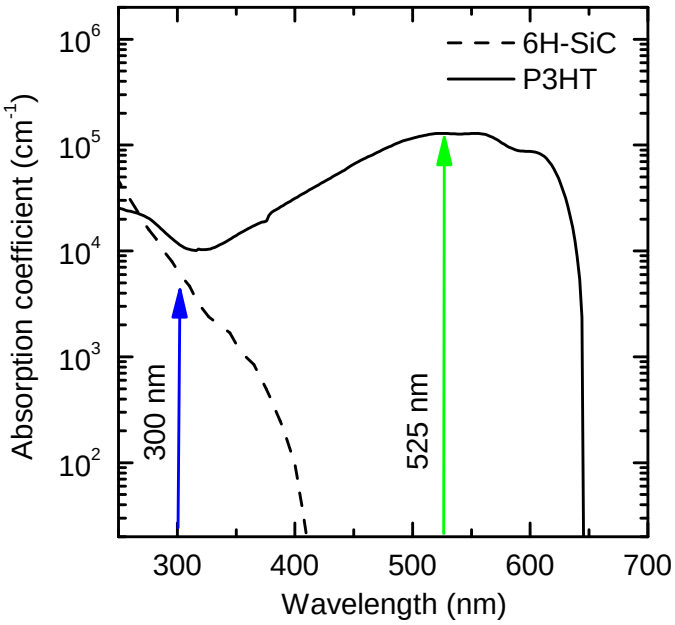

Figure 6.13: *Absorption spectra of 6H-SiC (dashed line) and P3HT (solid line). The arrows indicate the center wavelengths of the LEDs. Data for the 6H-SiC is taken from Reference [Phi60].*

6.2.2 Current-voltage characteristics under illumination

Current-voltage characteristics under illumination with different wavelengths

To examine the charge generation and separation mechanisms at the heterojunction under optical excitation, the current-voltage characteristics were measured under illumination with LEDs with center wavelengths of λ = 525 nm and λ = 300 nm. These wavelengths were chosen based on the absorption characteristics of P3HT and 6H-SiC: P3HT has an absorption onset at 650 nm and has an absorption maximum at about 550 nm, while 6H-SiC has an indirect bandgap of 3.0 eV and a corresponding absorption edge at about 400 nm. This can bee seen in the absorption spectra in Figure 6.13, in which also the center wavelengths of the LEDs are indicated.

If the sample is illuminated from the P3HT side of the junction, both wavelengths generate a photocurrent and an open-circuit voltage of up to $\approx$ 0.5 V, as shown in Figure 6.14 (a). In contrast, the current-voltage characteristics under illumination from the 6H-SiC side (Figure 6.14 (b)) reveal a photoresponse only for λ = 525 nm (green line). The last fact can be explained by the high absorption coefficient of $\alpha = 6.6\times10^3$ cm^{-1} for 6H-SiC at 300 nm, which leads to an absorption of all photons before they reach the interface. In addition, due to the short diffusion length for holes of approximately 1 - 4 μm in 6H-SiC [Pol05], all photo-excited charge carriers recombine before reaching the heterojunction. In contrast, under UV illumination (blue

line) from the P3HT side, photons reach 6H-SiC at the heterojunction interface, as P3HT has an absorption minimum at 300 nm (Figure 6.13). Thus, photons are absorbed in 6H-SiC near the heterojunction interface and, hence, contribute to the photocurrent. The higher photocurrent and open-circuit voltage under green illumination from the 6H-SiC side, compared to illumination from the P3HT side, can be understood by the fact that more photons reach the interface, since 6H-SiC, in contrast to P3HT, does not absorb at this wavelength. Photons absorbed in the bulk P3HT will not contribute significantly to the photocurrent because excitons in conjugated polymers have a binding energy of $0.1 - 0.4$ eV [Cam96, Alv98] and a diffusion length of only a few nanometers [Mar05, Zho06]. Thus, they can only be dissociated at the organic/inorganic interface. The strong reverse bias dependence of the photocurrent under green illumination on the electric field, in contrast to the photocurrent under UV illumination, can be explained by the fact that the charge carriers from the P3HT, even after exciton dissociation, are still bound by Coulomb attraction and can be dissociated by the electric field [Dei09].

In Figure 6.15 the wavelength-dependent photocurrent spectrum of a P3HT/6H-SiC heterojunction, which was illuminated from the P3HT side and measured at -1 V, is shown (black squares). The spectrum was recorded at 90 K and under a bias illumination of a LED with a center wavelength of 525 nm and an UV deuterium lamp. The bias illumination was used to generate photo-induced carriers which enhanced the conductivity of the sample, while the low temperature was chosen to reduce the dark current and enhance the signal-to-noise ratio. In addition, in Figure 6.15 the absorption spectra of 6H-SiC (dashed line) and P3HT (solid line) are shown. The photocurrent spectrum indicates that both materials contribute to the photocurrent, as the P3HT absorption onset is responsible for a strong increase in the photocurrent and at

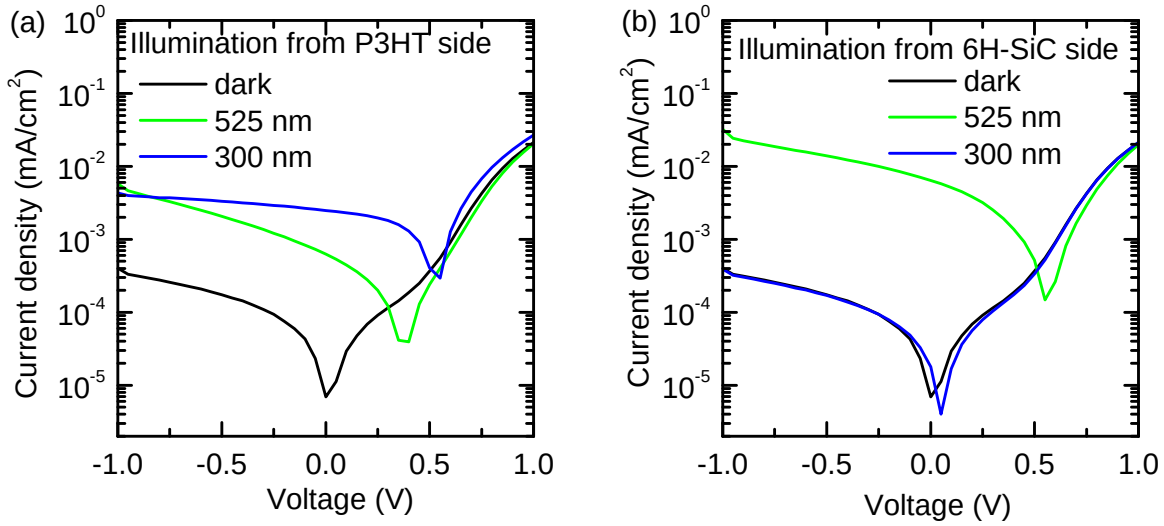

Figure 6.14: *Current-voltage characteristics of a P3HT/6H-SiC heterojunction in the dark (black line) and under illumination with λ = 525 nm (green line) and λ = 300 nm (blue line) from the P3HT (a) and 6H-SiC side (b).*

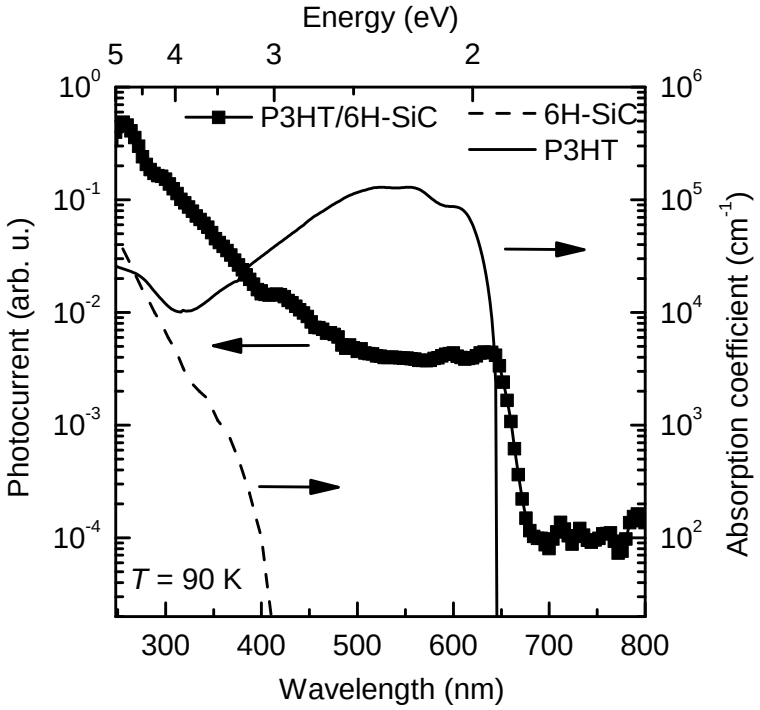

Figure 6.15: *Photocurrent of a P3HT/6H-SiC heterojunction (full squares) recorded at 90 K with an additional bias illumination of a LED with a center wavelength of 525 nm and an UV deuterium lamp. The absorption spectra of 6H-SiC (dashed line) and P3HT (solid line) are also shown. Data for 6H-SiC is taken from Reference [Phi60].*

smaller wavelengths the photocurrent follows the absorption of 6H-SiC. This observation is in accordance with the current-voltage characteristics under illumination at different wavelengths, as shown in Figure 6.14 (a).

The processes described above are shown schematically in Figure 6.16. Photon absorption, followed by exciton and charge carrier generation in P3HT and 6H-SiC, respectively, is illustrated by vertical straight arrows. The exciton dissociation at the P3HT/6H-SiC interface and the charge carrier transfer from the 6H-SiC are indicated by curved arrows, while the recombination of charge carriers is represented by dashed arrows.

Photovoltaic properties

When the heterojunction is illuminated from the 6H-SiC side by a halogen lamp with an intensity of 100 mW/cm^2, the current-voltage characteristics exhibits an open-circuit voltage of 0.55 V, a short-circuit current density of 8.2×10^{-3} mA/cm^2, and a fill factor of 0.22 which lead to an efficiency of $\approx$ 0.001 %. When the heterojunction is illuminated from the P3HT side, a slightly lower efficiency of $\approx$ 0.0009 % is achieved. The relevant quadrant of the current-voltage characteristics is shown in Figure 6.17 for illumination from the P3HT (a) and from the

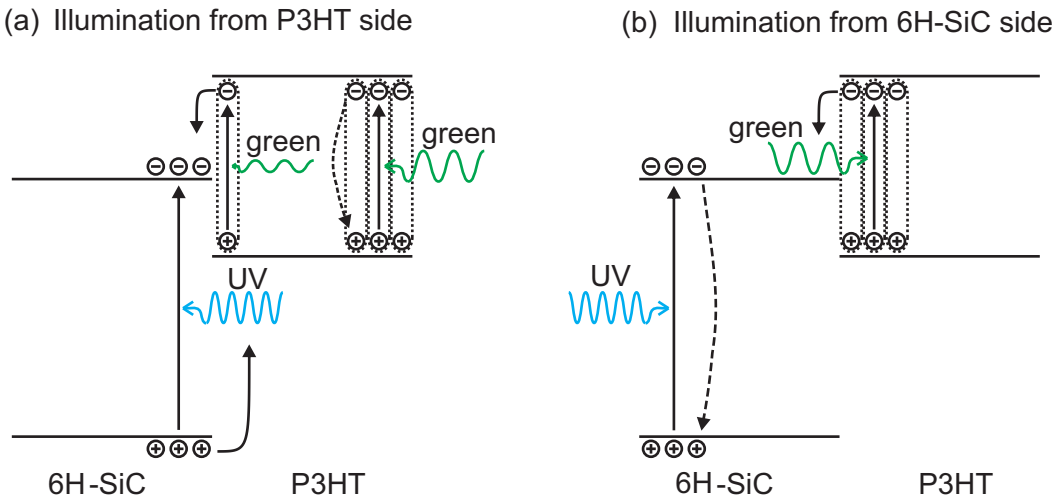

Figure 6.16: *Schematic representation of absorption, exciton generation and dissociation, charge generation and transfer, and recombination processes under illumination with different wavelengths from the P3HT (a) and the 6H-SiC side (b) of the heterojunction.*

6H-SiC side (b). The similar efficiencies can be understood by examination of Figure 6.14: Although the photocurrent under green light illumination from the P3HT side is smaller compared to the photocurrent under illumination from the 6H-SiC side, the spectral response is broader as also UV light contributes to the photocurrent generation. Thus, the total response under full spectrum illumination is similar for illumination from both sides of the junction. However, the overall efficiency is small for several reasons. First, the small interfacial area allows only partial exciton dissociation after absorption in the P3HT. Second, the spectrum of the halogen lamp is redshifted compared to the solar spectrum, which is unfavorable for this materials system which starts to absorb only at $\lambda \geq 650$ nm. In addition, the halogen lamp spectrum has only a small UV fraction, which leads to little contribution from the 6H-SiC. Above that, the gold front contact transmits only 50% - 70% of the light, depending on the exact wavelength. Furthermore, the fill factor is only 0.2, very likely due to SCLC effects (see Section 2.3), which also limit the fill factors of organic solar cells [Blo07].

6.2.3 Determination of the band alignment at the P3HT/6H-silicon carbide heterojunction

In order to obtain more detailed information about the band alignment at the P3HT/6H-SiC interface, the measurement of the open-circuit voltage was performed as a function of temperature under constant illumination by a xenon lamp. Here, a xenon lamp was used as the measurements were performed in a setup where the standard halogen lamp with an intensity of 100 mW/cm^2 could not be used. Instead, the highest light intensity on the sample in the spectral

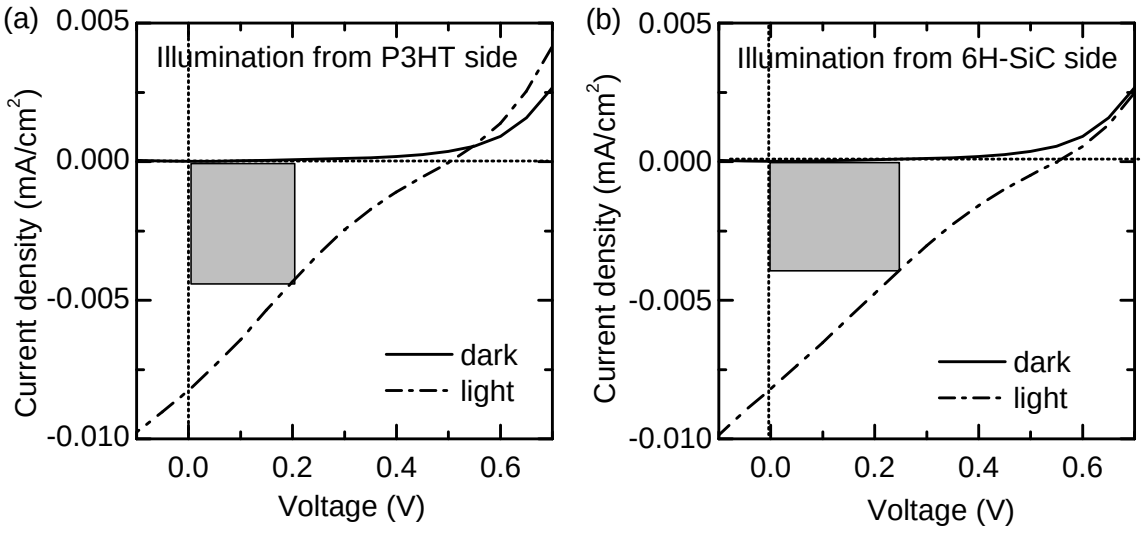

Figure 6.17: *Current voltage characteristics of a P3HT/6H-SiC heterojunction in the dark (solid line) and under illumination (dash-dotted line) with a halogen lamp with an intensity of 100 mW/cm^2 from the P3HT (a) and the 6H-SiC side (b).*

region below $\lambda \geq 650$ nm was achieved with a xenon lamp. Thus, the open circuit-voltage at 300 K is also lower than typically observed with the standard halogen lamp. The open-circuit voltage increases with decreasing temperature and finally saturates at a value of about 0.9 V, as shown in Figure 6.18. This behavior is also observed in organic solar cells, in which the open-circuit voltage saturates with decreasing temperature at the maximum open-circuit voltage $V_{\mathrm{OC}}^{\mathrm{max}}$ [Rie04, Ran07]. Similarly, the saturation value of 0.9 V can be identified as the $V_{\mathrm{OC}}^{\mathrm{max}}$ of the P3HT/6H-SiC heterojunction. The $V_{\mathrm{OC}}^{\mathrm{max}}$ in organic solar cells is defined as the difference between the HOMO of the donor and the LUMO of the acceptor of an organic heterojunction [Ran07, Bra01a], a definition which can be adapted to our system as follows:

$$eV_{\mathrm{OC}}^{\mathrm{max}} = E_{\mathrm{HOMO}}^{\mathrm{P3HT}} - E_{\mathrm{CB}}^{\mathrm{6H-SiC}}, \tag{6.1}$$

where $E_{\mathrm{CB}}^{\mathrm{6H-SiC}}$ and $E_{\mathrm{HOMO}}^{\mathrm{P3HT}}$ are the energy positions of the conduction band of 6H-SiC and of the HOMO of P3HT relative to vacuum, respectively. For this purpose, one can deduce from $V_{\mathrm{OC}}^{\mathrm{max}}$ that the energy difference between the HOMO of P3HT and the conduction band of 6H-SiC is 0.9 eV.

By adding this value to the value of $\mathrm{e}\varphi_{\mathrm{Bn}} = 1.1$ eV, the bandgap of P3HT is obtained with $\mathrm{e}V_{\mathrm{OC}}^{\mathrm{max}} + \mathrm{e}\varphi_{\mathrm{Bn}} = 2.0$ eV. The optical bandgap of P3HT was determined via absorption spectroscopy to approximately 1.9 eV. This value is in good agreement with the value of 2.0 eV determined here, since the exciton binding energy for polymers of $0.1 - 0.4$ eV [Cam96, Alv98] must be added to the value of the optical band gap to obtain the transport band gap. Thus, the values of $V_{\mathrm{OC}}^{\mathrm{max}}$ and φ_{Bn}, which both independently define the relative alignment of the energy bands, are consistent within the experimental accuracy. The determined alignment of the

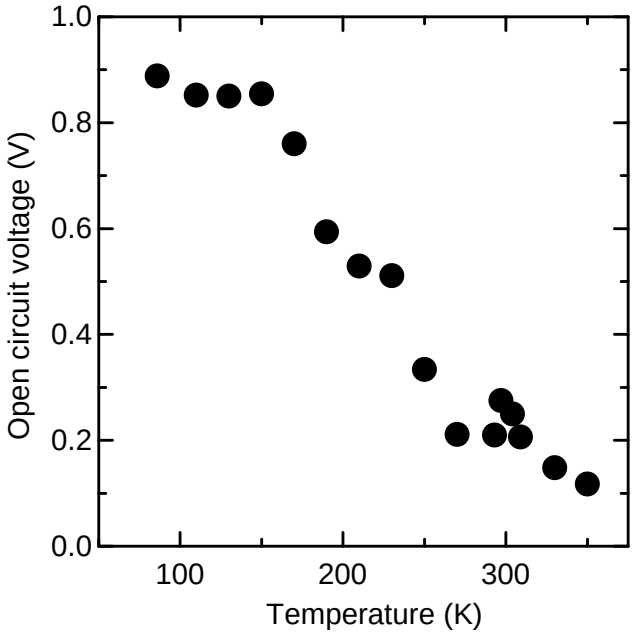

Figure 6.18: *The values of the open-circuit voltage for a P3HT/6H-SiC solar cell at different temperatures under white light illumination with a xenon lamp (see text for details). At low temperatures a saturation is observed at a value of about 0.9 eV.*

6H-SiC and the P3HT energy levels, as shown in Figure 6.19, is within the range of the literature values, shown in Figure 6.11 (a), which were used for prediction of the interface energetics. When using our experimental values for the work functions of 6H-SiC and P3HT, which were obtained by contact potential difference measurements, and the average literature values for the HOMO and LUMO of the P3HT, a good agreement between the predicted and the measured band alignment is achieved.

With the V_{OC}^{max} of 0.9 V and the φ_{Bn} of 1.1 V, the position of the conduction band minimum of 6H-SiC relative to the LUMO and the HOMO of P3HT is determined. Furthermore, for bulk 6H-SiC the energy difference between the Fermi level and the conduction band minimum is well defined. However, directly at the interface, we only know the total barrier height, φ_{Bn}, which may consist of two contributions: a depletion region in the 6H-SiC and the offset between the conduction band of 6H-SiC and the LUMO of P3HT. To clarify the different contributions and hence the exact band alignment at the interface of P3HT and 6H-SiC, surface photovoltage measurements of the freshly etched 6H-SiC surface were performed and an upward band bending of 0.3 - 0.4 eV was measured. This band bending at the surface of 6H-SiC was attributed to Fermi level pinning at surface defect states. When a further charge transfer between the 6H-SiC and the P3HT is neglected, this can be a rough estimate of the depletion layer in the 6H-SiC at the heterojunction interface. However, additional measurements will be required to specifically determine the interfacial band bending following junction formation.

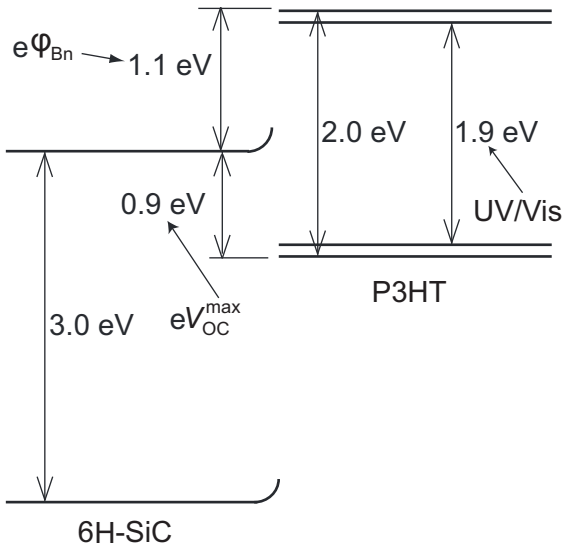

Figure 6.19: *Experimentally determined band alignment at the P3HT/6H-SiC heterojunction.*

Comparison of heterojunctions made of P3HT and silicon or 6H-SiC

When comparing the photovoltaic properties of a n-type 6H-SiC/P3HT heterojunction and a n-type Si/P3HT heterojunction, as described in the previous Section 6.1, the main difference is the hole transfer to P3HT: While holes can be transfered easily from the valence band of 6H-SiC to the HOMO of P3HT, in the P3HT/n-Si system this is not the case. Rather, a barrier for the photogenerated holes between the valence band of n-type silicon and the HOMO of P3HT is observed. This barrier explains the observation that the P3HT/n-Si heterojunction does not show a photovoltaic behavior. In addition, for a P3HT/p-Si heterojunction, where the holes are transferred from the HOMO of the P3HT to the valence band of silicon, a barrier for electrons exists and leads to a significant decrease of the efficiency which cancels out the broader absorption of silicon compared to 6H-SiC. In particular, under white light illumination with a halogen lamp with 100 mW/cm^2 the open-circuit voltage in the P3HT/p-Si heterojunction is smaller than in the P3HT/6H-SiC system. While an open-circuit voltage of 0.55 V is observed for the P3HT/6H-SiC heterojunction at room temperature, in the P3HT/p-Si heterojunction an open-circuit voltage of only about 0.1 V is measured. These findings show that a hybrid type II heterojunction, such as P3HT/6H-SiC, can work well as a solar cell when the band offsets at the heterojunction interface are large enough. In contrast, in a P3HT/Si heterojunction, barriers for charge carriers build up due to an unfavorable alignment of the energy levels.

7 Summary and Outlook

In this chapter, the most relevant findings which have been made during this work will be summarized. The demonstration of a hybrid bulk heterojunction solar cell based on silicon nanocrystals as well as the investigation of hybrid bilayer heterojunctions with bulk silicon and bulk 6H-SiC will be reviewed. Furthermore, an outlook will be given and further promising directions for the work with such material systems will be discussed.

Summary

Bulk heterojunctions, which are used for state-of-the-art organic solar cells, are also the basis for hybrid solar cells with inorganic nanoparticles. In this work, silicon nanocrystals with diameters ranging from $4-33$ nm, which were produced via gas-phase growth in a microwave reactor, were used for the fabrication of bulk heterojunction solar cells, where an organic semiconductor is mixed with silicon nanocrystals. On such bulk heterojunctions, LESR measurements were carried out to investigate if a photo-induced charge transfer between the silicon nanocrystals and the organic counterpart takes place. These measurements were performed for composites of silicon nanocrystals with either P3HT or PCBM, which typically act as electron donor or electron acceptor, respectively. In these composites, the photo-generation of either positive P3HT polarons or negative PCBM radicals could be detected via LESR. In the PCBM/Si-nc composite this photo-generation results in about one order of magnitude fewer light induced $PCBM^-$ anions than in the reference P3HT/PCBM bulk heterojunction. In contrast, in the P3HT/Si-nc composite this process takes place to a comparable degree as in the P3HT/PCBM heterojunction, resulting in a P3HT polaron density of 2.8×10^{17} g^{-1}. Due to this fact, and as P3HT has a higher absorption coefficient than PCBM, the P3HT/Si-nc composite was chosen as a material system for hybrid solar cells with silicon nanocrystals.

Wavelength-dependent LESR measurements on P3HT/Si-nc composites show that both materials, the P3HT and the silicon nanocrystals, contribute to the charge transfer. Furthermore, by means of time-dependent LESR measurements it could be observed that a fast (<1 s) charge transfer occurs in the P3HT/Si-nc bulk heterojunctions, which is in contrast to a slow trapping behavior on a timescale of minutes as observed in pure P3HT. Thus, it can be concluded that

a photo-induced charge transfer, in which both materials are involved, takes place in the heterojunction. Moreover, in EDMR experiments on P3HT/Si-nc bulk heterojunctions also the contribution of both materials to the charge transport could be identified.

The optical properties of the P3HT/Si-nc system were investigated via absorption spectroscopy, whereby an enhancement of the overall absorption range due to the incorporation of the silicon nanocrystals could be shown. In addition, it could be proven by absorption spectroscopy in the visible and infrared spectral range that the P3HT still has ordered domains upon mixing. However, a moderate decrease of the conjugation length of the P3HT in the composites was identified. The morphology of the P3HT/Si-nc composites was investigated with AFM and SEM measurements. Here, a considerable intermixing of the two materials was observed due to the use of chloroform as a common solvent, even if the silicon nanocrystals form agglomerates.

With bulk heterojunction solar cells made of a P3HT/Si-nc composite in a sandwich structure, open-circuit voltages of up to 0.76 V could be achieved. Thus, working hybrid solar cells with silicon nanocrystals could be demonstrated successfully. In addition, the contribution of both, the organic and the inorganic part, to the photo-induced current could be detected by photocurrent spectroscopy, which is in accordance with the findings of the wavelength-dependent LESR measurements. In particular, the photocurrent spectrum and also the open-circuit voltage are quite different as compared to P3HT Schottky solar cells without silicon nanocrystals. In the P3HT/Si-nc solar cells, the P3HT acts as electron donor, transferring photo-induced electrons to the conduction band of the silicon nanocrystals. The silicon nanocrystals, in return, transfer photo-induced holes to the HOMO of the P3HT. However, the efficiency of around 0.01 % needs to be optimized. This low value is most probably due to the large amount of interface defects, which are located at the silicon nanocrystal surface and act as recombination centers.

One promising approach to improve the efficiency of bulk heterojunction solar cells are ordered bulk heterojunctions. For this purpose, one semiconductor is textured with a high aspect ratio to obtain a large interfacial area and, hence, to efficiently dissociate excitons. In this work, soft lithography was applied to silicon nanocrystal layers to form an ordered bulk heterojunction. With this method, the structuring of silicon nanocrystal layers was demonstrated down to a lateral structure size of about 200 nm. However, as the aspect ratio was still low, no increase of the efficiency in P3HT/Si-nc heterojunctions with structured silicon nanocrystal layers could be achieved. Nevertheless, it has been demonstrated that soft lithography can be a tool to structure nanocrystal layers and may be used for ordered bulk heterojunctions.

In P3HT/Si-nc solar cells it is difficult to determine the exact band alignment of the energy levels of P3HT and the silicon nanocrystals at the heterojunction interface due to the large influence of the morphology. Thus, to achieve a better understanding of the interface energy level positions, heterojunctions of bulk crystalline silicon and P3HT were investigated as a

model system. On such bilayer heterojunctions current-voltage measurements were performed under illumination with high power LEDs of different wavelengths, which allow a selective excitation of charge carriers in P3HT, silicon, or both materials. From these measurements a disadvantageous energy band alignment of the valence band of silicon and the HOMO level of P3HT was observed. Hence, in contrast to bulk heterojunctions with silicon nanocrystals, only a small open-circuit voltage of 0.1 V is found in heterojunctions with bulk silicon. These findings reveal that for the silicon nanocrystals other effects, most likely the dangling bond defects at the surface of the nanocrystals, are responsible for the band alignment.

In hybrid heterojunctions with bulk silicon and P3HT a barrier for the transfer of photo-generated holes from the valence band of silicon into the HOMO of P3HT could be identified. To overcome this limitation, silicon was replaced by the semiconductor 6H-SiC for the formation of a hybrid P3HT/6H-SiC heterojunction. Here, the valence band edge of 6H-SiC is well below the HOMO of P3HT. To model the current-voltage characteristics of the P3HT/6H-SiC heterojunction, an equivalent circuit was proposed, which includes a diode, a space-charge limited current element, and a shunt resistance. The current-voltage characteristics of the P3HT/6H-SiC heterojunction could be described by thermionic emission of electrons from the conduction band of the n-type 6H-SiC over a barrier into the LUMO of P3HT. From the diode fitting parameters, this barrier was determined to 1.1 V. This value is in excellent agreement with the offset of 0.9 V between the conduction band of 6H-SiC and the HOMO of P3HT, which was determined from temperature-dependent measurements of the open-circuit voltage under illumination. Thus, the band alignment could be determined via two different approaches. Furthermore, under white light illumination a significant open-circuit voltage of 0.55 V at room temperature was achieved.

Outlook

One important challenge for bulk heterojunction solar cells with silicon nanocrystals is to increase the efficiency. However, the high defect density of the silicon nanocrystals is supposed to lead to large recombination losses. As shown recently, the efficiency of P3HT/Si-nc solar cells can be increased with silicon nanocrystals which exhibit a smaller surface defect density, which was achieved by etching and low-temperature annealing of the nanocrystals [Nie10, Nie11]. In addition, the regioregularity of the P3HT and the size of the silicon nanocrystals are further important material parameters to obtain higher efficiencies [Liu09, Nie11]. Thus, the development of the single components of the bulk P3HT/Si-nc solar cell is a promising way. Another option is the combination of the silicon nanocrystals with the organic semiconductor via the functionalization of the silicon nanocrystal surface with organic molecules. This could lead to an optimized morphology and to reduced losses at the interface. However, up to today only the functionalization with isolating molecules has been achieved [Man07b, Bau06b, Nel10].

Instead, a functionalization with semiconducting molecules with energy levels similar to the P3HT would be ideal. A further interesting possibility is the use of smaller nanocrystals, where the quantum confinement could lead to a larger bandgap, facilitating the hole transfer to the P3HT. In addition, SiGe alloys are a very interesting material system for nanocrystals, as they have a higher absorption coefficient than silicon, while the bandgap, up to a germanium fraction of about 80 %, is still about that of silicon [Gju07]. This would lead to a higher absorption in the inorganic part of a hybrid bulk heterojunction without a loss in the open-circuit voltage.

Another approach is the use of silicon nanowires, either from bulk silicon or from *e.g.* chemical vapor deposition [Tsa07]. This material system provides a large interfacial area and can lead to enhanced efficiencies due to a better charge extraction, similar to results on hybrid bulk heterojunction solar cells with nanowires of CdSe [Huy02]. To provide a better band alignment at the heterojunction interface, a functionalization with molecules which introduce a dipole may be performed, as shown in P3HT/TiO_2 heterojunctions [Goh07]. However, also the use of other organic semiconductors with different HOMO and LUMO levels, as compared to P3HT, is an interesting option.

Finally, 6H-SiC is an interesting material for hybrid bulk heterojunction solar cells. In particular, as solar cell prototypes made of P3HT/6H-SiC bilayer heterojunctions have been demonstrated in this work, further investigations on hybrid bulk heterojunctions with silicon carbide may be promising. For this purpose, silicon carbide nanoparticles or nanowires, which can be produced by various methods [Hon03, Liu07], can be used. Furthermore, by choosing different polytypes, silicon carbide with different band gaps can also be used in hybrid heterojunctions for photovoltaic applications.

Abbreviations and Symbols

Abbreviations

Abbreviation	Description
6H-SiC	6H silicon carbide
AFM	Atomic force microscopy
AM	Air mass
BET	Brunauer, Emmett, and Teller
CB	Conduction band
CPD	Contact potential difference
EDMR	Electrically detected magnetic resonance
EDX	Energy-dispersive X-ray spectroscopy
ESR	Electron spin resonance
FTIR	Fourier transform infrared
HOMO	Highest occupied molecular orbital
LED	Light-emitting diode
LESR	Light-induced electron spin resonance
LUMO	Lowest unoccupied molecular orbital
n-Si	n-type silicon
p-Si	p-type silicon
P^+	Positive polaron
P3HT	Poly(3-hexylthiophene)
PCBM	$[6,6]$-phenyl-C_{61}-butyric acid methyl ester
$PCBM^-$	Negative PCBM anion
PDMS	Poly(dimethylsiloxane)
PEDOT/PSS	Poly(3,4-ethylenedioxythiophene)/poly(styrenesulfonate)
SCLC	Space-charge limited current
SEM	Scanning electron microscope
Si-db	Silicon dangling bonds
Si-nc	Silicon nanocrystals
SiO_2-np	SiO_2 nanoparticles
TEM	Transmission electron microscope
VB	Valence band
UV	Ultra violet

Symbols

Symbol	Description	Unit
A	Area	m^2
A^*	Effective Richardson constant	$A/cm^2\,K^2$
B_0	External magnetic field	T
B_{res}	Resonant magnetic field	T
d	Thickness	cm
d_{BET}	Silicon nanocrystal diameter determined by BET	nm
D	Diffusion coefficient	cm^2/s
E	Energy	eV
E_F	Fermi level	eV
E_i	Intrinsic Fermi level	eV
E_t	Characteristic trap energy	eV
E_{gap}	Energy gap	eV
E_{vac}	Vacuum level	eV
E_{CB}^{6H-SiC}	Energy of the conduction band edge of 6H-SiC	eV
E_{HOMO}^{P3HT}	Energy of the HOMO of P3HT	eV
FF	Fill factor	–
g	g-factor	–
I	Current	A
I_m	Current at the maximum power point	A
I_S	Reverse saturation current	A
I_{Ph}	Photocurrent	A
I_{light}	Transmitted light intensity	W/m^2
I_{light}^0	Incident light intensity	W/m^2
J	Current density	A/cm^2
J_S	Reverse saturation current density	A/cm^2
J_{SC}	Short-circuit current density	A/cm^2
k_{SCLC}	Prefactor of the SCLC	$A/cm^2\,V^m$
k	Wave vector	cm^{-1}
l	$l = T_t/T$	–
L	Diffusion length	cm
m	Exponent of the SCLC	–
m^*	Effective mass	kg
n	Ideality factor	–
n_i	Intrinsic charge carrier concentration	cm^{-3}
$n(E)$	Trap density of states	cm^{-3}/eV
N_D	Donor impurity concentration	cm^{-3}

N_t	Total trap density	cm^{-3}
P_{Light}	Power of the light	W
$R(\lambda)$	Spectral reflectance	–
R_S	Series resistance	Ω
R_{Sh}	Shunt resistance per area	$\Omega\,cm^2$
T	Temperature	K
$T(\lambda)$	Spectral transmittance	–
T_t	Characteristic trap temperature	K
V	Voltage	V
V_{bi}	Build-in potential	V
V_m	Voltage at the maximum power point	V
V_J	Voltage drop at heterojunction	V
V_B	Voltage drop in the bulk	V
V_{OC}	Open-circuit voltage	V
V_{CPD}	Contact potential difference	V
V_{SPV}	Surface photovoltage	V
V_{OC}^{max}	Maximum open-circuit voltage	V
W	Width of the space charge region	cm
$\alpha(\lambda)$	Absorption coefficient	cm^{-1}
χ	Electronegativity	–
ΔE_{CB}	Offset of the conduction bands	eV
ΔE_{VB}	Offset of the valence bands	eV
ΔB_{pp}	Peak-to-peak linewidth of ESR spectrum	mT
ε_r	Relative permittivity	–
φ_{Bn}	Potential barrier height for electrons	V
φ_{Bp}	Potential barrier height for holes	V
Φ_M	Work function metal	eV
Φ_{SC}	Work function semiconductor	eV
η	Efficiency	%
λ	Wavelength	nm
μ	Mobility	$cm^2/V\,s$
σ	Standard deviation	–
σ_{BET}	Specific BET-surface	m^2/g
ξ	Electron affinity	eV

Acknowledgements

Finally, I would like to express my thanks to all the people that contributed to this work and made this thesis possible:

In particular I would like to thank

- **Prof. Dr. Martin Stutzmann** for giving me the possibility to work as a PhD student at his chair. Thank you for your support, the scientific freedom, the many interesting ideas, and for the friendly way to ask the right questions!
- My former diploma and bachelor students for their contributions to this thesis. It was a great time to work with you! Good luck with your PhD theses!

  Sabrina Niesar for the large variety of mixtures of silicon nanocrystals and P3HT you produced and measured.

  Helmut Nesswetter for establishing the right contacts for all the different bulk semiconductor/P3HT sandwich devices.

  Matthias Sachsenhauser for finding the parameters for the application of soft lithography to silicon nanocrystals.
- **Dr. André Ebbers, Dr. Martin Trocha, Dr. Frank-Martin Petrat, and Dr. Heiko Thiem** of Creavis, Evonik Degussa GmbH for the undoped silicon nanocrystals, the SEM pictures, and for financial support within the framework of the Science-to-Business Center Nanotronics in Marl. This project was founded by the government of **North Rhine-Westphalia** and was co-financed by the **European Union**.
- **Dr. Hartmut Wiggers** from the Universität Duisburg-Essen for the undoped and phosphorus-doped silicon nanocrystals of various sizes.
- The silicon nanocrystals group **Dr. Robert Lechner, Dr. André R. Stegner, and Dr. Rui N. Pereira**. It was really fun to explore the world of silicon nanocrystals together with you!
- **Prof. Dr. Martin S. Brandt** for the access to the state-of-the-art equipment of the ESR lab.

- **Sebastian J. Schöll and Dr. Ian D. Sharp** for the help concerning all SiC and contact potential difference measurement issues.
- **Dr. Stefan Harrer** for providing the silicon master for the soft lithography experiments.
- My roommates, as far as not already mentioned above, **Bernhard Laumer, Dr. Mario Gjukic, and Michael Fischer** for the good working atmosphere.
- **All other members of E25** for the nice time at the Walter Schottky Institute. **Veronika Enter** for taking care of all the organizational questions.
- **My wife Simone** for her love. Managing the balance act between working on your own PhD thesis and taking care of our lovely daughter wasn't always easy. Thank you!
- **My parents, my sister, and my brother** for supporting me all the time.

Thank You!

List of publications

1. A. Biebersdorf, R. Dietmueller, A. S. Susha, A. L. Rogach, S. K. Poznyak, D. V. Talapin, H. Weller, T. A. Klar, and J. Feldmann, *Semiconductor nanocrystals photosensitize C_{60} crystals*, Nano Lett. **6**, 1559 (2006).

2. R. N. Pereira, A. R. Stegner, K. Klein, R. Lechner, R. Dietmueller, H. Wiggers, M. S. Brandt, and M. Stutzmann, *Electronic transport through Si nanocrystal films: Spin-dependent conductivity studies*, Physica B **401-402**, 527 (2007).

3. A. Biebersdorf, R. Dietmueller, A. Ohlinger, T. A. Klar, J. Feldmann, D. V. Talapin, and H. Weller, *Photodoping with CdSe nanocrystals as a tool to probe trap state distributions in C_{60} crystals*, Appl. Phys. B **93**, 239 (2008).

4. A. R. Stegner, R. N. Pereira, K. Klein, R. Lechner, R. Dietmueller, M. S. Brandt, M. Stutzmann, and H. Wiggers, *Electronic transport in phosphorus-doped silicon nanocrystal networks*, Phys. Rev. Lett. **100**, 026803 (2008).

5. R. Lechner, A. R. Stegner, R. N. Pereira, R. Dietmueller, M. S. Brandt, A. Ebbers, M. Trocha, H. Wiggers, and M. Stutzmann, *Electronic properties of doped silicon nanocrystal films*, J. Appl. Phys. **104**, 053701 (2008).

6. R. Dietmueller, A. R. Stegner, R. Lechner, S. Niesar, R. N. Pereira, M. S. Brandt, A. Ebbers, M. Trocha, H. Wiggers, and M. Stutzmann, *Light-induced charge transfer in hybrid composites of organic semiconductors and silicon nanocrystals*, Appl. Phys. Lett. **94**, 113301 (2009).

7. S. Niesar, R. Dietmueller, H. Nesswetter, H. Wiggers, and M. Stutzmann, *Silicon/organic semiconductor heterojunction solar cells*, Phys. Status Solidi A **206**, 2775 (2009).

8. M. Stutzmann, J. Finley, C. Jirauschek, G. Csaba, P. Lugli, E. Biebl, R. Dietmueller, K. Müller, H. Langhuth, and U. Rührmair, *Method for security purposes*, European patent application EP 09157041.6, Technische Universität München, disclosure date: 31.03.2009 (2009).

9. R. Dietmueller, H. Nesswetter, S. J. Schoell, I. D. Sharp, and M. Stutzmann, *Band alignment at organic-inorganic heterojunctions between P3HT and n-type 6H-SiC*, ACS Appl. Mater. Interfaces **3**, 4286 (2011).

10. R. Dietmueller, S. Niesar, A. R. Stegner, M. S. Brandt, H. Wiggers, and M. Stutzmann, *Poly(3-hexylthiophene)/silicon nanocrystal bulk heterojunctions: Optical properties, photo-induced charge transfer and current transport*, in preparation (2012).

Bibliography

[Abd97] M. S. A. Abdou, F. P. Orfino, Y. Son, and S. Holdcroft: *Interaction of oxygen with conjugated polymers: Charge transfer complex formation with poly(3-alkylthiophenes)*, J. Am. Chem. Soc. **119**, 4518 (1997).

[Agn85] S. A. Agnihotry, K. K. Saini, T. K. Saxena, K. C. Nagpal, and S. Chandra: *Studies on e-beam deposited transparent conductive films of In_2O_3:Sn at moderate substrate temperatures*, J. Phys. D: Appl. Phys. **18**, 2087 (1985).

[AI05] M. Al-Ibrahim, H.-K. Roth, M. Schroedner, A. Konkin, A. Zhokhavets, G. Gobsch, P. Scharff, and S. Sensfuss: *The influence of the optoelectronic properties of poly(3-alkylthiophenes) on the device parameters in flexible polymer solar cells*, Org. Electron. **6**, 65 (2005).

[Ale07] P.-J. Alet, S. Palacin, P. R. I. Cabarrocas, B. Kalache, M. Firon, and R. de Bettignies: *Hybrid solar cells based on thin-film silicon and P3HT*, Eur. Phys. J. Appl. Phys. **36**, 231 (2007).

[Ale08] P.-J. Alet: *Hybrid thin-film solar cells based on nano-structured silicon and semiconducting polymer*, Ph.D. thesis, Ecole Polytechnique Paris (2008).

[Alv98] S. F. Alvarado, P. F. Seidler, D. G. Lidzey, and D. D. C. Bradley: *Direct determination of the exciton binding energy of conjugated polymers using a scanning tunneling microscope*, Phys. Rev. Lett. **81**, 1082 (1998).

[Ant02] J. A. Anta, J. Nelson, and N. Quirke: *Charge transport model for disordered materials: Application to sensitized TiO_2*, Phys. Rev. B **65**, 125324 (2002).

[Bau06a] E. F. Bauer: *Statik und Kinetik der Entnetzung ultradünner Polymerfilme*, Ph.D. thesis, Technische Universität München (2006).

[Bau06b] A. Baumer: *Structural and Electronic Properties of Hydrosilylated Silicon Surfaces*, Ph.D. thesis, Walter Schottky Institut, Technische Universität München (2006).

[Bec39] A. E. Becquerel: *On electric effects under the influence of solar radiation*, Compt. Rend. **9**, 561 (1839).

[Bee04] W. Beek, M. Wienk, and R. Janssen: *Efficient hybrid solar cells from zinc oxide nanoparticles and a conjugated polymer*, Adv. Mater. **16**, 1009 (2004).

[Beh99] W. S. Beh, I. T. Kim, D. Qin, Y. Xia, and G. M. Whitesides: *Formation of patterned microstructures of conducting polymers by soft lithography, and applications in microelectronic device fabrication*, Adv. Mater. **11**, 1038 (1999).

[Bin99] H. H. Binder: *Lexikon der chemischen Elemente*, S. Hirzel, Stuttgart (1999).

[Blo97] P. W. M. Blom, M. J. M. de Jong, and M. G. van Munster: *Electric-field and temperature dependence of the hole mobility in poly(p-phenylene vinylene)*, Phys. Rev. B **55**, R656 (1997).

[Blo07] P. W. M. Blom, V. D. Mihailetchi, L. J. A. Koster, and D. E. Markov: *Device physics of polymer:fullerene bulk heterojunction solar cells*, Adv. Mater. **19**, 1551 (2007).

[Bou07] J. Bouclé, P. Ravirajan, and J. Nelson: *Hybrid polymer-metal oxide thin films for photovotaic applications*, J. Mater. Chem. **17**, 3141 (2007).

[Bra01a] C. J. Brabec, A. Cravino, D. Meissner, N. S. Sariciftci, T. Fromherz, M. T. Rispens, L. Sanchez, and J. C. Hummelen: *Origin of the open circuit voltage of plastic solar cells*, Adv. Funct. Mater. **11**, 374 (2001).

[Bra01b] C. J. Brabec, N. S. Sariciftci, and J. C. Hummelen: *Plastic solar cells*, Adv. Funct. Mater. **11**, 15 (2001).

[Bra01c] C. J. Brabec, G. Zerza, G. Cerullo, S. D. Silvestri, S. Luzzati, J. C. Hummelen, and S. Sariciftci: *Tracing photoinduced electron transfer process in conjugated polymer/fullerene bulk heterojunctions in real time*, Chem. Phys. Lett. **340**, 232 (2001).

[Bra02] C. J. Brabec, A. Cravino, D. Meissner, N. S. Sariciftci, M. T. Rispens, L. Sanchez, J. C. Hummelen, and T. Fromherz: *The influence of materials work function on the open circuit voltage of plastic solar cells*, Thin Solid Films **403-404**, 368 (2002).

[Bra08] C. Brabec, V. Dyakonov, and U. Scherf: *Organic Photovoltaics*, Wiley-VCH, Weinheim (2008).

[Bra09] S. Braun, W. R. Salaneck, and M. Fahlman: *Energy-level alignment at organic/metal and organic/organic interfaces*, Adv. Mater. **21**, 1450 (2009).

[Bre09] O. Breitenstein, J. Bauer, A. Lotnyk, and J.-M. Wagner: *Defect induced non-ideal dark I-V characteristics of solar cells*, Superlatt. Microstr. **45**, 182 (2009).

[Bru38] S. Brunauer, P. Emmett, and E. Teller: *Adsorption of gases in multimolecular layers*, J. Am. Chem. Soc. **60**, 309 (1938).

[Brü08a] W. Brütting: *Physics of Organic Semiconductors*, Wiley-VCH, Weinheim (2008).

[Brü08b] W. Brütting and W. Rieß: *Grundlagen der organischen Halbleiter*, Physik Journal **5**, 33 (2008).

[Bur97] T. A. Burr, A. A. Seraphin, E. Werwa, and K. D. Kolenbrander: *Carrier transport in thin films of silicon nanoparticles*, Phys. Rev. B **56**, 4814 (1997).

[Cam96] I. H. Campbell, T. W. Hagler, D. L. Smith, and J. P. Ferraris: *Direct measurement of conjugated polymer electronic excitation energies using metal/polymer/metal structures*, Phys. Rev. Lett. **76**, 1900 (1996).

[Cas04] F. A. Castro, G. B. Silva, L. F. Santos, R. M. Faria, F. Nuesch, L. Zuppiroli, and C. F. O. Graeff: *Electrically detected magnetic resonance of organic and polymeric light emitting diodes*, J. Non-Cryst. Solids **338**, 622 (2004).

[Cas06] A. J. Cascio, J. E. Lyon, M. M. Beerbom, R. Schlaf, Y. Zhu, and S. A. Jenekhe: *Investigation of a polythiophene interface using photoemission spectroscopy in combination with electrospray thin-film deposition*, Appl. Phys. Lett. **88**, 062104 (2006).

[Cha54] D. M. Chapin, C. S. Fuller, and G. L. Pearson: *A new silicon p-n junction photocell for converting solar radiation into electrical power*, J. Appl. Phys. **25**, 676 (1954).

[Cha04] J.-F. Chang, B. Sun, D. W. Breiby, M. M. Nielsen, T. I. Solling, M. Giles, I. McCulloch, and H. Sirringhaus: *Enhanced mobility of poly(3-hexylthiophene) transistors by spin-coating from high-boiling-point solvents*, Chem. Mater. **16**, 4772 (2004).

[Cha08] Y.-M. Chang, W.-F. Su, and L. Wang: *Influence of photo-induced degradation on the optoelectronic properties of regioregular poly(3-hexylthiophene)*, Sol. Energy Mater. Sol. Cells **92**, 761 (2008).

[Che92] T.-A. Chen and R. D. Rieke: *The first regioregular head-to-tail poly(3-hexylthiophene-2,5-diyl) and a regiorandom isopolymer: Ni vs Pd catalysis of 2(5)-bromo-5(2)-(bromozincio)-3-hexylthiophene polymerization*, J. Am. Chem. Soc. **114**, 10087 (1992).

[Che95] T.-A. Chen, X. Wu, and R. D. Rieke: *Regiocontrolled synthesis of poly(3-alkylthiophenes) mediated by Rieke Zinc: Their characterization and solid-state properties*, J. Am. Chem. Soc. **117**, 233 (1995).

[Che07] Y. Cheng, G. Fang, C. Li, L. Yuan, L. Ai, B. Chen, X. Zhao, Z. Chen, W. Bai, and C. Zhan: *Fabrication and electrical, photosensitive properties of p-poly(9,9-diethylfluorene)/n-silicon nanowire heterojunction*, J. Appl. Phys. **102**, 083516 (2007).

[Che08] D. Cheyns, J. Poortmans, P. Heremans, C. Deibel, S. Verlaak, B. P. Rand, and J. Genoe: *Analytical model for the open-circuit voltage and its associated resistance in organic planar heterojunction solar cells*, Phys. Rev. B **77**, 165332 (2008).

[Che09] H.-Y. Chen, J. H. S. Zhang, Y. Liang, G. Yang, Y. Yang, L. Yu, Y. Wu, and G. Li: *Polymer solar cells with enhanced open-circuit voltage and efficiency*, Nat. Photonics **3**, 649 (2009).

[Chi03a] D. Chirvase, Z. Chiguvare, M. Knipper, J. Parisi, V. Dyakonov, and J. C. Hummelen: *Electrical and optical design and characterisation of regioregular poly(3-hexylthiophene-2,5-diyl)/fullerene-based heterojunction polymer solar cells*, Synth. Met. **138**, 299 (2003).

[Chi03b] D. Chirvase, Z. Chiguvare, M. Knipper, J. Parisi, V. Dyakonov, and J. C. Hummelen: *Temperature dependent characteristics of poly(3 hexylthiophene)-fullerene based heterojunction organic solar cells*, J. Appl. Phys. **93**, 3376 (2003).

[Chi04] Z. Chiguvare and V. Dyakonov: *Trap-limited hole mobility in semiconducting poly(3-hexylthiophene)*, Phys. Rev. B **70**, 235207 (2004).

[Cho04] S. A. Choulis, Y. Kim, J. Nelson, D. D. C. Bradley, M. Giles, M. Shkunov, and I. McCulloch: *High ambipolar and balanced carrier mobility in regioregular poly(3-hexylthiophene)*, Appl. Phys. Lett. **85**, 3890 (2004).

[Coa03a] K. M. Coakley, Y. Liu, M. D. McGehee, K. L. Frindell, and G. D. Stucky: *Infiltrating semiconducting polymers into self-assembled mesoporous titania films for photovoltaic applications*, Adv. Funct. Mater. **13**, 301 (2003).

[Coa03b] K. M. Coakley and M. D. McGehee: *Photovoltaic cells made from conjugated polymers infiltrated into mesoporous titania*, Appl. Phys. Lett. **83**, 3380 (2003).

[Coa05a] K. M. Coakley, Y. Liu, C. Goh, and M. D. McGehee: *Ordered organic-inorganic bulk heterojunction photovoltaic cells*, MRS Bull. **30**, 37 (2005).

[Coa05b] K. M. Coakley, B. S. Srinivasan, J. M. Ziebarth, C. Goh, Y. Liu, and M. D. McGehee: *Enhanced hole mobility in regioregular poythiophene infiltrated in straight nanopores*, Adv. Funct. Mater. **15**, 1927 (2005).

[Con05] M. A. Contreras, K. Ramanathan, J. AbuShama, F. Hasoon, D. L. Young, B. Egaas, and R. Noufi: *Diode characteristics in state-of-the-art* $ZnO/CdS/Cu(In_{1-x}Ga_x)Se_2$ *solar cells*, Prog. Photovolt: Res. Appl. **13**, 209 (2005).

[Cor07] V. Coropceanu, J. Cornil, D. A. da Silva Filho, Y. Olivier, R. Silbey, and J. Bredas: *Charge transport in organic semiconductors*, Chem. Rev. **107**, 926 (2007).

[Cow65] A. M. Cowley and S. M. Sze: *Surface states and barrier height of metal-semiconductor systems*, J. Appl. Phys. **36**, 3212 (1965).

[Cul75] P. R. Cullis and J. R. Marko: *Electron paramagnetic resonance properties of n-type silicon in the intermediate impurity-concetration range*, Phys. Rev. B **11**, 4184 (1975).

[Das55] W. C. Dash and R. Newman: *Intrinsic optical absorption in single-crystal germanium and silicon at 77 K and 300 K*, Phys. Rev. **99**, 1151 (1955).

[Day10] S. Dayal, N. Kopidakis, D. C. Olson, D. S. Ginley, and G. Rumbles: *Photovoltaic devices with a low band gap polymer and CdSe nanostructures exceeding 3% efficiency*, Nano Lett. **10**, 239 (2010).

[DC01] J. De Ceuster, E. Goovaerts, A. Bouwen, J. C. Hummelen, and V. Dyakonov: *High-frequency (95 GHz) electron paramagnetic resonance study of the photoinduced charge transfer in conjugated polymer-fullerene composites*, Phys. Rev. B **64**, 195206 (2001).

[Dei09] C. Deibel, T. Strobel, and V. Dyakonov: *Origin of the efficient polaron-pair dissociation in polymer-fullerene blends*, Phys. Rev. Lett. **103**, 036402 (2009).

[Del93] C. Delerue, G. Allan, and M. Lannoo: *Theoretical aspects of the luminescence of porous silicon*, Phys. Rev. B **48**, 11024 (1993).

[Dil59] J. A. Dillon, R. E. Schlier, and H. E. Farnsworth: *Some surface properties of silicon-carbide crystals*, J. Appl. Phys. **30**, 675 (1959).

[Dre96] M. S. Dresselhaus, G. Dresselhaus, and P. C. Eklund: *Science of Fullerenes and Carbon Nanotubes*, Academic Press, San Diego (1996).

[Due02] A. C. Duerr, F. Schreiber, M. Kelsch, H. D. Carstanjen, and H. Dosch: *Morphology and thermal stability of metal contacts on crystalline organic thin films*, Adv. Mater. **14**, 961 (2002).

[Dya97] V. Dyakonov: *Spectroscopy on Conjugated Polymer Devices,* in : *Primary Photoexcitations in Conjugated Polymers: Molecular Exciton versus Semiconductor Band Model*, edited by N. S. Sariciftci, World Scientific, New Jersey (1997).

[Dya99] V. Dyakonov, G. Zoriniants, M. Scharber, C. J. Brabec, R. A. J. Janssen, J. C. Hummelen, and N. S. Sariciftci: *Photoinduced charge carriers in conjugated polymer-fullerene composites studied with light-induced electron-spin resonance*, Phys. Rev. B **59**, 8019 (1999).

[Dye10a] American Dye Source, Inc., Product Bulletin: ADS306PT (2010).

[Dye10b] American Dye Source, Inc., http://www.adsdyes.com/solarcells.html (2010).

[Els08] A. Elschner and S. Kirchmeyer: *PEDOT-Type Materials in Organic Solar Cells,* in : *Organic Photovoltaics*, edited by C. Brabec, V. Dyakonov, and U. Scherf, Wiley-VCH, Weinheim (2008).

[Est08] M. Estrada, I. Mejia, A. Cerdeira, and B. Iniguez: *MIS polymeric structures and OTFTs using PMMA on P3HT layers*, Solid-State Electron. **52**, 53 (2008).

[Ett97] E. Ettedgui, B. R. Hsieh, and Y. Gao: *Interface formation of metals and poly(p-phenylene vinylene): Surface species and band bending*, Polym. Adv. Technol. **8**, 408 (1997).

[Fal06] H. R. Fallah, M. Ghasemi, A. Hassanzadeh, and H. Steki: *The effect of deposition rate on electrical, optical and structural properties of tin-doped indium oxide (ITO) films on glass at low substrate temperature*, Phys. B: Cond. Mat. **373**, 274 (2006).

[Fis90] G. R. Fisher and P. Barnes: *Towards a unified view of polytypism in silicon carbide*, Phil. Mag. B **61**, 217 (1990).

[For84a] S. R. Forrest, M. L. Kaplan, and P. H. Schmidt: *Organic-on-inorganic semiconductor contact barrier diodes. I. Theory with applications to organic thin films and prototype devices*, J. Appl. Phys. **55**, 1492 (1984).

[For84b] S. R. Forrest, M. L. Kaplan, and P. H. Schmidt: *Organic-on-inorganic semiconductor contact barrier diodes. II. Dependence on organic film and metal contact properties*, J. Appl. Phys. **56**, 543 (1984).

[För59] T. Förster: *Transfer mechanism of electronic excitation*, Discuss. Faraday Soc. **27**, 7 (1959).

[Fur87] Y. Furukawa, M. Akimoto, and I. Harada: *Vibrational key bands and electrical conductivity of polythiophene*, Synth. Met. **18**, 151 (1987).

[Gap98] S. V. Gaponenko: *Optical properties of semiconductor nanocrystals*, Cambridge University Press, Cambridge (1998).

[Gat05] B. D. Gates, Q. Xu, M. Stewart, D. Ryan, C. G. Willson, and G. M. Whitesides: *New approaches to nanofabrication: Molding, printing, and other techniques*, Chem. Rev. **105**, 1171 (2005).

[Ge07] Y. Ge and J. E. Whitten: *Energy level alignment between sexithiophene and buckminsterfullerene films*, Chem. Phys. Lett. **448**, 65 (2007).

[Geo00] J. George and C. S. Menon: *Electrical and optical properties of electron beam evaporated ITO thin films*, Surf. Coat. Technol. **132**, 45 (2000).

[Gju07] M. Gjukic: *Metal-Induced Crystallization of Silicon-Germanium Alloys*, Ph.D. thesis, Walter Schottky Institut, Technische Universität München (2007).

[Gün03] H. Günzler and H.-U. Gremlich: *IR-Spektroskopie*, Wiley-VCH, Weinheim (2003).

[Goh05a] C. Goh, K. M. Coakley, and M. D. McGehee: *Nanostructuring titania by embossing with polymer molds made from anodic alumina templates*, Nano Lett. **5**, 1545 (2005).

[Goh05b] C. Goh, R. J. Kline, M. D. McGehee, E. N. Kadnikova, and J. M. J. Frechet: *Molecular-weight-dependent mobilities in regioregular poly(3-hexyl-thiophene) diodes*, Appl. Phys. Lett. **86**, 122110 (2005).

[Goh07] C. Goh, S. R. Scully, and M. D. McGehee: *Effects of molecular interface modification in hybrid organic-inorganic photovoltaic cells*, J. Appl. Phys. **101**, 114503 (2007).

[Gow06] V. Gowrishankar, S. R. Scully, M. D. McGehee, Q. Wang, and H. M. Branz: *Exciton splitting and carrier transport across the amorphous-silicon/polymer solar cell interface*, Appl. Phys. Lett. **89**, 252102 (2006).

[Gow08] V. Gowrishankar, S. R. Scully, A. T. Chan, M. D. McGehee, Q. Wang, and H. M. Branz: *Exciton harvesting, charge transfer, and charge-carrier transport in amorphous-silicon nanopillar/polymer hybrid solar cells*, J. Appl. Phys. **103**, 064511 (2008).

[Goy85] R. P. Goyal, D. Raviendra, and B. R. K. Gupta: *Electroless deposition of In_2O_3 and In_2O_3 : Sn (ITO)*, Phys. Status Solidi A **87**, 79 (1985).

[Gra76] C. Granqvist and R. Buhrman: *Ultrafine metal particles*, J. Appl. Phys. **47**, 2200 (1976).

[Gre96] N. C. Greenham, X. G. Peng, and A. P. Alivisatos: *Charge separation and transport in conjugated-polymer/semiconductor-nanocrystal composites studied by photoluminescence quenching and photoconductivity*, Phys. Rev. B **54**, 17628 (1996).

[Gre10] M. A. Green, K. Emery, X. Hishikawa, and W. Warta: *Solar cell efficiency tables (version 36)*, Prog. Photovolt: Res. Appl. **18**, 346 (2010).

[Gue07] S. Guenes, K. P. Fritz, H. Neugebauer, N. S. Sariciftci, S. Kumar, and G. D. Scholes: *Hybrid solar cells using PbS nanoparticles*, Sol. Energy Mater. Sol. Cells **91**, 420 (2007).

[Gue08] S. Guenes and N. S. Sariciftci: *Hybrid solar cells*, Inorg. Chim. Acta **361**, 581 (2008).

[Guo07] L. J. Guo: *Nanoimprint lithography: Methods and material requirements*, Adv. Mater. **19**, 495 (2007).

[Gup10] D. Gupta, S. Mukhopadhyay, and K. S. Narayan: *Fill factor in organic solar cells*, Sol. Energy Mater. Sol. Cells **94**, 1309 (2010).

[Har07] S. Harrer, J. K. W. Yang, G. A. Salvatore, K. K. Berggren, F. Ilievski, and C. A. Ross: *Pattern generation by using multistep room-temperature nanoimprint lithography*, IEEE Trans. Nanotech. **6**, 639 (2007).

[Hee01] A. J. Heeger: *Nobel lecture: Semiconducting and metallic polymers: The fourth generation of polymeric materials*, Rev. Mod. Phys. **73**, 681 (2001).

[Hei65] V. Heine: *Theory of surface states*, Phys. Rev. **138**, A1689 (1965).

[Hei09] M. D. Heinemann, K. von Maydell, F. Zutz, J. Kolny-Olesiak, H. Borchert, I. Riedel, and J. Parisi: *Photo-induced charge transfer and relaxation of persistent charge carriers in polymer/nanocrystal composites for applications in hybrid solar cells*, Adv. Funct. Mater. **19**, 3788 (2009).

[Hik03] R. A. M. Hikmet, D. V. Talapin, and H. Weller: *Study of conduction mechanism and electroluminescence in CdSe/ZnS quantum dot composites*, J. Appl. Phys. **93**, 3509 (2003).

[Ho07] P.-H. Ho, L.-L. Chua, M. Dipankar, X. Gao, D. Qi, A.-S. Wee, J.-F. Chang, and R. Friend: *Solvent effects on chain orientation and interchain π-interaction in conjugated polymer thin films: Direct measurements of the air and substrate interfaces by near-edge X-ray absorption spectroscopy*, Adv. Mater. **19**, 215 (2007).

[Hon03] S.-I. Honda, Y.-G. Baek, T. Ikuno, H. Kohara, M. Katayama, K. Oura, and T. Hirao: *SiC nanofibers grown by high power microwave plasma chemical vapor deposition*, Appl. Surf. Sci. **212-213**, 378 (2003).

[Hop04a] H. Hoppe, M. Niggemann, C. Winder, J. Kraut, R. Hiesgen, A. Hinsch, D. Meissner, and N. S. Sariciftci: *Nanoscale morphology of conjugated polymer/fullerene-based bulk-heterojunction solar cells*, Adv. Funct. Mater. **14**, 1005 (2004).

[Hop04b] H. Hoppe and N. S. Sariciftci: *Organic solar cells: An overview*, J. Mater. Res. **19**, 1924 (2004).

[Hop06] H. Hoppe and N. S. Sariciftci: *Morphology of polymer/fullerene bulk heterojunction solar cells*, J. Mater. Chem. **16**, 45 (2006).

[Hsu10] J. W. P. Hsu and M. T. Lloyd: *Organic/inorganic hybrids for solar energy generation*, MRS Bull. **35**, 422 (2010).

[Hug04] S. Hugger, R. Thomann, T. Heinzel, and T. Thurn-Albrecht: *Semicrystalline morphology in thin films of poly(3-hexylthiophene)*, Colloid Polym. Sci. **282**, 932 (2004).

[Hul99] R. Hull: *Properties of Crystalline Silicon*, INSPEC, The Institution of Electrical Engineers, London (1999).

[Huy02] W. U. Huynh, J. J. Dittmer, and A. P. Alivisatos: *Hybrid nanorod-polymer solar cells*, Science **295**, 2425 (2002).

[Huy03] W. U. Huynh, J. J. Dittmer, N. Teclemariam, D. J. Milliron, A. P. Alivisatos, and K. W. J. Barnham: *Charge transport in hybrid nanorod-polymer composite photovoltaic cells*, Phys. Rev. B **67**, 115326 (2003).

[Ima07] J. Imasu and Y. Sakka: *Large-scale patterning of TiO_2 nano powders using micro molds*, J. Ceram. Soc. Jpn. **115**, 697 (2007).

[Iof10] Ioffe Physico-Technical Institut Electronic Archive: *New semiconductor materials. Characteristics and properties*, available online at: http://www.ioffe.ru/SVA/NSM (2010).

[Ish99] H. Ishii, K. Sugiyama, E. Ito, and K. Seki: *Energy level alignment and interfacial electronic structures at organic/metal and organic/organic interfaces*, Adv. Mater. **11**, 605 (1999).

[Ish05] H. Ishii, N. Hayashi, E. Ito, Y. Washizu, K. Sugi, Y. Kimura, M. Niwano, O. Ouchi, and K. Seki: *Kelvin Probe Study of Band Bending at Organic Semiconductor/Metal Interfaces: Examination of Fermi Level Alignment,* in : *Physics of Organic Semiconductors*, edited by W. Brütting, Wiley-VCH, Weinheim (2005).

[Kah03] A. Kahn, N. Koch, and W. Y. Gao: *Electronic structure and electrical properties of interfaces between metals and π-conjugated molecular films*, J. Polym. Sci., Part B: Polym. Phys. **41**, 2529 (2003).

[Kim98] J. S. Kim, M. Granstroem, R. H. Friend, N. Johansson, W. R. Salaneck, R. Daik, W. J. Feast, and F. Cacialli: *Indium-tin oxide treatments for single- and double-layer polymeric light-emitting diodes: The relation between the anode physical, chemical, and morphological properties and the device performance*, J. Appl. Phys. **84**, 6859 (1998).

[Kim99] J. S. Kim, F. Cacialli, M. Granström, R. H. Friend, N. Johansson, W. R. Salaneck, R. Daik, and W. J. Feast: *Characterization of the properties of surface-treated indium-tin oxide thin films*, Synth. Met. **101**, 111 (1999).

[Kim05] Y. Kim, S. A. Choulis, J. Nelson, D. D. C. Bradley, S. Cook, and J. R. Durrant: *Device annealing effect in organic solar cells with blends of regioregular poly(3-hexylthiophene) and soluble fullerene*, Appl. Phys. Lett. **86**, 063502 (2005).

[Kim06] Y. Kim, S. Cook, S. M. Tuladhar, S. A. Choulis, J. Nelson, J. R. Durrant, D. D. C. Bradley, M. Giles, I. McCulloch, C.-S. Ha, and M. Ree: *A strong regioregularity effect in self-organizing conjugated polymer films and high-efficiency polythiophene:fullerene solar cells*, Nat. Mater. **5**, 197 (2006).

[Kim07] M.-S. Kim, J.-S. Kim, J. C. Cho, M. Shtein, L. J. Guo, and J. Kim: *Flexible conjugated polymer photovoltaic cells with controlled heterojunctions fabricated using nanoimprint lithography*, Appl. Phys. Lett. **90**, 123113 (2007).

[Kle08] K. Klein: *Spin-dependent transport in silicon nanocrystals*, Diploma thesis, Walter Schottky Institut, Technische Universität München (2008).

[Kni04] J. Knipping, H. Wiggers, B. Rellinghaus, P. Roth, D. Konjhodzic, and C. Meier: *Synthesis of high purity silicon nanoparticles in a low pressure microwave reactor*, J. Nanosci. Nanotechnol. **4**, 1039 (2004).

[Kon95] K. Konstadinidis, F. Papadimitrakopoulos, M. Galvin, and R. L. Opila: *In situ x-ray photoelectron spectroscopy study of aluminum/poly (p-phenylenevinylene) interfaces*, J. Appl. Phys. **77**, 5642 (1995).

[Kon05] D. V. Konarev, R. N. Lyubovskaya, G. Zerza, M. C. Scharber, and N. S. Sariciftci: *Photoinduced electron transfer in solid C_{60} donor/acceptor complexes studied by light-induced electron-spin resonance*, Mol. Cryst. Liq. Cryst. **427**, 315 (2005).

[Kon10] Konarka Technologies, Inc.: http://www.konarka.com (2010).

[Kos05] L. J. A. Koster, V. D. Mihailetchi, R. Ramaker, and P. W. M. Blom: *Light intensity dependence of open-circuit voltage of polymer-fullerene solar cells*, Appl. Phys. Lett. **86**, 123509 (2005).

[Kri07] V. Krinichnyi, H.-K. Roth, S. Sensfuss, M. Schrödner, and M. Al-Ibrahim: *Dynamics of photoinduced radical pairs in poly(3-dodecylthiophene)/fullerene composite*, Physica E **36**, 98 (2007).

[Kro99] L. Kronik and Y. Shapira: *Surface photovoltage phenomena: Theory, experiment, and applications*, Surf. Sci. Rep. **37**, 1 (1999).

[Kro03] J. E. Kroeze, T. J. Savenije, M. J. W. Vermeulen, and J. M. Warman: *Contactless determination of the photoconductivity action spectrum, exciton diffusion length, and charge separation efficiency in polythiophene-sensitized TiO_2 bilayers*, J. Phys. Chem. B **107**, 7696 (2003).

[Kum09] A. Kumar, S. Sista, and Y. Yang: *Dipole induced anomalous S-shape I-V curves in polymer solar cells*, J. Appl. Phys. **105**, 094512 (2009).

[Lam56] M. A. Lampert: *Simplified theory of space-charge-limited currents in an insulator with traps*, Phys. Rev. **103**, 1648 (1956).

[Lüe04] L. Lüer, H. J. Egelhaaf, D. Oelkrug, G. Cerullo, G. Lanzani, B. H. Huisman, and D. de Leeuw: *Oxygen-induced quenching of photoexcited states in polythiophene films*, Org. Electron. **5**, 83 (2004).

[Lec08a] R. Lechner: *Silicon Nanocrystal Films for Electronic Applications*, Ph.D. thesis, Walter Schottky Institut, Technische Universität München (2008).

[Lec08b] R. Lechner, A. R. Stegner, R. N. Pereira, R. Dietmueller, M. S. Brandt, A. Ebbers, M. Trocha, H. Wiggers, and M. Stutzmann: *Electronic properties of doped silicon nanocrystal films*, J. Appl. Phys. **104**, 053701 (2008).

[Led00] G. Ledoux, O. Guillois, D. Porterat, C. Reynaud, F. Huisken, B. Kohn, and V. Paillard: *Photoluminescence properties of silicon nanocrystals as a function of their size*, Phys. Rev. B **62**, 15942 (2000).

[Lee94] C. H. Lee, G. Yu, B. Kraabel, D. Moses, and V. I. Srdanov: *Effects of oxygen on the photocarrier dynamics in a C_{60} film: Studies of transient and steady-state photoconductivity*, Phys. Rev. B **49**, 10572 (1994).

[Lev96] M. E. Levinshtein and S. L. Rumyantsev: *Handbook Series on Semiconductor Parameters, Vol. 1*, World Scientific, London (1996).

[Lev01] M. E. Levinshtein, S. L. Rumyantsev, and M. S. Shur: *Properties of Advanced Semiconductor Materials: GaN, AlN, InN, BN, SiC, SiGe*, John Wiley & Sons, Inc., New York (2001).

[Lev04] I. A. Levitsky, W. B. Euler, N. Tokranova, B. Xu, and J. Castracane: *Hybrid solar cells based on porous Si and copper phthalocyanine derivatives*, Appl. Phys. Lett. **85**, 6245 (2004).

[Lew07] N. S. Lewis: *Powering the planet*, MRS Bull. **32**, 808 (2007).

[Li05] G. Li, V. Shrotriya, J. Huang, Y. Yao, T. Moriarty, K. Emery, and Y. Yang: *High-efficiency solution processable polymer photovoltaic cells by self-organization of polymer blends*, Nat. Mater. **4**, 864 (2005).

[Liu05] Y. Liu, M. A. Summers, C. Edder, J. M. J. Fréchet, and M. D. McGehee: *Using resonance energy transfer to improve exciton harvesting in organic-inorganic hybrid photovoltaic cells*, Adv. Mater. **17**, 2960 (2005).

[Liu07] Z. Liu, L. Ci, N. Y. Jin-Philipp, and M. Ruehle: *Vapor-solid reaction for silicon carbide hollow spherical nanocrystals*, J. Phys. Chem. C **111**, 12517 (2007).

[Liu09] C.-Y. Liu, Z. C. Holman, and U. R. Kortshagen: *Hybrid solar cells from P3HT and silicon nanocrystals*, Nano Lett. **9**, 449 (2009).

[Llo01] G. Lloyd and B. Eccleston: *Conjugated polymer thin film transistors constructed using ohmic and Schottky source/drain contacts*, Mat. Res. Soc. Symp. Proc. **660**, JJ5.12.1 (2001).

[Loo08] Y.-L. Loo and I. McCulloch: *Progress and challenges in commercialization of organic electronics*, MRS Bull. **33**, 653 (2008).

[Ma05] W. L. Ma, C. Y. Yang, X. Gong, K. Lee, and A. J. Heeger: *Thermally stable, efficient polymer solar cells with nanoscale control of the interpenetrating network morphology*, Adv. Funct. Mater. **15**, 1617 (2005).

[Man07a] M. M. Mandoc, W. Veurman, L. J. A. Koster, B. de Boer, and P. W. M. Blom: *Origin of the reduced fill factor and photocurrent in MDMO-PPV:PCNEPV all-polymer solar cells*, Adv. Funct. Mater. **17**, 2167 (2007).

[Man07b] L. Mangolini and U. Kortshagen: *Plasma-assisted synthesis of silicon nanocrystal inks*, Adv. Mater. **19**, 2513 (2007).

[Mar05] D. E. Markov, E. Amsterdam, P. W. M. Blom, A. B. Sieval, and J. C. Hummelen: *Accurate measurement of the exciton diffusion length in a conjugated polymer using a heterostructure with a side-chain cross-linked fullerene layer*, J. Phys. Chem. A **109**, 5266 (2005).

[Mar06] K. Marumoto, Y. Nagano, T. Sakamoto, S. Ukai, H. Ito, and S. Kuroda: *ESR studies of field-induced polarons in MIS diode structures with self-organized regioregular poly(3-hexylthiophene)*, Colloids Surf. A **284-285**, 617 (2006).

[Mat91] L. G. Matus, J. A. Powell, and C. S. Salupo: *High-voltage 6H-SiC p-n junction diodes*, Appl. Phys. Lett. **59**, 1770 (1991).

[May07] A. C. Mayer, S. R. Scully, B. E. Hardin, M. W. Rowell, and M. D. McGehee: *Polymer-based solar cells*, Mater. Today **10**, 28 (2007).

[McG09] M. D. McGehee: *Nanostructured organic-inorganic hybrid solar cells*, MRS Bull. **34**, 95 (2009).

[Mei03] E. J. Meijer, C. Detcheverry, P. J. Baesjou, E. van Veenendaal, D. M. de Leeuw, and T. M. Klapwijk: *Dopant density determination in disordered organic field-effect transistors*, J. Appl. Phys. **93**, 4831 (2003).

[Mih03] V. D. Mihailetchi, J. K. J. van Duren, P. W. M. Blom, J. C. Hummelen, R. A. J. Janssen, J. M. Kroon, M. T. Rispens, W. J. H. Verhees, and M. M. Wienk: *Electron transport in a methanofullerene*, Adv. Funct. Mater. **13**, 43 (2003).

[Mil05] D. J. Milliron, I. Gur, and A. P. Alivisatos: *Hybrid organic-nanocrystal solar cells*, MRS Bull. **30**, 41 (2005).

[Mil07] R. W. Miles, G. Zoppi, and I. Forbes: *Inorganic photovoltaic cells*, Mater. Today **10**, 20 (2007).

[Miz80] M. Mizuhashi: *Electrical properties of vacuum-deposited indium oxide and indium tin oxide films*, Thin Solid Films **70**, 91 (1980).

[Mol04] A. Moliton and R. C. Hiorns: *Review of electronic and optical properties of semiconducting π-conjugated polymers: Applications in optoelectronics*, Polym. Int. **53**, 1397 (2004).

[Mol06] A. Moliton and J.-M. Nunzi: *How to model the behaviour of organic photovoltaic cells*, Polym. Int. **55**, 583 (2006).

[Mot40] N. F. Mott and R. W. Gurney: *Electronic Processes in Ionic Crystals*, Clarendon, Oxford (1940).

[Mur98] K. Murata, Y. Shimoi, S. Abe, S. Kuroda, T. Noguchi, and T. Ohnishi: *Photogenerated polarons in poly(paraphenylene vinylene)*, Chem. Phys. **227**, 191 (1998).

[Mus98] I. Musa and W. Eccleston: *Properties of regioregular poly(3-alkylthiophene) schottky diodes*, Jpn. J. Appl. Phys. **37**, 4288 (1998).

[Nel10] J. Nelles, D. Sendor, F.-M. Petrat, and U. Simon: *Electric properties of surface functionalized silicon nanoparticles*, J. Nanopart. Res. **12**, 1367 (2010).

[Neu78] H. Neubrand: *ESR from boron in silicon at zero and small external stress*, Phys. Status Solidi B **86**, 269 (1978).

[Nie09] S. Niesar, R. Dietmueller, H. Nesswetter, H. Wiggers, and M. Stutzmann: *Silicon/organic semiconductor heterojunctions for solar cells*, Phys. Status Solidi A **12**, 2775 (2009).

[Nie10] S. Niesar, A. R. Stegner, R. N. Pereira, M. Hoeb, H. Wiggers, M. S. Brandt, and M. Stutzmann: *Defect reduction in silicon nanocrystals by low-temperature vacuum annealing*, Appl. Phys. Lett. **96**, 193112 (2010).

[Nie11] S. Niesar, W. Fabian, N. Petermann, D. Herrmann, E. Riedle, H. Wiggers, M. S. Brandt, and M. Stutzmann: *Efficiency enhancement in hybrid P3HT/silicon nanocrystal solar cells*, Green **1**, 339 (2011).

[Nik03] V. R. Nikitenko, H. Heil, and H. von Seggern: *Space-charge limited current in regioregular poly-3-hexyl-thiophene*, J. Appl. Phys. **94**, 2480 (2003).

[Nis02] K. Nishiguchi, X. Zhao, and S. Oda: *Nanocrystalline silicon electron emitter with a high efficiency enhanced by a planarization technique*, J. Appl. Phys. **92**, 2748 (2002).

[Odo02] T. W. Odom, J. C. Love, D. B. Wolfe, K. E. Paul, and G. M. Whitesides: *Improved pattern transfer in soft lithography using composite stamps*, Langmuir **18**, 5314 (2002).

[Oku08] T. Oku, S. Nagaoka, A. Suzuki, K. Kikuchi, Y. Hayashi, H. Inukai, H. Sakuragi, and T. Soga: *Formation and characterization of polymer/fullerene bulk heterojunction solar cells*, J. Phys. Chem. Solids **69**, 1276 (2008).

[Ols07] D. C. Olson, S. E. Shaheen, M. S. White, W. J. Mitchell, M. F. A. M. van Hest, R. T. Collins, and D. S. Ginley: *Band-offset engineering for enhanced open-circuit voltage in polymer-oxide hybrid solar cells*, Adv. Funct. Mater. **17**, 264 (2007).

[O´R91] B. O´Regan and M. Graetzel: *A low-cost, high-efficiency solar cell based on dye-sensitized colloidal TiO_2 films*, Nature **353**, 737 (1991).

[Pac06] R. Pacios, A. Chatten, K. Kawano, J. Durrant, D. Bradley, and J. Nelson: *Effects of photo-oxidation on the performance of poly[2-methoxy-5-(3´,7´-dimethyloctyloxy)-1,4-phenylene vinylene]:[6,6]-phenyl C_{61}-butyric acid methyl ester solar cells*, Adv. Funct. Mater. **16**, 2117 (2006).

[Pad01] F. Padinger, T. Fromherz, P. Denk, C. J. Brabec, J. Zettner, T. Hierl, and N. S. Sariciftci: *Degradation of bulk heterojunction solar cells operated in an inert gas atmosphere: A systematic study*, Synth. Met. **121**, 1605 (2001).

[Pal93] J. Palmour, J. Edmond, H. Kong, and C. Carter: *6H-silicon carbide devices and applications*, Phys. B: Cond. Mat. **185**, 461 (1993).

[Pal06a] V. Palermo, M. Palma, and P. Samorì: *Electronic characterization of organic thin films by kelvin probe force microscopy*, Adv. Mater. **18**, 145 (2006).

[Pal06b] J. Pallares, R. Cabre, L. F. Marsal, and R. E. I. Schropp: *A compact equivalent circuit for the dark current-voltage characteristics of nonideal solar cells*, J. Appl. Phys. **100**, 084513 (2006).

[Pan66] F. A. Pandovi and R. Stratton: *Field and thermionic-field emission in Schottky barriers*, Solid-State Electron. **9**, 695 (1966).

[Pan75] J. I. Pankove: *Optical processes in semiconductors*, Dover, New York (1975).

[Pan00] S. S. Pandey, W. Takashima, S. Nagamatsu, T. Endo, M. Rikukawa, and K. Kaneto: *Regioregularity vs regiorandomness: Effect on photocarrier transport in poly(3-hexylthiophene)*, Jpn. J. Appl. Phys. **39**, L94 (2000).

[Pap05] V. Papaefthimiou and S. Kennou: *Electronic properties of a semiconducting oligomer/silicon (111) interface: Influence of silicon doping*, Appl. Phys. Lett. **86**, 222105 (2005).

[Pap06] V. Papaefthimiou, A. Siokou, and S. Kennou: *The electronic structure of the interface between thin conjugated oligomer films and inorganic substrates with different work function*, Surf. Sci. **600**, 3987 (2006).

[Pei00] H. Peisert, T. Schwieger, M. Knupfer, M. S. Golden, and J. Fink: *Interface properties of organic/indium–tin oxide and organic/GeS(001) studied using photoemission spectroscopy*, J. Appl. Phys. **88**, 1535 (2000).

[Pei03] H. Peisert, M. Knupfer, and J. Fink: *Comparison of the electronic structure of $CuPCF_4/ITO$ and $CuPCF_4/Au$ interfaces*, Synth. Met. **137**, 869 (2003).

[Pel84] J. Pelletier, D. Gervais, and C. Pomot: *Application of wide-gap semiconductors to surface ionization: Work functions of AlN and SiC single crystals*, J. Appl. Phys. **55**, 994 (1984).

[Pen01] Z. A. Peng and X. Peng: *Formation of high-quality CdTe, CdSe, and CdS nanocrystals using CdO as precursor*, J. Am. Chem. Soc. **123**, 183 (2001).

[Per07] R. N. Pereira, A. R. Stegner, K. Klein, R. Lechner, R. Dietmueller, H. Wiggers, M. S. Brandt, and M. Stutzmann: *Electronic transport through Si nanocrystal films: Spin-dependent conductivity studies*, Physica B **401-402**, 527 (2007).

[Peu03] P. Peumans, A. Yakimov, and S. R. Forrest: *Small molecular weight organic thin-film photodetectors and solar cells*, J. Appl. Phys. **93**, 3693 (2003).

[Phi60] H. R. Philipp and E. A. Taft: *Silicon Carbide - A High Temperature Semiconductor*, Pergamon Press, Oxford (1960).

[Pie04] M. Pientka, V. Dyakonov, D. Meissner, A. Rogach, D. Talapin, H. Weller, L. Lutsen, and D. Vanderzande: *Photoinduced charge transfer in composites of conjugated polymers and semiconductor nanocrystals*, Nanotechnology **15**, 163 (2004).

[Pol05] A. Y. Polyakov, Q. Li, S. W. Huh, M. Skowronski, O. Lopatiuk, L. Chernyak, and E. Sanchez: *Minority carrier diffusion length measurements in 6H-SiC*, J. Appl. Phys. **97**, 053703 (2005).

[Poo07] J. Poortmans and V. Arkhipov: *Thin Film Solar Cells*, John Wiley & Sons Ltd., Hoboken (2007).

[Pop99] M. Pope and C. E. Swenberg: *Electronic Processes in Organic Crystals and Polymers*, Oxford University Press, New York (1999).

[Raf05] M. A. Rafiq, Y. Tsuchiya, H. Mizuta, S. Oda, S. Uno, Z. A. K. Durrani, and W. I. Milne: *Charge injection and trapping in silicon nanocrystals*, Appl. Phys. Lett. **87**, 182101 (2005).

[Raf06] M. A. Rafiq, Y. Tsuchiya, H. Mizuta, S. Oda, S. Uno, Z. A. K. Durrani, and W. I. Milne: *Hopping conduction in size-controlled Si nanocrystals*, J. Appl. Phys. **100**, 014303 (2006).

[Ran07] B. P. Rand, D. P. Burk, and S. R. Forrest: *Offset energies at organic semiconductor heterojunctions and their influence on the open-circuit voltage of thin-film solar cells*, Phys. Rev. B **75**, 115327 (2007).

[Ree00] C. A. Reed and R. D. Bolskar: *Discrete fulleride anions and fullerenium cations*, Chem. Rev. **100**, 1075 (2000).

[Ren05] V. D. Renzi, R. Rousseau, D. Marchetto, R. Biagi, S. Scandolo, and U. del Pennino: *Metal work-function changes induced by organic adsorbates: A combined experimental and theoretical study*, Phys. Rev. Lett. **95**, 046804 (2005).

[Rey06] J. Reynaert, V. Arkhipov, P. Heremans, and J. Poortmans: *Photomultiplication in disordered unipolar organic materials*, Adv. Funct. Mater. **16**, 784 (2006).

[Rie04] I. Riedel, J. Parisi, V. Dyakonov, L. Lutsen, D. Vanderzande, and J. C. Hummelen: *Effect of temperature and illumination on the electrical characteristics of polymer-fullerene bulk-heterojunction solar cells*, Adv. Funct. Mater. **14**, 38 (2004).

[Ros55] A. Rose: *Space-charge-limited currents in solids*, Phys. Rev. **97**, 1538 (1955).

[Ros00] J. Rostalski and D. Meissner: *Photocurrent spectroscopy for the investigation of charge carrier generation and transport mechanisms in organic p/n-junction solar cells*, Sol. Energy Mater. Sol. Cells **63**, 37 (2000).

[Ros09] M. Rosso, M. Giesbers, A. Arafat, K. Schroen, and H. Zuilhof: *Covalently attached organic monolayers on SiC and Si_xN_4 surfaces: Formation using UV light at room temperature*, Langmuir **25**, 2172 (2009).

[RR05] M. Reyes-Reyes, K. Kim, and D. L. Carroll: *High-efficiency photovoltaic devices based on annealed poly(3-hexylthiophene) and 1-(3-methoxycarbonyl)-propyl-1-phenyl-(6,6)C_{61} blends*, Appl. Phys. Lett. **87**, 083506 (2005).

[Ruf94] M. Ruff, H. Mitlehner, and R. Helbig: *SiC devices: Physics and numerical simulation*, IEEE Trans. Electron Devices **41**, 1040 (1994).

[Sal98] A. Salehi: *The effects of deposition rate and substrate temperature of ITO thin films on electrical and optical properties*, Thin Solid Films **324**, 214 (1998).

[Sar92] N. S. Sariciftci, L. Smilowitz, A. J. Heeger, and F. Wudl: *Photoinduced electron transfer from a conducting polymer to buckminsterfullerene*, Science **258**, 1474 (1992).

[Sar93] N. S. Sariciftci, D. Braun, C. Zhang, V. I. Srdanov, A. J. Heeger, G. Stucky, and F. Wudl: *Semiconducting polymer-buckminsterfullerene heterojunctions: Diodes, photodiodes, and photovoltaic cells*, Appl. Phys. Lett. **62**, 585 (1993).

[Sav05] T. J. Savenije, J. E. Kroeze, X. Yang, and J. Loos: *The effect of thermal treatment on the morphology and charge carrier dynamics in a polythiophene-fullerene bulk heterojunction*, Adv. Func **15**, 1260 (2005).

[Sca08] G. Scavia, W. Porzio, S. Destri, L. Barba, G. Arrighetti, S. Milita, L. Fumagalli, D. Natali, and M. Sampietro: *Effect of the silanization and annealing on the morphology of thin poly(3-hexylthiophene) (P3HT) layer on silicon oxide*, Surf. Science **602**, 3106 (2008).

[Sca10] G. Scarpa, A. Abdellah, A. Exner, S. Harrer, G. P. Blanco, W. Wiedemann, L. Schmidt-Mende, and P. Lugli: *Patterning poly(3-hexylthiophene) in the sub-50nm region by nanoimprint lithography*, IEEE Trans. Nanotech. , accepted (2010).

[Sch38] W. Schottky: *Halbleitertheorie der Sperrschicht*, Naturwiss. **26**, 843 (1938).

[Sch84] D. Schroder and D. Meier: *Solar cell contact resistance - A review*, IEEE Trans. Electron Devices **31**, 637 (1984).

[Sch00] H. Schmid and B. Michel: *Siloxane polymers for high-resolution, high-accuracy soft lithography*, Macromolecules **33**, 3042 (2000).

[Sch01] N. A. Schultz, M. C. Scharber, C. J. Brabec, and N. S. Sariciftci: *Low-temperature recombination kinetics of photoexcited persistent charge carriers in conjugated polymer/fullerene composite films*, Phys. Rev. B. **64**, 245210 (2001).

[Sch02] P. Schilinsky, C. Waldauf, and C. J. Brabec: *Recombination and loss analysis in polythiophene based bulk heterojunction photodetectors*, Appl. Phys. Lett. **81**, 3885 (2002).

[Sch04] R. D. Schaller and V. I. Klimov: *High efficiency carrier multiplication in PbSe nanocrystals: Implications for solar energy conversion*, Phys. Rev. Lett. **92**, 186601 (2004).

[Sch05] M. Schwoerer and H. C. Wolf: *Organische Molekulare Festkörper*, Wiley-VCH, Weinheim (2005).

[Sch06] S. J. Schoell: *Funktionalisierung von Siliziumkarbid*, Master's thesis, Walter Schottky Institut, Technische Universität München (2006).

[Sch08] S. J. Schoell, M. Hoeb., I. D. Sharp, W. Steins, M. Eickhoff, M. Stutzmann, and M. S. Brandt: *Functionalization of 6H-SiC surfaces with organosilanes*, Appl. Phys. Lett. **92**, 153301 (2008).

[Sek01] K. Seki, N. Hayashi, H. Oji, E. Ito, Y. Ouchi, and H. Ishii: *Electronic structure of organic/metal interfaces*, Thin Solid Films **393**, 298 (2001).

[Sey04] T. Seyller: *Passivation of hexagonal SiC surfaces by hydrogen termination*, J. Phys.: Condens. Matter **16**, S1755 (2004).

[Sha08] P. E. Shaw, A. Ruseckas, and I. D. W. Samuel: *Exciton diffusion measurements in poly(3-hexylthiophene)*, Adv. Mater. **20**, 3516 (2008).

[She03] G. Shen, D. Chen, K. Tang, Y. Qian, and S. Zhang: *Silicon carbide hollow nanospheres, nanowires and coaxial nanowires*, Chem. Phys. Lett. **375**, 177 (2003).

[She04] Y. Shen, A. R. Hosseini, M. H. Wong, and G. G. Malliaras: *How to make ohmic contacts to organic semiconductors*, ChemPhysChem **5**, 16 (2004).

[Shi07] M. Shibao, T. Morita, W. Takashima, and K. Kaneto: *Ambipolar transport in field-effect transistors based on composite films of poly(3-hexylthiophene) and fullerene derivative*, Jpn. J. Appl. Phys. **46**, L123 (2007).

[Sho61] W. Shockley and H. J. Queisser: *Detailed balance limit of efficiency of p-n junction solar cells*, J. Appl. Phys. **32**, 510 (1961).

[Shr06] V. Shrotriya, G. Li, Y. Yao, T. Moriarty, K. Emery, and Y. Yang: *Accurate measurement and characterization of organic solar cells*, Adv. Funct. Mater. **16**, 2016 (2006).

[Sie02] N. Sieber: *Wasserstoff- und Sauerstoffstabilisierte 6H-SiC(0001)-Oberflächen - Eine Studie chemischer und elektronischer Eigenschaften*, Ph.D. thesis, Universität Erlangen-Nürnberg (2002).

[Sir98] H. Sirringhaus, N. Tessler, and R. H. Friend: *Integrated optoelectronic devices based on conjugated polymers*, Science **280**, 1741 (1998).

[Sna04] H. J. Snaith, N. C. Greenham, and R. H. Friend: *The origin of collected charge and open-circuit voltage in blended polyfluorene photovoltaic devices*, Adv. Mater. **16**, 1640 (2004).

[Ste07] A. R. Stegner, R. N. Pereira, K. Klein, H. Wiggers, M. S. Brandt, and M. Stutzmann: *Phosphorus doping of Si nanocrystals: Interface defects and charge compensation*, Physica B **401-402**, 541 (2007).

[Ste08] A. R. Stegner, R. N. Pereira, K. Klein, R. Lechner, R. Dietmueller, M. S. Brandt, M. Stutzmann, and H. Wiggers: *Electronic transport in phosphorus-doped silicon nanocrystal networks*, Phys. Rev. Lett. **100**, 026803 (2008).

[Ste09] A. R. Stegner, R. N. Pereira, R. Lechner, K. Klein, H. Wiggers, M. Stutzmann, and M. S. Brandt: *Doping efficiency in freestanding silicon nanocrystals from the gas phase: Phophorus incorporation and defect-induced compensation*, Phys. Rev. B **80**, 165326 (2009).

[Ste10] M. Steenackers, I. D. Sharp, K. Larsson, N. A. Hutter, M. Stutzmann, and R. Jordan: *Structured polymer brushes on silicon carbide*, Chem. Mater. **22**, 272 (2010).

[Stu94] M. Stutzmann: *Amorphous Semiconductors,* in : *Handbook on Semiconductors*, edited by T. S. Moss, Vol. 3, Elsevier, Amsterdam (1994).

[Stu05] M. Stutzmann: *The physics and applications of amorphous, nano-, and microcrystalline semiconductors*, in *ICANS 21 Tutorial, Lisbon*, (2005).

[Suh01] K. Y. Suh, Y. S. Kim, and H. H. Lee: *Capillary force lithography*, Adv. Mater. **13**, 1386 (2001).

[Sun89] M. Sundberg, O. Inganas, S. Stafstrom, G. Gustafsson, and B. Sjogren: *Optical absorption of poly(3-alkylthiophenes) at low temperatures*, Solid State Commun. **71**, 435 (1989).

[Sun06] B. Sun and N. C. Greenham: *Improved effciency of photovoltaics based on CdSe nanorods and poly(3-hexylthiophene) nanofibers*, Phys. Chem. Chem. Phys. **8**, 3557 (2006).

[Swa92] L. S. Swanson and J. Shinar: *Electroluminescence-detected magnetic-resonance study of polyparaphenylenevinylene (PPV)-based light-emitting diodes*, Phys. Rev. B **46**, 15072 (1992).

[Sze07] S. M. Sze and K. K. Ng: *Physics of Semiconductor Devices*, John Wiley & Sons, Inc., Hoboken (2007).

[Tah98] R. B. H. Tahar, T. Ban, Y. Ohya, and Y. Takahashi: *Tin doped indium oxide thin films: Electrical properties*, J. Appl. Phys. **83**, 2631 (1998).

[Tak05] K. Takahashi, Y. Takano, T. Yamaguchi, J. Nakamura, C. Yokoe, and K. Murata: *Porphyrin dye-sensitization of polythiophene in a conjugated polymer/TiO_2 p-n hetero-junction solar cell*, Synth. Met. **155**, 51 (2005).

[Tan86] C. W. Tang: *Two-layer organic photovoltaic cell*, Appl. Phys. Lett. **48**, 183 (1986).

[Tan03] J.-H. Tan and W. A. Anderson: *Current transport in copper indium gallium diselenide solar cells comparing mesa diodes to the full cell*, Sol. Energy Mater. Sol. Cells **77**, 283 (2003).

[Ten06] C. Tengstedt, W. Osikowicz, W. R. Salaneck, I. D. Parker, C.-H. Hsu, and M. Fahlman: *Fermi-level pinning at conjugated polymer interfaces*, Appl. Phys. Lett. **88**, 053502 (2006).

[Ter85] J. Tersoff: *Schottky barriers and semiconductor band structures*, Phys. Rev. B **32**, 6968 (1985).

[Tha07] A. K. Thakur, A. K. Mukherjee, D. M. G. Preethichandra, W. Takashima, and K. Kaneto: *Charge injection mechanism across the Au-poly(3-hexylthiophene-2,5-diyl) interface*, J. Appl. Phys. **101**, 104508 (2007).

[Tsa07] L. Tsakalakos, J. Balch, J. Fronheiser, B. A. Korevaar, O. Sulima, and J. Rand: *Silicon nanowire solar cells*, Appl. Phys. Lett. **91**, 233117 (2007).

[Tsu00] T. Tsuzuki, Y. Shirota, J. Rostalski, and D. Meissner: *The effect of fullerene doping on photoelectric conversion using titanyl phthalocyanine and a perylene pigment*, Sol. Energy Mater. Sol. Cells **61**, 1 (2000).

[Wag10] A. Wagenpfahl, D. Rauh, M. Binder, C. Deibel, and V. Dyakonov: *On the s-shape current-voltage characteristics of organic solar devices* , arXiv:1005.5669v1 (2010).

[Wal03] C. G. van de Walle and J. Neugebauer: *Universal alignment of hydrogen levels in semiconductors, insulators and solutions*, Nature **423**, 626 (2003).

[Wal06] C. Waldauf, M. C. Scharber, P. Schilinsky, J. A. Hauch, and C. J. Brabec: *Physics of organic bulk heterojunction devices for photovoltaic applications*, J. Appl. Phys. **99**, 104503 (2006).

[Wer94] J. H. Werner, U. Spadaccini, and F. Banhart: *Low-temperature ohmic Au/Sb contacts to n-type Si*, J. Appl. Phys. **75**, 994 (1994).

[Wie10] W. Wiedemann, L. Sims, A. Abdellah, A. Exner, R. Meier, K. P. Musselman, J. L. MacManus-Driscoll, P. Müller-Buschbaum, G. Scarpa, P. Lugli, and L. Schmidt-Mende: *Nanostructured interfaces in polymer solar cells*, Appl. Phys. Lett. **96**, 263109 (2010).

[Wik10] Wikipedia: http://en.wikipedia.org/wiki/PCBM (2010).

[Wil04] E. J. Wilhelm and J. M. Jacobson: *Direct printing of nanoparticles and spin-on-glasses by offset liquid embossing*, Appl. Phys. Lett. **84**, 3507 (2004).

[Wu02] X. Wu, J. Keane, R. Dhere, C. DeHart, A. Duda, T. Gessert, S. Asher, D. Levi, and P. Sheldon: *16.5%-efficient CdS/CdTe polycrystalline thin film solar cell*, Proc. 17th European Photovoltaic Solar Energy Conference , 995 (2002).

[Wue00] P. Wuerfel: *Physik der Solarzellen*, Spektrum Akademischer Verlag, Heidelberg (2000).

[Xia98] Y. Xia and G. M. Whitesides: *Soft lithography*, Angew. Chem. Int. Ed. **37**, 550 (1998).

[Xue04] J. Xue, S. Uchida, B. R. Rand, and S. R. Forrest: *4.2% efficient organic photovoltaic cells with low series resistances*, Appl. Phys. Lett. **84**, 3013 (2004).

[Yan02] L. Yan, N. J. Watkins, S. Zorba, Y. Gao, and C. W. Tang: *Thermodynamic equilibrium and metal-organic interface dipole*, Appl. Phys. Lett. **81**, 2752 (2002).

[Yi06] Y. Yi, J. E. Lyon, M. M. Beerbom, and R. Schlaf: *Characterization of indium tin oxide surfaces and interfaces using low intensity x-ray photoemission spectroscopy*, J. Appl. Phys. **100**, 093719 (2006).

[You97a] C. F. Young, E. H. Poindexter, and G. J. Gerardi: *Electron paramagnetic resonance of porous silicon: Observation and identification of conduction-band electrons*, J. Appl. Phys. **81**, 7468 (1997).

[You97b] C. F. Young, E. H. Poindexter, G. J. Gerardi, W. L. Warren, and D. J. Keeble: *Electron paramagnetic resonance of conduction-band electrons in silicon*, Phys. Rev. B **55**, 16245 (1997).

[Yu95] G. Yu, J. Gao, J. C. Hummelen, F. Wudl, and A. J. Heeger: *Polymer photovoltaic cells: Enhanced efficiencies via a network of internal donor-acceptor heterojunctions*, Science **270**, 1789 (1995).

[Zha98] J. Zhao, A. Wang, and M. A. Green: *19.8% efficient "'honeycomb"' textured multicrystalline and 24.4% monocrystalline silicon solar cells*, Appl. Phys. Lett. **73**, 1991 (1998).

[Zho01] X. Zhou, J. Blochwitz, M. Pfeiffer, A. Nollau, T. Fritz, and K. Leo: *Enhanced hole injection into amorphous hole-transport layers of organic light-emitting diodes using controlled p-type doping*, Adv. Funct. Mater. **11**, 310 (2001).

[Zho06] U. Zhokhavets, T. Erb, H. Hoppe, G. Gobsch, and N. S. Sariciftci: *Effect of annealing of poly(3-hexylthiophene)/fullerene bulk heterojunction composites on structural and optical properties*, Thin Solid Films **496**, 679 (2006).